

*Reconstructing Western Australian climate history from
marine archives over the past 450 kyr*

Dissertation

In fulfillment of the requirements for the degree “Dr. rer. nat.”

Of the Faculty of Mathematics and Natural Sciences

At Kiel University

Submitted by

Renjie Pei

Kiel, 2021

Referent: Prof. Dr. Wolfgang Kuhnt

Koreferent: Prof. Dr. Martin Frank

Tag der Disputation: 30.06.2021

Zum Druck genehmigt:

Der Dekan: Prof. Dr. Frank Kempken

Eidesstattliche Erklärung


Hiermit erkläre ich an Eides statt, dass die vorliegende Dissertation mit dem Titel „Reconstructing Western Australian climate history from marine archives over the past 450 kyr“, abgesehen von der Beratung durch meine akademischen Lehrer, in Inhalt und Form meine eigene Arbeit darstellt.

Ich habe diese Arbeit, ganz oder zum Teil, an keiner anderen Stelle im Rahmen eines Prüfungsverfahrens vorgelegt. Teile dieser Arbeit wurden zur Veröffentlichung in Fachzeitschriften eingereicht oder sind in Vorbereitung eingereicht zu werden.

Diese Arbeit ist unter Einhaltung der Regeln guter wissenschaftlicher Praxis der Deutschen Forschungsgemeinschaft (DFG) entstanden.

Ich versichere weiterhin, dass mir bisher kein akademischer Grad entzogen worden ist.

Kiel, den 11.05.2021



Renjie Pei

Abstract

A meridional transect of high-resolution Holocene to late Pleistocene sediment archives along the Northwestern Australian Margin provides crucial information to explore the spectrum of natural climate variability and to untangle dynamic processes and feedbacks controlling climate evolution. This information is needed to constrain modeling experiments of past and future climate change, as modern greenhouse gases emission rates constantly increase. A multitude of proxy reconstructions at drill sites located in the eastern Indian Ocean along the Northwestern Australian Margin is presented in this thesis, with the main objectives of: (1) evaluating the phase relationship between orbital forcing and Australian monsoonal climate and (2) increasing our knowledge on the coupling between local climate variability in northwest Australia and global climate changes (Intertropical Convergence Zone (ITCZ) and Indonesian Throughflow).

The variability in sediment discharge from northwestern Australia provides a powerful tool to monitor changes in the position and intensity of the Australian monsoonal rainbelt. Elemental composition of core-top samples retrieved during R/V Sonne cruise SO257 along the Northwestern Australian Margin closely match elemental signatures of major river catchments and sediment accumulation rates generally increase northward. We integrate high-resolution X-ray fluorescence (XRF) scanning elemental records, carbon and oxygen isotopes and Mg/Ca derived sea surface temperatures from Core SO257–18548 and International Ocean Discovery Program (IODP) Site U1482, situated southwest of the Scott Plateau at the southern edge of the present-day monsoonal belt, from Core SO257–18571, located within the dust-cyclone belt offshore Northwest Cape south of the Exmouth Plateau, and from Core MD01-2378 and IODP Site U1483, located within the Timor Sea in the easternmost Indian Ocean. The chronology of these sediment successions is based on ^{14}C dating over the last glacial

termination and on correlation of the benthic oxygen isotope record to the LR04 stack (Lisiecki and Raymo, 2005).

We use XRF scanner-derived estimates of terrigenous fluvial discharge and eolian dust combined with foraminiferal isotope and Mg/Ca-derived sea surface temperature data in a suite of sediment cores to reconstruct monsoonal climate evolution over the last four glacial cycles. This latitudinal transect includes the tropical monsoon region of northwestern Australia, and the arid zone where rainfall mainly occurs during landfall of tropical cyclones. Our results suggest that the intensity of Australian monsoon precipitation and the position of ITCZ were strongly affected by changes in Southern Hemisphere temperatures and the interhemispheric temperature gradient. Interglacial and suborbital Southern Hemisphere warm periods were associated with intensification and southward migration of the Australian monsoonal rain belt and heightened cyclone activity, whereas cold periods were characterized by weakened monsoon, extended aridity and intensified trade winds increasing dust fluxes. The intensity of summer monsoon rainfall during glacial terminations is strongly correlated to Antarctic ice core greenhouse gas (CO_2 and CH_4) concentrations and SST records off northwestern Australia. Distinct $p\text{CO}_2$ and methane maxima at the end of Terminations I-IV, in particular the characteristic methane-spike at the end of the last glacial termination ($\sim 10\text{--}7$ ka), are paralleled by massive increases in monsoonal runoff from northwestern Australia. Comparison of our precipitation record with published precipitation records from the northern margin and meteorological center of the Indo-Pacific ITCZ shows that precipitation changed nearly in-phase between the hemispheres on the precession band, possibly linked to expansion and contraction in the latitudinal extent of the Indo-Pacific ITCZ. In contrast, interhemispheric precipitation was nearly in anti-phase on the obliquity band, likely due to latitudinal migration of the Indo-Pacific ITCZ. Our findings imply that tropical hydroclimate cycles were regulated by the orbital forcing but with significantly different response to changes of the ITCZ on

precession and obliquity bands. In Chapter 2, the additional oxygen isotopes and Mg/Ca based temperature of planktonic foraminifers data from core top samples collected during R/V Sonne Cruise SO257 in May 2017 present a steep Southward increase in planktonic $\delta^{18}\text{O}$, associated with a decrease in SST, which indicates that the southwestern front of the Indo-Pacific Warm Pool is located between 23 and 24°S during austral fall. In Chapter 3 benthic and planktonic carbon isotopes integrated with XRF scanner derived barium, Log(iodine/calcium) and bromine enable us to determine that productivity fluctuations over the last 450 kyr were strongly influenced by Australian summer monsoon variability offshore northwestern Australia (23 and 19 kyr) and were also modulated by glacial-interglacial variability (100 kyr) associated with the intensity of trade winds and sea level–related variations in the intensity of the Indonesian Throughflow (100 kyr).

Zusammenfassung

Ein meridionaler Transekt hochauflösender holozäner bis spätpleistozäner Sedimentarchive entlang des westaustralischen Kontinentalrandes liefert wichtige Informationen, um das Spektrum der natürlichen Klimavariabilität zu erkunden und dynamische Prozesse und Rückkopplungen zu entwirren, die die Klimaentwicklung steuern. Diese Informationen werden außerdem nützlich sein, um Modellierungsexperimente des vergangenen und zukünftigen Klimawandels, wenn die Treibhausgasemissionsraten ständig steigen, zu unterstützen. In dieser Arbeit wird eine Vielzahl von Proxy-Rekonstruktionen an Bohrstellen im östlichen Indischen Ozean entlang des westlichen australischen Kontinentalrandes vorgestellt, mit den Hauptzielen: (1) Bewertung der Phasenbeziehung zwischen Orbitaltrieb und australischem Monsunklima und (2) Beitrag zum Verständnis der Kopplung zwischen der lokalen nordwestaustralischen Klimavariabilität und globalen Klimaveränderungen (Intertropische Konvergenzzone (ITCZ) und indonesischer Durchstrom).

Die Variabilität des fluviatilen Sedimenteintrags aus dem Nordwesten Australiens bietet ein leistungsstarkes Instrument zur Rekonstruktion von Änderungen der Position und Intensität des australischen Monsunregengürtels. Die Elementzusammensetzung der Sedimentoberflächen-Proben, die während der R / V Sonne-Expedition SO257 entlang des nördlichen und westlichen australischen Randes entnommen wurden, stimmt eng mit den Elementarsignaturen der wichtigsten Flusseinzugsgebiete überein, und die Sedimentakkumulationsraten nehmen im Allgemeinen nach Norden hin zu. Wir integrieren hochauflösende Röntgenfluoreszenz (XRF)-Scanner-Elementaufzeichnungen, Kohlenstoff- und Sauerstoffisotope und von Mg / Ca abgeleitete Meeresoberflächentemperaturen (SST) aus dem Sedimentkern SO257–18548 und IODP (International Ocean Discovery Program)-Bohrung U1482 südwestlich des Scott-Plateaus am südlichen Rand des heutigen Monsungürtels, von Core SO257–18571, innerhalb des Staubsturmregens vor dem

Nordwestkap südlich des Exmouth-Plateaus, und von Core MD01-2378 und IODP-Bohrung U1483, in der nordöstlichen Timor Sea. Die Chronologie dieser Sedimentfolgen basiert auf der ^{14}C -Datierung über die letzte glaziale Termination und auf der Korrelation des benthischen Sauerstoffisotopendatensatzes mit dem globalen LR04-Stack.

Wir verwenden vom RFA-Scanner abgeleitete Schätzungen des terrigenen Flusseintrags und äolischen Staubes in Kombination mit an oberflächennah lebenden planktonischen Foraminiferen gemessenen Sauerstoffisotopen- und Mg/Ca-Daten rekonstruierten SST, um in einer Reihe von Sedimentkernen die Monsunklimaentwicklung über die letzten vier Glazialzyklen zu rekonstruieren. Der durch die drei Kernlokationen abgedeckte Transekt umfasst die tropische Monsunregion im Nordwesten Australiens und die südlich anschließende aride Zone, in der Niederschläge fast ausschließlich während des Landfalls tropischer Wirbelstürme (Zyklone) auftreten. Unsere Ergebnisse legen nahe, dass die Intensität des australischen Monsunniederschlags und die Position des ITCZ stark von Änderungen der Temperaturen der südlichen Hemisphäre und des interhemisphärischen Temperaturgradienten beeinflusst wurden. Interglaziale und suborbitale Warmperioden der südlichen Hemisphäre waren mit einer Intensivierung und Verschiebung des australischen Monsunregengürtels nach Süden sowie einer erhöhten Zyklonaktivität verbunden, während Kälteperioden durch abgeschwächten Monsun, verlängerte Trockenperioden und verstärkte Passatwinde gekennzeichnet waren, die den Staubfluss erhöhten. Die Intensität der sommerlichen Monsunregenfälle während der glazialen Terminationen korreliert stark mit den Treibhausgaskonzentrationen (CO_2 und CH_4) in den antarktischen Eiskernen und den Meeresoberflächentemperaturen vor Westaustralien. Deutliche $p\text{CO}_2$ - und Methan-Maxima am Ende der Terminationen I-IV, insbesondere die charakteristische Methanspitze am Ende der letzten Termination ($\sim 10\text{-}7$ ka), gehen mit einem massiven Anstieg des monsunalen Sedimenteintrags aus Nordwestaustralien einher. Ein Vergleich unserer Niederschlags-

Rekonstruktionen mit veröffentlichten Rekonstruktionen vom nördlichen Rand und vom meteorologischen Zentrum der indopazifischen ITCZ zeigt, dass sich die Niederschläge in den beiden Hemisphären auf dem Präzessionsband (23 kyr) nahezu gleichphasig verändert haben, möglicherweise im Zusammenhang mit einer Expansion und Kontraktion in der Breitenausdehnung der indopazifischen ITCZ. Im Gegensatz dazu war der interhemisphärische Niederschlag auf dem Obliquitätsband (41 kyr) nahezu gegenphasig war. Unsere Ergebnisse deuten darauf hin, dass tropische Hydroklimazyklen durch den Orbitalantrieb reguliert wurden, jedoch mit einer unterschiedlichen Reaktion der ITCZ auf die Variabilität der Präzession und Schiefe der Erdachse. In Kapitel 2 zeigen in einem N-S Transekt von Oberflächen-Sedimentproben der R/V Sonne-Expedition SO257 im Mai 2017 die Sauerstoffisotope und die auf Mg/Ca planktischer Foraminiferen basierenden Meeresoberflächentemperaturen einen steilen Anstieg des planktischen $\delta^{18}\text{O}$ -Werte südlich von 23°S auf, der mit einer Abnahme der Meeresoberflächentemperatur (SST) verbunden ist. Dies weist darauf hin, dass sich die südwestliche Front des Indopazifischen Warmpools im australischen Herbst heute zwischen 23° und 24° S befindet. Der Gradient zwischen planktischen und benthischen Kohlenstoffisotopwerten, zusammen mit Schwankungen im Barium, Jod und Brom-Gehalt der Sedimente aus XRF-Scannerdaten ermöglichen es uns, die Variabilität der Oberflächenproduktivität über die letzten 450 kyr zu rekonstruieren. Diese zeigt eine starke Variabilität im Bereich des Präzessionsbandes (23 und 19 kyr) und ist zusätzlich durch glaziale-interglaziale Variabilität kontrolliert. Diese Phasenbeziehungen lassen darauf schließen, dass die Produktivität vor der Küste Nordwestaustraliens stark von der Intensität des australischen Wintermonsuns (Passatwinde) und der Intensität des Indonesischen Durchstroms beeinflusst wurde.

Contents

<i>Abstract</i>	i
<i>Zusammenfassung</i>	v
<i>Contents</i>	ix
1. Introduction	1
1.1 <i>Background and motivation</i>	3
1.2 <i>Research questions and thesis outline</i>	6
1.3 <i>References</i>	8
2. Publications and Manuscripts	11
Chapter 1: Monitoring Australian Monsoon variability over the past four glacial cycles.....	13
Supporting information for <i>Chapter 1</i>	55
Chapter 2: Evolution of sea surface hydrology along the Northwestern Australian Margin over the past 450 kyr.....	73
Supporting information for <i>Chapter 2</i>	113
Chapter 3: Evolution of paleoproductivity and $\delta^{13}\text{C}$ gradients along the Northwestern Australian Margin over the last 450 kyr	123
Supporting information for <i>Chapter 3</i>	153
Chapter 4: Indo-Pacific Hydroclimate in Response to Changes of the Intertropical Convergence Zone: Discrepancy on Precession and Obliquity Bands Over the Last 410 kyr.....	157
Supporting information for <i>Chapter 4</i>	177
3. Conclusions and highlights for future research	193
3.1 <i>Conclusions</i>	195
3.2 <i>Highlights for future research</i>	197
<i>Acknowledgements</i>	199
<i>Appendix</i>	201

1. Introduction

1.1 Background and Motivation

The Intertropical Convergence Zone (ITCZ) is commonly defined as an equatorial zone where the trade winds converge. As the ascending branch of the Hadley circulation (Waliser & Gautier, 1993), the ITCZ is characterized by deep convective and heavy precipitation (Schneider et al., 2014) and thus exerts a significant influence on global hydroclimate change. Today, the ITCZ moves seasonally toward the Southern or Northern Hemisphere, but the mean position of the ITCZ is mostly north of the equator, likely linked to the northward energy transport of the Atlantic meridional overturning circulation (Marshall, 2014).

Western Australia is located at the southern limit of the seasonal (austral summer) displacement of the ITCZ and is marginally affected by the Australasian monsoon system today. The climate and hydrography are strongly influenced by seasonal changes in wind direction associated with the southward migration of the ITCZ during austral summer. During December–February, NW winds predominate and rainfall increases over Indonesia and northern Australia (Australian summer monsoon), whereas dry SE Trade Winds prevail during austral winter (June–November). On longer timescales, Variations in Australian summer monsoon are related to changes in precessional summer insolation, sea level fluctuations and atmospheric CO₂ concentrations (e.g. Dinezio & Tierney, 2013; Griffiths et al., 2009; Kuhnt et al., 2015; Wyrwoll et al., 2007) and the latitudinal extent of monsoonal rainfall controlled by the meridional position of the ITCZ which is highly possibly dependent on the interhemispheric temperature gradient (e.g Mohtadi et al., 2016; Schneider et al., 2014). Climate models predict drier subtropics in the Southern Hemisphere during interstadials (Broccoli et al., 2006; Chiang et al., 2008) due to northward shift of the ITCZ during Northern Hemisphere warming (B-A, 15 – 12.9ka) and intensification of the austral summer monsoon during Northern Hemisphere cooling (Heinrich Stadial 1 (HS 1), 18 – 15 ka and YD, 12.9 –

11.7 ka). However, model predictions of a hemispherical seesaw during the last glacial termination are not fully supported by climate proxy data (De Deckker et al., 2012; Denton et al., 2010; Shakun et al., 2012) and remain contradictory in particular for the earliest part of the last deglaciation (HS 1). The response of the Australian Monsoon to high-latitude temperature fluctuations on orbital, suborbital and millennial timescales is still poorly understood due to the scarcity of continuous high-resolution precipitation and runoff records from the Australian continent.

The oceanography of Western Australia, in particular regional temperature, salinity and productivity, is fundamentally influenced by the Indonesian Throughflow (ITF) and Leeuwin Current. The ITF transfers surface and intermediate waters from the Pacific Ocean, thus regulating the heat and freshwater budgets of tropical water masses and affecting regional and global climate. The Leeuwin Current is initiated through a build-up of sea-level by monsoonal winds during December – February in the Gulf of Carpentaria (Ridgway and Godfrey, 2015) and propagates further southwest along the continental shelf of Western Australia as a warm, fresh and oligotrophic current compared to adjacent surface water masses (Weller et al., 2011). The ITF and Leeuwin Current volume transport varies during the El Niño–Southern Oscillation (ENSO) cycle, being stronger during the La Niña phase and weaker during the El Niño phase (Clarke and Liu, 1994; Feng et al., 2005; Feng and Meyers, 2003; Liu et al., 2015; Meyers, 1996). ENSO is the most important year-to-year fluctuation of the climate system on our earth, which is the positive feedback between trade wind intensity and zonal contrasts in sea surface temperature (SST) (e.g. Cai et al., 2015; McPhaden et al., 2006). This inter-ocean transmittance of lower frequency climate signals by the ITF must also have affected insolation-modulated long-term ENSO variability and thus impacted the orbital scale variability of temperature and salinity variability along the northNorthwestern Australian Margin. The

region represents a key area to chart the temporal variability of the ITF and Leeuwin Current, thereby to determine the relationships to ENSO and high and low latitude climate change.

In my thesis, I present temperature, salinity and runoff data from high-resolution Holocene to late Pleistocene sediment archives from a transect along the Northwestern Australian Margin (Figure 1) that provide crucial information to explore the spectrum of natural climate variability and to untangle dynamic processes and feedbacks controlling climate evolution in relation to high latitude climate change. These data will additionally be useful to constrain modeling experiments of past and future climate change.

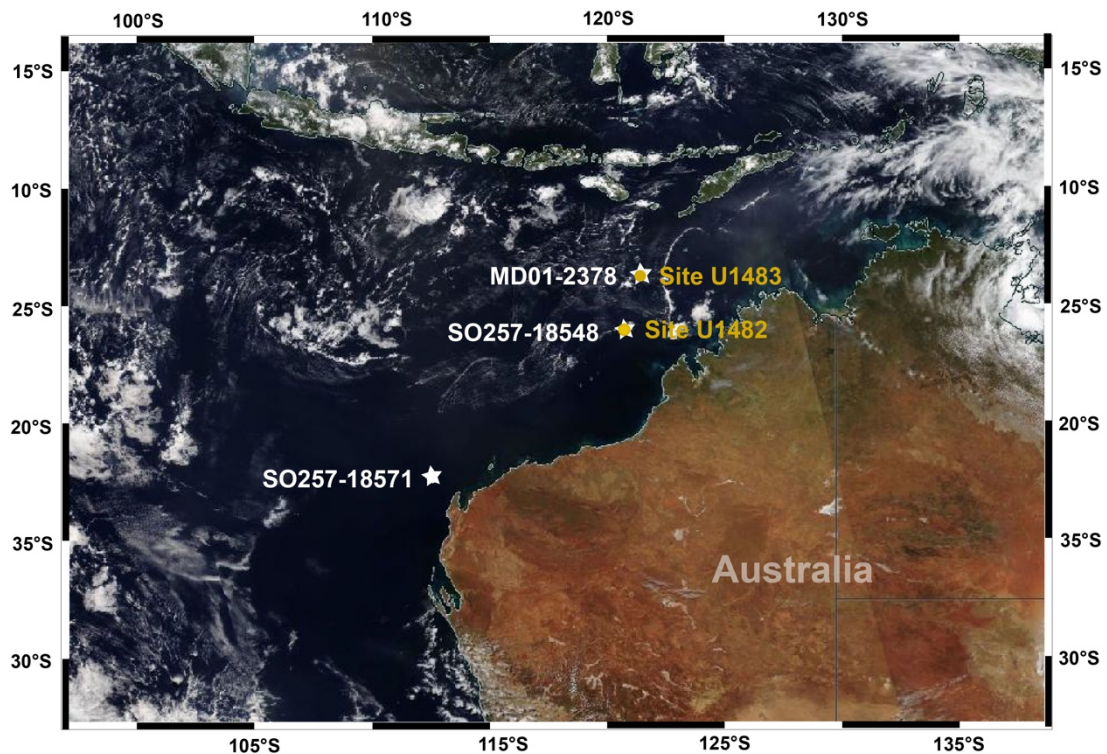


Figure 1. Locations of cored sites studied in the present thesis. Integrated Ocean Drilling Program (IODP) Expedition 363 Sites U1482, U1483 (yellow dots), MD01-2378 and SO257-18548 and -18571 (white dots) Base map created with <https://worldview.earthdata.nasa.gov>.

1.2 Research Questions and Thesis Outline

RQ I: How did the Australian Monsoon respond to the variability in atmospheric greenhouse gas concentrations and high-latitude temperature fluctuations over the last four glacial cycles?

RQ II: What was the phase relationship between insolation, high latitude climate and Australian Monsoon variability?

RQ III: How did the ITF and Leeuwin Current temporally vary and how were fluctuations in these current systems connected to ENSO-like climate variability and to changes in Western Australian monsoonal climate?

RQ IV: How was Southern Hemisphere deglacial warming related to insolation changes and atmospheric carbon dioxide increases? What was the phase relationship between changes in insolation, deglaciation, Southern Hemisphere/tropical warming and greenhouse gases?

RQ V: How did the Western Australian arid zone and dust belt evolve over the last four glacial cycles?

The main objectives of this thesis are:

Chapter 1: We compare X-ray fluorescence (XRF) core scanner-derived elemental records in two extended sediment successions retrieved at the southern edge of the present-day monsoonal belt southwest of the Scott Plateau and within the dust-cyclone belt offshore Northwest Cape to monitor monsoonal runoff and dust fluxes on millennial timescales over the last four glacial cycles. Our main objectives are to reconstruct the variability of the tropical convection along the southernmost displacement of the ITCZ during austral summer in relation to changes in high-latitude climate, sea level and atmospheric greenhouse gas concentration in order to monitor changes in the latitudinal temperature gradient and the intensity of the Walker circulation.

Chapter 2: We monitor the variability of Southern Hemisphere tropical and subtropical hydrology in core top samples collected during R/V Sonne Cruise SO257 in May 2017 at sensitive locations along the southwestern front of the Indo-Pacific Warm Pool (IPWP). We additionally reconstruct SST, sea surface salinity (SSS) and $\delta^{18}\text{O}$ seawater ($\delta^{18}\text{O}_{\text{sw}}$) over the last 450 kyr in two sediment successions located at the southwestern edge of the IPWP (within the monsoonal rain belt) and southwest of the IPWP (outwith the monsoonal rain belt). Our main objectives are to monitor the variability of Southern Hemisphere tropical and subtropical SST and SSS on millennial timescales and to relate their variability to sediment discharge records of the Australian Monsoon, insolation forcing, high latitude climate evolution and changing atmospheric greenhouse gas concentrations.

Chapter 3: We present multi-proxy records of productivity from two sediment cores retrieved at the western edge of the IPWP, and within the dust-cyclone belt offshore Northwest Cape to track changes in intermediate water ventilation and paleoproductivity over the last 450 kyr. Both cores are located downstream of the main outflow of the ITF through the Timor Strait and are well suited for investigating variations in tropical productivity that may be related to thermohaline circulation changes and tropical climate dynamics. Our main objectives are (1) to determine the geochemical proxies for reconstruction of paleoproductivity. (2) to investigate changes in the productivity driven particle flux to the deep ocean in relation to orbital forcing, (3) to assess linkages of paleoproductivity and carbon flux variations to Austral Summer monsoon precipitation and winter monsoon (4) to investigate the connections between the benthic $\delta^{13}\text{C}$ and glacial-interglacial global carbon cycle changes.

Chapter 4: We present a new well-dated and high-resolution long-term summer monsoonal precipitation record spanning the past 410 kyr from IODP Site U1483 situated at the southern margin of the Indo-Pacific ITCZ and compare our rainfall records to published data from different regions. Our main objectives is to form a meridional transect across the full

extent of the Indo-Pacific ITCZ, providing an unprecedented opportunity for us to gain insight into the overall dynamics of the ITCZ on orbital timescales.

1.3 References

- Broccoli, A. J., Dahl, K. A., & Stouffer, R. J. (2006). Response of the ITCZ to Northern Hemisphere cooling. *Geophysical Research Letters*, 33(1), 1–4. <https://doi.org/10.1029/2005GL024546>
- Cai, W., Santoso, A., Wang, G., Yeh, S. W., An, S. Il, Cobb, K. M., et al. (2015). ENSO and greenhouse warming. *Nature Climate Change*, 5(9), 849–859. <https://doi.org/10.1038/nclimate2743>
- Chiang, J. C. H., Fang, Y., & Chang, P. (2008). Interhemispheric thermal gradient and tropical Pacific climate. *Geophysical Research Letters*, 35(14), 2–6. <https://doi.org/10.1029/2008GL034166>
- Clarke, A. J., & Liu, X. (1994). Interannual Sea Level in the Northern and Eastern Indian Ocean. *Journal of Physical Oceanography*, 24(6), 1224–1235. [https://doi.org/10.1175/1520-0485\(1994\)024<1224:ISLITN>2.0.CO;2](https://doi.org/10.1175/1520-0485(1994)024<1224:ISLITN>2.0.CO;2)
- De Deckker, P., Moros, M., Perner, K., & Jansen, E. (2012). Influence of the tropics and southern westerlies on glacial interhemispheric asymmetry. *Nature Geoscience*, 5(4), 266–269. <https://doi.org/10.1038/ngeo1431>
- Denton, G. H., Anderson, R. F., Toggweiler, J. R., Edwards, R. L., Schaefer, J. M., & Putnam, A. E. (2010). The last glacial termination. *Science*, 328(5986), 1652–1656. <https://doi.org/10.1126/science.1184119>
- Dinezio, P. N., & Tierney, J. E. (2013). The effect of sea level on glacial Indo-Pacific climate. *Nature Geoscience*, 6(6), 485–491. <https://doi.org/10.1038/ngeo1823>
- Duane E. Waliser, & Gautier Catherine. (1993). A Satellite-derived Climatology of the ITCZ. *Journal of Climate*, 6(11), 2162–2174. [https://doi.org/10.1175/1520-0442\(1993\)006<2162:ASDCOT>2.0.CO;2](https://doi.org/10.1175/1520-0442(1993)006<2162:ASDCOT>2.0.CO;2)
- Feng, M., & Meyers, G. (2003). Interannual variability in the tropical Indian Ocean: A two-year time-scale of Indian Ocean Dipole. *Deep-Sea Research Part II: Topical Studies in Oceanography*, 50(12–13), 2263–2284. [https://doi.org/10.1016/S0967-0645\(03\)00056-0](https://doi.org/10.1016/S0967-0645(03)00056-0)
- Feng, M., Wijffels, S., Godfrey, S., & Meyers, G. (2005). Do eddies play a role in the momentum balance of the Leeuwin Current? *Journal of Physical Oceanography*, 35(6), 964–975. <https://doi.org/10.1175/JPO2730.1>
- Griffiths, M. L., Drysdale, R. N., Gagan, M. K., Zhao, J. X., Ayliffe, L. K., Hellstrom, J. C., et al. (2009). Increasing Australian-Indonesian monsoon rainfall linked to early Holocene sea-level rise. *Nature Geoscience*, 2(9), 636–639. <https://doi.org/10.1038/ngeo605>
- Kuhnt, W., Holbourn, A., Xu, J., Opdyke, B., De Deckker, P., Röhl, U., & Mudelsee, M. (2015). Southern Hemisphere control on Australian monsoon variability during the late deglaciation and Holocene. *Nature Communications*, 6. <https://doi.org/10.1038/ncomms6916>

- Liu, Q., Feng, M., Wang, D., & Wijffels, S. (2015). Interannual variability of the Indonesian Throughflow transport: A revisit based on 30 year expendable bathythermograph data. *Journal of Geophysical Research: Oceans*, 120, 8270–8282. <https://doi.org/10.1002/2015JC011351>
- Marshall, M. (2014). Researchers-in-residence: a solution to the challenge of evidence-informed improvement? *Primary Health Care Research & Development*, 15(4), 337–338. <https://doi.org/10.1017/S1463423614000310>
- McPhaden, M. J., Zebiak, S. E., & Glantz, M. H. (2006). ENSO as an integrating concept in earth science. *Science*, 314(5806), 1740–1745. <https://doi.org/10.1126/science.1132588>
- Meyers, G. (1996). Variation of Indonesian throughflow and the El Niño - Southern Oscillation. *Journal of Geophysical Research C: Oceans*, 101(C5), 12255–12263. <https://doi.org/10.1029/95JC03729>
- Mohtadi, M., Prange, M., & Steinke, S. (2016). Palaeoclimatic insights into forcing and response of monsoon rainfall. *Nature*, 533(7602), 191–199. <https://doi.org/10.1038/nature17450>
- Ridgway, K. R., & Godfrey, J. S. (2015). *Journal of Geophysical Research : Oceans*. *Journal of Geophysical Research: Oceans*, 120(10), 6843–6864. <https://doi.org/10.1002/2015JC011049>
- Schneider, T., Bischoff, T., & Haug, G. H. (2014). Migrations and dynamics of the intertropical convergence zone. *Nature*, 513(7516), 45–53. <https://doi.org/10.1038/nature13636>
- Shakun, J. D., Clark, P. U., He, F., Marcott, S. A., Mix, A. C., Liu, Z., et al. (2012). Global warming preceded by increasing carbon dioxide concentrations during the last deglaciation. *Nature*, 484(7392), 49–54. <https://doi.org/10.1038/nature10915>
- Weller, E., Holliday, D., Feng, M., Beckley, L., & Thompson, P. (2011). A continental shelf scale examination of the Leeuwin Current off Western Australia during the austral autumn-winter. *Continental Shelf Research*, 31(17), 1858–1868. <https://doi.org/10.1016/j.csr.2011.08.008>
- Wyrwoll, K. H., Liu, Z., Chen, G., Kutzbach, J. E., & Liu, X. (2007). Sensitivity of the Australian summer monsoon to tilt and precession forcing. *Quaternary Science Reviews*, 26(25–28), 3043–3057. <https://doi.org/10.1016/j.quascirev.2007.06.026>

2. Publications and Manuscripts

Monitoring Australian Monsoon variability over the past four glacial cycles

Renjie Pei¹, Wolfgang Kuhnt¹, Ann Holbourn¹, Johanna Hingst^{1,2}, Matthias Koppe¹, Jan Schultz¹, Peer Kopetz¹, Peng Zhang³, Nils Andersen⁴

¹*Institute for Geosciences, Kiel University, Ludewig-Meyn Str. 10-14, 24118 Kiel, Germany*

²*MARUM, University of Bremen University, Leobener Str. 8, 28359 Bremen, Germany*

³*State Key Laboratory of Continental Dynamics, Department of Geology, Northwest University, Xi'an 710069, China*

⁴*Leibniz Laboratory for Radiometric Dating and Stable Isotope Research, Kiel University, Max-Eyth-Str. 11-13, 24118 Kiel, Germany*

Key findings:

- Rapid intensification of Australian Monsoon at end of glacial Terminations I to IV
- Monsoon intensification coincided with atmospheric CO₂ increase
- Austral spring insolation drove southward shift of ITCZ and monsoon intensification
- Formation of regional heat lows instrumental for monsoonal hydroclimate
- Aeolian dust dominant during glacials and MIS 5a-d south of 20°S.

Keywords:

ITCZ, Glacial terminations, Dust, Terrigenous discharge, Oxygen isotopes, X-Ray fluorescence

Abstract

We analyse changes in terrigenous sedimentation along the Northwestern Australian Margin to monitor the latitudinal migration of the Intertropical Convergence Zone (ITCZ) and the shifting boundaries of climatic belts during the last four glacial cycles. We integrate high-resolution X-ray fluorescence (XRF) scanning elemental records from Core SO257–18548 and International Ocean Discovery Program Site U1482, situated southwest of the Scott Plateau at

the southern edge of the present-day monsoonal belt, and from Core SO257–18571, located within the dust-cyclone belt offshore Northwest Cape south of the Exmouth Plateau. The chronology of these sediment successions is based on ^{14}C dating over the last glacial termination and on correlation of the benthic oxygen isotope record to the LR04 stack (Lisiecki and Raymo, 200) and Antarctic ice core chronology. Our XRF derived records of riverine terrigenous run-off and aeolian dust input reveal rapid intensification of monsoonal precipitation and reduction of atmospheric dust during the Younger Dryas and early Holocene as well as during the terminal phase of other major deglaciations. Short-lived monsoonal maxima in the early Holocene (~10 ka), MIS 5e (~130 ka), MIS 7 (~200, ~220 and ~240 ka), and MIS 9 (~280, ~305 and ~330 ka) coincide with maxima in atmospheric carbon dioxide and methane concentrations. Monsoon intensification occurs during maxima in Southern Hemisphere spring (September) insolation, when intense heat low pressure cells over the Pilbara region trigger the southward shift of the ITCZ. Within the dust-cyclone belt, riverine sediment discharge was restricted to intervals of high atmospheric CO_2 concentrations, when sea surface temperature thresholds promoted cyclone formation in the tropical Indian Ocean. Northwestern Australia remained dry and arid during MIS 5a-d, when the ITCZ was locked in a more northerly position and temperature thresholds were not attained.

1. Introduction

The climate and hydrography of the eastern Indian Ocean (Timor Sea) and northwestern Australia are strongly influenced by seasonal changes in wind direction associated with the southward migration of the Intertropical Convergence Zone (ITCZ) during austral summer. During December–February, NW winds predominate and rainfall increases over Indonesia and northern Australia (Australian summer monsoon), whereas dry SE Trade Winds prevail during austral winter (June–November). Today, a striking feature of northwestern Australian climate

is the formation of low pressure cells between September and November, which precede the monsoon season by up to three months. The development of these heat lows is a critical factor in the formation of the Australian summer monsoon circulation, as they trigger strong westerly winds (Suppiah, 1992). These heat lows form over the desert regions under clear skies at high insolation in areas where surface albedo is high. The intensity and geographic extent of these heat lows are highly sensitive to changes in insolation, thus responding to both external insolation and internal greenhouse forcing.

On longer timescales, variations in monsoonal rainfall are related to changes in precessional summer insolation, sea level fluctuations and atmospheric CO₂ concentrations (e.g., Wyrwoll et al., 2007; Griffiths et al., 2009; DiNezio and Tierney, 2013; Kuhnt et al., 2015). There is also a broad consensus that the meridional position of the ITCZ, which controls the latitudinal extent of monsoonal rainfall, is strongly dependent on the interhemispheric temperature gradient (e.g., Schneider et al., 2014; Mohtadi et al., 2016). Climate models predict drier subtropics in the Southern Hemisphere during interstadials due to a northward shift of the ITCZ during Dansgaard-Oeschger (D/O) warming events in the Northern Hemisphere and a southward displacement of the ITCZ during Northern Hemisphere cooling (Claussen et al., 2003; Broccoli et al., 2006; Chiang et al., 2008). These changes likely result from shifts in the atmospheric heat exchange between the tropics and mid latitudes and attendant variations in Trade Winds (e.g., Broccoli et al., 2006). However, the response of the Australian Monsoon to high-latitude temperature fluctuations on orbital, suborbital and millennial timescales is still poorly understood due to the scarcity of continuous high-resolution precipitation and runoff records from the Australian continent.

The sedimentary archives along the northNorthwestern Australian Margin, south of the fulcrum of the ITCZ's seesaw, are ideally situated to test the validity of these model predictions. The seasonal southward and northward migrations of the ITCZ and associated austral

monsoonal rain belt directly influence sedimentation patterns in the Timor Sea. Austral summer monsoon rainfall during southward shifts of the ITCZ increases river discharge, leading to enhanced deposition of terrigenous sediment along the continental margin. In contrast, when the ITCZ is locked into a more northerly position, the austral summer monsoon weakens, vast areas of northern Australia dry out and intensified Trade Winds in austral winter carry increased amounts of dust from the arid zones of central and northwestern Australia into the SE Timor Sea. Sedimentation patterns along the northNorthwestern Australian Margin are, thus, directly related to the latitudinal migration of the monsoon rain belt, making this area ideally suited to test model predictions of Southern (Northern) Hemisphere temperature forcing of the Australian Monsoon.

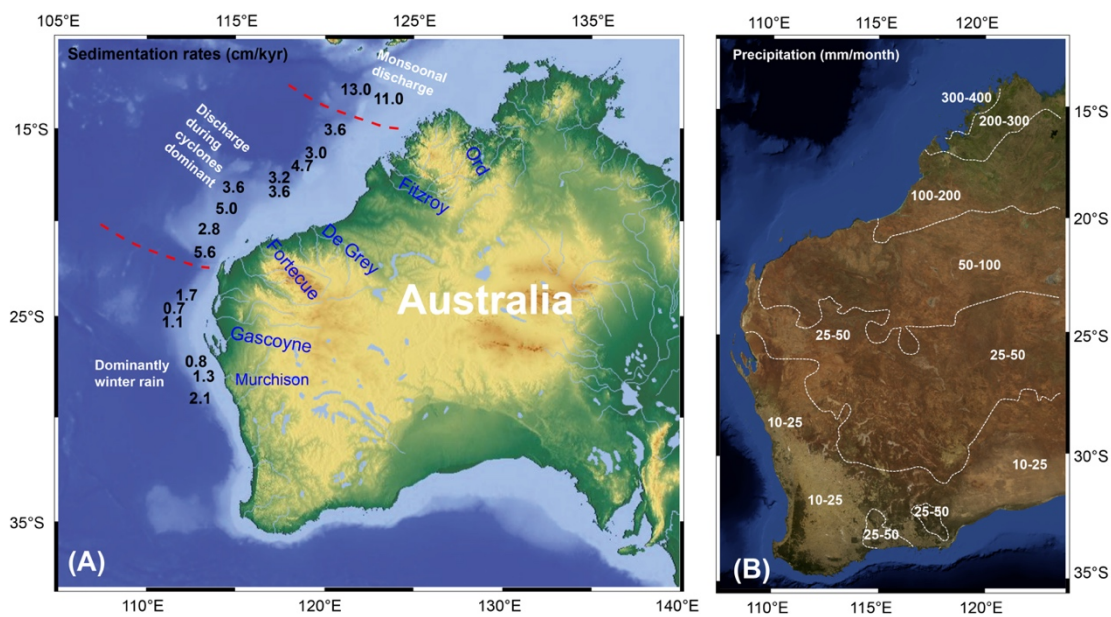


Fig. 1. A. Main rivers discharging sediment to the north Northwestern Australian Margin and average Holocene-MIS-6 sedimentation rates (cm/kyr) along the margin. Water depth scale in m. **B.** Summer monsoonal (February) vegetation and precipitation patterns. Average sedimentation rates (cm/kyr) are from Sonne 257 cores offshore Australia (from Keep et al., 2018; Kuhnt et al., 2018). February precipitation is based on 30 yr standard climatology (1961–1990) in mm/month from Australian Bureau of Meteorology (2010). Satellite Image is from February 2004 from NASA Blue Marble. (For interpretation of the references to colour in this figure legend, the reader is referred to the web version of this article.)

Today, the delivery of dust from the Australian continent towards the eastern Indian Ocean is controlled by the seasonal change in wind direction associated with the southward migration of the ITCZ during austral summer. During December–February, NW winds predominate and rainfall increases over Indonesia and northern Australia (Australian summer monsoon), whereas dry SE Trade Winds, which transport dust particles originating from the central Australian deserts, prevail during austral winter-spring in June–October. Pioneering sedimentologic studies of sediment cores offshore northwestern Australia suggested that changes in grain size offer a valuable proxy to estimate the amount of wind-blown desert dust in the terrigenous fraction of hemipelagic sediments in this area (Heirtzler, 1974; McTainsh, 1989; Hesse and McTainsh, 2003). Furthermore, these studies provided evidence that provenance and transport mechanisms (wind direction and intensity) were highly variable over orbital timescales. For example, grain size analysis in Core SO14-08-05 (16° 21' S, 118° 23' E) on the Rowley terrace between the Scott Plateau and Exmouth Plateau indicated that the dust flux consisted of coarser grains during the Last Glacial Maximum (LGM) in comparison to the early Holocene (Turney et al., 2006). This record also exhibits maxima in dust flux at ~8, 14, 30 and 150 ka (MIS 6), associated with Southern Hemisphere cooler climate phases (Hesse and McTainsh, 2003; Hesse et al., 2004; Turney et al., 2006). Spikes of aeolian quartz grains in Lake Carpentaria also coincide with Northern Hemisphere warm phases/Southern Hemisphere cool phases (De Deckker, 2001), in particular dust peaks centered at 24.0, 25.4 and 29.5 ka and two peaks within broader maxima at ~34.6 and ~38.6 ka are associated with D/O-Events 3, 4, 7 and 8.

Previous studies of Australian sedimentary archives also suggested that the northern Australian monsoonal rainbelt expanded and intensified during suborbital cooling and drying phases in the Northern Hemisphere. The Lynch's Crater sediment records provided evidence for intensified monsoonal rainfall over northern Australia during Heinrich 1–3 stadials (HS 1–

3) and the Holocene 8.2 ka cold event (Muller et al., 2008). By contrast, Northern Hemisphere tropical and equatorial rainfall was weakest during these cold phases. In records from the SE Asian Maritime Continent, such as northern Borneo (Partin et al., 2007), the Sulu Sea (Rosenthal et al., 2003) and Sulawesi (Schröder et al., 2016, 2018), the weakest tropical convection and driest conditions characterize the early deglaciation HS 1 (18–15 ka). While there is evidence of a suborbital seesaw in monsoonal rainfall intensity for the LGM, deglaciation and early Holocene, the long-term orbital and suborbital evolution of the Australian Monsoon remains enigmatic, mainly due to the scarcity of continuous high-resolution records extending beyond the last glacial cycle. The only high-resolution monsoonal records that cover this extended time interval are located further to the northeast and are strongly influenced by upwelling-related productivity changes of the Indonesian Throughflow, driven by monsoonal winds during glacial low stands (Holbourn et al., 2005; Kawamura et al., 2006; Sarnthein et al., 2011). IMAGES Core MD00–2361, located at the margin of the Exmouth Plateau near the North West Cape, tracked glacial-interglacial changes in riverine and dust supply over the last 550 kyr, but the relatively low mean sedimentation rates of 2.5 cm/kyr with substantially lower rates during glacials did not allow full reconstruction of millennial scale monsoonal variability at this location (Stuut et al., 2014).

Here, we compare X-ray fluorescence (XRF) core scanner-derived elemental records in two extended sediment successions retrieved at the southern edge of the present-day monsoonal belt southwest of the Scott Plateau and within the dust-cyclone belt offshore Northwest Cape to monitor monsoonal runoff and dust fluxes on millennial timescales over the last four glacial cycles. Our main objectives are to reconstruct the variability of the tropical convection along the southernmost displacement of the ITCZ during austral summer in relation to changes in high-latitude climate, sea level and atmospheric greenhouse gas concentration in

order to monitor changes in the latitudinal temperature gradient and the intensity of the Walker circulation.

2. Regional setting

2.1. Climate archives along the northNorthwestern Australian Margin

Deep-water sediments along the north Northwestern Australian Margin consist of autochthonous biogenic carbonate with a small biosiliceous component and fine-grained terrigenous input from the Australian continent, which bypasses the broad shelf in suspension. One of the most prominent features is a distinct NE-SW decrease in late Pleistocene – Holocene sedimentation rates (Keep et al., 2018; Kuhnt et al., 2018). This trend has been explained by a combination of southward decreasing subsidence and accommodation space with increasing distance from the northern margin of the Australian plate (Keep et al., 2018) and decreasing discharge of riverine sediment southward of the Australian monsoonal rain belt (Gingele and De Deckker, 2004; De Deckker et al., 2014; Kuhnt et al., 2015). R/V Sonne Cruise 257 (WACHEIO) retrieved a suite of sediment cores along transects seaward of the northwestern Australian shelf to better understand the sediment transport offshore and the dynamics of depositional systems and to reconstruct long-term climate evolution from these high-resolution sediment archives. Preliminary evaluation indicates that sedimentation rates exceeded 5 cm/kyr during the late Pleistocene to Holocene in the northeastern part of the margin, whereas the Rowley Terrace between the Scott Plateau and Exmouth Plateau displays intermediate sedimentation rates ranging between 2.8 and 5.0 cm/kyr (Fig. 1). South of the Exmouth Peninsula, sedimentation rates are generally below 2 cm/kyr and increase basin-wards, which highlights the important role of slope-parallel sediment advection in this area (Fig. 1).

2.2. Factors influencing fluvial sediment discharge

The amount and chemical composition of sediment discharge by rivers from the Australian continent are influenced by multiple factors including the catchment-basin size, the relief and associated stream gradient, the bedrock lithology, the tectonic setting, and ultimately the amount and seasonality of rainfall. The succession of climate belts in northwestern Australia from (1) monsoonal tropical humid in the north through (2) tropical semiarid with sporadic rainfall from cyclones during the summer monsoon season, (3) arid and (4) temperate with dominant rain in austral winter in the south (Fig. 1) is reflected in the composition of the river sediment loads and marine surface sediments along the adjacent margin. However, clay mineral distribution offshore northwestern Australia does not exhibit a simple latitudinal distribution pattern, with kaolinite (Al– Fe rich) dominating in warm and humid latitudes and illite/chlorite (K-rich) in cold and arid regions (Gingele et al., 2001). High illite and chlorite concentrations also occur near the equator and high kaolinite concentrations were observed south of 35°, which has been attributed to specific local sources (Gingele et al., 2001; Gingele and De Deckker, 2004). These authors found illite concentrations of 25–36% in rivers discharging from the monsoonal climate zone in northern Australia with particularly high illite concentrations (50 and 54% of the clay mineral content) in sediments from the Ashburton River and adjacent Mangrove Creek, which discharge from the semiarid Pilbara mountain range. These results are consistent with potassium (K) concentrations in chemical analyses of sediments from these rivers and adjacent offshore regions (Fig. 2). A possible explanation for the high illite content in clay mineral assemblages and the associated high K concentrations in the elemental composition of the fine grained sediment from the semiarid zone is the intense erosion in elevated parts of the catchment during catastrophic rainfall events and the rapid and direct sediment transport in sporadic flash floods.

3. Material and methods

3.1. Core locations and sediment recovery

Piston Core SO257–18548 (15° 3.591' S, 120° 18.846' E, 1608.2 m water depth, 11.2 m core length) and International Ocean Discovery Program (IODP) Site U1482 (15° 3.32' S, 120° 26.10' E, 1466 m water depth), located close to the modern southern limit of the seasonal (austral summer) displacement of the ITCZ, are influenced by the monsoonal discharge from the nearby Fitzroy River (Fig. 2). Core SO257–18548 is located ~7 nm west of IODP Site U1482 at the western edge of an elevated plateau that forms the northeastern part of the Rowley Terrace between the Scott Plateau and Exmouth Plateau. Core SO257–18548 was retrieved during a site survey in the vicinity of IODP Site U1482. The main objective of coring at this location was to recover the upper Pleistocene to Recent sedimentary record, which is missing at Site U1482, as a local sediment gravity flow eroded sediments younger than MIS 9. Recovered sediments consist of homogenous mottled olive greenish gray to dark gray clay-rich calcareous ooze (Kuhnt et al., 2018; Rosenthal et al., 2018; Supplementary Fig. S1).

Gravity Core SO257–18571 (22° 667' S, 113° 29,688' N, 1052 m water depth, 20.1 m core length) was retrieved offshore the North West Cape Peninsula south of the Exmouth Plateau (Fig. 2). The core is located within the “dust-cyclone” climate belt at the northern end of the arid climatic zone in Western Australia and is only marginally affected by the austral summer monsoon rain belt. This area receives mainly water and sediment from the Ashburton, Fortescue, Gascoyne and De Grey Rivers, which sporadically have high discharges following torrential rainfall after the landfall of tropical cyclones (Fig. 2C). Core SO257–18571 is located at the western edge of an *E-W* orientated ridge at a position, where 8 khz seismic reflectors indicated locally higher sedimentation rates. Recovered sediments consist of clay-rich nannoplankton ooze with distinct intercalations of dark reddish brown, clay-rich intervals and light olive gray calcareous ooze (Kuhnt et al., 2018; Supplementary Figs. S2 and S3).

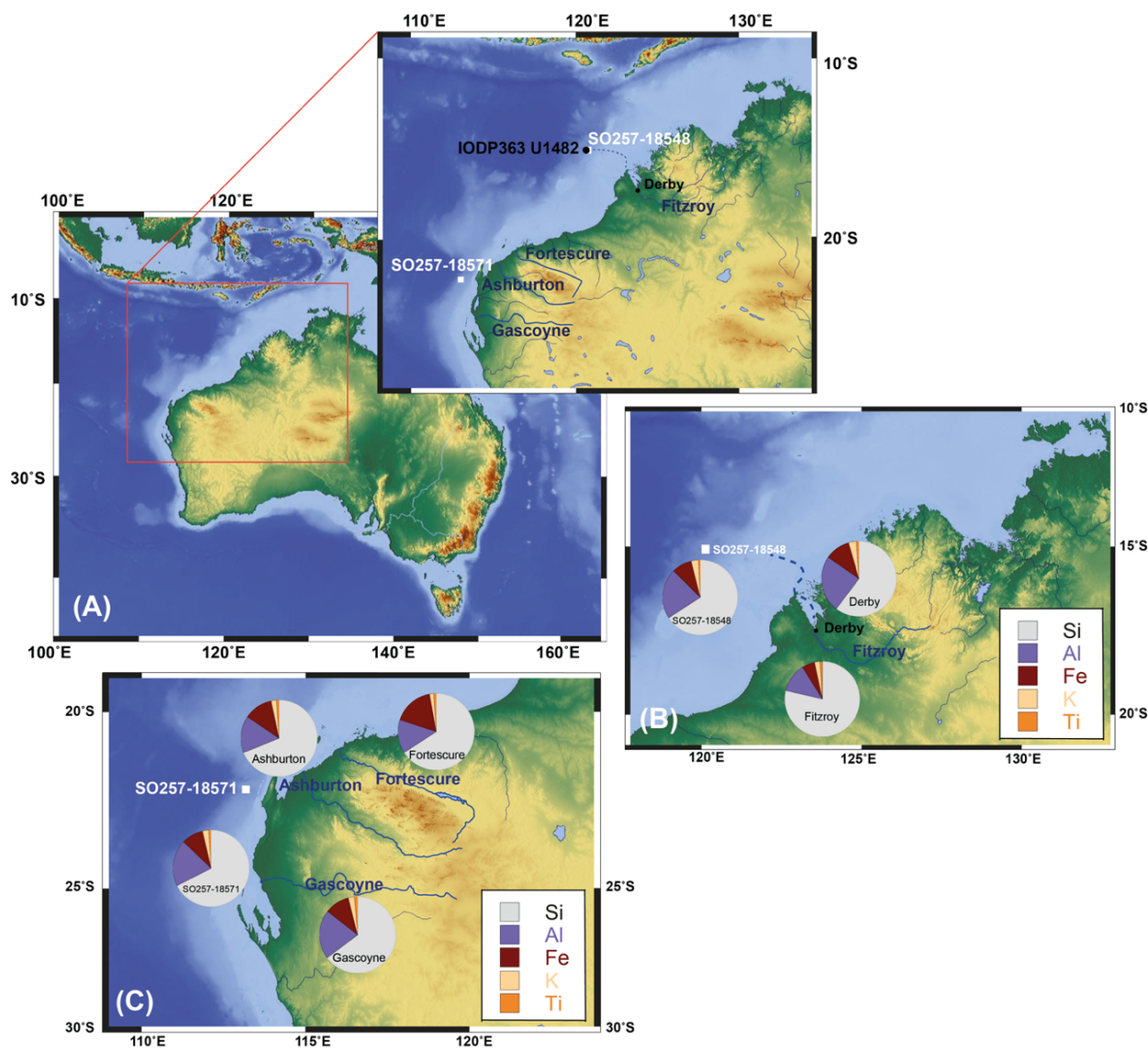


Figure 2. Location of Cores SO257-18548 and -18571 and IODP Site U1482 offshore northwestern Australia (A). Base map created using www.maps-for-free.com. Detailed maps (B-C) show positions of coring sites in relation to adjacent main rivers and concentrations of main terrigenous elements (Si, Al, Fe, K and Ti) in fine-grained (<63 μm) fractions of terrigenous material in marine sediment cores (B) and river sediments (C). Approximate extension of glacial Fitzroy River on shelf is indicated by blue dashed line in B.

3.2. Sampling and processing

The working halves of Cores SO257–18548 and –18571 were initially sampled at 10 cm intervals (1 cm-thick half slices of 11 cm diameter cores). Additional samples were taken over Termination I (6 samples from Core SO257–18548 between 94.5 and 204.5 cm depth) and Termination II (10 samples from Core SO257–18548 between 456.5 and 576.5 cm depth)

to refine the age model. Four holes were cored at Site U1482 during IODP Expedition 363 (Rosenthal et al., 2017, 2018). The working halves from the composite sediment succession (shipboard splice) between 24.76 and 30.22 m composite depth (mcd) were sampled at 20 cm intervals (2 cm-thick half slices of ~7 cm diameter cores). The sediment succession from Core SO257–18548 and nearby Site U1482 were combined, based on correlation of the high-resolution XRF scanner elemental records (Supplementary Figs. S4 and S5). The tie point, corresponding to an age of ~324 ka, is located at 10.84 m in Core SO257–18548 and at 24.97 mcd in Site U1482. All samples were oven dried at 40 °C and weighed prior to washing over a 63 µm sieve. Residues were oven dried at 40 °C on filter paper, then weighed and sieved into the fractions >315, 315–250, 250–150 and 150–63 µm.

3.3. Stable isotope analysis

Stable oxygen isotopes of the epibenthic foraminifera *Cibicidoides wuellerstorfi* were measured in 132 samples from Core SO257–18548, 28 samples from Site U1482 and 150 samples from Core SO257–18571. In each sample, 3–6 well-preserved specimens of *C. wuellerstorfi* were picked from the fraction >315 µm and/or 315–250 µm. Selected well-preserved specimens were crushed into large fragments, agitated with ethanol for 2–3 s in an ultrasonic bath, decanted and dried at 40 °C prior to analysis with a Thermo Finnigan MAT 253 mass spectrometer at the Leibniz Laboratory for Radiometric Dating and Isotope Research, Kiel University, Kiel. The mass spectrometer is coupled to a Kiel-Carbo IV device for automated CO₂ preparation from carbonate samples. Sample reaction was induced by individual acid addition (99% H₃PO₄ at 75 °C) under vacuum. The evolved carbon dioxide was analyzed eight times for each individual sample. As documented by the performance of international [NBS19: +1.95‰ VPDB (¹³C), –2.20‰ VPDB (¹⁸O); IAEA-603: +2.46‰ VPDB (¹³C), –2.37‰ VPDB (¹⁸O)] and laboratory-internal carbonate standards [Hela1: +0.91‰

VPDB (^{13}C), +2.48‰ VPDB (^{18}O); HB1: -12.10‰ VPDB (^{13}C), - 18.10‰ VPDB (^{18}O); SHK: +1.74‰ VPDB (^{13}C), - 4.85‰ VPDB (^{18}O)], analytical precision of stable isotope analysis is better than $\pm 0.08\text{‰}$ for $\delta^{18}\text{O}$ and better than $\pm 0.05\text{‰}$ for $\delta^{13}\text{C}$. Values are calibrated relative to Vienna Pee Dee Belemnite.

3.4. Age models

Between 0 and ~ 21 ka, the age models of Cores SO257-18548 and SO257-18571 are based on ^{14}C dates obtained from the surface-dwelling planktonic foraminifera *Globigerinoides ruber* (white). Between 600 and 800 specimens of the planktonic foraminifer *G. ruber* $> 250\ \mu\text{m}$ were picked for AMS dating in order to reach a sample weight of 12 mg. In both cores, we selected samples at depths close to the transition between the Bølling-Allerød and the Younger Dryas and close to the center of the LGM. Samples were measured at the Leibniz Laboratory for Radiometric Dating and Isotope Research, Kiel University, Kiel. Conventional radiocarbon ages were converted into calendar ages using Calib 7.1 (Stuiver et al., 2019). We applied a marine reservoir age of 510 years for the sample at a depth of 70 cm in Core 18548 (>13 ka), 200 years for the sample at a depth of 140 cm in Core 18571 (>10 ka) and 1600 years for the samples at a depth of 100 cm in Core 18548 and at a depth of 190 cm in Core 18571 (<20 ka), following corrections determined at the nearby Core MD01–2378 (Sarnthein et al., 2011).

For the interval older than 21 ka, we derived age models for Cores SO257-18548 and -18571 and for Site U1482 (between 24.76 and 30.22 mcd) by correlating the benthic foraminiferal $\delta^{18}\text{O}$ records to the reference benthic isotope stack LR04 (Lisiecki and Raymo, 2005), using linear interpolation between tie points (Linage) in AnalySeries 2.08 (Paillard et al., 1996).

3.5. XRF scanner derived elemental composition

Bulk-chemical composition of the sediment cores was determined using a 2nd generation Avaatech XRF core scanner at the Institute of Geosciences, Kiel University. Before measurement, the sediment surface was smoothed and covered with a 4.0 μm thick Prolene® Thin-Film foil to minimize surface irregularities and to avoid direct contact between the sediment and the detector. Measurements were carried out on the archive halves at 1 cm intervals over a 1.2 cm^2 area with a down core slit size of 10 mm, using generator settings of 10, 30 and 50 kV tube voltages. We performed measurements for 15 s with 200 μA without filter for the 10 kV runs and for 10 s with 1000 μA using a Pb and Cu-filter for the 30 and 50 kV runs, respectively. The spectra were transferred into elemental area counts using the software bAxil Batch by Brightspec NV and are reported as area counts per second. Results are reported in logarithms of elemental ratios, which provide the most easily interpretable signals of relative changes in chemical composition downcore and minimize the risk of measurement artefacts from variable signal intensities and matrix effects (Weltje and Tjallingii, 2008).

We used the sum of the spectral area counts of the elements aluminium (Al), silicon (Si), potassium (K), iron (Fe), titanium (Ti) as proxies for the terrigenous derived sediment component (abbreviated as “Terr”) mainly originating from riverine transport from the Australian continent. We normalized these elements against calcium (Ca), derived from the biogenic carbonate of marine plankton. An alternative normalization was performed against barium (Ba), which is related to particulate organic matter and/or the precipitation of barite by marine bacteria and is, thus, independent of carbonate production and dissolution. The $\text{Log}(\text{Terr}/\text{Ba})$ curve exhibit similar trends in all cores as $\text{Log}(\text{Terr}/\text{Ca})$, suggesting that the variability of these records is mainly driven by increasing or decreasing terrigenous flux (Supplementary Fig. S6). Core scanner measurements of the split core sediment surface

commonly underestimate concentrations of the light elements Al and Si, due to the influence of pore water in unconsolidated sediment (Tjallingii et al., 2007). However, replicate XRF scanner measurements of compressed dry powder from the same core interval show that pore water bias affects only the uppermost ~100 cm of our cores. The Log(Al/Ca) and Log(Si/Ca) curves in this interval become noisier in both cores, but do not substantially differ from curves of the heavier elements (Log(K/Ca), Log(Ti/Ca), and Log(Fe/Ca)) over the last glacial termination and Holocene (Supplementary Fig. S7A and B).

Differences in the abundance of zirconium (Zr) and light elements (Al, K or rubidium (Rb)) reflect the grain size and transport pathway of terrigenous particles, since K, Al and Rb are preferentially incorporated in river-transported fine-grained clay, whereas larger and/or heavier wind-blown grains from the Australian desert have relatively high Zr values. Zirconium is the main component of the heavy mineral zircon, which is subject to sorting and preferential settling close to river mouths and on the continental shelf, and thus mainly characterizes wind transported dust at distal locations. In particular, Zr/Rb in sediment has been shown to reflect the initial grain size distribution (coarser sediment Zr-enriched, finer sediments clay mineral bound Rb-enriched) of wind-blown sediments, due to the immobility of the two elements during post depositional processes (Liu et al., 2002).

3.6. Calibration of XRF scanner data by melt XRF analysis of discrete samples

To calibrate the XRF scanner data, 11 homogenized and discrete samples of the terrigenous sediment component from Core SO257–18571 and 9 samples from Core SO257–18548 were analyzed using quantitative XRF analysis of fused beads. For discrete sample measurements, all samples were decarbonated by adding 10% HCl until the reaction stopped. The suspension was neutralized after centrifugation for 10 min at 3000 revolutions/min, decanted and refilled with deionized water. This neutralization was repeated six times. The

neutralized suspension was wet sieved over a 63 μm sieve and the fine fraction ($<63 \mu\text{m}$) collected and filled into beakers. After 5 weeks, the supernatant was carefully pumped out. After drying at 50 $^{\circ}\text{C}$, aliquots of each sample were used to produce fused beads and pressed pellets (Garbe-Schönberg and Müller, 2014). Fused beads were produced by mixing the sample material with lithium-tetraborate and heated to $\sim 1050^{\circ}\text{C}$. Major and trace elements were determined on the fused lithium-tetraborate glass disks with a X-ray fluorescence spectrometer (XRF - Panalytical MagixPro) at Hamburg University using the software of Vogel and Kuipers (1987). Accuracy was controlled by analyses of several international standards. The precision of the instrument is 1–2% for major elements and 5–20% for trace elements depending on the concentration. Loss on ignition (LOI) was determined gravimetrically after heating the samples to 1050 $^{\circ}\text{C}$ for 3 h (Lechler and Desilets, 1987). Pressed pellets were produced by grinding down the dried material first with a mortar and afterwards with a Pulverisette 7 premium line from Fritsch, pressed into pellets and measured with the second generation Avaatech XRF core scanner at the Institute of Geosciences, Kiel University. Analytical results of quantitative fused beads XRF and corresponding XRF scanner area counts for Core SO257–18548 are provided in Supplementary Table S1A and B and for Core SO257–18571 in Supplementary Table S2A and B. Linear regression plots are shown in Supplementary Fig. S8.

3.7. Elemental signatures of Western Australian river sediments

To determine the provenance of the terrigenous component of marine sediments, samples from Core SO257–18548 (core-top samples) and Core SO257–18571 (core depth 113.5 cm) were compared with fine-grained ($<63 \mu\text{m}$) sediments from the main rivers in northwestern Australia. The chemical composition of marine and river sediments was analyzed by melt XRF analysis of discrete samples. Aliquots of the same samples were additionally analyzed in discrete pellets with the XRF scanner at Kiel University. After decarbonatization,

the samples were pulverized in an agate mortar and pressed into pellets with a Pulverisette 7 premium line from Fritsch, then analyzed with the XRF core scanner at Kiel University.

4. Results

4.1. Chronology and sedimentation rates

Between 0 and ~ 21 ka, the age models of Cores SO257–18548 and – 18571 are based on ^{14}C AMS dates (Table 1). To derive age models prior to 21 ka in Cores SO257–18548 and – 18571 and at Site U1482, we selected consistent tie points between the benthic foraminiferal $\delta^{18}\text{O}$ curves and the reference benthic isotope stack LR04 (Lisiecki and Raymo, 2005) (Table 2, Figs. 3-4). For the interval from 24.76 to 30.22 mcd at Site U1482, shipboard biostratigraphic datums provided additional age constraints between 0.29 and 0.44 Ma (Rosenthal et al., 2018) (Fig. 3).

Sedimentation rates (SR) in Core SO257–18571 exhibit a distinct glacial-interglacial variability (Fig. 4). Mean SR range between 8.6 cm/ kyr during MIS 5e and 11.5 cm/kyr during the Holocene, whereas mean SR are substantially lower during glacial periods, varying between 3.7 cm/kyr during MIS 6 and 4.5 cm/kyr during the LGM. Sedimentation rates during MIS 3, 4 and 5a-d also remain low, as during the LGM and MIS 6. By contrast, sedimentation rates for Core SO257–18548 and at Site U1482 show more consistent trends of 2.5 to 5.5 cm/kyr without major glacial and interglacial differences (Fig. 3).

We additionally tested the robustness of the age models by correlating our oxygen isotope records to the Antarctic δD derived temperature record (Bazin et al., 2013). Within the range of error in our intermediate resolution (~2–4 kyr) isotope records, the onset of glacial terminations occurs simultaneously, whereas the end of glacial terminations (temperature maximum) is 2 to 5 kyr later in the marine record (Supplementary Fig. S9).

Table 1. AMS ^{14}C dates from analysis of *Globigerinoides ruber* (white)

Kiel AMS Laboratory Number	Core	Depth (cm)	Foraminiferal species	Uncorr. ^{14}C Age (years B.P.)	Error bar	Reservoir Age (years)	Calibrated Age (years B.P.)
KIA 53786	SO257-18548	70	<i>G. ruber</i>	11765	45	510	13114
KIA 53787	SO257-18548	100	<i>G. ruber</i>	18305	70	1600	20154
KIA 53788	SO257-18571	140	<i>G. ruber</i>	9980	40	250	10738
KIA 53789	SO257-18571	190	<i>G. ruber</i>	18830	75	1600	20778

Table 2. Age tie points to LR04 benthic isotope stack (Lisiecki and Raymo, 2005)

SO257-18548 and U1482		SO257-18571		Age (ka)	Descriptions of tie points
Core Depth (m)	$\delta^{18}\text{O}$ (‰ VPDB)	Core Depth (m)	$\delta^{18}\text{O}$ (‰ VPDB)		
2.7	3.68	3.6	3.3	62	$\delta^{18}\text{O}$ maximum in center of MIS 4
3.7	3.11	5.1	3.05	87	$\delta^{18}\text{O}$ maximum in center of MIS 5b
4.4	3.11	6.9	3.07	109	$\delta^{18}\text{O}$ maximum in center of MIS 5d
5.1	3.76	9.2	3.6	135	Onset of Termination II
6.5	3.4	11.1	3.12	188	Onset of MIS 6
7.6	3.49	14.4	3.3	223	Onset of Termination IIIb
8.4	3.56	16.2	3.17	252	Onset of Termination IIIa
9	3.49	16.9	3.1	277	Onset of second $\delta^{18}\text{O}$ maximum in MIS 8
9.7	3.38	17.7	2.9	294	First $\delta^{18}\text{O}$ maximum in MIS 8
10.5	2.86	19.3	2.43	318	End of first $\delta^{18}\text{O}$ minimum in MIS 9
11.7	3.73			342	Onset of Termination IV
13.9	3.3			392	End of first $\delta^{18}\text{O}$ minimum in MIS 11
15.5	3.8			433	Onset of Termination V

4.2. Composition and provenance of terrigenous sediment discharge

Comparison of the terrigenous elemental composition of Core SO257–18548 with that of the riverine sediment discharge from the Kimberley coast, which is the closest sediment source on the Australian continent shows a high degree of affinity (Fig. 2, Table 3). In particular, the terrigenous component of Core SO257–18548 is very close to that of the fine-grained clay-fraction dominating the King Sound sediment near Derby, where the Fitzroy River enters into

the shelf sea. The coarser grained, silt-dominated sediment, sampled upstream of the Fitzroy River exhibits higher Si percentages, which is mainly due to the higher quartz content of the silt fraction. The elevated K content is typical for this area, which agrees with clay mineral analyses showing higher percentages of the K-rich clay mineral illite (Gingele and De Deckker, 2004). In the vicinity of the Northwest Cape Peninsula, the sediment loads of the Ashburton, Fortescue and Gascoyne Rivers exhibit similar elemental compositions with higher Fe concentrations, which are closely reflected in the composition of the Holocene terrigenous sediment fraction in Core SO257–18571, located offshore from these rivers (Fig. 2, Table 3).

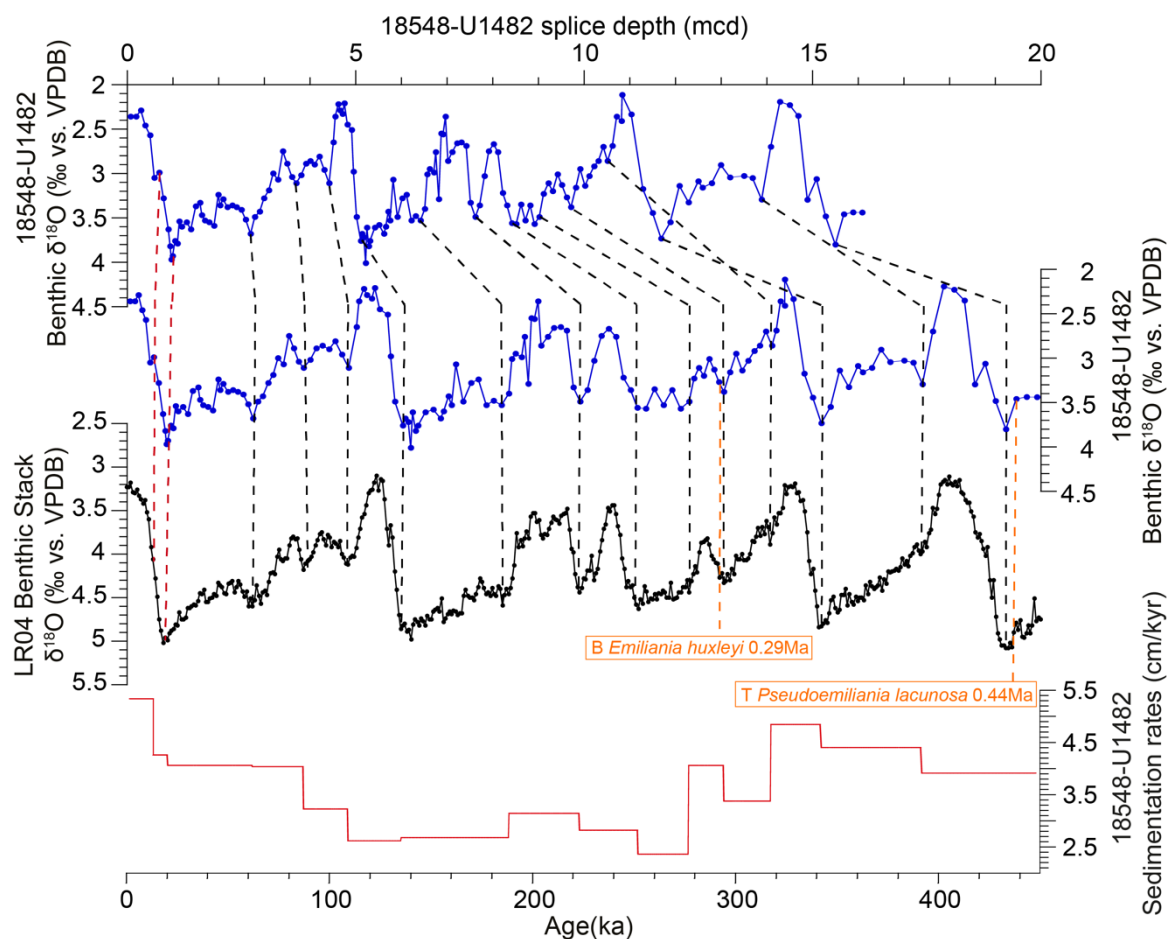


Figure 3. Correlation of benthic foraminiferal $\delta^{18}\text{O}$ from Core SO257-18548 and Site U1482 to benthic isotope stack LR04 (Lisiecki and Raymo, 2005). Dashed black lines indicate tie points used to derive age model. Dashed red lines indicate AMS ^{14}C ages. Orange dashed lines indicate biostratigraphic datums: B = Base, T = Top (from Rosenthal et al., 2018).

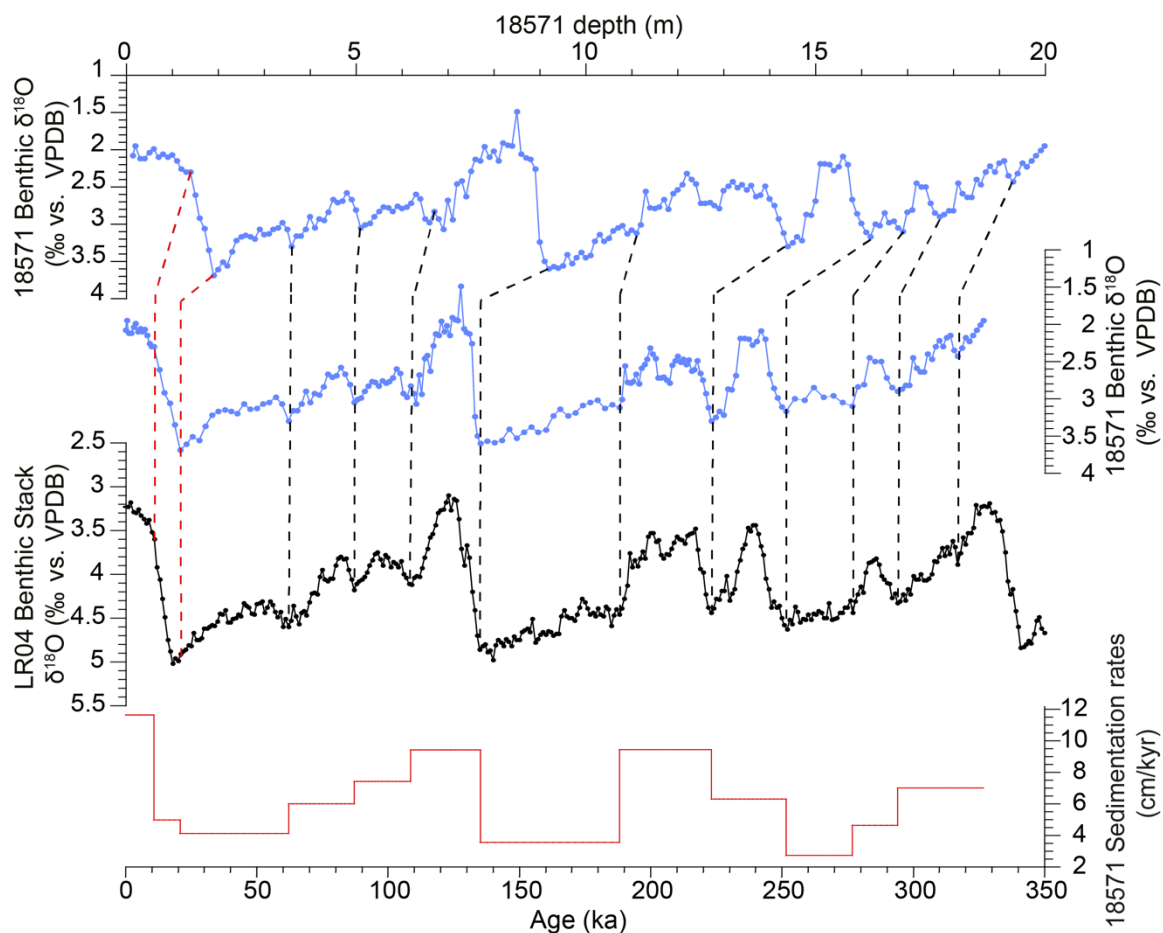


Figure 4. Correlation of benthic foraminiferal $\delta^{18}\text{O}$ of Core SO257-18571 to the benthic isotope stack LR04 (Lisiecki and Raymo, 2005). Dashed black lines indicate tie points used to derive age model. Dashed red lines indicate AMS ^{14}C ages.

4.3. Variations in riverine terrigenous sediment input

Log (Terr/Ca) is used to estimate the contribution of terrigenous sediment discharge normalized against the marine biogenic carbonate flux, which is considered to be relatively constant offshore northwestern Australia (Kuhnt et al., 2015). In Cores SO257–18571 and –18548 and at Site U1482, Log (Terr/Ca) shows glacial-interglacial variability that is generally coherent with the $\delta^{18}\text{O}$ records (Supplementary Fig. S10A). In Core SO257–18548, glacial-interglacial (~100 kyr) coherence is >0.8 with an out-of-phase relationship (highest Log(Terr/Ca) coincide with lowest $\delta^{18}\text{O}$), while coherence at the precessional band (23 kyr) is highest (0.83). However, there is a distinct mismatch between $\delta^{18}\text{O}$ and terrigenous runoff during MIS 5a and 5c, when terrigenous runoff remains comparable to glacial levels in Cores

SO257–18548 and – 18571. In Core SO257–18571, coherence is highest (~ 0.85) at the glacial-interglacial scale, whereas it is lower (~ 0.76) at the precessional band (Supplementary Fig. S10B).

Table 3. Concentration of main terrigenous elements in Cores SO257-18548 and -18571 and close by rivers. Fitz = Fitzroy River, Ashb = Ashburton River, Fort = Fortescue River, Gasc = Gascoyne River

Elements	18548	Derby	Fitz1	Fitz2	18571	Ashb1	Fort1	Fort2	Gasc1	Gasc2
	(%)	(%)	(%)	(%)	(%)	(%)	(%)	(%)	(%)	(%)
Si	65.72	60.28	79.67	77.34	67.37	68.84	66.08	65.63	63.18	66.38
Al	21.75	24.35	11.81	13.19	19.72	15.69	14.15	14.27	22.10	19.26
Fe	8.56	10.90	5.25	6.04	9.30	12.03	16.85	17.27	11.08	10.44
K	3.06	3.44	2.05	2.39	2.37	2.33	1.72	1.71	2.50	2.43
Ti	0.90	1.03	1.22	1.03	1.24	1.10	1.21	1.12	1.14	1.50

During glacial stages, mean $\text{Log}(\text{Terr}/\text{Ca})$ is distinctly lower in Core SO257–18571 than in Core SO257–18548, with a minimum value of -1.5 during MIS 5d to MIS 2 and higher values of -1.2 to -1.3 during MIS 8 and MIS 6, respectively. In Core SO257–18548, mean $\text{Log}(\text{Terr}/\text{Ca})$ is -1.1 for MIS 5d and MIS 2 and -0.9 for MIS 8 and MIS 6. Maximum values are reached in both cores as distinct peaks at the end of glacial terminations or at the beginning of interglacials: at ~ 10 ka (end of Termination I/early Holocene), ~ 130 ka (end of Termination II/early MIS 5e), ~ 200 , ~ 220 and ~ 240 ka (end of Termination III/ early MIS 7 and precessional insolation maxima within MIS 7) and at ~ 280 , ~ 305 and ~ 330 ka (end of Termination IV/early MIS 9 and precessional insolation maxima within MIS 9 and MIS 8). Maxima are comparable (between -0.2 and -0.5) in both cores, although minima are distinctly lower in Core SO257–18571, suggesting a higher amplitude change of sediment discharge from the semiarid zone in northwestern Australia than from catchments within the monsoonal rainbelt. In addition, the deglacial onset of enhanced discharge from the semiarid zone was more rapid, in particular during Termination II, when $\text{Log}(\text{Terr}/\text{Ca})$ in Core SO257–18548

already exhibits an increasing trend in the late MIS 6, whereas Core SO257–18571 Log(Terr/Ca) shows an abrupt change point at the onset of the glacial termination. The runoff pattern across MIS 11 differs markedly from the later interglacial trends: the Log(Terr/Ca) curve is almost symmetrical without a distinct peak in the early part of the interglacial.

Accumulation rates of the terrigenous component in Core SO257–18571 are lower than ~ 1 g/(cm²kyr) during glacial MIS 2–4, 6 and 8 and reach maxima of >4 g/(cm²kyr) during interglacial MIS 9, 7, 5e and 1 (Supplementary Fig. S11). The increases in accumulation rates occur abruptly close to the end of glacial terminations in parallel to increases in carbonate accumulation associated with increasing biogenic carbonate production (Supplementary Figs. S11 and S13). The deglacial increase in terrigenous accumulation rates in Core SO257–18548 is less dramatic and restricted to MIS 7 and MIS 1, while the accumulation rates of both the carbonate and terrigenous components remain low during MIS 5e (Supplementary Figs. S11 and S12). Carbonate accumulation rates are below ~ 1 g/(cm²kyr) during MIS 5e, which is lower than during the preceding glacial stage. During MIS 5d to MIS 5a, carbonate accumulation rates increase continuously, then fluctuate at ~ 2 g/(cm²kyr) during MIS 4 to 2, which is ~ 0.5 g/(cm²kyr) lower than average Holocene values. In contrast, changes in sedimentation rates between glacial and interglacial stages at Site SO257–18548 are relatively low or even absent in the case of MIS 5, although the sediment composition changes significantly from carbonate dominated during glacials to terrigenous clay dominated during interglacials.

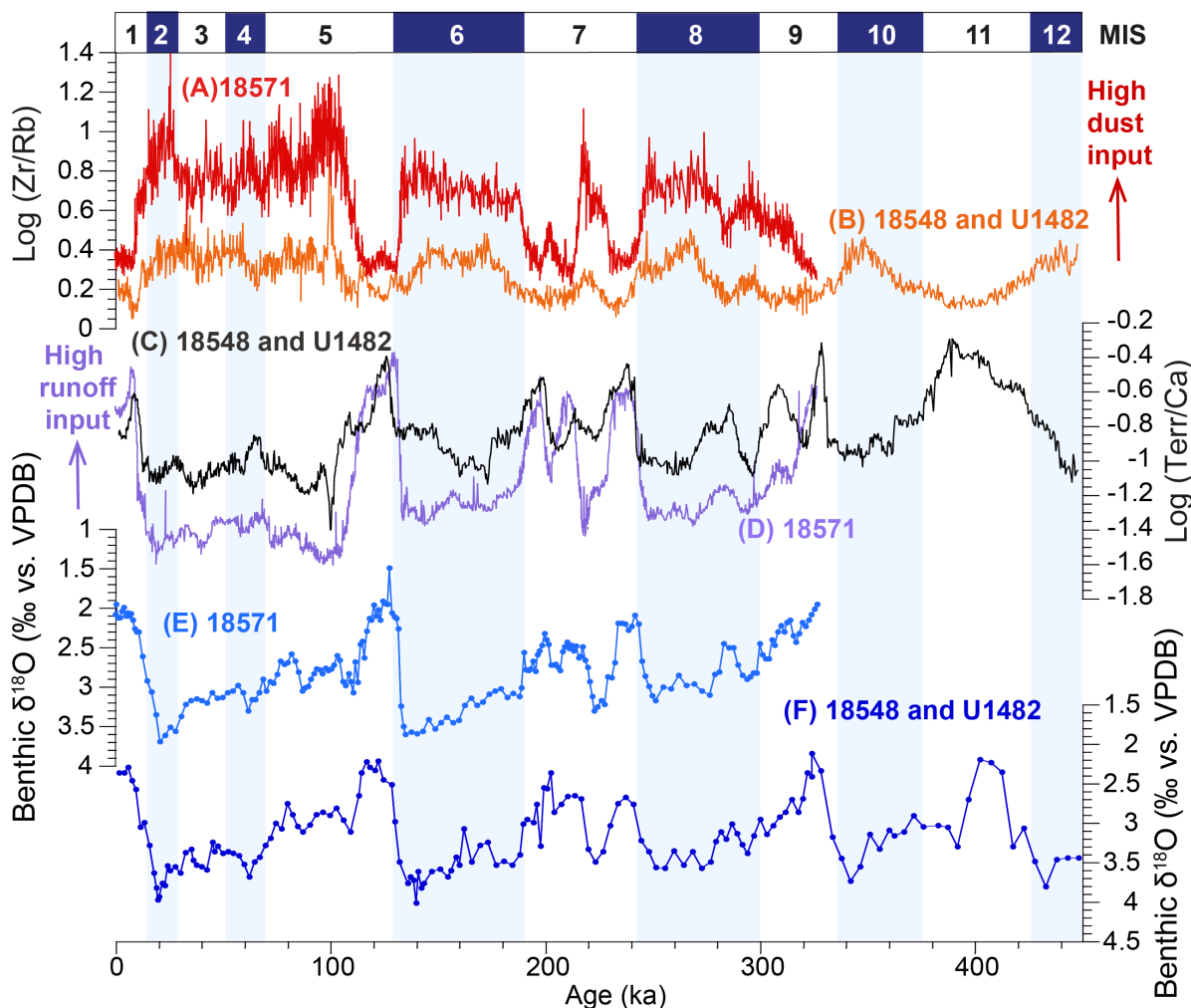


Figure 5. Temporal evolution of XRF scanner derived elemental ratios and benthic foraminiferal $\delta^{18}\text{O}$ in Core SO257-18548, Site U1482 and Core SO257-18571. MIS = marine isotope stages. (A-B) Log(Zr/Rb) from Core SO257-18548 and Site U1482 (orange) and from Core SO257-18571 (red); (C-D) Log(Terr/Ca) from Core SO257-18548 and Site U1482 (black) and from Core SO257-18571 (purple); (E-F) benthic $\delta^{18}\text{O}$ from SO257-18548 and Site U1482 (dark blue) and from Core SO257-18571 (light blue). Blue shading indicates marine isotope glacial stages (MIS), following Lisiecki and Raymo (2005).

4.4. Variations in dust input

Log (Zr/Rb) in Core SO257–18571 exhibits a distinct glacial/interglacial cyclicality, in contrast to the record from Core SO257–18548 and Site U1482, which shows relatively low values with only subtle shifts between glacial and interglacial periods. This distinct cyclicality in Core SO257–18571 parallels the oxygen isotope trend and is in antiphase to that of Log (Terr/Ca). The abrupt decreases in dust input and increases in riverine terrigenous input of clay minerals occur almost simultaneously during Terminations I, II and III. During interglacial

periods, Log (Zr/Rb) remains low, ranging between 0.28 and 0.5 (20 point smoothed data), whereas mean values are high (0.6 to 1.0) during glacial stages. Parallel to the marked decrease in Log (Terr/Ca) at the end of MIS 5e, Log (Zr/Rb) displays the largest increase within the record and exhibits a distinct maximum during MIS 5d. Between this maximum and the next pronounced peak during the LGM, three smaller maxima with an amplitude ≤ 0.2 occur. These peaks approximately coincide with the cold MIS 5b and MIS 4 intervals and the central part of MIS 3 (Fig. 5). Between the LGM and the Holocene, Log (Zr/Rb) decreases markedly once again. This decline is not continuous, but is interrupted by small plateaus at ~ 25 to 23 ka, ~ 21 to 17.5 ka, and ~ 14 to 10 ka. During the Holocene, Log (Zr/Rb) ranges between 0.27 and 0.43 with a standard deviation of 0.03.

5. Discussion

5.1. Reconstruction of monsoonal discharge

Terrigenous flux reconstructions are based on XRF scanner derived concentrations of Al, Si, K, Fe and Ti. These elements are commonly used to estimate the proportion of terrigenous (lithogenic) content in marine sediments, however, there are various caveats associated with each element. The concentration of Al is preferentially used to estimate the total lithogenic content of sediments because its concentration is very consistent in the continental lithosphere (Turekian and Wedepohl, 1961; Wedepohl, 1971; Taylor and McLennan, 1985). Silicon is present in all aluminosilicates and also occurs as quartz (SiO₂), which is the main component in the silt fraction of sediments and sedimentary rocks (Calvert and Pedersen, 2007). Core scanner measurements of the splitcore sediment surface commonly underestimate concentrations of the light elements Al and Si, due to the influence of pore water in unconsolidated sediment (Tjallingii et al., 2007). However, replicate XRF scanner measurements of compressed dry powder from the same core interval show that pore water

bias affects only the uppermost ~100 cm of our cores and does not substantially affect the shape of the $\text{Log}(\text{Terr}/\text{Ca})$ curve over the last glacial Termination and Holocene (Supplementary Fig. S6).

Potassium predominantly occurs as a component of the clay mineral illite in fine-grained riverine runoff. Its concentration is reliably estimated by the XRF scanning technique (Tjallingii et al., 2007) and it has been previously used to monitor monsoonal riverine runoff across the last glacial termination (Kuhnt et al., 2015). Iron and Ti were used to evaluate the changing input of fine-grained terrigenous siliciclastic sediment from adjacent continental margin offshore Venezuela and Java (Jansen et al., 1998; Mohtadi et al., 2011; Haug et al., 2001), which was driven by variations in rainfall and runoff from the watersheds of local rivers. However, Ti usually exhibits fairly low counts, when analyzed with the XRF scanner, and the Fe content may be partly biased by the formation of authigenic iron/manganese crusts or pyrite (Calvert and Pedersen, 2007; Poulton and Raiswell, 2002).

Using the sum of terrigenous elements instead of individual elements reduces the noise in XRF scanner data, since this produces higher counts and reduces the effects of possible biases in single element counts. Here, we used the logarithmic ratio of the sum of the terrigenous elements Al, Si, K, Fe, and Ti to Ca ($\text{Log}(\text{Terr}/\text{Ca})$). This approach is commonly used in carbonate-rich pelagic environments, where carbonate dissolution plays no major role (Kuhnt et al., 2015). The carbonate concentrations vary between 54 and 80.5% in Core SO257–18548 and between 50 and 86% in Core SO257–18571. We assume that the variability in $\text{Log}(\text{Terr}/\text{Ca})$ in these two cores is mainly driven by changes in terrigenous input. Calcium is relatively rare in terrigenous sediments and in marine deep-water environments mainly derived from biogenic carbonate. To further test this hypothesis, we normalized against Ba (Supplementary Fig. S6), which is related to particulate organic matter flux and/or the precipitation of barite by marine bacteria (Gonzalez-Muñoz et al., 2012; Griffith and Paytan,

2012) and, thus, has no direct relation to carbonate flux. In previous records from the northNorthwestern Australian Margin, CaCO₃ and organic productivity indicators such as total organic carbon (TOC) and chlorins did not show any positive correlation (Holbourn et al., 2005). Thus, we conclude that the consistent behavior of terrigenous elements normalized against Ca or Ba indicates that fluctuations in the Ca-normalized terrigenous elemental curves are caused by fluctuations in terrigenous input rather than changing marine carbonate production/ dissolution.

5.2. Monsoonal response to changes in atmospheric greenhouse gas concentrations and high-latitude temperature fluctuations

Model predictions of changes in the latitudinal extent of the ITCZ's seasonal swing and the development of an interhemispheric seesaw during the last glacial cycle are contradictory and not fully supported by climate proxy data, which are still scarce for the Southern Hemisphere (Denton et al., 2010; Shakun et al., 2012; De Deckker et al., 2012; Kuhnt et al., 2015). In particular, increasing greenhouse gas concentrations during HS 1 (Lüthi et al., 2008; Shakun et al., 2012) should have resulted in tropical expansion (Seidel et al., 2008) at the end of the LGM. Expansion and contraction of the monsoonal rain belt triggered by greenhouse gas concentrations are supported by a comparison of high-resolution Northern and Southern Hemisphere speleothem records over the last three millennia, which indicates coeval intensification/ poleward shift and weakening/equatorward shift of monsoonal rain belts on suborbital timescales in both hemispheres (Denniston et al., 2016). However, substantial regional cooling associated with wide-spread drying in the subtropics and tropics in the Northern Hemisphere during HS 1 and preceding Heinrich stadials was attributed to a southward shift of the ITCZ and associated monsoonal rain belt (Claussen et al., 2003; Chiang and Bitz, 2005; Chiang et al., 2003, 2008; Broccoli et al., 2006; Muller et al., 2008, 2012;

Bayon et al., 2017; Stríkis et al., 2018; Lauterbach et al., 2020). By contrast, a recent compilation of model ensembles for different forcings demonstrated the importance of additional forcings on the variability of the ITCZ, including disturbance of the global ocean circulation by North Atlantic hosing and LGM boundary conditions (Atwood et al., 2020). While insolation differences between hemispheres and atmospheric $p\text{CO}_2$ are important, they may not alone force a mean shift of the tropical rainbelt. Moreover, precipitation proxy data compilations demonstrated that the height of HS 1 coincided with a latitudinally widespread drought, which also affected the Southern Hemisphere (Stager et al., 2011). According to these authors, the widespread geographic range of aridification during HS 1 suggests a severe weakening of the tropical rainfall systems probably as a response to global sea surface cooling.

Our high-resolution runoff records from Core SO257–18548 and Site U1482, and from Core SO257–18571 also exhibit no distinct increase in riverine discharge in the early part of Termination I, suggesting that northwestern Australia remained largely arid during HS 1. A massive and rapid increase in riverine discharge started only at ~13 ka at these sites following the Antarctic Cold Reversal (~15–13 ka). This is consistent with records within the core area of the Australian monsoonal rain belt further to the northeast, where terrigenous runoff also did not significantly increase prior to 13 ka (Kuhnt et al., 2015). These generally dry conditions were only locally interspersed by transient rainfall episodes during HS 1, HS 2, and HS 4, as indicated by composite stalagmite $\delta^{13}\text{C}$ records from caves in the Kimberleys in northwestern Australia (Denniston et al., 2017). On orbital timescales, it is remarkable that the ITCZ appears to have consistently remained in a more northerly position during MIS 5b and 5d and associated stadials and that northwestern Australia remained consistently dry and dusty. By contrast, eastern Australia experienced increased precipitation linked to southward expansion of the ITCZ (Bayon et al., 2017). Recent modelling studies underline the role of longitudinally variable responses of the ITCZ to different climate forcings (Atwood et al., 2020) which could

explain different responses to Northern Hemisphere cooling in eastern (Bayon et al., 2017; Muller et al., 2008) and western Australia.

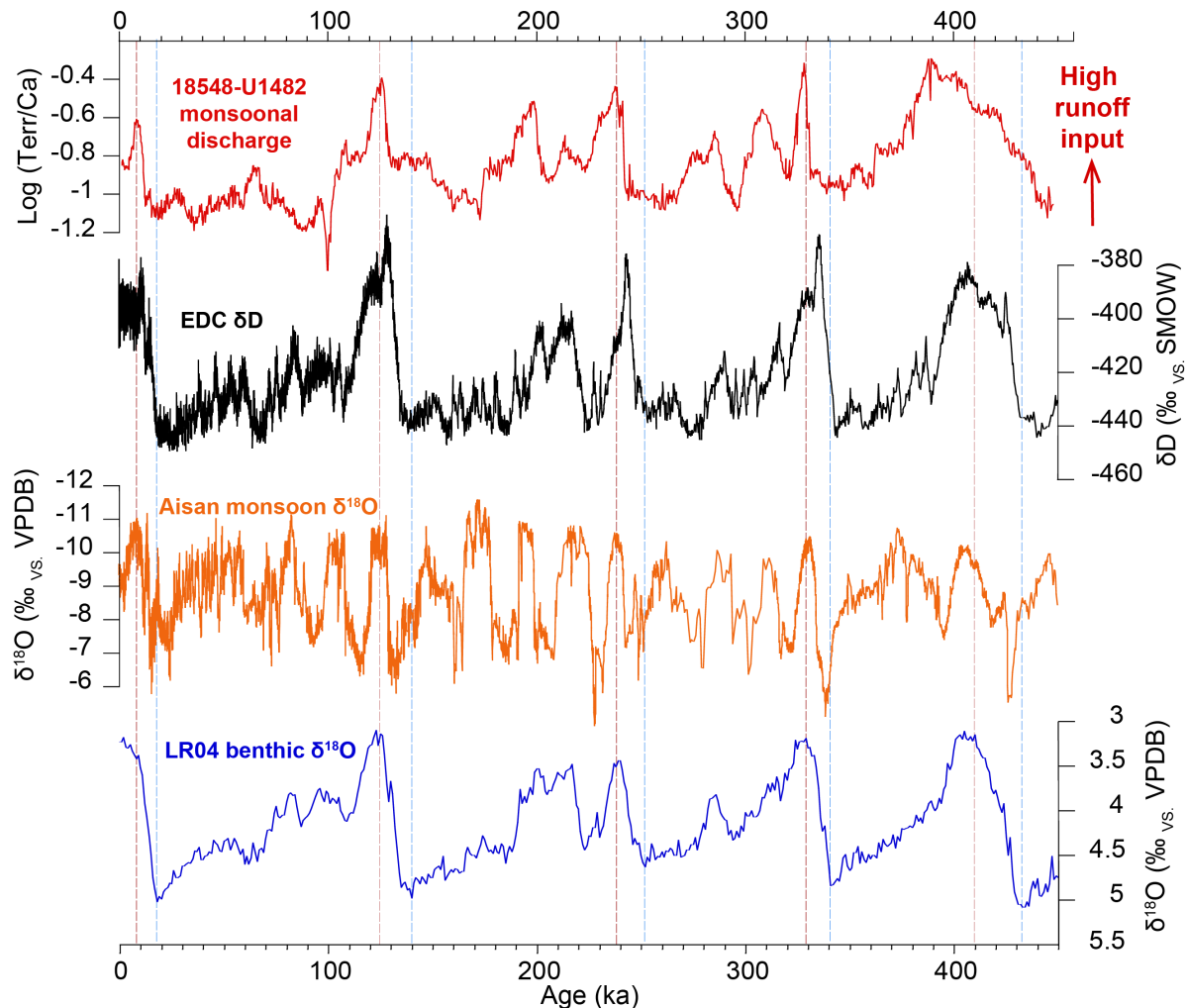


Figure 6. Comparison of monsoonal discharge ($\text{Log}(\text{Terr}/\text{Ca})$) in composite record from Core SO157-18548 and Site U1482 with evolution of Antarctic temperatures (Epica Dome Concordia (EDC) δD from Bazin et al., 2013) and Northern Hemisphere monsoon intensity (Chinese speleothem $\delta^{18}\text{O}$ record from Dongge, Hulu and Sanbao Caves. Wang et al., 2001,2008; Dykoski et al., 2005; Kelly et al., 2006; Cheng et al., 2009, 2016). Note that monsoonal discharge record is tuned to LR04 stack (Lisiecki and Raymo, 2005) and, thus, independent of EDC ice core age model. Glacial Terminations I-V in LR04 stack are marked with blue (onset) and red (end) dashed lines; corresponding ages are 18-9 ka (Termination I), 135-126 ka (Termination II), 252-240 ka (Termination III), 341-329 ka (Terminations IV) and 431-410 ka (Termination V).

Although our records do not resolve short-term local precipitation changes, they may provide a better estimate of time- and regional- averaged long-term precipitation and runoff trends on millennial time- scales. The dampened response to changes in the interhemispheric temperature gradient in these “smooth” records supports the hypothesis of global subtropical megadroughts during intervals of globally cool climate and low atmospheric $p\text{CO}_2$. Major wet periods in northwestern Australia are restricted to warmer-than-present climate intervals in the early Holocene (~ 10 ka), early MIS 5e (~ 130 ka), MIS 7 (~ 200 , ~ 220 and ~ 240 ka), and MIS 9 (~ 280 , ~ 305 and ~ 330 ka), when monsoonal rainfall also increased in many Northern Hemisphere monsoonal regions (Liu et al., 2014; Cheng et al., 2016; Kathayat et al., 2016). In particular, the intense monsoonal peaks centered at ~ 10 , ~ 130 , ~ 240 and ~ 330 ka, which follow Southern Hemisphere high-latitude temperature maxima at the end of glacial terminations (Fig. 6), suggest an enhanced regional response of the Australian Monsoon, driven through internal feedbacks. The general coherence between the intensity of the Australian Monsoon and global $p\text{CO}_2$ and climate trends is also reflected in the high coherence and consistent antiphase behavior of benthic $\delta^{18}\text{O}$ and monsoonal discharge in our records (Supplementary Fig. S10). Model experiments with warm Pliocene boundary conditions indicated that an intensification of subtropical precipitation in both hemispheres may have been driven by reduced meridional sea-surface temperature gradients in a warmer world (Burls et al., 2017) and was decoupled from shifts of the ITCZ on millennial timescales (Sniderman et al., 2019).

5.3. Temporal changes in the extent of the northwestern Australian arid zone

Today, estimates of terrigenous dust accumulation off northwestern Australia range between 1 and 5 $\text{g}/(\text{m}^2\text{yr})$ (Jickells et al., 2005), which represents $\sim 2\text{--}5\%$ of the total sediment mass accumulation or $> 10\%$ of the terrigenous component at marine sites within the dust belt with typical deglacial sedimentation rates of ~ 5 cm/kyr (Fig. 1A) (Kuhnt et al., 2018). The

proportion of dust-blown sediment considerably decreases towards the northeast, where sedimentation rates increase and dust accumulation decreases, implying that a substantial proportion of the Zr, Ti and Fe content is of aeolian origin only at the southerly location of Core SO257–18571. The aeolian terrigenous material that reaches distal marine locations is usually deposited during extreme dust outbreaks (Rea, 1994). The occurrence of discrete Zr-, Ti- and Fe- enriched layers in the glacial intervals of Core SO257–18571 may, thus, represent a record of major dust storms (Rea, 1994; Hanebuth and Henrich, 2009).

Riverine transported fine-grained terrigenous discharge and aeolian dust input in Core SO257–18571 exhibit a clear antiphase relationship with no recognizable phase lags, suggesting coeval and abrupt changes towards wetter climate and increased fluvial discharge during glacial terminations and rapid re-aridification at the end of the unusually warm isotope stages MIS 9, 7 and 5e. Increased dust transport to the eastern Indian Ocean implies a reduced vegetation cover during periods of increased seasonal aridity in the source area, following changes in preferential wind direction and/or strengthening of winds. The rapid intensification of monsoonal rainfall and rearidification at the onset and end of the warmest intervals with highest atmospheric greenhouse gas levels suggest that these rapid transitions were defined by transgressing boundary condition thresholds. However, there are striking differences in the sedimentation processes and the climate of the catchment area at the locations of Core SO257–18548 and Site U1482 within the monsoonal belt and of the more southwestern Core SO257–18571 within the dust-cyclone belt. Precipitation in the arid zone almost exclusively occurs during the landfall of major tropical cyclones, which form in the tropical Indian Ocean during the monsoonal season, when SST thresholds of 26–27 °C are reached (Tory and Dare, 2015). Increased cyclone activity during monsoon intensification is also reflected by massive increases in sedimentation rates during the warm stages MIS 1, MIS 5e and the warm parts of MIS 7 and MIS 9 in Core SO257–18571 (Fig. 4), whereas sedimentation rates in Core SO257–

18548, which is dominated by seasonal monsoonal discharge, remain more consistent (Fig. 3). Southern Hemisphere subtropical sea surface temperatures may have played a major role in setting these boundary conditions. However, boundary conditions remained below the threshold necessary for the formation of tropical cyclones during the slightly cooler interglacial MIS 5a and MIS 5c, which remained dry and dusty within the dust-cyclone belt (Fig. 5).

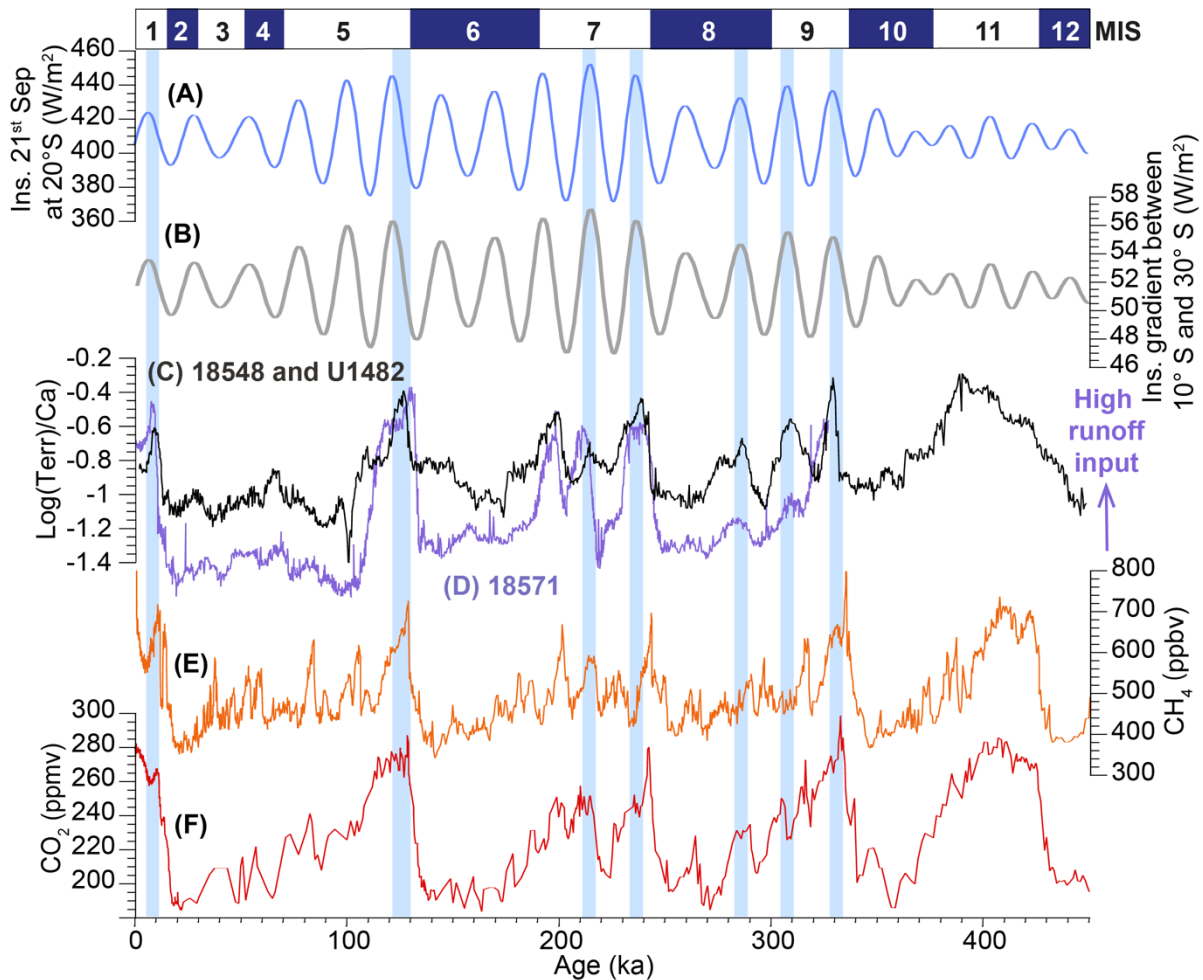


Figure 7. Comparison of terrigenous discharge records from Cores SO257-18571, SO257-18548 and Site U1482 to external and internal forcing mechanisms. (A) Insolation 21st of September at 20°S; (B) Insolation gradient between 10 and 30°S; (C) Log(Terr/Ca) from Core SO257-18548 and Site U1482 (black); (D) Log(Terr/Ca) from Core SO257-18571 (purple); (E) EPICA Dome Concordia (EDC) CH₄ record (Loulergue et al., 2008); (F) EDC CO₂ record (Lüthi. et al., 2008.). Green shading marks monsoonal peaks associated with *p*CO₂ maxima occurring at austral spring insolation maxima and minimal gradient between 10 and 30° S insolation, which favors southward migration of the ITCZ.

5.4. Monsoon forcing mechanisms

The intensity, seasonality and latitudinal extent of monsoonal rainfall during the summer season depend on the seasonal displacement of the ITCZ, which is influenced by insolation differences between the Northern and Southern Hemispheres (Broccoli et al., 2006) and is also highly sensitive to greenhouse gas forcing (Cai et al., 2012). However, the response of the ITCZ to interhemispheric insolation and temperature differences appears regionally variable and dependent on additional local forcings (Atwood et al., 2020). Sedimentary successions at the more northeasterly situated Site U1483 and Core MD01–2378 in the Timor Sea display a similar monsoonal runoff pattern as Core SO257–18548 and Site U1482 (Zhang et al., 2020). The runoff record at these locations exhibits in-phase variability with Northern Hemisphere monsoonal precipitation records on the precession band, which was interpreted as an expansion (contraction) of the latitudinal extent of the ITCZ during Northern Hemisphere insolation maxima (minima) (Zhang et al., 2020).

Our comparison of two sedimentary succession providing a transect across the southernmost limit of the Australian Monsoon shows that regional factors additionally play a crucial role in controlling the seasonal position of the ITCZ and intensity of monsoonal rainfall over northwestern Australia. In particular, the seasonal and interannual heat and air pressure variability over the more elevated Pilbara area acts as a main driver of monsoonal hydroclimate. In austral winter and spring, subtropical high-pressure systems are positioned over the central part of the Australian continent forcing dry easterly or southeasterly Trade Winds over the Pilbara region, thus maintaining intensely arid conditions (Charles et al., 2015; Sudmeyer, 2016). The seasonal southward movement of subtropical high-pressure systems in September results in the dominance of tropical heat lows over the Pilbara region during the extremely hot and dry spring and the summer wet season. The position of this heat low is related to the location of the Pilbara region between the relatively cooler marine area to the north and

latitudinally decreasing solar insolation to the south. In recent decades, an expansion of the Southern Hemisphere Hadley Cell in association with global warming caused a northward shift of frontal systems at the northern end of the Hadley Cell during austral winter and intensification of winter aridity in the Pilbara region (Lu et al., 2007; Risbey et al., 2009; Frederiksen et al., 2013).

The most intense phase of the heat low, which occurs in spring and early summer (September–November), precedes the monsoon season and is not associated with local rainfall (Charles et al., 2015). However, the intensity and position of the heat low have significant repercussions in “pulling” the monsoonal rain belt southwards, resulting in a coupled relationship between the strength of the monsoonal circulation and associated heavy rainfall with the intensity of the heat low (Suppiah, 1992). Important controlling factors on the variability in the intensity and position of the heat low on multidecadal, millennial and orbital timescales include (1) the precessional variability of spring (September–October) Southern Hemisphere orbital insolation, (2) the insolation gradient between tropical ($\sim 10^\circ$ S) and subtropical ($\sim 30^\circ$ S) insolation, which prevents the heat low from moving southwards into areas of lower insolation when the gradient is steep and, (3) the concentration of atmospheric greenhouse gases, which contributes to the intensity of the heat low. During the last 450 kyr, maxima in these three factors occurred at ~ 10 , ~ 130 , ~ 200 , ~ 220 , ~ 240 , ~ 280 , ~ 305 and ~ 330 ka, when terrigenous flux from monsoonal runoff strongly increased or was at a maximum, mostly close to the end of glacial terminations (Figs. 6-7, Supplementary Fig. S14).

During MIS 12 to 10, insolation forcing over the Pilbara region was minimal and the insolation gradient between 10 and 30° S remained elevated, which resulted in a more gradual monsoonal onset with muted response to precessional forcing. This weaker and more gradual monsoon intensification at the end of glacial Termination V (MIS 11) may have been additionally affected by pronounced vegetation changes leading to lower austral spring albedo

of the Pilbara mountains. Palynological data indicate a major change in northwestern Australian subtropical vegetation patterns and hydroclimate associated with the onset of intense aridification at ~350 ka during MIS 10 (Kershaw et al., 2003; Kawamura et al., 2006). This major, long-term change in Australian subtropical hydroclimate was associated with the Mid-Brunhes Climate Transition (Jansen et al., 1986; Barth et al., 2018), which occurred during an interval of low precessional insolation forcing between 430 and 350 ka and was followed by an increase in the amplitude of the Earth's 100 kyr glacial-interglacial climate cycles.

6. Conclusions

XRF scanner derived increases in terrigenous discharge indicate rapid intensification of the Australian Monsoon at the end of glacial terminations with short-lived peaks in the early Holocene (~10 ka), MIS 5e (~130 ka), MIS 7 (~200, ~220 and ~240 ka), and MIS 9 (~280, ~305 and ~330 ka). The correlation of monsoonal precipitation and runoff proxies and Antarctic temperature, CO₂ and CH₄ concentrations during the last five glacial terminations suggests that the intensification of heat low pressure cells over northwestern Australia at the end of glacial terminations was mainly driven by rapidly increasing atmospheric greenhouse gas concentrations in conjunction with a low insolation gradient between Southern Hemisphere tropics and subtropics and rising and/or high Southern Hemisphere spring-early summer insolation. The formation of intense heat low pressure cells in the Pilbara region of northwestern Australia in late September may have played a crucial role in driving the ITCZ southwards and triggering intensified monsoonal rainfall on orbital timescales, when Southern Hemisphere insolation was at a maximum. Changes in riverine terrigenous sediment supply at the onset of MIS 11 were more gradual and do not indicate an abrupt change from arid to monsoonal wet conditions, suggesting that an extended period of low variability in precessional spring insolation and expanded vegetation cover over northwestern Australia weakened the

heat low pressure cell over the Pilbara mountains. Southward swings of the ITCZ amplified and deglacial monsoonal onsets intensified with aridification of northwestern Australia ~350 kyr ago.

Acknowledgements

This research used data and samples provided by the International Ocean Discovery Program (IODP). We are grateful to the Sonne 257 and IODP Expedition 363 shipboard scientific parties for all their efforts. Renjie Pei gratefully acknowledges financial support from the State Scholarship Fund of China Scholarship Council. We thank Matthias Hüls for AMS ¹⁴C analyses at the Leibniz Laboratory for Radiometric Dating and Isotope Research, Kiel and Stefan Jung for fused beam XRF measurements at the Institute of Mineralogy and Petrography in Hamburg. We are grateful for constructive comments from two anonymous reviewers, which helped us to improve the manuscript. This study was funded by the German Federal Ministry of Education and Research (Grant SO-257, WACHEIO, 03G0257A).

References

- Atwood, A.R., Donohoe, A., Battisti, D.S., Liu, X., Pausata, F.S.R., 2020. Robust Longitudinally Variable responses of the ITCZ to a Myriad of climate Forcings. *Geophys. Res. Lett.* 47 <https://doi.org/10.1029/2020GL088833>.
- Barth, A.M., Clark, P.U., Bill, N.S., He, F., Piasias, N.G., 2018. Climate evolution across the Mid-Brunhes transition. *Clim. Past* 14 (12). <https://doi.org/10.5194/cp-14-2071-2018>.
- Bayon, G., De Deckker, P., Magee, J.W., Germain, Y., Bermell, S., Tachikawa, K., Norman, M.D., 2017. Extensive wet episodes in late Glacial Australia resulting from high-latitude forcings. *Sci. Rep.* 7, 1–7. <https://doi.org/10.1038/srep44054>.
- Bazin, L., Landais, A., Lemieux-Dudon, B., Kele, H.T.M., Veres, D., Parrenin, F., Martinerie, P., Ritz, C., Capron, E., Lipenkov, V., Loutre, M.F., 2013. An optimized multi-proxy, multi-site Antarctic ice and gas orbital chronology (AICC2012): 120- 800 ka. *Climate of the Past*, European Geosciences Union (EGU) 9 (4), 1715–1731. <https://doi.org/10.5194/cp-9-1715-2013>.

- Bock, M., Schmitt, J., Beck, J., Seth, B., Chappellaz, J., Fischer, H., 2017. Glacial/ interglacial wetland, biomass burning, and geologic methane emissions constrained by dual stable isotopic CH₄ ice core records. *PNAS*, E5778-E5786. [https://doi.org/ 10.1073/pnas.1613883114](https://doi.org/10.1073/pnas.1613883114).
- Broccoli, A.J., Dahl, K.A., Stouffer, R.J., 2006. Response of the ITCZ to Northern Hemisphere cooling. *Geophys. Res. Lett.* 33 (1) [https://doi.org/10.1029/ 2005GL024546](https://doi.org/10.1029/2005GL024546).
- Burls, N.J., Fedorov, A.V., Sigman, D.M., Jaccard, S.L., Tiedemann, R., Haug, G.H., 2017. Active Pacific meridional overturning circulation (PMOC) during the warm Pliocene. *Science advances* 3 (9). <https://doi.org/10.1126/sciadv.1700156>
- Cai, W., Lengaigne, M., Borlace, S., Collins, M., Cowan, T., McPhaden, M.J., Timmermann, A., Power, S., Brown, J., Menkes, C., Ngari, A., 2012. More extreme swings of the South Pacific convergence zone due to greenhouse warming. *Nature* 488 (7411), 365–369. <https://doi.org/10.1038/nature11358>.
- Calvert, S.E., Pedersen, T.F., 2007. Chapter fourteen elemental proxies for palaeoclimatic and palaeoceanographic variability in marine sediments: interpretation and application. *Developments in Marine Geology* 1, 567–644. [https://doi.org/10.1016/ S1572-5480\(07\)01019-6](https://doi.org/10.1016/S1572-5480(07)01019-6).
- Chappellaz, J., Barnola, J.M., Raynaud, D., Korotkevich, Y.S., Lorius, C., 1990. Ice-core record of atmospheric methane over the past 160,000 years. *Nature* 345 (6271), 127–131. <https://doi.org/10.1038/345127a0>.
- Charles, S., Fu, G., Silberstein, R., Mpelasoka, F., McFarlane, D., Hogson, G., Teng, J., Gabrovesk, C., Ali, R., Barron, O., Aryal, A., Dawes, W., 2015. Hydroclimate of the Pilbara: Past, Present and Future. A report to the Government of Western Australia and industry partners from the CSIRO Pilbara Water Resource Assessment. CSIRO Land and Water, Australia. <https://doi.org/10.4225/08/584af1c180bda>, 114 pp.
- Cheng, H., Edwards, R.L., Broecker, W.S., Denton, G.H., Kong, X., Wang, Y., Zhang, R., Wang, X., 2009. Ice age terminations. *Science* 326 (5950), 248–252. [https://doi.org/ 10.1126/science.1177840](https://doi.org/10.1126/science.1177840).
- Cheng, H., Edwards, R.L., Sinha, A., Spořil, C., Yi, L., Chen, S., Kelly, M., Kathayat, G., Wang, X., Li, X., Kong, X., 2016. The Asian monsoon over the past 640,000 years and ice age terminations. *Nature* 534 (7609), 640–646. <https://doi.org/10.1038/nature18591>.
- Chiang, J.C., Bitz, C.M., 2005. Influence of high latitude ice cover on the marine Intertropical Convergence Zone. *Clim. Dyn.* 25 (5), 477–496. [https://doi.org/ 10.1007/s00382-005-0040-5](https://doi.org/10.1007/s00382-005-0040-5).
- Chiang, J.C., Biasutti, M., Battisti, D.S., 2003. Sensitivity of the Atlantic intertropical convergence zone to last glacial maximum boundary conditions. *Paleoceanography* 18 (4). <https://doi.org/10.1029/2003PA000916>.
- Chiang, J.C., Fang, Y., Chang, P., 2008. Interhemispheric thermal gradient and tropical Pacific climate. *Geophys. Res. Lett.* 35 (14) [https://doi.org/10.1029/ 2008GL034166](https://doi.org/10.1029/2008GL034166).
- Claussen, M., Brovkin, V., Ganopolski, A., Kubatzki, C., Petoukhov, V., 2003. Climate change in northern Africa: the past is not the future. *Clim. Chang.* 57 (1–2), 99–118. <https://doi.org/10.1023/A:1022115604225>.

- De Deckker, P., 2001. Late Quaternary cyclic aridity in tropical Australia. *Palaeogeogr. Palaeoclimatol. Palaeoecol.* 170 (1–2), 1–9. [https://doi.org/10.1016/S0031-0182\(01\)00233-4](https://doi.org/10.1016/S0031-0182(01)00233-4).
- De Deckker, P., Moros, M., Perner, K., Jansen, E., 2012. Influence of the tropics and southern westerlies on glacial interhemispheric asymmetry. *Nature Geoscience* 5 (4), 266–269. <https://doi.org/10.1038/ngeo1431>.
- De Deckker, P., Barrows, T.T., Rogers, J., 2014. Land–sea correlations in the Australian region: post-glacial onset of the monsoon in northwestern Western Australia. *Quat. Sci. Rev.* 105, 181–194. <https://doi.org/10.1016/j.quascirev.2014.09.030>.
- Denniston, R.F., Ummenhofer, C.C., Wanamaker, A.D., Lachniet, M.S., Villarini, G., Asmerom, Y., Polyak, V.J., Passaro, K.J., Cugley, J., Woods, D., Humphreys, W.F., 2016. Expansion and contraction of the Indo-Pacific tropical rain belt over the last three millennia. *Sci. Rep.* 6 (1), 1–9. <https://doi.org/10.1038/srep34485>.
- Denniston, R.F., Asmerom, Y., Polyak, V.J., Wanamaker Jr., A.D., Ummenhofer, C.C., Humphreys, W.F., Cugley, J., Woods, D., Lucker, S., 2017. Decoupling of monsoon activity across the northern and southern Indo-Pacific during the late Glacial. *Quat. Sci. Rev.* 176, 101–105. <https://doi.org/10.1016/j.quascirev.2017.09.014>.
- Denton, G.H., Anderson, R.F., Toggweiler, J.R., Edwards, R.L., Schaefer, J.M., Putnam, A. E., 2010. The last glacial termination. *Science* 328 (5986), 1652–1656. <https://doi.org/10.1126/science.1184119>.
- DiNezio, P.N., Tierney, J.E., 2013. The effect of sea level on glacial Indo-Pacific climate. *Nat. Geosci.* 6 (6), 485–491. <https://doi.org/10.1038/ngeo1823>.
- Dykoski, C.A., Edwards, R.L., Cheng, H., Yuan, D., Cai, Y., Zhang, M., Lin, Y., Qing, J., An, Z., Revenaugh, J., 2005. A high-resolution, absolute-dated Holocene and deglacial Asian monsoon record from Dongge Cave, China. *Earth Planet. Sci. Lett.* 233 (1–2), 71–86. <https://doi.org/10.1016/j.epsl.2005.01.036>.
- Frederiksen, C.S., Zheng, X., Grainger, S., 2013. Teleconnections and predictive characteristics of Australian seasonal rainfall. *Clim. Dyn.* 43 (5–6), 1381–1408. <https://doi.org/10.1007/s00382-013-1952-0>.
- Garbe-Schönberg, D., Müller, S., 2014. Nano-particulate pressed powder tablets for LA- ICP-MS. *J. Anal. At. Spectrom.* 29 (6), 990–1000. <https://doi.org/10.1039/C4JA00007B>.
- Gingele, F.X., De Deckker, P., 2004. Fingerprinting Australia’s rivers with clay minerals and the application for the marine record of climate change. *Aust. J. Earth Sci.* 51 (3), 339–348. <https://doi.org/10.1111/j.1400-0952.2004.01061.x>.
- Gingele, F.X., De Deckker, P., Hillenbrand, C.D., 2001. Clay mineral distribution in surface sediments between Indonesia and NW Australia—source and transport by ocean currents. *Mar. Geol.* 179 (3–4), 135–146. [https://doi.org/10.1016/S0025-3227\(01\)00194-3](https://doi.org/10.1016/S0025-3227(01)00194-3).

- Gonzalez-Munoz, M.T., Martinez-Ruiz, F., Morcillo, F., Martin-Ramos, J.D., Paytan, A., 2012. Precipitation of barite by marine bacteria: a possible mechanism for marine barite formation. *Geology* 40 (8), 675–678. <https://doi.org/10.1130/G33006.1>.
- Griffith, E.M., Paytan, A., 2012. Barite in the ocean—occurrence, geochemistry and palaeoceanographic applications. *Sedimentology* 59 (6), 1817–1835. <https://doi.org/10.1111/j.1365-3091.2012.01327.x>.
- Griffiths, M.L., Drysdale, R.N., Gagan, M.K., Zhao, J.X., Ayliffe, L.K., Hellstrom, J.C., Hantoro, W.S., Frisia, S., Feng, Y.X., Cartwright, I., Pierre, E.S., 2009. Increasing Australian–Indonesian monsoon rainfall linked to early Holocene Sea-level rise. *Nat. Geosci.* 2 (9), 636–639. <https://doi.org/10.1038/ngeo605>.
- Guo, Z., Zhou, X., Wu, H., 2011. Glacial-interglacial water cycle, global monsoon and atmospheric methane changes. *Clim. Dyn.* 39 (5), 1073–1092. <https://doi.org/10.1007/s00382-011-1147-5>.
- Hanebuth, T.J., Henrich, R., 2009. Recurrent decadal-scale dust events over Holocene western Africa and their control on canyon turbidite activity (Mauritania). *Quat. Sci. Rev.* 28 (3–4), 261–270. <https://doi.org/10.1016/j.quascirev.2008.09.024>.
- Haug, G.H., Hughen, K.A., Sigman, D.M., Peterson, L.C., Röhl, U., 2001. Southward migration of the intertropical convergence zone through the Holocene. *Science* 293 (5533), 1304–1308. <https://doi.org/10.1126/science.1059725>.
- Heirtzler, J.R., 1974. Aeolian transport of dust off western Australia. In: Veevers, J.J., Heirtzler, J.R., et al. (Eds.), *Initial reports of the Deep Sea Drilling Project*, v. 27. U. S. Government Printing Office, Washington, pp. 397–399.
- Hesse, P.P., McTainsh, G.H., 2003. Australian dust deposits: modern processes and the Quaternary record. *Quat. Sci. Rev.* 22 (18–19), 2007–2035. [https://doi.org/10.1016/S0277-3791\(03\)00164-1](https://doi.org/10.1016/S0277-3791(03)00164-1).
- Hesse, P.P., Magee, J.W., van der Kaars, S., 2004. Late Quaternary climates of the Australian arid zone: a review. *Quat. Int.* 118, 87–102. [https://doi.org/10.1016/S1040-6182\(03\)00132-0](https://doi.org/10.1016/S1040-6182(03)00132-0).
- Holbourn, A., Kuhnt, W., Kawamura, H., Jian, Z., Grootes, P., Erlenkeuser, H., Xu, J., 2005. Orbitally paced paleoproductivity variations in the Timor Sea and Indonesian Throughflow variability during the last 460 kyr. *Paleoceanography* 20 (3). <https://doi.org/10.1029/2004PA001094>.
- Jansen, J.H.F., Kuijpers, A., Troelstra, S.R., 1986. A mid-Brunhes climatic event: long-term changes in global atmosphere and ocean circulation. *Science* 232 (4750), 619–622. <https://doi.org/10.1126/science.232.4750.619>.
- Jansen, J.H.F., Van der Gaast, S.J., Koster, B., Vaars, A.J., 1998. CORTEX, a shipboard XRF-scanner for element analyses in split sediment cores. *Mar. Geol.* 151 (1–4), 143–153. [https://doi.org/10.1016/S0025-3227\(98\)00074-7](https://doi.org/10.1016/S0025-3227(98)00074-7).
- Jickells, T.D., An, Z.S., Andersen, K.K., Baker, A.R., Bergametti, G., Brooks, N., Cao, J.J., Boyd, P.W., Duce, R.A., Hunter, K.A., Kawahata, H., 2005. Global iron connections between desert dust, ocean biogeochemistry, and climate. *Science* 308 (5718), 67–71. <https://doi.org/10.1126/science.1105959>.

- Kathayat, G., Cheng, H., Sinha, A., Spötl, C., Edwards, R.L., Zhang, H., Li, X., Yi, L., Ning, Y., Cai, Y., Lui, W.L., 2016. Indian monsoon variability on millennial-orbital timescales. *Sci. Rep.* 6, 24374. <https://doi.org/10.1038/srep24374>.
- Kawamura, H., Holbourn, A., Kuhnt, W., 2006. Climate variability and land–ocean interactions in the Indo Pacific warm Pool: a 460-ka palynological and organic geochemical record from the Timor Sea. *Mar. Micropaleontol.* 59 (1), 1–14. <https://doi.org/10.1016/j.marmicro.2005.09.001>.
- Keep, M., Holbourn, A., Kuhnt, W., Gallagher, S.J., 2018. Progressive Western Australian collision with Asia: implications for regional orography, oceanography, climate and marine biota. *J. R. Soc. West. Aust.* 101, 1–16.
- Kelly, M.J., Edwards, R.L., Cheng, H., Yuan, D., Cai, Y., Zhang, M., Lin, Y., An, Z., 2006. High resolution characterization of the Asian Monsoon between 146,000 and 99,000 years BP from Dongge Cave, China and global correlation of events surrounding termination II. *Palaeogeogr. Palaeoclimatol. Palaeoecol.* 236 (1–2), 20–38. <https://doi.org/10.1016/j.palaeo.2005.11.042>.
- Kershaw, A.P., van der Kaars, S., Moss, P.T., 2003. Late Quaternary Milankovitch-scale climatic change and variability and its impact on monsoonal Australasia. *Mar. Geol.* 201 (1–3), 81–95. [https://doi.org/10.1016/S0025-3227\(03\)00210-X](https://doi.org/10.1016/S0025-3227(03)00210-X).
- Kuhnt, W., Holbourn, A., Xu, J., Opdyke, B., De Deckker, P., Röhl, U., Mudelsee, M., 2015. Southern Hemisphere control on Australian monsoon variability during the late deglaciation and Holocene. *Nat. Commun.* 6 (1), 1–7. <https://doi.org/10.1038/ncomms6916>.
- Kuhnt, W., Holbourn, A., Schönfeld, J., Lindhorst, K., Gallagher, S., Keep, M., Sadekov, A., Dunlea, A., Clemens, S., Wilkens, R., Sarnthein, M., Leutert, T., Zhang, P., Maicher, D., Manceau, R., Dillon, A., Gonzalez, J.-L., Fabian, S., McCaffrey, J., Kochhann, K., Lübbers, J., Jo hnck, J., Hingst, J., Parplies, K., Koppe, M., Steffen, S., Schultz, J., Heinrich, S., Avers, T., Evers, F., 2018. Cruise Report Sonne 257, WACHEIO - Western Australian Climate History from Eastern Indian Ocean Sediment Archives, Darwin - Fremantle, May 12, 2017 - June 04, 2017. Christian-Albrechts-Universita t Kiel, Institut für Geowissenschaften. https://doi.org/10.2312/cr_so257, 260 pp.
- Lauterbach, S., Andersen, N., Wang, Y.V., Blanz, T., Larsen, T., Schneider, R.R., 2020. An ~130 kyr record of surface water temperature and $\delta^{18}\text{O}$ from the northern Bay of Bengal: investigating the linkage between Heinrich events and Weak Monsoon Intervals in Asia. *Paleoceanography and Paleoclimatology* 35. <https://doi.org/10.1029/2019PA003646> e2019PA003646.
- Lechler, P.J., Desilets, M.O., 1987. A review of the use of loss on ignition as a measurement of total volatiles in whole-rock analysis. *Chem. Geol.* 63 (3–4), 341–344. [https://doi.org/10.1016/0009-2541\(87\)90171-9](https://doi.org/10.1016/0009-2541(87)90171-9).
- Lisiecki, L.E., Raymo, M.E., 2005. A Pliocene-Pleistocene stack of 57 globally distributed benthic $\delta^{18}\text{O}$ records. *Paleoceanography* 20 (1). <https://doi.org/10.1029/2004PA001071>.
- Liu, L., Chen, J., Chen, Y., Ji, J., Lu, H., 2002. Variation of Zr/Rb ratios on the Loess Plateau of Central China during the last 130000 years and its implications for winter monsoon. *Chin. Sci. Bull.* 47 (15), 1298–1302. <https://doi.org/10.1360/02tb9288>.

- Liu, Z., Wen, X., Brady, E.C., Otto-Bliesner, B., Yu, G., Lu, H., Cheng, H., Wang, Y., Zheng, W., Ding, Y., Edwards, R.L., 2014. Chinese cave records and the East Asia summer monsoon. *Quat. Sci. Rev.* 83, 115–128. <https://doi.org/10.1016/j.quascirev.2013.10.021>.
- Loulergue, L., Schilt, A., Spahni, R., Masson-Delmotte, V., Blunier, T., Lemieux, B., Barnola, J.M., Raynaud, D., Stocker, T.F., Chappellaz, J., 2008. Orbital and millennial-scale features of atmospheric CH₄ over the past 800,000 years. *Nature* 453 (7193), 383–386. <https://doi.org/10.1038/nature06950>.
- Lu, J., Vecchi, G.A., Reichler, T., 2007. Expansion of the Hadley cell under global warming. *Geophys. Res. Lett.* 34 (6) <https://doi.org/10.1029/2006GL028443>.
- Lüthi, D., Le Floch, M., Bereiter, B., Blunier, T., Barnola, J.M., Siegenthaler, D., Raynaud, J., Jouzel, H., Fischer, K., Kawamura and Stocker, T. F., 2008. High-resolution carbon dioxide concentration record 650,000–800,000 years before present. *Nature* 453 (7193), 379–382. <https://doi.org/10.1038/nature06949>.
- McTainsh, G.H., 1989. Quaternary aeolian dust processes and sediments in the Australian region. *Quat. Sci. Rev.* 8 (3), 235–253. [https://doi.org/10.1016/0277-3791\(89\)90039-5](https://doi.org/10.1016/0277-3791(89)90039-5).
- Mohtadi, M., Oppo, D.W., Steinke, S., Stuut, J.B.W., De Pol-Holz, R., Hebbeln, D., Lückge, A., 2011. Glacial to Holocene swings of the Australian–Indonesian monsoon. *Nat. Geosci.* 4 (8), 540–544. <https://doi.org/10.1038/ngeo1209>.
- Mohtadi, M., Prange, M., Steinke, S., 2016. Palaeoclimatic insights into forcing and response of monsoon rainfall. *Nature* 533 (7602), 191–199. <https://doi.org/10.1038/nature17450>.
- Muller, J., Kylander, M., Wüst, R.A., Weiss, D., Martinez-Cortizas, A., LeGrande, A.N., Jennerjahn, T., Behling, H., Anderson, W.T., Jacobson, G., 2008. Possible evidence for wet Heinrich phases in tropical NE Australia: the Lynch’s Crater deposit. *Quat. Sci. Rev.* 27 (5–6), 468–475. <https://doi.org/10.1016/j.quascirev.2007.11.006>.
- Muller, J., McManus, J.F., Oppo, D.W., Francois, R., 2012. Strengthening of the Northeast Monsoon over the Flores Sea, Indonesia, at the time of Heinrich event 1. *Geology* 40 (7), 635–638. <https://doi.org/10.1130/G32878.1>.
- Paillard, D., Labeyrie, L., Yiou, P., 1996. Macintosh program performs time-series analysis. *Eos, Transactions American Geophysical Union* 77 (39), 379. <https://doi.org/10.1029/96EO00259>.
- Partin, J.W., Cobb, K.M., Adkins, J.F., Clark, B., Fernandez, D.P., 2007. Millennial-scale trends in West Pacific warm pool hydrology since the last Glacial Maximum. *Nature* 449 (7161), 452–455. <https://doi.org/10.1038/nature06164>.
- Poulton, S.W., Raiswell, R., 2002. The low-temperature geochemical cycle of iron: from continental fluxes to marine sediment deposition. *Am. J. Sci.* 302, 774–805. <https://doi.org/10.2475/ajs.302.9.774>.
- Rea, D.K., 1994. The paleoclimatic record provided by eolian deposition in the deep sea: the geologic history of wind. *Rev. Geophys.* 32 (2), 159–195. <https://doi.org/10.1029/93RG03257>.

- Rhodes, R.H., Brook, E.J., Chiang, J.H.C., Bunier, T., Maselli, O.J., McConnell, J.R., Romanini, J.R., Severinghaus, J.P., 2015. Enhanced tropical methane production in response to iceberg discharge in the North Atlantic. *Science* 1016–1019. <https://doi.org/10.1126/science.1262005>, 348/6238.
- Risbey, J.S., Pook, M.J., McIntosh, P.C., Wheeler, M.C., Hendon, H.H., 2009. On the remote drivers of rainfall variability in Australia. *Mon. Weather Rev.* 137 (10), 3233–3253. <https://doi.org/10.1175/2009MWR2861.1>.
- Rosenthal, Y., Oppo, D.W., Linsley, B.K., 2003. The amplitude and phasing of climate change during the last deglaciation in the Sulu Sea, western equatorial Pacific. *Geophys. Res. Lett.* 30 (8) <https://doi.org/10.1029/2002GL016612>.
- Rosenthal, Y., Holbourn, A., Kulhanek, D.K., the Expedition 363 Scientists, 2017. Expedition 363 Preliminary Report: Western Pacific Warm Pool. International Ocean Discovery Program, pp. 11–13.
- Rosenthal, Y., Holbourn, A.E., Kulhanek, D.K., and the Expedition 363 Scientists, 2018. Western Pacific Warm Pool. Proceedings of the International Ocean Discovery Program, 363: College Station, TX (International Ocean Discovery Program). doi:10.14379/iodp.proc.363.2018.
- Sarnthein, M., Grootes, P.M., Holbourn, A., Kuhnt, W., Kühn, H., 2011. Tropical warming in the Timor Sea led deglacial Antarctic warming and atmospheric CO₂ rise by more than 500 yr. *Earth Planet. Sci. Lett.* 302 (3–4), 337–348. <https://doi.org/10.1016/j.epsl.2010.12.021>.
- Schneider, T., Bischoff, T., Haug, G.H., 2014. Migrations and dynamics of the intertropical convergence zone. *Nature* 513 (7516), 45–53. <https://doi.org/10.1038/nature13636>.
- Schröder, J.F., Holbourn, A., Kuhnt, W., Küssner, K., 2016. Variations in sea surface hydrology in the southern Makassar Strait over the past 26 kyr. *Quat. Sci. Rev.* 154, 143–156. <https://doi.org/10.1016/j.quascirev.2016.10.018>.
- Schröder, J.F., Kuhnt, W., Holbourn, A., Beil, S., Zhang, P., Hendrizon, M., Xu, J., 2018. Deglacial warming and hydroclimate variability in the central Indonesian Archipelago. *Paleoceanography and Paleoclimatology* 33 (9), 974–993. <https://doi.org/10.1029/2018PA003323>.
- Seidel, D.J., Fu, Q., Randel, W.J., Reichler, T.J., 2008. Widening of the tropical belt in a changing climate. *Nat. Geosci.* 1, 21–24.
- Shakun, J.D., Clark, P.U., He, F., Marcott, S.A., Mix, A.C., Liu, Z., Otto-Bliesner, B., Schmittner, A., Bard, E., 2012. Global warming preceded by increasing carbon dioxide concentrations during the last deglaciation. *Nature* 484 (7392), 49–54. <https://doi.org/10.1038/nature10915>.
- Sniderman, J.K., Brown, J.R., Woodhead, J.D., King, A.D., Gillett, N.P., Tokarska, K.B., Lorbacher, K., Hellstrom, J., Drysdale, R.N., Meinshausen, M., 2019. Southern Hemisphere subtropical drying as a transient response to warming. *Nat. Clim. Chang.* 9 (3), 232–236. <https://doi.org/10.1038/s41558-019-0397-9>.

- Stager, J.C., Ryves, D.B., Chase, B.M., Pausata, F.S., 2011. Catastrophic drought in the Afro-Asian monsoon region during Heinrich event 1. *Science* 331 (6022), 1299–1302.
<https://doi.org/10.1126/science.1198322>.
- Stríkis, N.M., Cruz, F.W., Barreto, E.A., Naughton, F., Vuille, M., Cheng, H., Voelker, A. H., Zhang, H., Karmann, I., Edwards, R.L., Auler, A.S., 2018. South American monsoon response to iceberg discharge in the North Atlantic. *Proc. Natl. Acad. Sci.* 115 (15), 3788–3793.
<https://doi.org/10.1073/pnas.1717784115>.
- Stuiver, M., Reimer, P.J., Reimer, R.W., 2019. Calib Radiocarbon calibration 7.0. In: World Wide Web.
<http://calib.qub.ac.uk/calib/>. Accessed, 1.
- Stuut, J.B.W., Temmesfeld, F., De Deckker, P., 2014. A 550 ka record of aeolian activity near North West Cape, Australia: inferences from grain-size distributions and bulk chemistry of SE Indian Ocean deep-sea sediments. *Quat. Sci. Rev.* 83, 83–94. <https://doi.org/10.1016/j.quascirev.2013.11.003>.
- Sudmeyer, R., 2016. Climate in the Pilbara, Bulletin 4873, Department of Agriculture and Food. Western Australia, Perth, 46 pp.
- Suppiah, R., 1992. The Australian summer monsoon: a review. *Prog. Phys. Geogr.* 16 (3), 283–318.
<https://doi.org/10.1177/030913339201600302>.
- Taylor, S.R., McLennan, S.M., 1985. *The Continental Crust: Its Composition and Evolution*. Blackwell Scientific, Oxford, 312 pp.
- Thirumalai, K., Clemens, S.C., Partin, J.W., 2020. Methane, Monsoons, and Modulation of Millennial-Scale Climate. *Geophysical Research Letters* 47 (9). <https://doi.org/10.1029/2020GL087613>
e2020GL087613.
- Tjallingii, R., Rohlf, U., Kölling, M., Bickert, T., 2007. Influence of the water content on X-ray fluorescence core-scanning measurements in soft marine sediments. *Geochem. Geophys. Geosyst.* 8 (2)
<https://doi.org/10.1029/2006GC001393>.
- Tory, K.J., Dare, R.A., 2015. Sea surface temperature thresholds for tropical cyclone formation. *J. Clim.* 28, 8171–8183. <https://doi.org/10.1175/JCLI-D-14-00637.1>.
- Turekian, K.K., Wedepohl, K.H., 1961. Distribution of the elements in some major units of the earth's crust. *Geol. Soc. Am. Bull.* 72 (2), 175–192. [https://doi.org/10.1130/0016-7606\(1961\)72\[175:DOTEIS\]2.0.CO;2](https://doi.org/10.1130/0016-7606(1961)72[175:DOTEIS]2.0.CO;2).
- Turney, C.S., Haberle, S., Fink, D., Kershaw, A.P., Barbetti, M., Barrows, T.T., Black, M., Cohen, T.J., Correge, T., Hesse, P.P., Hua, Q., 2006. Integration of ice-core, marine and terrestrial records for the Australian last Glacial Maximum and termination: a contribution from the OZ INTIMATE group. *Journal of Quaternary Science: Published for the Quaternary Research Association* 21 (7), 751–761.
<https://doi.org/10.1002/jqs.1073>.
- Vogel, W., Kuipers, G., 1987. A pre-calibrated program for geological applications, Phillips New Developments. *X-Ray Spectrometry.* 11, 2–8.

- Wang, Y., Cheng, H., Edwards, R.L., Kong, X., Shao, X., Chen, S., Wu, J., Jiang, X., Wang, X., An, Z., 2008. Millennial-and orbital-scale changes in the East Asian monsoon over the past 224,000 years. *Nature* 451 (7182), 1090–1093. <https://doi.org/10.1038/nature06692>.
- Wang, Y.J., Cheng, H., Edwards, R.L., An, Z.S., Wu, J.Y., Shen, C.C., Dorale, J.A., 2001. A high-resolution absolute-dated late Pleistocene monsoon record from Hulu Cave, China. *Science* 294 (5550), 2345–2348. <https://doi.org/10.1126/science.1064618>.
- Wedepohl, K., 1971. *Geochemistry*: Holt, Rinehart and Winston, New York, 231 pp. Weltje, G.J., Tjallingii, R., 2008. Calibration of XRF core scanners for quantitative geochemical logging of sediment cores: Theory and application. *Earth Planet. Sci. Lett.* 274 (3–4), 423–438. <https://doi.org/10.1016/j.epsl.2008.07.054>.
- Wyrwoll, K.H., Liu, Z., Chen, G., Kutzbach, J.E., Liu, X., 2007. Sensitivity of the Australian summer monsoon to tilt and precession forcing. *Quat. Sci. Rev.* 26 (25–28), 3043–3057. <https://doi.org/10.1016/j.quascirev.2007.06.026>.
- Zhang, P., Xu, J., Holbourn, A., Kuhnt, W., Beil, S., Li, T., Xiong, Z., Dang, H., Yan, H., Pei, R., Ran, Y., 2020. Indo-Pacific hydroclimate in response to changes of the Intertropical Convergence Zone: Discrepancy on precession and obliquity bands over the last 410 kyr. *Journal of Geophysical Research: Atmospheres*. <https://doi.org/10.1029/2019JD032125> e2019JD032125.

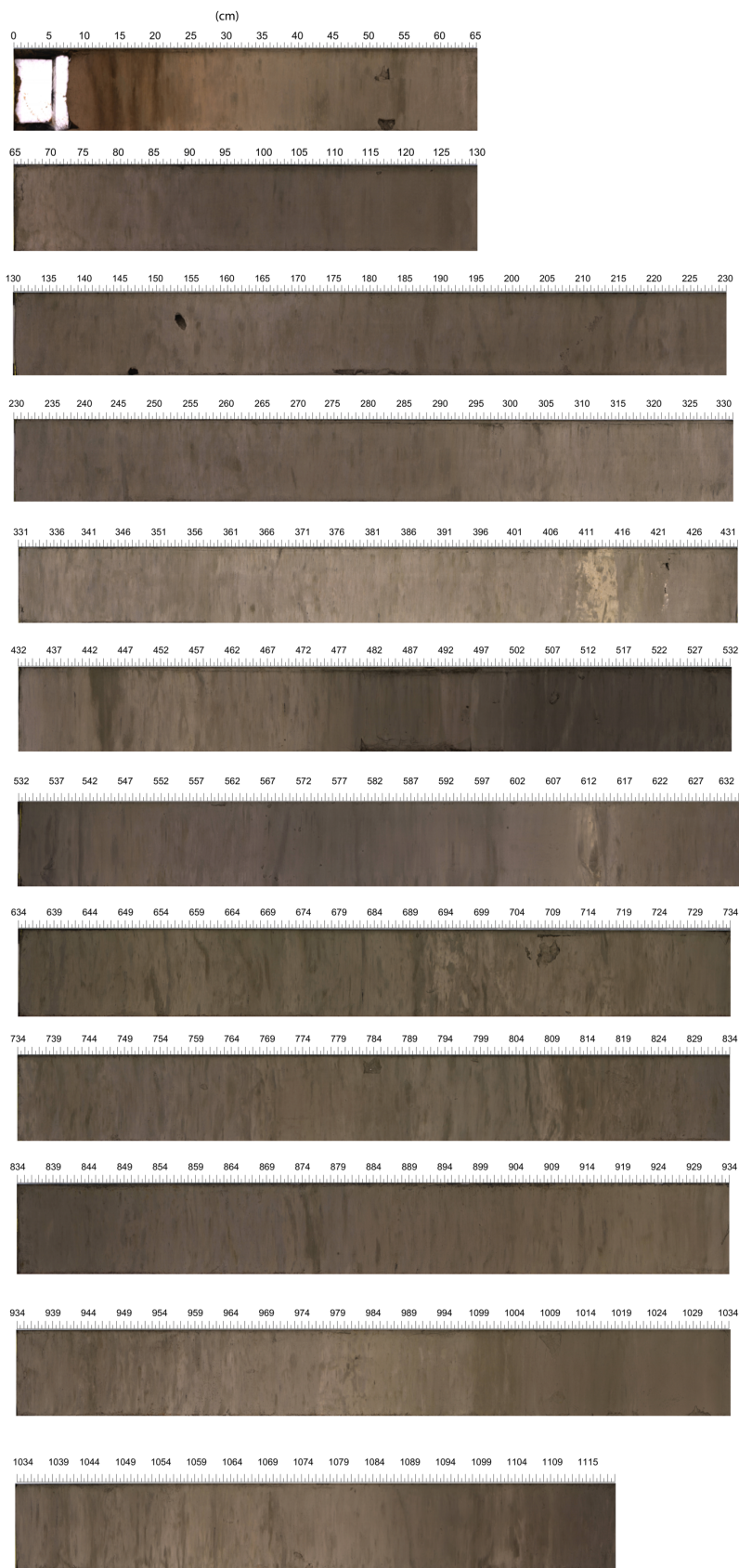
Supplementary Information for
Monitoring Australian Monsoon variability over the past four glacial cycles

Renjie Pei, Wolfgang Kuhnt, Ann Holbourn, Johanna Hingst, Matthias Koppe, Jan Schultz, Peer
Kopetz, Peng Zhang, Nils Andersen

1. Line scan images of Cores SO257-18548 and SO257-18571

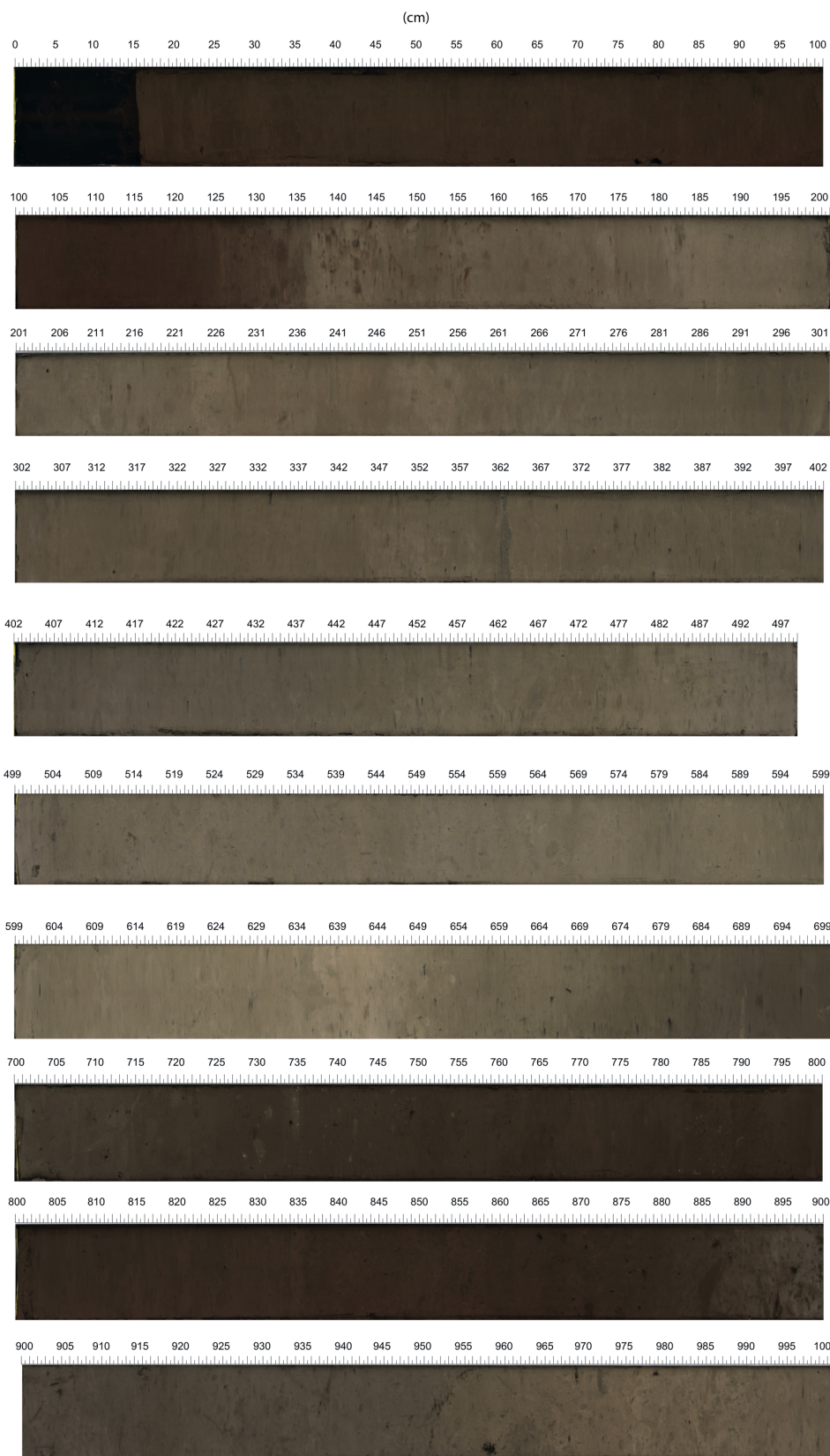
Line scan photographs and RGB measurements (resolution of 143 pixel per 1 cm or 70 μm per pixel) were acquired from the cleaned surface of Cores SO257-18548 and -18571. We used a Jai CV-L107 3 CCD color line scan camera equipped with a Nikon 60 mm macro lens and three sensors of 2048 pixels and dichroic RGB beam splitter prism (RGB channels at 630 nm, 535 nm and 450 nm). The camera is mounted on the Avaatech XRF-scanner at the Institute of Geosciences, Kiel University. Line scan photographs of the 1 m archive halves (12 for Core SO257-18548 and 20 for Core SO257-18571) are labeled with cumulative core depth in cm and shown in Supplementary Figures S1-S3:

SO257-18548



Supplementary Figure S1: Line scan images of Core SO257-18548, Sections 1-12.

SO257-18571



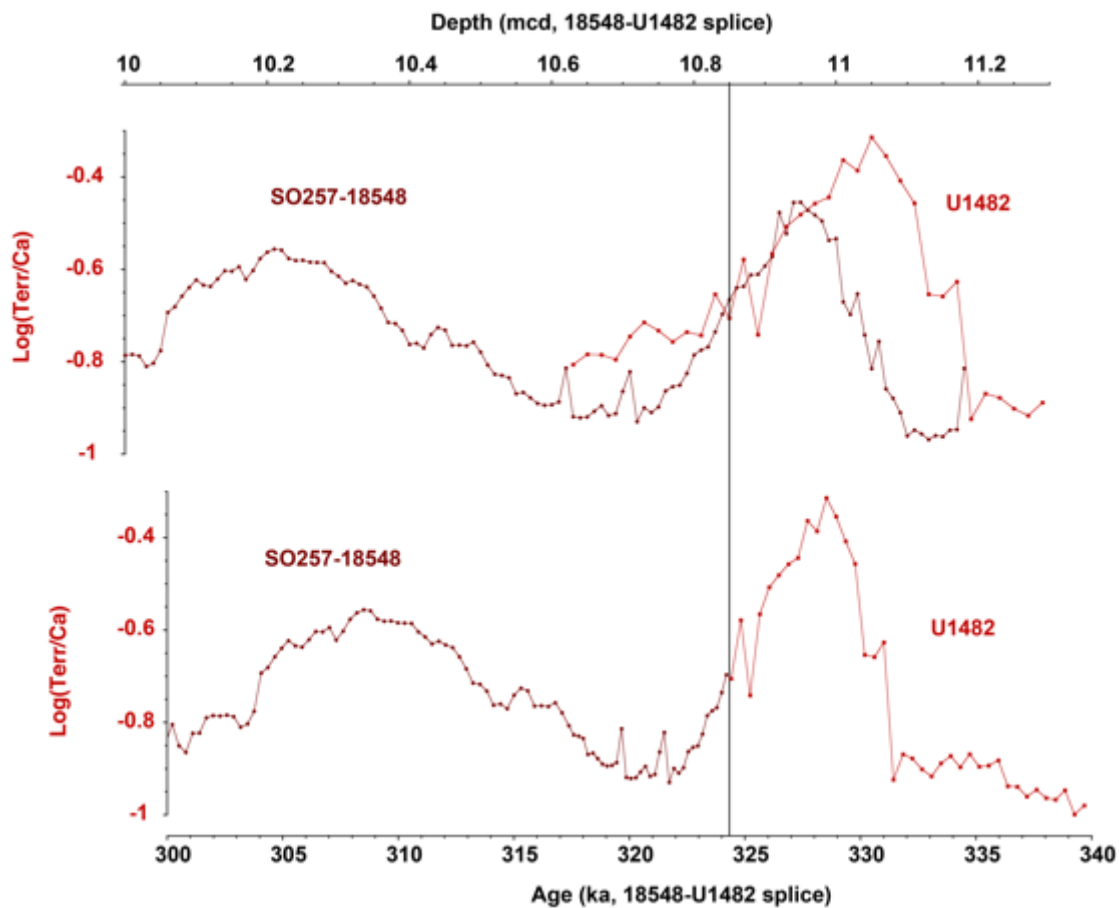
Supplementary Figure S2: Line scan images of Core SO257-18571, Sections 1-10.



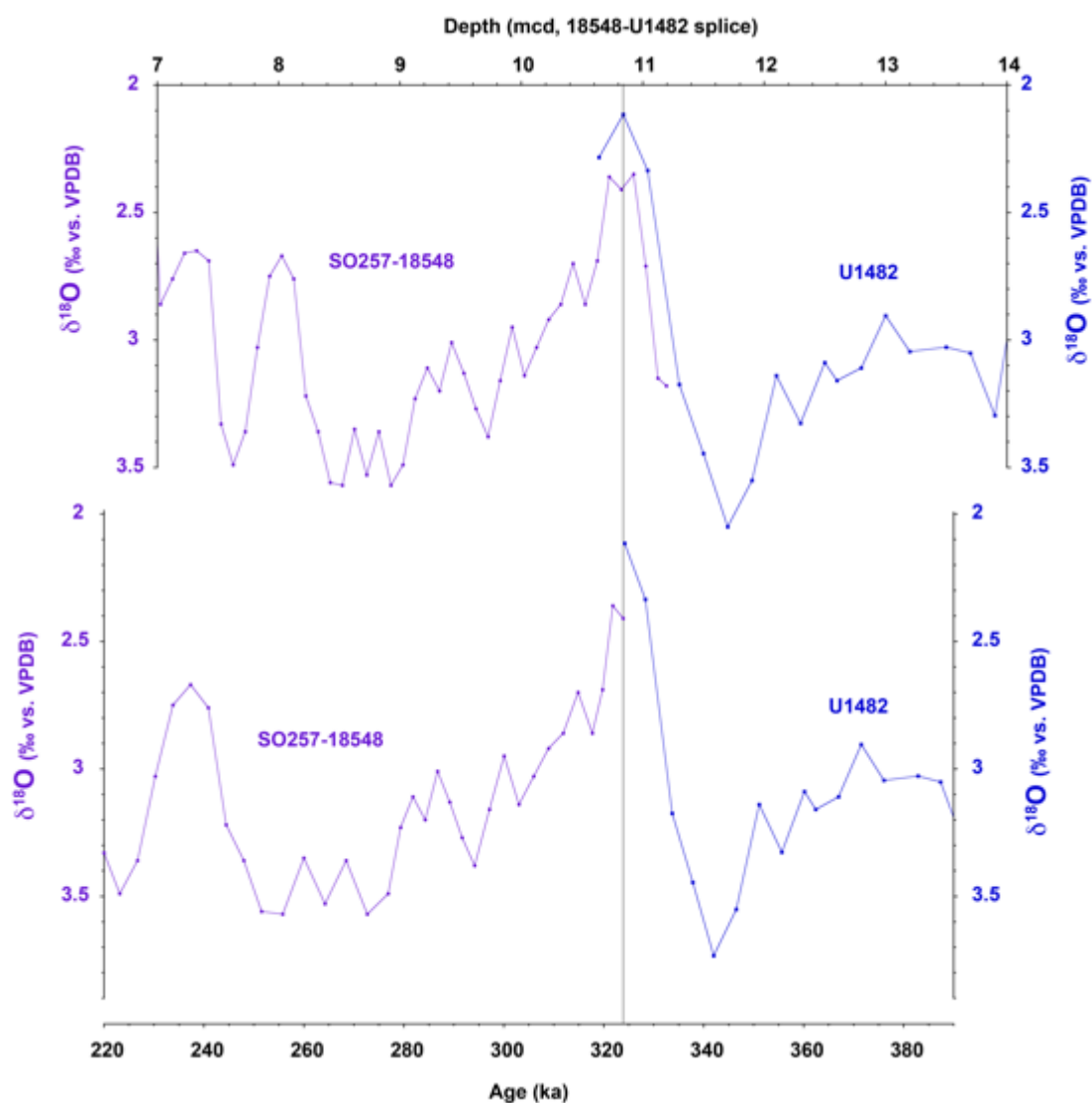
Supplementary Figure S3: Line scan images of Core SO257-18571, Sections 11-20.

2. Splicing of Core SO257-18548 with composite sediment succession from IODP Site U1482 using XRF scanner Log(Terr/Ca)

The sediment successions from Core SO257-18548 and nearby Site U1482 were spliced using the XRF scanner Log(Terr/Ca) records (Supplementary Figure S1).

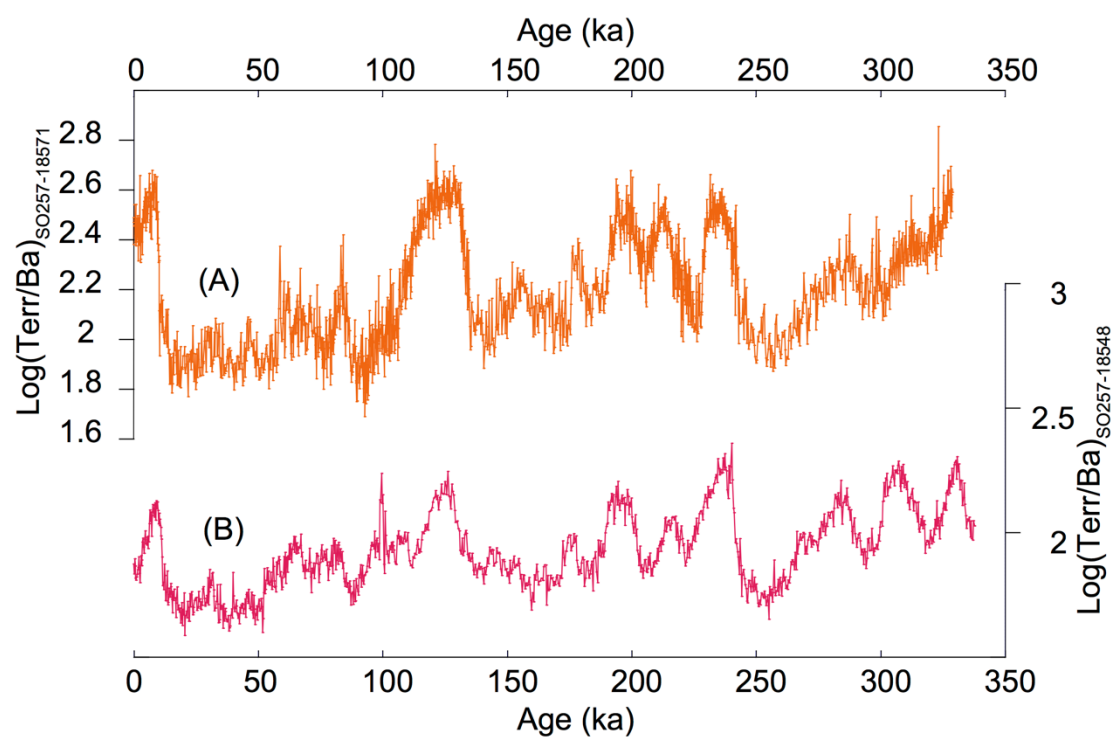


Supplementary Figure S4: Correlation between Core SO257-18548 and Site U1482, based on high-resolution XRF scanner-derived Log(Terr/Ca) records. Composite sediment succession plotted on new composite depth scale (mcd = meters composite depth) (A) and plotted against age (B). Vertical black line indicates splice tie point.



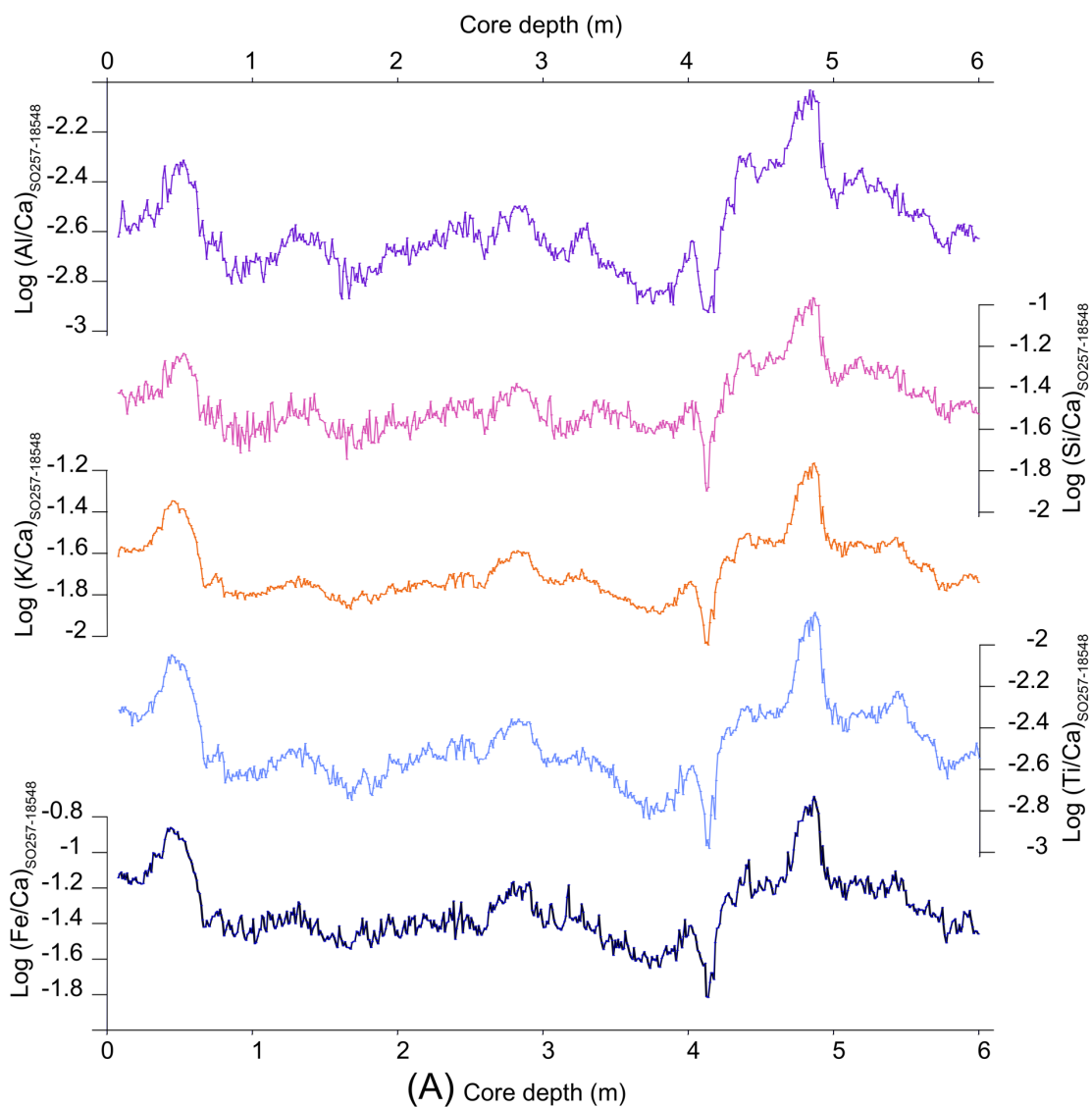
Supplementary Figure S5: Correlation of benthic $\delta^{18}\text{O}$ records from Core SO257-18548 and Site U1482 plotted on new composite depth scale (mcd = meters composite depth) (A) and plotted against age (B). Vertical black line indicates splice tie point.

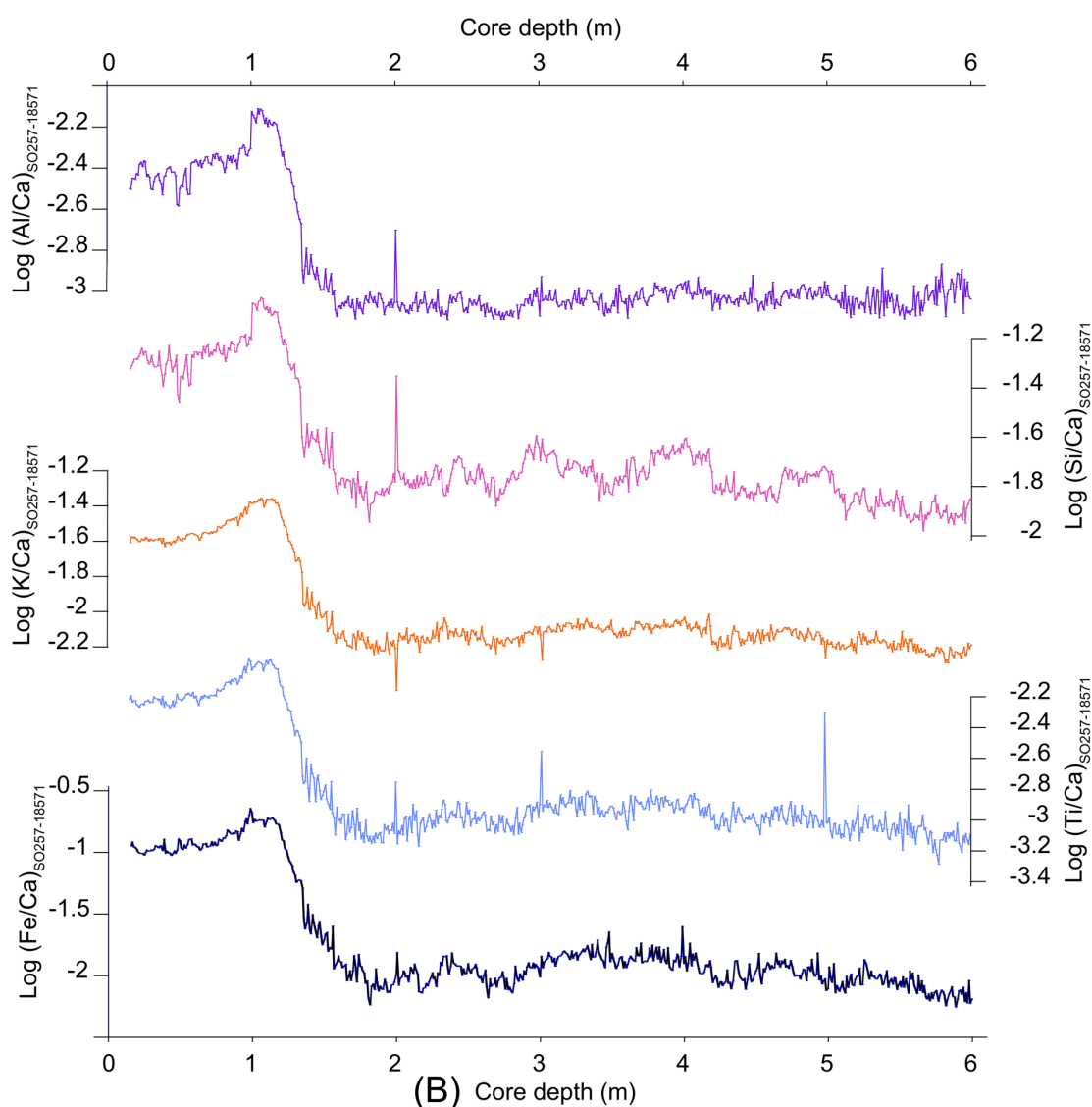
3. Normalization of terrigenous elements against barium



Supplementary Figure S6. Log(Terr/Ba) in Core SO257-18571 (A) and Core SO257-18548 (B).

4. Effect of pore-water content on XRF-scanner derived $\text{Log}(T_{err}/Ca)$





Supplementary Figure S7. Comparison of light elements aluminium and silicon (plotted as $\text{Log}(\text{Al}/\text{Ca})$ and $\text{Log}(\text{Si}/\text{Ca})$) to heavy elements potassium, iron and titanium (plotted as $\text{Log}(\text{K}/\text{Ca})$, $\text{Log}(\text{Fe}/\text{Ca})$ and $\text{Log}(\text{Ti}/\text{Ca})$) derived from XRF scanning in Core SO257-18548 (A) and Core SO257-18571 (B). The similarity of the curves for light and heavy elements demonstrates that there is no significant effect of increasing pore-water content on the shape of the $\text{Log}(\text{Terr}/\text{Ca})$ records in the upper part of the cores.

5. Calibration of XRF-scanner measurements

Supplementary Table S1A. Major element concentrations in selected samples of Core SO257-18548, based on fused beads XRF of decarbonatized sediment. Values were recalculated as percentages of total sediment including carbonate.

	SO257-18548-1W_41-42 cm	SO257-18548-3W_19-20 cm	SO257-18548-4W_28-29 cm	SO257-18548-5W_79-80 cm	SO257-18548-6W_19-20 cm	SO257-18548-7W_69-70 cm	SO257-18548-9W_53-54 cm	SO257-18548-10W_46-47 cm	SO257-18548-12W_55-56 cm
depth (cm)	42.5	150.5	259.5	411.5	452.5	602	788	881	1090
Si (%)	21.8148	14.5644	15.1065	10.2804	20.2279	15.6996	23.7497	15.9740	24.9412
Al (%)	7.8792	4.1049	4.2876	3.2819	6.4454	4.4436	7.8676	4.3120	8.2018
Fe (%)	2.7552	1.3277	1.4337	1.0940	2.0239	1.3832	2.6300	1.3776	2.6220
Mg (%)	0.6762	0.3869	0.3807	0.2477	0.5254	0.3444	0.6675	0.3584	0.6762
Mn (%)	0.0084	0.0080	0.0081	0.0039	0.0074	0.0084	0.0089	0.0084	0.0092
Ca (CaO) (%)	0.2982	0.2041	0.1890	0.1209	0.2183	0.1652	0.2492	0.1568	0.2576
K (%)	1.0584	0.5592	0.5697	0.4661	0.8584	0.6104	1.1214	0.5824	1.1500
Ti (%)	0.4074	0.2226	0.2376	0.1892	0.3367	0.2492	0.4228	0.2520	0.4324
Rb (%)	0.0071	0.0032	0.0032	0.0028	0.0051	0.0035	0.0070	0.0033	0.0071
Zr (%)	0.0066	0.0046	0.0050	0.0034	0.0058	0.0051	0.0070	0.0057	0.0075
carbonate (%)	58.00	73.50	73	80.50	63.00	72	55.50	72	54

Supplementary Table S1B. Major element α -area counts (cps) in selected samples of Core SO257-18548, using Avaatech second generation XRF-scanner

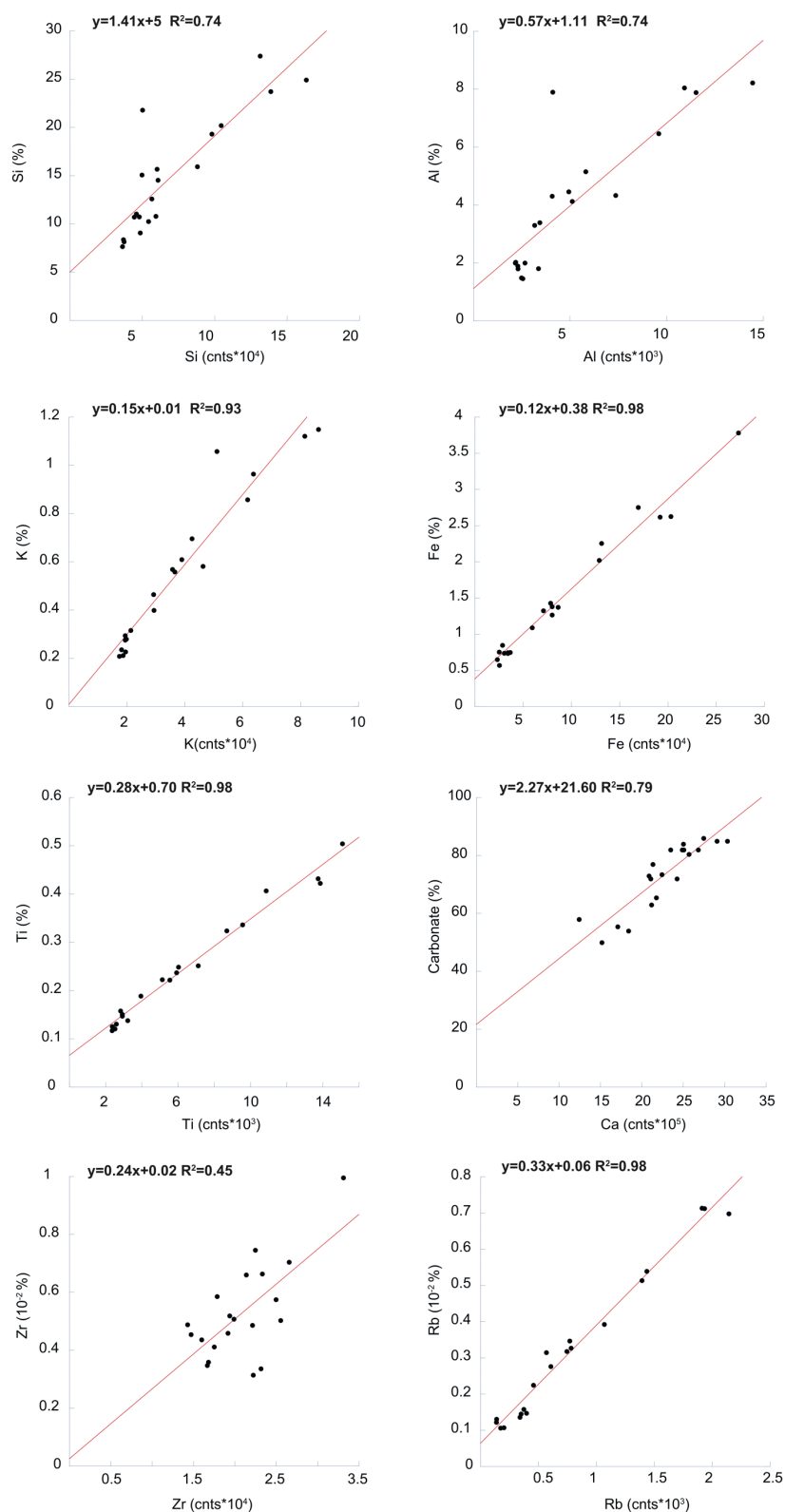
	SO257-18548-1W_41-42 cm	SO257-18548-3W_19-20 cm	SO257-18548-4W_28-29 cm	SO257-18548-5W_79-80 cm	SO257-18548-6W_19-20 cm	SO257-18548-7W_69-70 cm	SO257-18548-9W_53-54 cm	SO257-18548-10W_46-47 cm	SO257-18548-12W_55-56 cm
Depth (cm)	42.5	150.5	259.5	411.5	452.5	602	788	881	1090
Si	49856	60534	49538	53991	104187	59881	138393	87817	162921
Al	4084	5096	4053	3144	9569	4911	11506	7342	14435
Fe	168937	70702	77986	59007	128554	79633	202657	85834	191426
Mg	411	541	441	402	641	412	837	543	1036
Mn	2995	2991	2685	2381	3913	4785	2992	4156	2592
Ca	1237095	2238436	2082853	2565279	2111130	2102140	1703889	2420087	1834232
K	50921	36432	35642	29043	61571	38808	81286	46180	85989
Ti	10846	5528	5897	3928	9547	6001	13841	7093	13719
Rb	1908	565	743	604	1390	767	2141	779	1930
Zr	2133	1910	2549	2311	1781	1985	2651	2492	2243

Supplementary Table S2A. Major element concentrations in selected samples from Core SO257-18571 using fused beads XRF of decarbonatized sediment. Values were recalculated as percentages of total sediment including carbonate.

	SO257-18571-2W_3-4 cm	SO257-18571-2W_36-37 cm	SO257-18571-2W_98-99 cm	SO257-18571-3W_50-51 cm	SO257-18571-4W_29-30 cm	SO257-18571-4W_62-63 cm	SO257-18571-5W_1-2 cm	SO257-18571-5W_44-45 cm	SO257-18571-6W_12-13 cm	SO257-18571-7W_14-15 cm	SO257-18571-8W_14-15 cm
depth (cm)	103.5	136.5	198.5	251.5	329.5	364.5	403.5	446.5	512.5	613.5	714.5
Si (%)	27.4250	12.6339	9.0975	11.0754	10.7424	10.7712	10.8144	8.4048	8.1746	7.6965	19.3476
Al (%)	8.0300	3.3787	1.4415	1.8756	1.9836	2.0070	1.9836	1.7808	1.4686	1.7895	5.1371
Fe (%)	3.7850	1.2696	0.5745	0.7416	0.7524	0.7398	0.7488	0.7568	0.6552	0.8520	2.2598
Mg (%)	0.7650	0.2691	0.1080	0.1512	0.1512	0.1404	0.1188	0.1216	0.1050	0.1215	0.5969
Mn (%)	0.0100	0.0046	0.0030	0.0036	0.0036	0.0036	0.0036	0.0032	0.0014	0.0030	0.0069
Ca (CaO) (%)	0.2950	0.0736	0.0855	0.0936	0.0828	0.0792	0.0774	0.0656	0.0560	0.0600	0.1863
Na (%)	0.1900	0.0759	0.0765	0.0864	0.0792	0.0900	0.1134	0.0608	0.0644	0.0615	0.1380
K (%)	0.9650	0.4002	0.2130	0.2772	0.2808	0.2952	0.3168	0.2368	0.2100	0.2280	0.6969
Ti (%)	0.5050	0.2231	0.1215	0.1476	0.1512	0.1584	0.1386	0.1312	0.1176	0.1260	0.3243
Rb (%)	0.0054	0.0023	0.0011	0.0014	0.0015	0.0015	0.0016	0.0013	0.0011	0.0012	0.0039
Zr (%)	0.0100	0.0049	0.0041	0.0049	0.0045	0.0052	0.0044	0.0035	0.0036	0.0031	0.0066
Carbonate (%)	50	77	85	82	82	82	82	84	86	85	65.5

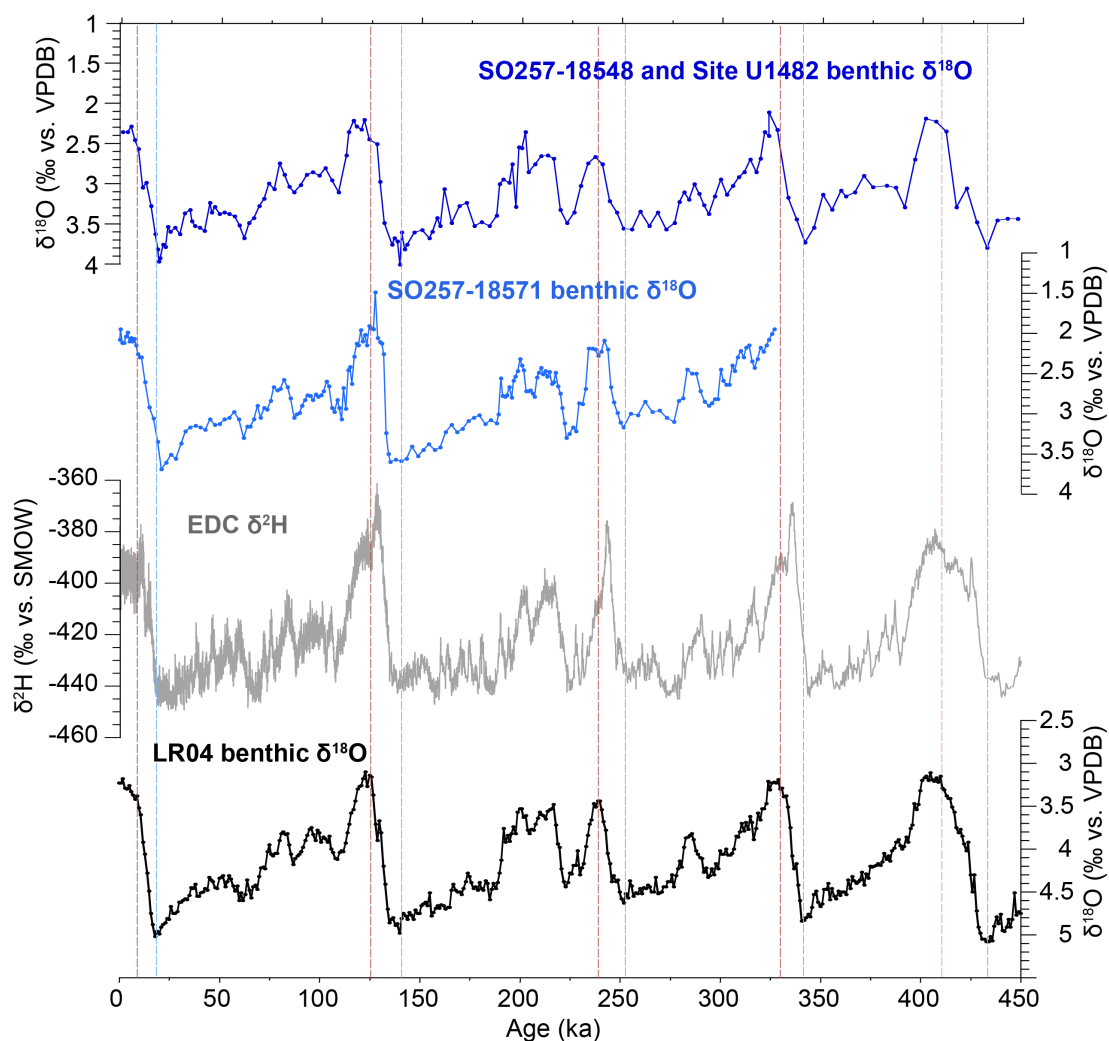
Supplementary Table S2B. Major element α -area counts (cps) in selected samples of Core SO257-18571 using Avaatech second generation XRF-scanner.

	SO257-18571-2W_3-4 cm	SO257-18571-2W_36-37 cm	SO257-18571-2W_98-99 cm	SO257-18571-3W_50-51 cm	SO257-18571-4W_29-30 cm	SO257-18571-4W_62-63 cm	SO257-18571-5W_1-2 cm	SO257-18571-5W_44-45 cm	SO257-18571-6W_12-13 cm	SO257-18571-7W_14-15 cm	SO257-18571-8W_14-15 cm
Depth (cm)	103	136	198	251	329	364	403	446	512	613	714
Si	127231	49636	50378	44036	41598	52488	50687	34121	42263	32085	85967
Al	10209	2746	2789	2054	1991	2273	2149	2103	2360	3086	6049
Fe	261323	63004	25690	29289	35821	34917	27846	23966	20676	28268	131142
Mg	854	517	768	510	406	455	448	410	484	483	665
Mn	1676	1026	889	905	591	603	692	780	444	661	847
Ca	1462297	2173011	3051209	2608208	2288047	2540524	2202014	2403031	2861377	2915024	2165677
K	60878	24127	19495	16939	19378	20488	17643	17593	17532	18568	43561
Ti	14362	4179	2603	2865	2676	3664	2785	2571	2225	2078	9146
Rb	1433	454	170	337	393	346	370	136	198	134	1066
Zr	3307	2208	1746	1424	1467	1933	1595	1661	1675	2217	2327



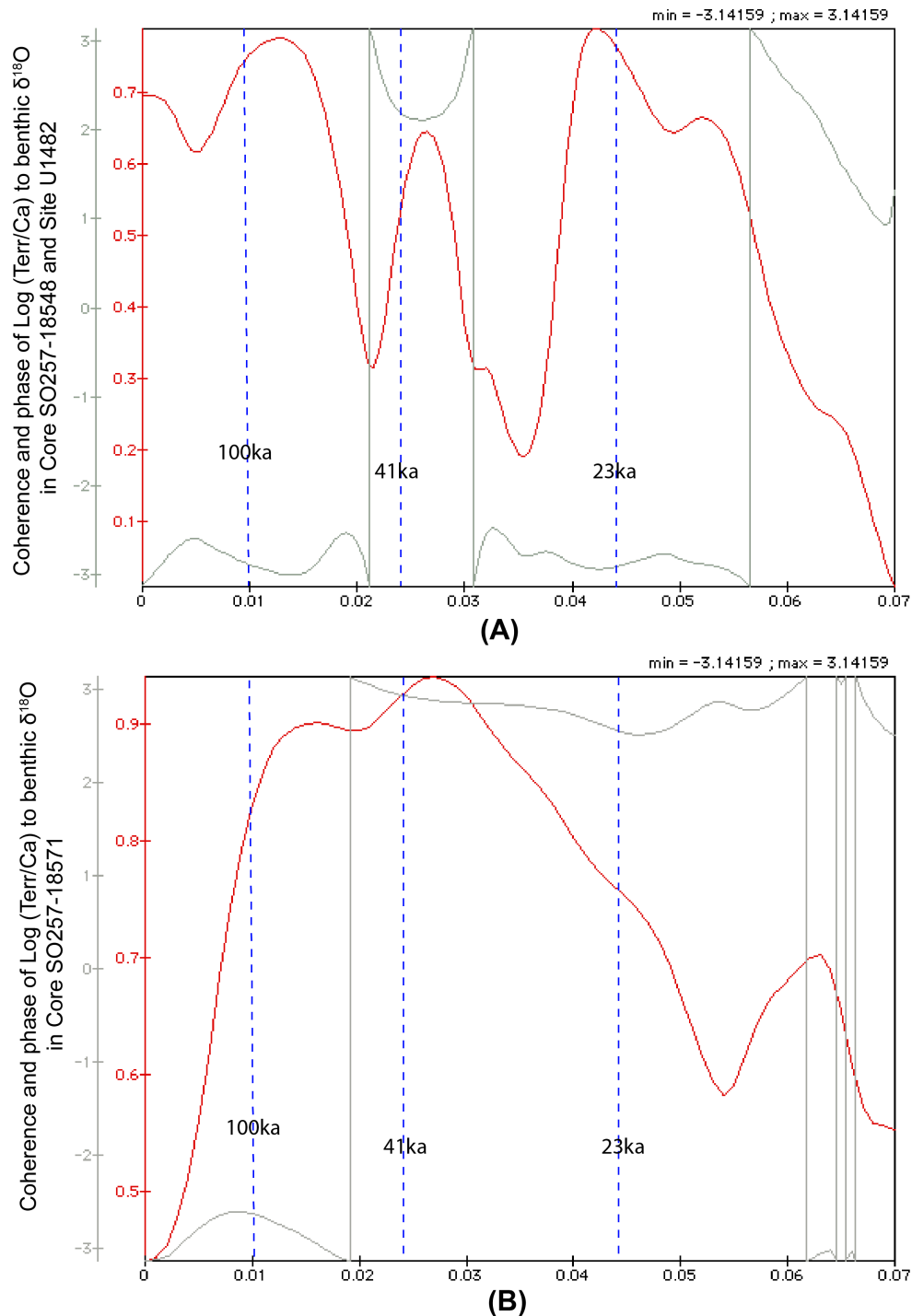
Supplementary Figure S8. Regression plots between XRF-scanner area counts (cps) and fused beats XRF analyses of discrete samples from the same depth intervals in Cores SO257-18548 and -18571. Red line indicates linear least-squares regression.

6. Comparison to Antarctic temperature record



Supplementary Figure S9. Comparison of chronology based on correlation of benthic oxygen isotope records to the LR04 stack (Lisiecki and Raymo, 2005) with Antarctic δD derived temperature record (Bazin et al., 2013).

7. Coherence, phase and response of benthic $\delta^{18}\text{O}$

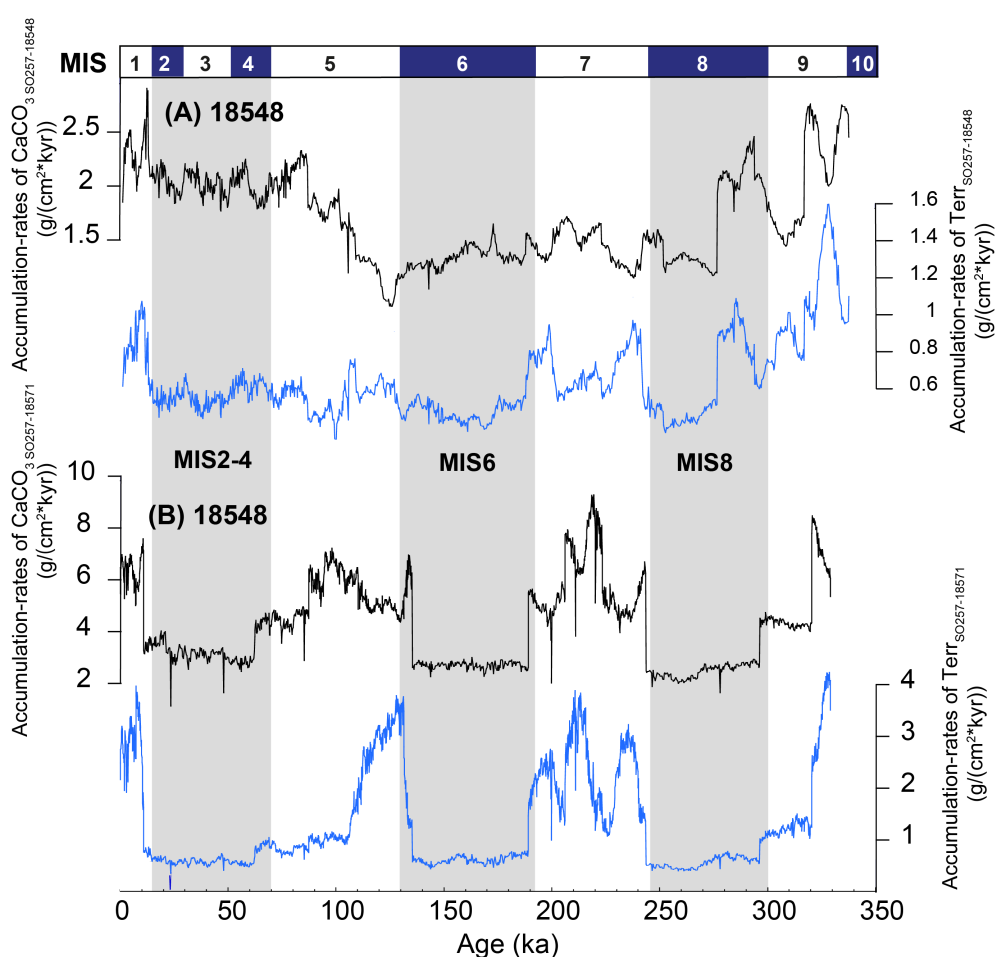


Supplementary Figure S10: Coherence and phase of Log(Terr/Ca) to benthic foraminiferal $\delta^{18}\text{O}$ in the spliced sediment record from Core SO257-18548 and Site U1482 (A) and from Core SO257-18571 (B). Blackman Tukey spectrum using a Bartlett window. Bandwidth is 0.011194. Non-zero coherence > 0.550342 . Error estimation on power spectrum is $0.488632 < \Delta\text{Power} / \text{Power} < 3.0732$.

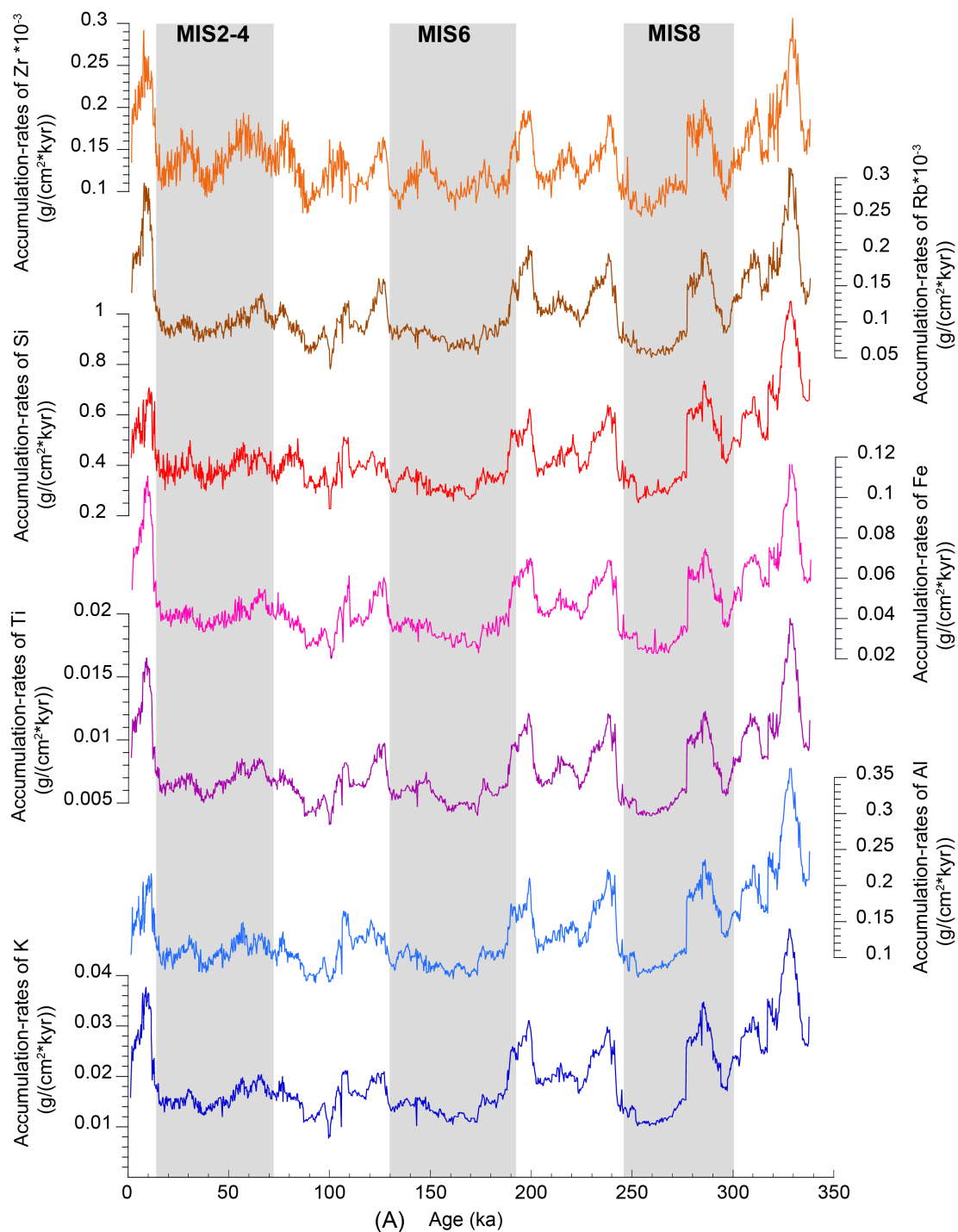
8. Accumulation rates of terrigenous elements and carbonate in Cores SO257-18548 and SO257-18571

Bulk sediment mass accumulation rates (MARs) were calculated by multiplying linear sedimentation rates (LSRs derived from the age model of Cores SO257-18548 and -18751) with average dry bulk density (DBD) in 9 samples from Core SO257-18548 (0.7346 g/cm^3 , standard deviation 0.0747) and 11 samples from Core SO257-18571 (0.9024 g/cm^3 , standard deviation 0.0767).

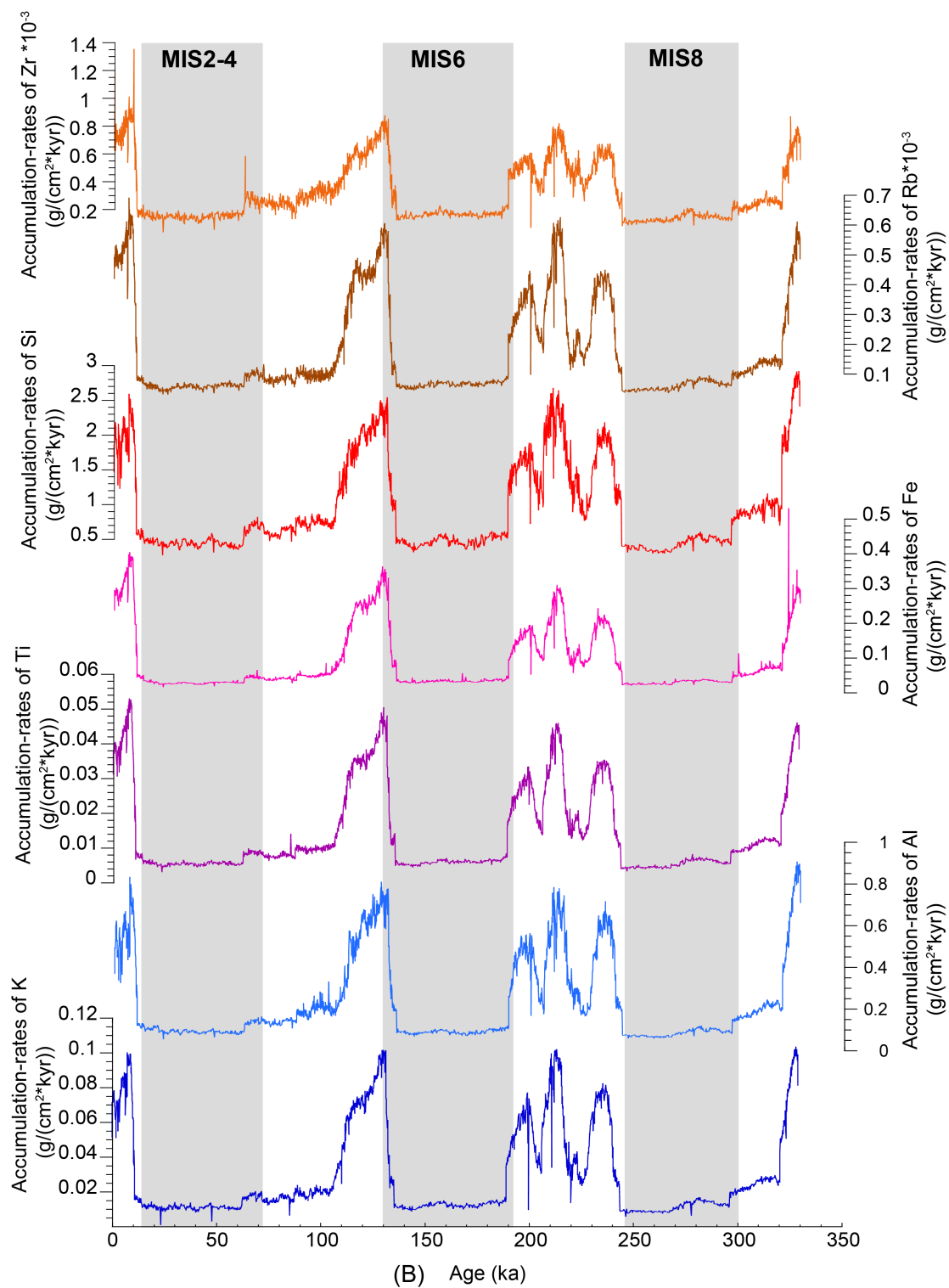
Accumulation rates of individual elements or groups of elements were calculated by multiplying MARs with the proportion (weight percent/100) of each element or group of elements.



Supplementary Figure S11. Accumulation rates of terrigenous elements and carbonate in Core SO257-18548 (A) and Core SO257-18571 (B).

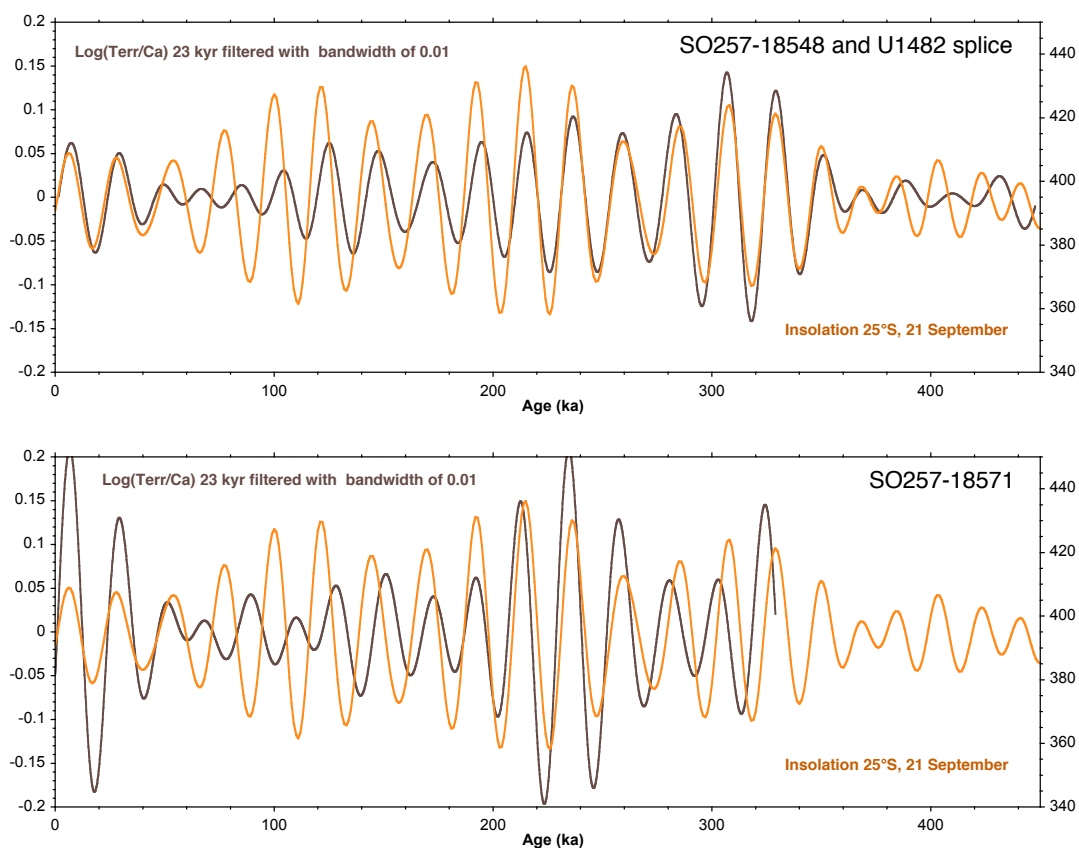


Supplementary Figure S12. Accumulation rates of individual terrigenous elements in Core SO257-18548



Supplementary Figure S13. Accumulation rates of individual terrigenous elements in Core SO257-18571

9. Riverine runoff proxy ($\text{Log}(\text{Terr}/\text{Ca})$) time series in comparison to 23 kyr precessional insolation



Supplementary Figure S14: Comparison of 23 kyr filtered $\text{Log}(\text{Terr}/\text{Ca})$ (black) to 21st September insolation at 25°S (yellow).

Evolution of sea surface hydrology along the Northwestern Australian Margin over the past 450 kyr

Renjie Pei¹, Wolfgang Kuhnt¹, Ann Holbourn¹, Janika Jöhnck¹, Johanna Hingst^{1,2}, Sebastian Beil¹, Julia Lübbers¹, Nils Andersen³

¹*Institute of Geosciences, Christian-Albrechts-University, Kiel D-24118, Germany.*

²*MARUM – Center for Marine Environmental Sciences, University of Bremen, Bremen D-28359, Germany.*

³*Laboratory for Radiometric Dating and Stable Isotope Research, Christian-Albrechts-University, Kiel D-24118, Germany.*

Corresponding author: Renjie Pei (renjie.pei@ifg.uni-kiel.de)

Key Points:

- Southwest front of modern Indo-Pacific Warm Pool is located between 23 and 24°S during austral fall
- Northwestern Australian Margin north of 15°S remained seasonably influenced by Indo-Pacific Warm Pool throughout past 450 kyr
- Ningaloo-Niño type warming and freshening lead to unusually warm and wet conditions following glacial terminations

Keywords

Australian monsoon, Mg/Ca paleothermometry, SST, IODP, IPWP, SSS

Abstract

We collected a suite of core top samples during R/V Sonne Cruise SO257 in May 2017 along the southwestern front of the Indo-Pacific Warm Pool (IPWP) to monitor the variability of Southern Hemisphere tropical and subtropical sea surface hydrology and to assess

temperature and salinity reconstructions with data sets reflecting conditions in the post-monsoonal season. In our core top samples, a steep increase in planktonic $\delta^{18}\text{O}$, associated with a decrease in sea surface temperature (SST), indicates that the southwestern front of the IPWP is located between 23 and 24°S during austral fall. We additionally reconstructed SST, sea surface salinity (SSS) and $\delta^{18}\text{O}$ seawater ($\delta^{18}\text{O}_{\text{sw}}$) over the last 450 kyr in two sediment successions located within and beyond the monsoonal rain belt. The regional differences in the SST and SSS records reveal that the Northwestern Australian Margin north of 15°S remained seasonally under the influence of IPWP water masses, even during glacials. The temporal variability in SSS along the Northwestern Australian Margin differs from local monsoonal sediment discharge, which is highly coherent to precessional insolation forcing. By contrast, SSS variability represents an integrated signal of precipitation, runoff and advective mixing along the pathway of the Indonesian Throughflow. Our records also show that SST maxima at the end of glacial terminations coincided with maxima in atmospheric $p\text{CO}_2$, Southern Hemisphere spring insolation and latitudinal insolation gradients. We speculate that these combined forcings contributed to more frequent Ningaloo-Niño type events, leading to unusually warm and wet conditions off Western Australia following glacial terminations.

1. Introduction

The influence of precessional insolation and latitudinal insolation gradients on tropical hydrology, in particular the intensity and spatial extent of the Indonesian-Australian monsoonal rain belt, is still a matter of debate, since extended, orbital scale records remain extremely scarce (e.g. Holbourn et al., 2005; Zhang et al., 2020), as most studies focused on the last glacial cycle (e.g. Mohtadi et al., 2011; Ayliffe et al., 2013; Denniston et al., 2013; Kuhnt et al., 2015; Eroglu et al., 2016; Field et al., 2017; Ishiwa et al., 2019). Global sea surface temperature (SST) stacks over the last deglaciation indicated significant inter-hemispheric

differences during deglacial warming, in particular for the phasing between globally increasing atmospheric carbon dioxide and regional warming in both hemispheres (Shakun et al., 2012b). This global compilation included high-resolution SST reconstructions over the last two glacial terminations in the Timor Sea (Xu et al., 2006, 2008, 2010), at locations situated within the Indo-Pacific Warm Pool (IPWP). However, these reconstructions were based on Mg/Ca thermometry of near-surface and upper thermocline planktonic foraminifers in an area directly influenced by the Indonesian Throughflow (ITF) and, thus, inherit some Northern Hemisphere temperature signature, such as a cool Heinrich Stadial 1 (HS1, ~15 to 18 ka) and an onset of deglacial warming during the Bølling/Allerød (~13 to 15 ka). Cores in the tropical Indian Ocean offshore southern Java, within the Timor Strait, Flores Sea, and Makassar Strait exhibit a similar delayed warming trend following HS 1 (Holbourn et al., 2011; Mohtadi et al., 2011; Schröder et al., 2018).

Substantial regional cooling in the Northern Hemisphere and widespread drying in the subtropics and tropics in the early stage of the last deglaciation (HS 1) were originally attributed to a southward shift of the Inter Tropical Convergence Zone (ITCZ) and associated tropical rain belt (Broccoli et al., 2006; Chiang et al., 2003, 2008; Chiang & Bitz, 2005; Claussen et al., 2003; Muller et al., 2008, 2012). However, a global data compilation demonstrated that the height of this stadial (~16 to 17 ka) coincided with an extreme and widespread megadrought, which also affected the Southern Hemisphere (Stager et al., 2011). The widespread extent of the HS 1 megadrought suggests a severe weakening of the entire tropical convective rainfall system, probably as a response to tropical sea surface cooling on a global scale. Temperature, precipitation and monsoonal sediment discharge proxy records from the subtropical Indian Ocean and off northwestern Australia indicated a subsequent major intensification of the Australian Monsoon at ~13 to 14 ka (De Deckker et al., 2014; Denniston et al., 2013; Field et al., 2017; Ishiwa et al., 2019; Kuhnt et al., 2015). However, the occurrence of widespread

tropical aridification reaching into the Southern Hemisphere during the early stage of deglaciation, when atmospheric $p\text{CO}_2$ levels were still substantially lower than pre-industrial, remains uncertain. Insights into the phase relationships between precessional insolation, atmospheric $p\text{CO}_2$, local SST and monsoonal discharge over several glacial terminations are, thus, critical for a better understanding of the processes driving climate warming and convective rainfall intensification in the Southern Hemisphere.

On orbital timescales, Northern and Southern Hemisphere temperature records exhibit an unexpected similar response to precessional insolation forcing with temperature maxima at precession minima (Northern Hemisphere insolation maxima) (Huybers & Denton, 2008; Laepple et al., 2011; Uemura et al., 2018). Southern Hemisphere monsoonal proxy records display a similar response to insolation/temperature forcing with maxima in monsoonal intensity close to precession minima even though Southern Hemisphere peak daily summer insolation was at a minimum (e.g. Zhang et al., 2020). Several mechanisms have been suggested to explain this phase-locked behavior of climate on the precessional band in the two hemispheres: (1) extended austral summer duration (maximum number of days with high average insolation in the Southern Hemisphere) at precession minima (Huybers, 2009); (2) maximum daily insolation in austral spring (September) at precession minima, which decreases sea ice cover around Antarctica and intensifies heat transfer towards the Antarctic interior with repercussions over the entire Southern Hemisphere (Timmermann et al., 2009); (3) zonal and cross-equatorial transfer of the Northern Hemispheric insolation signal to the Southern Hemisphere by atmospheric or ocean circulation (Chiang et al., 2008; Deininger et al., 2020); (4) steepening of latitudinal insolation gradients driven by the interference of precessional forcing and orbital obliquity (Bosmans et al., 2018; Chiang & Friedman, 2012; Mantsis et al., 2014).

Here, we monitor the variability of Southern Hemisphere tropical and subtropical hydrology in core top samples collected during R/V Sonne Cruise SO257 in May 2017 at sensitive locations along the southwestern front of the IPWP. We additionally reconstruct SST, sea surface salinity (SSS) and $\delta^{18}\text{O}$ seawater ($\delta^{18}\text{O}_{\text{sw}}$) over the last 450 kyr in two sediment successions located at the southwestern edge of the IPWP (within the monsoonal rain belt) and southwest of the IPWP (outwith the monsoonal rain belt). Our main objectives are to monitor the variability of Southern Hemisphere tropical and subtropical SST and SSS on millennial timescales and to relate their variability to sediment discharge records of the Australian Monsoon, insolation forcing, high latitude climate evolution and changing atmospheric greenhouse gas concentrations.

2. Regional oceanographic and climatic setting

The hydrologic setting at the southwestern margin of the IPWP is crucial for understanding climate evolution on the Australian continent and tropical climate interactions between the Pacific and Indian Oceans. The Northwestern Australian Margin along the eastern Indian Ocean is characterized by a steep SST gradient from temperatures above 28°C within the IPWP to the northeast to cooler temperatures with stronger seasonal variability between 22 and 25°C to the southwest (Figure 1A). There is also a marked northeastern-southwestern SSS gradient with higher salinities to the southwest (Figure 1B). The seasonal variability of SST and SSS along the margin is affected by the intensity of the ITF and Leeuwin Current, which carry warm, low salinity water from the Timor Strait and eastern part of the North West Shelf towards the southwest (Church et al., 1989; Feng et al., 2015; Fieux et al., 2005).

The seasonal salinity gradient is influenced both by the lower salinity of Banda and Arafura Sea waters that are transported by the ITF through the Timor Strait and along the North

West Shelf and by freshwater discharge from the large rivers that drain the northern Australian monsoonal region (Phillips et al., 2005). The seasonal dynamics of the IPWP southwestern front are strongly influenced by the interplay of the ITF and Leeuwin Current. The latter is initiated through a sea-level build-up by monsoonal winds during December-February in the Gulf of Carpentaria (Ridgway & Godfrey, 2015). The Leeuwin Current flows southward along the continental shelf of northwestern Australia as a shallow (<300 m), narrow band (<100 km wide) of warm, lower salinity, nutrient depleted water of tropical origin, which mixes with cooler and saltier waters from the northward flowing West Australian Current during austral summer (Church et al., 1989; Cresswell & Peterson, 1993; Pattiaratchi, 2006; Ridgway & Condie, 2004; Smith et al., 1991). The unusually warm Leeuwin Current is seasonally strongest during austral fall and winter (May-July) and on an interannual time scale during La Niña years. Intensification of the Leeuwin Current promotes evaporative heat loss and upper ocean stratification and reduces upper ocean mixing, nutrient fluxes, and productivity (Feng et al., 2009). The current intensity is additionally increased by the heat flux over the Pilbara region during late austral summer, since increasing depth-averaged temperatures on the Pilbara shelf contribute to elevated sea level, when the warm surface water is vertically mixed by strong tides. This leads to seasonal advection of warm water westward and southward (Ridgway & Godfrey, 2015). The sea-level anomaly that drives the current system propagates southward against the prevailing wind direction and dominates the surface ocean along the Western Australia Margin during austral fall and early winter.

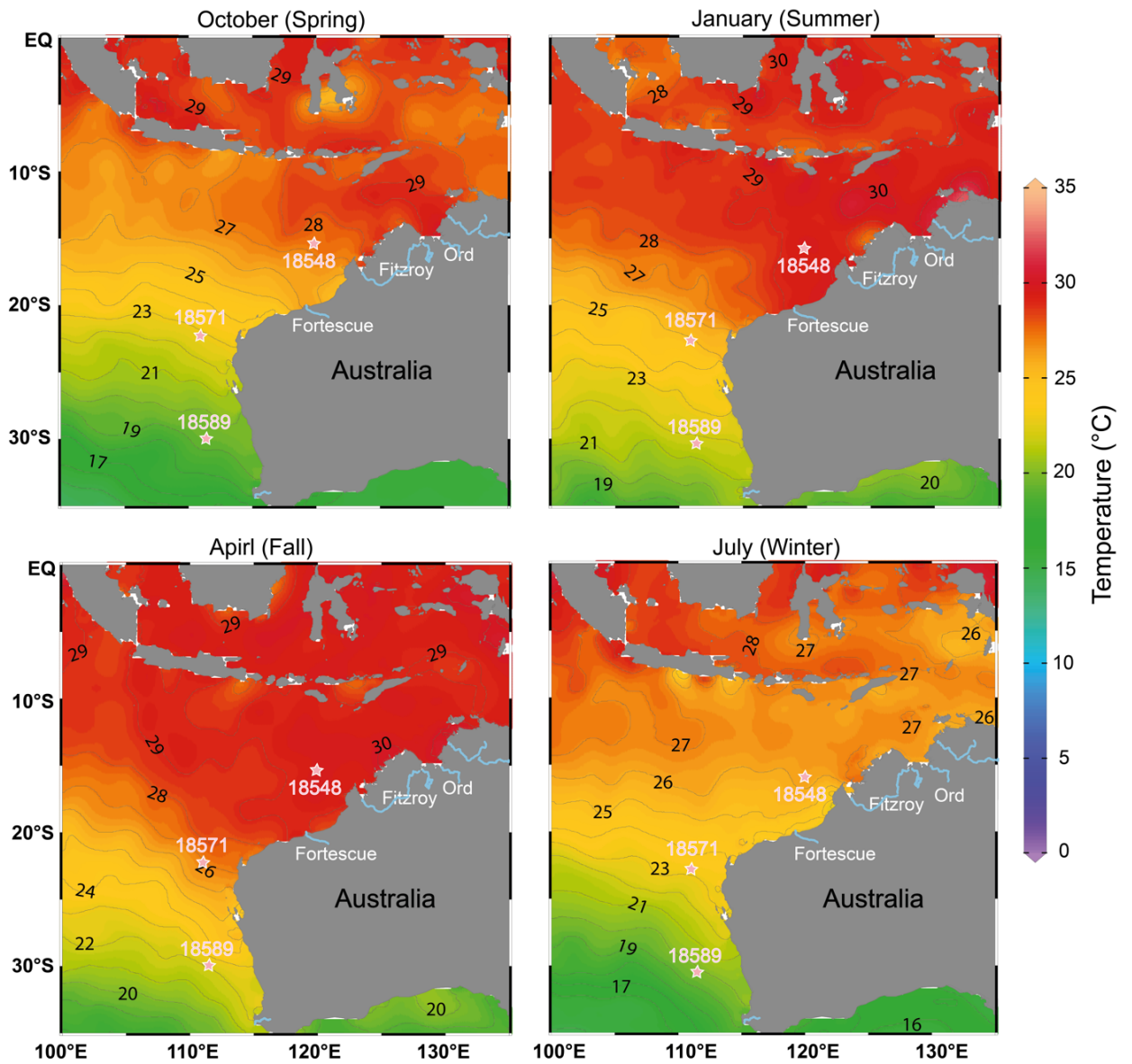


Figure 1A. Seasonal distribution of modern sea surface (0 m) temperatures in the eastern Indian Ocean and along the Northwestern Australian Margin. Data from WOA13 (Locarnini et al., 2013) plotted using Ocean Data View (Schlitzer, 2020).

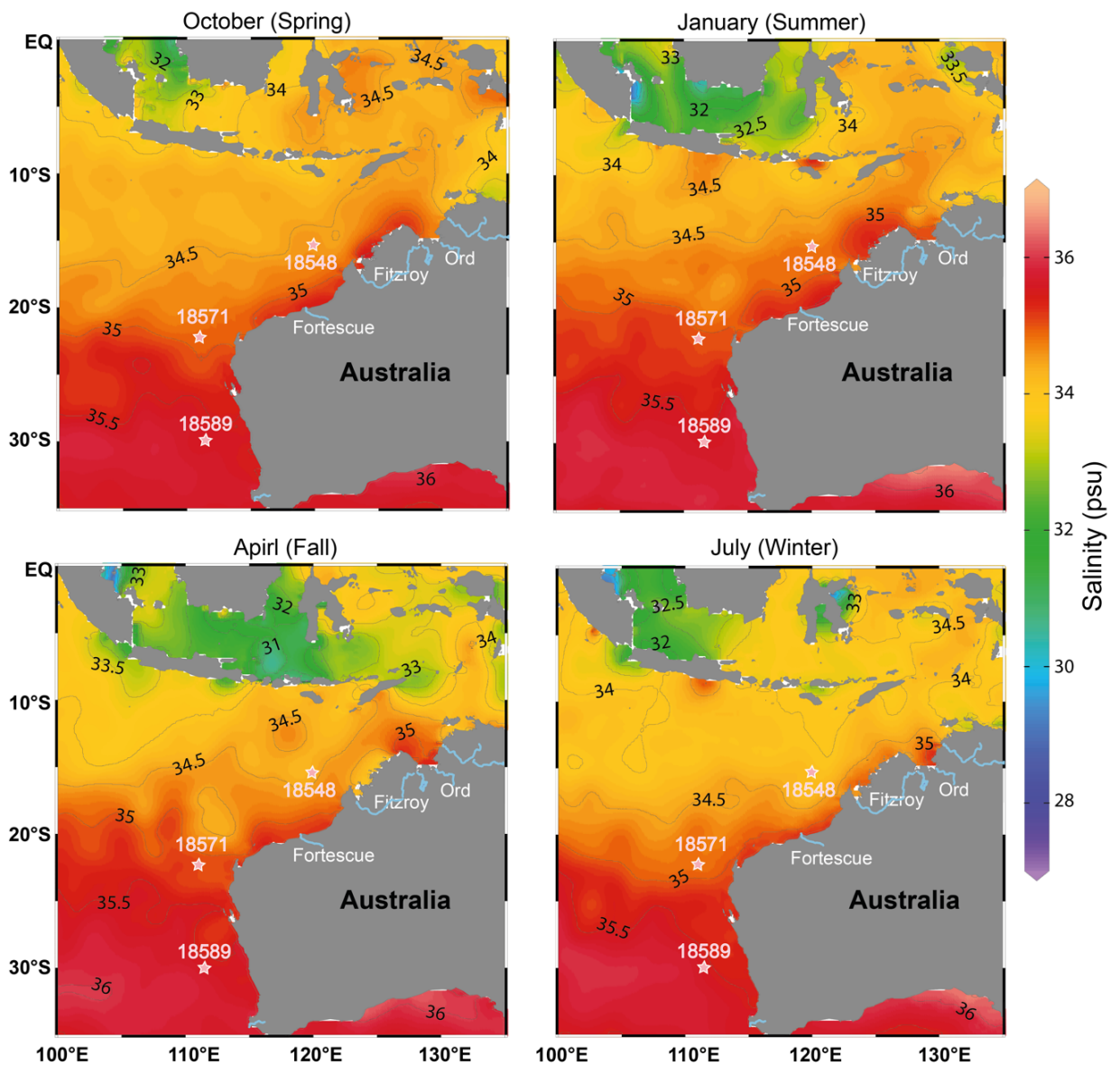


Figure 1B. Seasonal distribution of modern sea surface (0 m) salinities in the eastern Indian Ocean and along the Northwestern Australian Margin. Data from WOA13 (Zweng et al., 2013) plotted using Ocean Data View (Schlitzer, 2020).

The seasonal discharge of the major northern (Alligator, Daly, Johnson, Pentecost, Victoria, Mary) and northwestern (Fitzroy, Ord) Australian rivers reaches the coast at the end of the austral summer monsoon season (Figure 1C). The total annual discharge of these larger rivers is relatively low (in the order of 56 km³/yr, Milliman & Farnsworth, 2011), but highly seasonal with $\delta^{18}\text{O}$ values of precipitation in the range of -6‰ vs. VSMOV (Vienna Standard Mean Ocean Water) during the monsoonal season in the Darwin area (J. Liu et al., 2010). This

discharge affects SSS and $\delta^{18}\text{O}$ mainly in the post-monsoonal season in the areas adjacent to the river mouths. However, the signal is intensified by direct precipitation into the sea, and contributes to a first salinity minimum along the Northwestern Australian Margin in early austral fall (March-May) (Figure 1C). For the few rivers, where sediment load and discharge data are available (e.g. Ord River, Milliman & Farnsworth, 2011), the ratio of sediment to freshwater discharge is high, which is likely due to the high seasonality and lack of vegetation cover in the more elevated parts of the catchments.

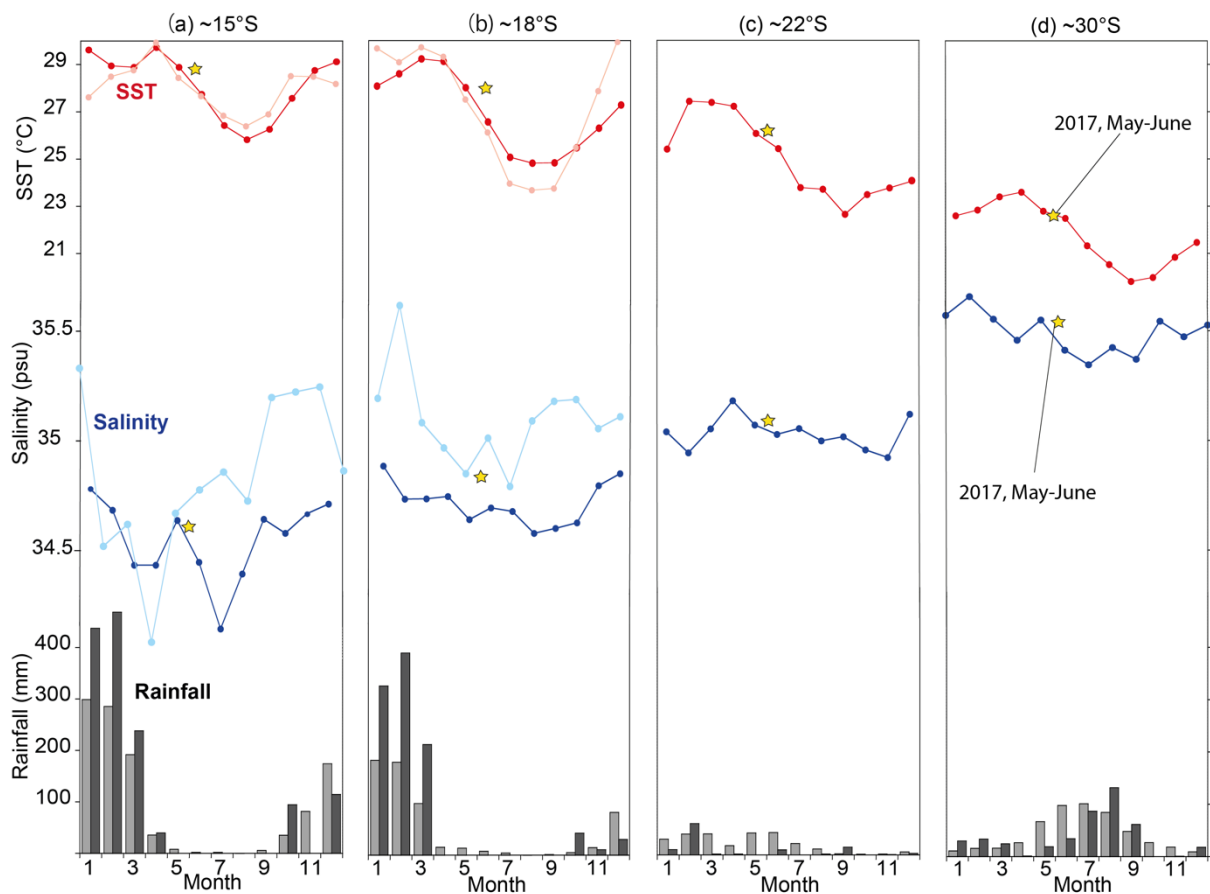


Figure 1C. Monthly records of sea surface temperature (SST), salinity (WOA13) and rainfall (<http://www.bom.gov.au/climate>) along the Northwestern Australian Margin. Red and blue curves indicate temperature and salinity at 0 m from WOA13: (a) 15.1°S/120.3°E; (b) 18.4°S, 115.2°E; (c) 22.1°S/113.5°E; (d) 29.0°S/112.9°E. Pink and light blue curves indicate temperature and salinity closed to mouths of Ord River and Fitzroy River: (a) 15°S, 124.6°E; (b) 18°S, 121.9°E. Grey columns show mean precipitation from 1961 to 2020; black columns show precipitation in 2017: (a) Station Legune, 15.21°S/129.45°E; (b) Station Yeeda, 17.62°S/123.65°E; (c) Station Learmonth airport, 22.24°S/114.10°E; (d) Station Badgingarra, 30.34°S/115.54°E). Yellow stars indicate SST and SSS measured during R/V Sonne Cruise SO257 in May 2017.

3. Materials and Methods

3.1. Core locations and sediment recovery

We analyzed a suite of surface sediment samples from core tops retrieved with a multicorer in May 2017 during R/V Sonne Cruise SO257 WACHEIO (Kuhnt et al., 2017). The 37 core top sediment samples were retrieved within the area of 15°3.591'S, 120°18.846'E and 27°15.325'S, 112°2.177'E along the Northwestern Australian Margin (Figure 2, Table S1). This data set from the sediment-water interface is compared to downcore measurements in two sediment successions spanning the last four glacial-interglacial cycles that are located in contrasting oceanographic and climatic settings along the Northwestern Australian Margin (Figure 2).

The composite sediment succession from piston Core SO257-18548 (15°3.591'S, 120°18.846'E, 1608 m water depth, 11.2 m core length) and nearby International Ocean Discovery Program (IODP) Expedition 363 Site U1482 (15°3.32'S, 120°26.10'E, 1466 m water depth) is located close to the modern southern limit of the seasonal (austral summer) displacement of the ITCZ (Figure 2b). The sediment records from Core SO257-18548 and Site U1482 were spliced into a composite record because a local sediment gravity flow eroded sediments younger than MIS 9 at Site U1482. The sediment from these locations consists of homogenous mottled olive greenish grey to dark grey clay-rich calcareous ooze (Kuhnt et al., 2017; Rosenthal et al., 2018). Gravity Core SO257-18571 (22°6.666'S, 113°29.688'E, 1052 m water depth, 20.1 m core length), retrieved in the southern part of the Exmouth Plateau, offshore the North West Cape Peninsula (Figure 2c), is situated south of the modern southern limit of the ITCZ. The sediment at this location consists of clay-rich nannoplankton ooze with distinct intercalations of dark reddish brown, clay-rich intervals and light olive grey calcareous ooze (Kuhnt et al., 2017).

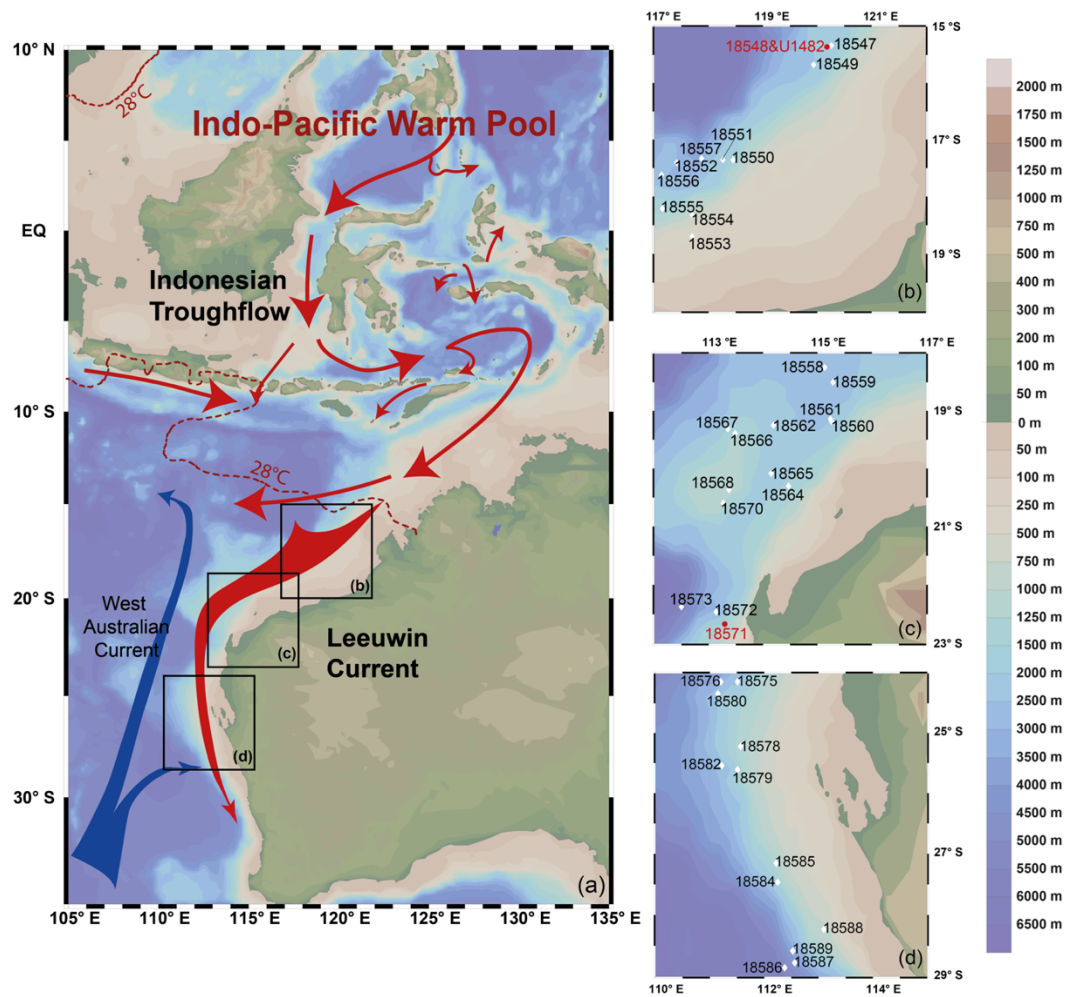


Figure 2. Oceanographic setting and core locations along the Northwestern Australian Margin. (a) Major ocean circulation pathways. Red thin arrows: Indonesian Throughflow (Gordon et al., 2012), red thick arrow: Leeuwin Current, blue thick arrow: West Australian Current (Gallagher et al., 2009). Red dashed lines indicate the 28°C limit of annual SST from WOA13. (b-d) Locations cored during R/V Sonne Cruise SO257. Red dots indicate positions of Core SO257-18548, IODP Expedition 363 Site U1482 and Core SO257-18571. White dots indicate locations of core top samples analyzed in this study. Map created with Ocean Data View (Schlitzer, 2020).

3.2 Sampling and processing

We measured austral fall SST, SSS, and $\delta^{18}\text{O}_{\text{sw}}$ in the second half of May 2017 during R/V Sonne Cruise SO257 and compared these measurements to reconstructed SST, SSS, and $\delta^{18}\text{O}$ from multi-corer core tops retrieved between the 1000 and 2000 m water isobaths. The year 2017 was an unusually wet and warm year in the monsoonal region of the Northern Territories and the northeastern part of Western Australia, while the west coast of Western Australia was drier than usual. Total annual rainfall across the Northern Territories was 19%

above average mainly due to several wet months in the rainy season earlier in the year. Western Australian annual rainfall was 42% above average, mainly recorded in the monsoonal northern and eastern parts of Western Australia (<http://www.bom.gov.au>).

Multicores were sampled immediately after retrieval in 1 cm slices and the uppermost five slices were preserved in a mixture of ethanol and Rose Bengal in 300 ml Kautex bottles. A SBE 911 plus CTD (Conductivity Temperature Depth) profiler was used at 10 stations to record the vertical variability of temperature, salinity, and oxygen, and to obtain water samples over the water profiles. The shipboard CTD of R/V Sonne is equipped with a rosette sampler with 24 Niskin bottles. $\delta^{18}\text{O}_{\text{sw}}$ was analyzed with a Gasbench II, which is connected to a DeltaPlusXL mass spectrometer from the three uppermost Niskin bottles deployed at 5, 10 and 20 m below sea surface. Between stations, SST and SSS were continuously measured using a Seabird thermosalinograph mounted to the hull of R/V Sonne.

The working halves of Cores SO257-18548 and -18571 were initially sampled at 10 cm intervals (1 cm-thick half slices of 11 cm core diameter). Additional samples were taken over Termination I (six samples from Core SO257-18548 between 94.5 and 204.5 cm core depth) and Termination II (10 samples from Core SO257-18548 between 456.5 and 576.5 cm core depth) to refine the age model. Four holes were cored at Site U1482 during IODP Expedition 363 (Rosenthal et al., 2017, 2018). The working halves from the composite sediment succession (shipboard splice) between 24.76 and 30.22 meters composite depth (mcd) were sampled at 20 cm intervals (2 cm-thick half slices of ~7 cm core diameter). The sediment succession from Core SO257-18548 and nearby Site U1482 were combined, based on correlation of the high-resolution resolution X-ray fluorescence (XRF) scanner elemental records. The tie point between these records, corresponding to an age of ~324 ka, is located at 10.84 m in Core SO257-18548 and at 24.97 mcd in Site U1482 (Pei et al., 2021).

All samples were oven dried at 40°C and weighed prior to washing over a 63 µm sieve. Residues were oven dried at 40°C on filter paper, then weighed and sieved into the fractions >315, 315–250, 250–150 and 150–63 µm.

3.3. Chronology

The age models of Cores SO257-18548 and -18571 over the last glacial termination and Holocene are based on ¹⁴C accelerator mass spectrometry (AMS) dates obtained from *Globigerinoides ruber* (white) >250 µm. The age model prior to 21 ka was generated by correlating the benthic foraminiferal δ¹⁸O to the benthic isotope stack LR04 (Lisiecki & Raymo, 2005). Details of the ¹⁴C and oxygen isotope stratigraphy of Cores SO257-18548, SO257-18571 and Site U1482 between 24.76 and 30.22 mcd are provided in Pei et al. (2021).

3.4. *Globigerinoides ruber* (white) stable isotopes and Mg/Ca

We selected 45 to 50 well preserved specimens per sample of the planktonic foraminifer *G. ruber* (white) (size fraction 250–315 µm) for paired Mg/Ca and stable isotope analysis. All tests were checked under the microscope for cement encrustations and infillings before being broken into large fragments. Samples were crushed between two glass plates to open all chambers of the tests. Approximately one quarter of the sample material was used for stable isotope analysis. After crushing, samples for isotope analysis were cleaned with ethanol (≥99.7%) for two to three seconds in an ultrasonic bath, decanted and dried at 40°C prior to analysis with a Thermo Finnigan MAT 253 mass spectrometer at the Leibniz Laboratory for Radiometric Dating and Isotope Research, Kiel University, Kiel. The mass spectrometer is coupled to a *Kiel-Carbo IV* device for automated CO₂ preparation from carbonate samples. Sample reaction was induced by individual acid addition (99% H₃PO₄ at 75°C) under vacuum.

The evolved carbon dioxide was analyzed eight times for each individual sample. As documented by the performance of international [NBS19: -2.20‰ VPDB (^{18}O); -2.37‰ VPDB (^{18}O)] and laboratory-internal carbonate standards [Hela1: $+2.48\text{‰}$ VPDB (^{18}O); HB1: -18.10‰ VPDB (^{18}O); SHK: -4.85‰ VPDB (^{18}O)], analytical precision of stable isotope analysis is better than $\pm 0.08\text{‰}$ for $\delta^{18}\text{O}$. Values are calibrated relative to Vienna Pee Dee Belemnite (VPDB) scale.

Mg/Ca was measured on approximately three quarters of the picked *G. ruber* tests. The samples were cleaned of the contaminant phases using the cleaning procedure with a reductive step detailed in Martin and Lea (2002) and Barker et al. (2003). The elemental composition of the foraminiferal calcite was analyzed with a Spectro Ciros SOP CCD inductively coupled plasma optical emission spectrometer (ICP-OES) at the Institute of Geosciences, CAU, Kiel. To control the quality of the measurement and the machine drift over the measuring period, every sixth sample is a calibration standard consisting of the certified reference material ECRM 752-1 with a mean value of 3.821 mmol/mol Mg/Ca (Greaves et al., 2008).

3.5. *Mg/Ca temperature estimates*

Sea surface and mixed-layer temperatures were estimated from *G. ruber* Mg/Ca in down-core and core top samples using the calibration derived from sediment trap samples (Anand et al., 2003):

$$\text{Mg/Ca} = 0.395 \pm 0.009 \exp(0.090 * T).$$

We chose this equation because it has consistently been used for temperature reconstructions in this region (Schröder et al., 2016; Xu et al., 2006, 2008) and yields comparable results to other widely used equations (e.g. Dekens et al., 2002; Figure 3a). We compared the results of the local core top calibration data to seasonal and annual mean SST

from the World Ocean Atlas (WOA13) and to shipboard thermosalinograph measurements taken during R/V Sonne Cruise SO257 in late May 2017 (Figure S1A). Errors in SST reconstructions were calculated by propagating the errors introduced by Mg/Ca measurements and the Mg/Ca temperature calibrations mentioned above, following the approach described in Mohtadi et al. (2014). A comparison of SST based on different calibrations for the two cores is shown in Figure S1B.

3.6. Sea surface water $\delta^{18}\text{O}$ ($\delta^{18}\text{O}_{\text{sw}}$) reconstructions

We calculated $\delta^{18}\text{O}_{\text{sw}}$ from $\delta^{18}\text{O}$ of foraminiferal calcite and Mg/Ca-based temperature estimates of *G. ruber* for near surface waters in sediment successions from Core SO257-18548, Site U1482 and Core SO257-18571. We applied the equation from Bemis et al. (1998) to calculate $\delta^{18}\text{O}_{\text{sw}}$ in surface waters.

$$\delta^{18}\text{O}_{\text{sw}} = 0.27 + (T - 16.5 + 4.8 * \delta^{18}\text{O}_{G.ruber}) / 4.8$$

We applied an ice volume correction of 60% of the original benthic foraminiferal $\delta^{18}\text{O}$ variability in Core SO257-18548, Site U1482 and Core SO257-18571 (Pei et al., 2021; Figure S2). Since the gradient of the original benthic foraminiferal $\delta^{18}\text{O}$ between modern and the LGM (1.6‰) exceeds the global mean value of $\sim 1.1\text{‰}$ (Waelbroeck et al., 2002), we assume that the contribution of deep water temperature accounts for the difference. A comparison of corrected $\delta^{18}\text{O}_{\text{sw}}$ values for different estimates of the ice volume component in benthic foraminiferal $\delta^{18}\text{O}$ is shown in Figure S2.

4. Results

4.1. Calibration of temperature reconstructions using modern sea surface data

We followed two different approaches to calibrate *G. ruber* Mg/Ca to sea surface temperatures. We used (1) published calibration equations (Anand et al., 2003; Dekens et al., 2002), which are frequently applied globally, and (2) a local regression of *G. ruber* Mg/Ca against annual average SST from WOA13 at our core top locations (Figure 3a). Additionally, we compared the results of these two approaches to regressions of *G. ruber* Mg/Ca to seasonal, in particular late summer/fall (March-May), SST from the WOA13 and to direct measurements during R/V Sonne Cruise 257 in May 2017 (Table S1, Figure S1A). We observe a systematic deviation of the reconstructed temperatures from local annual average temperatures using the global calibration equations. This deviation increases towards the southwestern (south of 23°S latitude) stations, where reconstructed temperatures are in the range of ~25°C, whereas calibration against local annual average temperatures results in substantially cooler temperatures of ~22°C. In contrast, temperatures reconstructed with the global calibration equation closely match austral late summer-fall temperatures in this area (Figure 3b). This suggests that the deviation of reconstructed temperatures from annual average SST along the Northwestern Australian Margin is caused by a seasonal bias of *G. ruber* abundances towards the late summer-fall season, when the Leeuwin Current is intensified. Differences between the two calibration approaches are less pronounced at stations within the IPWP further to the northwest, where the seasonality of SST is reduced and summer SST is close to the annual average. At the northernmost stations SO257-18547 and -18548, modern SST is on average ~29°C during austral summer (January-March) and ~27°C during austral winter (July-September) with an annual average of 28.2°C (Figures 1, 3; Table S1). This annual average is within error matched by *G. ruber* Mg/Ca temperatures using

both the regression against the local annual average temperatures and the global calibration equation (Figure 3a).

4.2. Modern distribution of *Globigerinoides ruber* $\delta^{18}\text{O}$ along the Northwestern Australian Margin

Globigerinoides ruber $\delta^{18}\text{O}$ measured along the SO257 NE-SW transect in the second half of May 2017 increases consistently from a minimum of nearly -3.0‰ at the northeastern end of the transect to values between 1.3 and 1.6‰ at the southernmost stations (Figure 4). We recognize a distinct break between two clusters of values, a northerly group with $\delta^{18}\text{O}$ values of -2.1‰ or lower and a southerly group with values above 1.8‰. The limit between these two groups, which is located offshore the Northwest Cape at 23°S (Figure 2), can be defined as the seasonal position of the oceanic front at the southwestern edge of the IPWP.

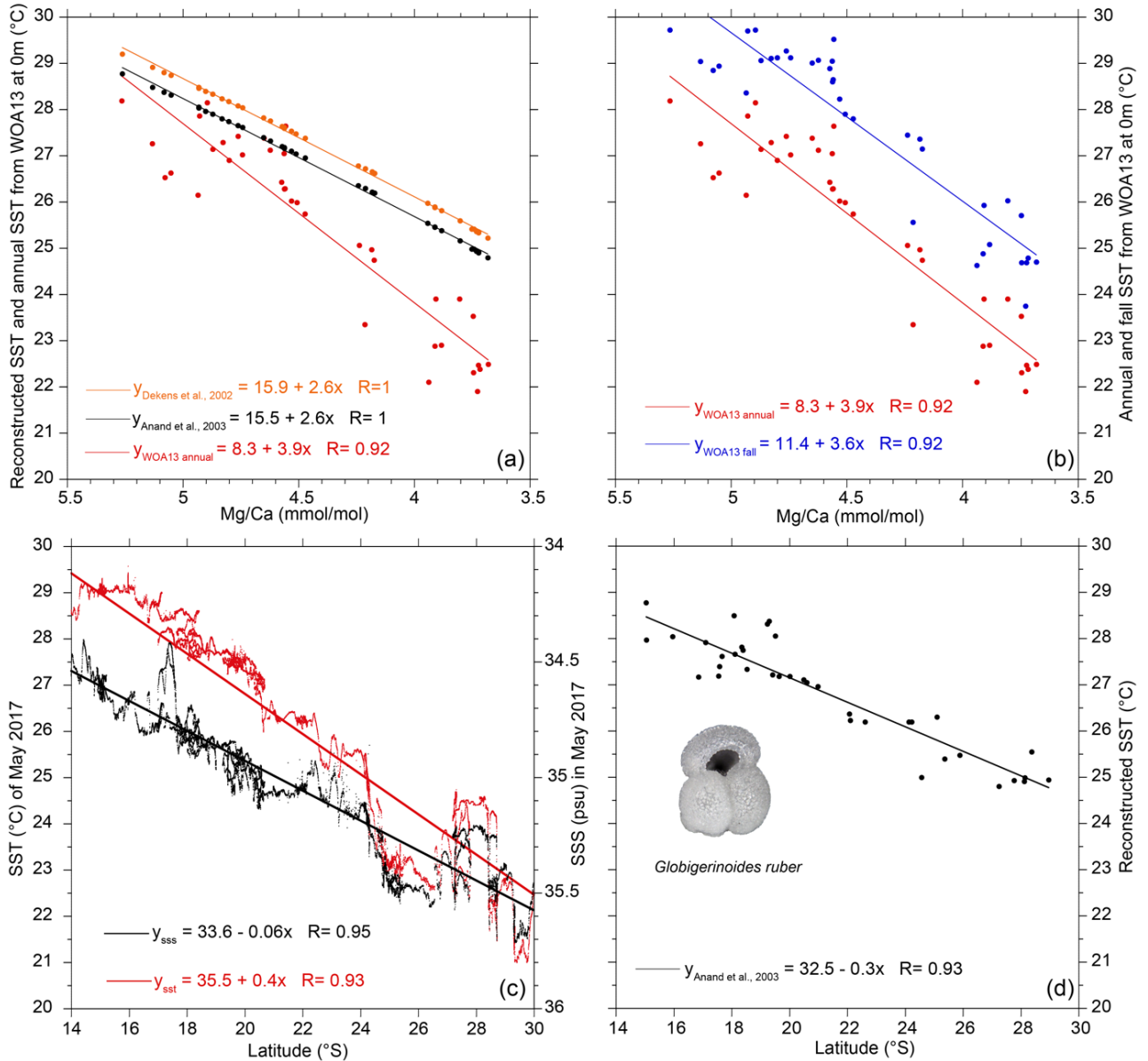


Figure 3. (a) Comparison of *G. ruber* Mg/Ca-derived SST in SO257 core top samples using calibrations of Dekens et al. (2002) (orange dots), Anand et al. (2003) (black dots) and calibration based on annual average SST (red dots) at 0 m WOA13. (b) Comparison of *G. ruber* Mg/Ca-derived SST in SO257 core top samples using calibration based on annual average (red dots) and austral late summer/fall (March-May, blue dots) SST at 0 m from WOA13. (c) Latitudinal change of SST (red) and SSS (black) from SO257 shipboard thermosalinograph. (d) Latitudinal change of *G. ruber* Mg/Ca-derived SST from core top samples (calibration based on Anand et al., 2003). *Globigerinoides ruber* image from Core SO257-18571 (5.15 m core depth).

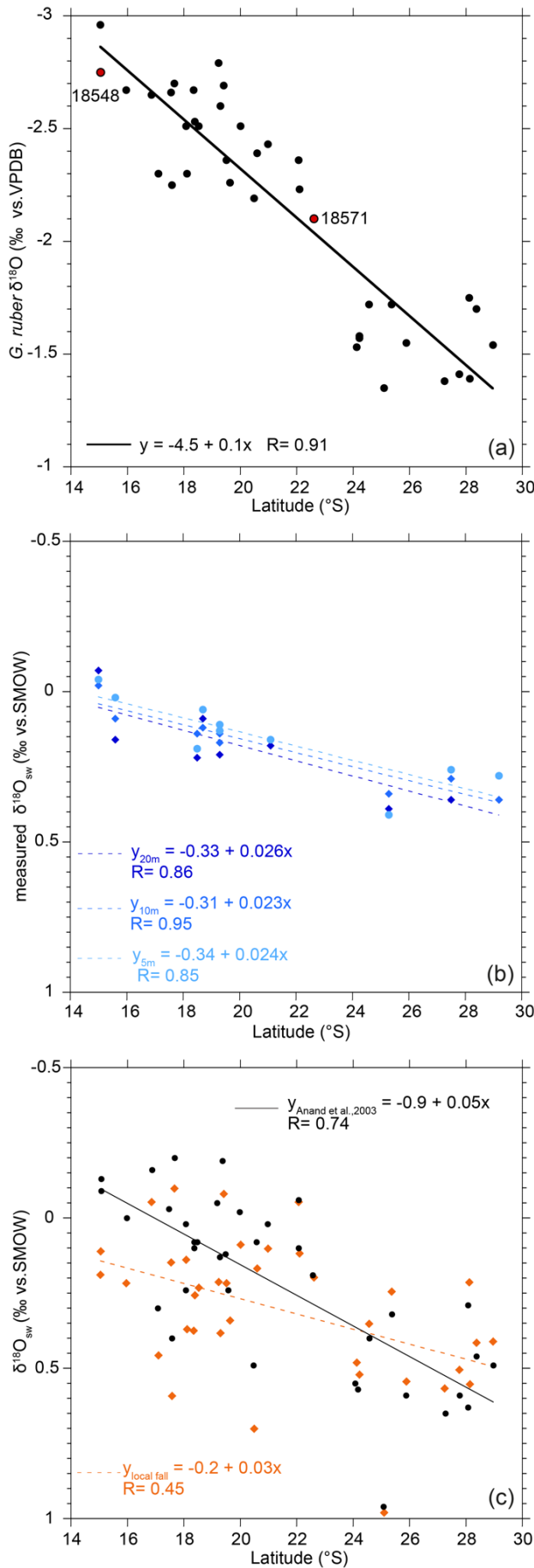


Figure 4. (a) Latitudinal variability in *G. ruber* $\delta^{18}O$ measured in SO257 core top samples. (b) Latitudinal variability in mixed layer (5, 10 and 20 m water depth) $\delta^{18}O_{sw}$ measured from CTD bottles in May 2017 during R/V Sonne Cruise SO257. (c) Comparison of reconstructed $\delta^{18}O_{sw}$ from paired *G. ruber* $\delta^{18}O$ and Mg/Ca-derived SST data (black dots) with reconstructed $\delta^{18}O_{sw}$ from paired *G. ruber* $\delta^{18}O$ and fall SST at 0 m from WOA13 (orange diamonds).

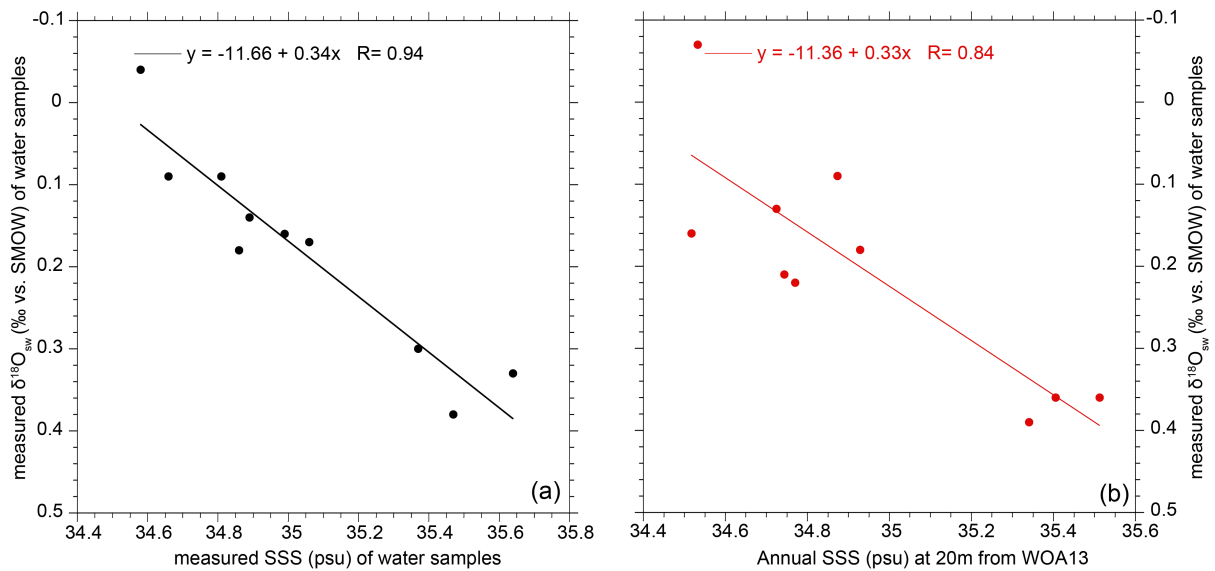


Figure 5. (a) Average SSS versus average $\delta^{18}\text{O}_{\text{sw}}$ measured from CTD bottles in May 2017 (mean of 5, 10 and 20 m water depth). (b) Annual average SSS (psu) at 20 m from WOA13 versus average measured $\delta^{18}\text{O}_{\text{sw}}$ from CTD bottles (mean of 5, 10 and 20 m water depth).

4.3. Measured and reconstructed seasonal and annual average surface $\delta^{18}\text{O}$ seawater:

Relation to seasonal and annual average SSS

We reconstructed $\delta^{18}\text{O}_{\text{sw}}$ from $\delta^{18}\text{O}$ and Mg/Ca-based temperature estimates of *G. ruber* in core top samples using the relationship of Bemis et al. (1998). We then compared the results to measured $\delta^{18}\text{O}_{\text{sw}}$ at 5, 10 and 20 m water depth at 10 stations along the SO257 latitudinal transect (Figure 5a, b). Measured $\delta^{18}\text{O}_{\text{sw}}$ ranges between -0.07‰ at 20 m water depth at the most northeasterly CTD station SO257-18546 (15°S) and 0.36 to 0.39‰ at 20 m water depth at the three southwestern CTD Station SO257-18577, -18583 and -18590 between 25 and 29°S (Table S2). Measured $\delta^{18}\text{O}_{\text{sw}}$ increases steadily southward with a slope of 0.025‰ per degree latitude. By contrast, reconstructed $\delta^{18}\text{O}_{\text{sw}}$ exhibits a much steeper slope than measured $\delta^{18}\text{O}_{\text{sw}}$ with an increase of 0.05‰ per degree latitude. The increase with

latitude is less uniform and characterized by two distinct clusters with low values north of 23°S and high values south of 23°S . Our data also show a clear $\delta^{18}\text{O}_{\text{sw}}$ -salinity correlation along the Northwestern Australian Margin, indicating that $\delta^{18}\text{O}_{\text{sw}}$ reconstructions are highly

suiting to evaluate the amount of monsoonal freshwater flux in this region. The local relationship of measured SSS and $\delta^{18}\text{O}_{\text{sw}}$ at 5 to 20 m water depth is:

$$\delta^{18}\text{O}_{\text{sw}} = -11.66 + 0.34 * \text{SSS}$$

which corresponds to a slope of 0.34‰ per psu (Table S2, Figure 5a). This is in the range of tropical central Pacific mixed layer values and closely matches the relatively steep $\delta^{18}\text{O}_{\text{sw}}$ per SSS slope in the center of the IPWP near Palau (Morimoto et al., 2002; Conroy et al., 2014, 2017).

4.4. Globigerinoides ruber $\delta^{18}\text{O}$ variability over the last 450 kyr

The *G. ruber* $\delta^{18}\text{O}$ record displays marked glacial-interglacial variability with values oscillating between -2.75 and -0.73 ‰ in Core SO257-18548 and Site U1482 and between -2.27 and -0.47 ‰ in Core SO257-18571 (Figure 6). In Core SO257-18548 and Site U1482, *G. ruber* $\delta^{18}\text{O}$ fluctuates between -1.25 and -0.81 ‰ during MIS 12, then decreases to -2.59 ‰ during Termination V. Values increase consistently from -2.00 to -1.04 ‰ during MIS 10 and vary between -1.70 and -2.71 ‰ during MIS 9, increasing to a maximum of -1.06 ‰ during MIS 8. Values fluctuate between -1.50 and -2.37 ‰ during MIS 7, reaching a peak of -0.97 ‰ during MIS 6. After the onset of Termination II, $\delta^{18}\text{O}$ decreases sharply to a minimum of -2.75 ‰ before increasing to reach highest values (-0.73 ‰) during the LGM. During Termination I, $\delta^{18}\text{O}$ exhibits a decrease from -0.73 to -2.61 ‰. In Core SO257-18571, *G. ruber* $\delta^{18}\text{O}$ increases from -2.07 to -0.35 ‰ during mid MIS 9 and mid MIS 8, then decreases to -1.91 ‰ during Termination III. Values oscillate between -0.81 and -1.97 ‰ during MIS 7 and fluctuate between -1.50 and -0.60 ‰ during MIS 6, before decreasing to their lowest value of -2.37 ‰ during MIS 5e. During the last glacial cycle, values increase once more to reach a maximum of -0.47 ‰ during the LGM. Holocene values exhibit a minimum of -2.15 ‰.

4.5. SST variability over the last 450 kyr

Globigerinoides ruber Mg/Ca varies between 3.29 and 5.57 mmol/mol over the past 450 kyr in Core SO257-18548 and Site U1482, corresponding to SSTs between 23.5 and 29.4°C (Figure 6), in comparison to the modern annual SST average of 28.2°C at this location (WOA13) (Table S1). During MIS 6 to 12, SSTs show marked glacial-interglacial variability, fluctuating between ~24 and 28°C. Peak temperatures of 29.4°C and 28.8°C were reached during MIS 5e and the early Holocene, respectively. The glacial-interglacial SST difference is ~4°C for Terminations I and II. During Termination II, SSTs exhibit a sharp increase, rising from 25.3°C to a maximum of 29.4°C during MIS 5e. SSTs decreased to their lowest values (~23°C) during MIS3 and the LGM, then rose to a second maximum of 28.8°C during the early Holocene (Figure 6a).

In Core SO257-18571 the glacial-interglacial temperature contrast is lower, which is mainly due to lower interglacial SSTs (Figure 6a). Mg/Ca fluctuates between 3.38 and 4.99 mmol/mol and SSTs range from 23.8 to 28.2°C, in comparison to the modern annual SST average of 25.0°C at this location (WOA13) (Table S1). During MIS 6 to 9, SSTs show glacial-interglacial variability between 23.8 and 27.9°C, which is less pronounced than in Core SO257-18548 and Site U1482. During MIS 5e, SSTs were ~2°C higher than today, fluctuating between ~27 and 28°C. An abrupt cooling by ~2°C occurred at the end of MIS 5e followed by an overall cooling trend from ~26 to ~24°C during MIS 5d to MIS 2. During Termination I, SSTs display a steady rise, reaching 27.3°C in the Holocene, which is ~1°C lower than during MIS 5e (Figure 6).

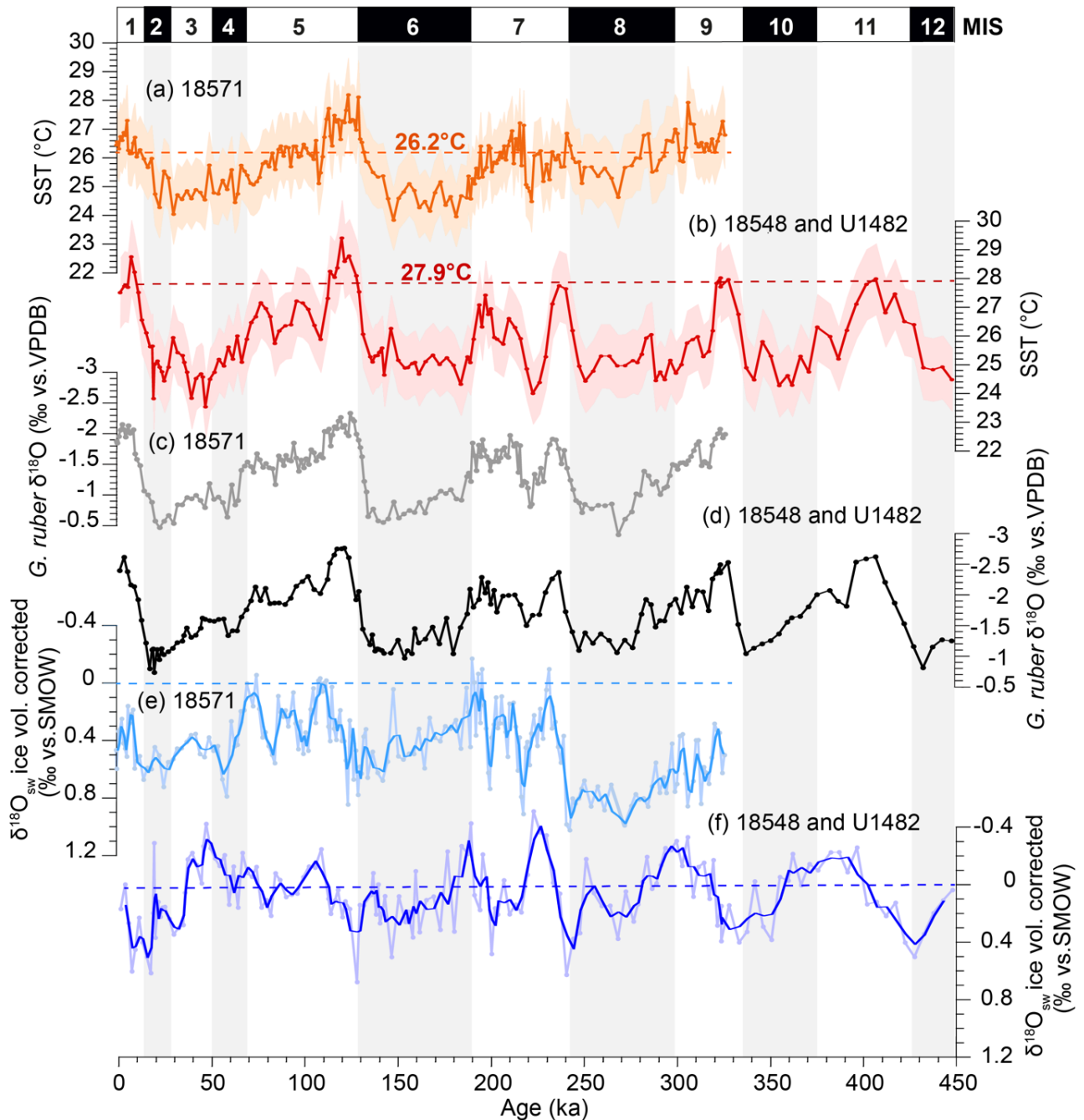


Figure 6. Evolution of sea surface hydrology along the Northwestern Australian Margin over the past 450 kyr. Mg/Ca-derived SST in (a) Core SO257-18571 (orange), (b) Core SO257-18548 and Site U1482 (red), based on calibration from Anand et al. (2003). Envelopes in (a) and (b) denote uncertainties in SST records estimated by propagating errors, which are $\sim 1^\circ\text{C}$. Dashed orange and red lines in (a) and (b) indicate modern reconstructed SST in multicorer core top samples from Sites SO257-18548 and -18571. Planktonic $\delta^{18}\text{O}$ in (c) Core SO257-18571 (grey), (d) Core SO257-18548 and Site U1482 (black), $\delta^{18}\text{O}_{\text{sw}}$ in (e) Core SO257-18571 (light blue) with 3 pt running average (blue), (f) Core SO257-18548 and Site U1482 (light blue) with 3 pt running average (dark blue). Blue dashed lines in (e) and (f) mark 0. MIS: marine isotope

4.6. Seawater oxygen isotope composition and salinity variability over the last 450 kyr

Today, the northeasterly Core SO257-18548 and Site U1482, which are more directly influenced by river discharge from the Australian monsoon region and advection of freshwater from the Indonesian archipelago, exhibit annual average core top $\delta^{18}\text{O}_{\text{sw}}$ of 0.17‰ (reconstructed from core top *G. ruber* Mg/Ca-derived temperatures and *G. ruber* $\delta^{18}\text{O}$) and seasonally lighter seawater $\delta^{18}\text{O}_{\text{sw}}$ of -0.04‰ in May 2017 (direct measurement of seawater sampled with the CTD Niskin bottle at 5 m water depth). The southwesterly Core SO257-18571 displays an annual average $\delta^{18}\text{O}_{\text{sw}}$ of 0.47‰ and a seasonal value of 0.17‰ in May 2017, resulting in seasonal offsets between ~0.2 and 0.3‰ and regional offsets in the same order of magnitude for annual average and the post-monsoonal season. Mean $\delta^{18}\text{O}_{\text{sw}}$ in Core SO257-18571 (0.43‰) is ~0.3‰ higher than in Core SO257-18548 and Site U1482 (0.07‰) over the last four glacial cycles, corresponding to a salinity, which is higher by as much as ~1 psu (Figure 6). Today, the annual average salinity difference at these stations is 0.5‰ and the salinity difference in austral fall 2017 was in the same order of magnitude (Table S2). The highest $\delta^{18}\text{O}_{\text{sw}}$ and salinities occurred during glacials and in the early phase of glacial terminations. Lowest salinity is synchronous in the early part of interglacials at both sites with the exceptions of MIS 3, which is characterized by low “interglacial” values ($\delta^{18}\text{O}_{\text{sw}}$ between -0.2 and -0.4‰) in Core SO257-18548 and Site U1482. In contrast, Core SO257-18571 exhibits a high “glacial” salinity (ice volume corrected $\delta^{18}\text{O}_{\text{sw}}$ between 0.4 and 0.8‰).

5. Discussion

5.1. Factors influencing seasonal and annual SST and SSS reconstructions along the Northwestern Australian Margin

5.1.1. Seasonality in *G. ruber* distribution

Reconstruction of $\delta^{18}\text{O}_{\text{sw}}$ /salinity is usually based on temperature correction of *G. ruber* $\delta^{18}\text{O}$ with Mg/Ca-derived SST reconstructed with globally applicable calibrations such as Dekens et al. (2002) and Anand et al. (2003). However, we recognized that reconstructed temperatures in our core top dataset overestimate annual average temperatures at the southwestern (cooler) stations by ~ 2 to 3°C (Figure 3). Warm temperatures that match Mg/Ca-derived estimates at these southwestern locations are only reached during austral fall (March-May), when the warm Leeuwin Current is active (Fieux et al., 2005). A bias by dissolution or carbonate ion effects can be excluded, since warm temperatures at the most northeastern stations are accurately reconstructed and deviations towards higher Mg/Ca and warmer temperatures only occur at the southwestern stations. A potential cause for this discrepancy is a seasonal bias of the *G. ruber* population density towards the warm season at the cooler southwestern stations. This bias may be accentuated by the fact that *G. ruber* tests are carried southward from the warm area east of the Northwest Cape to the cooler waters along the Northwestern Australian Margin with the strengthening Leeuwin Current, as is the case for clay minerals (Gingele et al., 2001).

To evaluate the impact of this seasonal bias on our SST reconstructions, we compared the results of global Mg/Ca calibrations to measured annual average and seasonal SST from WOA13 and shipboard CTD and thermosalinograph measurements in May 2017 at 40 stations sampled during R/V Sonne Cruise SO257 along the Northwestern Australian Margin (Figure S1A). This comparison shows that global Mg/Ca calibrations closely match the SSTs of the

post-monsoonal WOA13 fall dataset and temperatures measured in the near surface CTD and thermosalinograph measurements in May 2017 (Figure 3a and b, Figure S1A). Using the local annual average temperatures as a base for regional calibrations results in temperature estimates that are $\sim 2^{\circ}\text{C}$ cooler and exhibit slightly higher glacial-interglacial temperature gradients (Figure S1B). Thus, we use the calibration of Anand et al. (2003) to estimate downcore SST, since seasonal population dynamics of *G. ruber* along the Northwestern Australian Margin are not known over the last four glacial cycles. However, this approach may lead to slightly amplified glacial-interglacial gradients in reconstructed SST and SSS, since the seasonality of *G. ruber* populations may have been enhanced during glacials.

5.1.2. Temporal and spatial variability of the oceanic front at the southeastern margin of the IPWP

The most significant feature in the mixed layer temperature record along the SO257 latitudinal transect is the rapid southward decrease in Mg/Ca-derived SST, associated with a salinity ($\delta^{18}\text{O}_{\text{sw}}$) increase at the southeastern margin of the IPWP (Figure 4). This steep gradient, which represents the seasonal position of the oceanic front at the southeastern margin of the IPWP, was identified between 23 and 24°S towards the end of May to early June during previous cruises (e.g. Weller et al., 2011). This temperature gradient is associated with southward shallowing of the thermocline and intensified current activity, formation of eddies, enhanced upper ocean mixing and increased nutrient levels in surface water masses (Thompson & Richards, 2011; Weller et al., 2011). Although this boundary was situated $\sim 1^{\circ}\text{S}$ south of Station SO257-18571 at the end of May 2017 during R/V Sonne Cruise SO257, the site would have been bathed by cooler, nutrient rich surface water masses of southern origin during austral winter. Temperature and salinity reconstructions at this site are, thus, well suited to monitor

the spatial expansion and contraction of the IPWP and changes in the related intensity of the warm Leeuwin Current over the last glacial cycles.

5.2. Phasing of deglacial warming to atmospheric carbon dioxide increase and Southern Hemisphere insolation forcing

Centennial-scale SST records in combination with AMS ^{14}C dates tuned to independently dated deglacial ^{14}C plateaus previously suggested that deglacial tropical warming in the Indonesian Seas and off northwestern Australia led atmospheric CO_2 measured in Antarctic ice cores by ~ 500 years during Termination I (Sarnthein et al., 2011; Schröder et al., 2018). This relatively short lead is not resolved in our millennial-scale SST records, and the onset of deglacial warming and atmospheric $p\text{CO}_2$ rise at the beginning of Terminations I, II, III and IV appears coeval in Cores SO257-18571 and SO257-18548 and Site U1482 (Figure 7). Temperature maxima occur in MIS 1 (~ 8 ka), MIS 5e (~ 121 ka), MIS 7e (~ 238 ka) and MIS 9 (~ 324 ka), which, within the limitation of our age models, coincide with atmospheric $p\text{CO}_2$ maxima in Antarctic ice core records and with maxima in monsoonal terrigenous discharge from the Australian continent (Figure 7). This covariance of atmospheric $p\text{CO}_2$, SST and monsoonal terrigenous discharge (Figure S4) suggests that the rise in atmospheric $p\text{CO}_2$ and SST in the late phase of glacial terminations triggered an intensification of the Australian Monsoon during precessional minima.

The atmospheric $p\text{CO}_2$, SST and monsoonal runoff maxima at the end of glacial terminations also coincide with precession minima at obliquity maxima. This orbital configuration results in a combination of maximum Northern Hemisphere summer insolation with maximum cross-equatorial heat transfer, due to obliquity induced steepening of summer inter-tropical latitudinal insolation gradients (Bosmans et al., 2014; Davis & Brewer, 2009;

Rossignol-Strick, 1983). In addition to Northern Hemisphere summer insolation, Southern Hemisphere insolation may have contributed to warming in the southeastern Indian Ocean. Austral spring insolation (daily insolation on 10 September at 65°S) in combination with the duration of austral summer (days on which diurnal average insolation exceeds 250 W/m² at 77°S) may have triggered Southern Hemisphere warming (as recorded in Antarctic ice cores) in phase with Northern Hemisphere warming (Huybers, 2009). The variability of austral spring insolation and the duration of austral summer over the last 450 kyr exhibit close similarities to Northern Hemisphere precessional summer insolation (daily insolation on 21 June at 65°N) (Huybers, 2009). A possible underlying mechanism is that enhanced austral spring insolation promoted decreases in the sea ice cover around Antarctica and increases in the heat transport into the interior of Antarctica with repercussions for the entire Southern Hemisphere climate (Timmermann et al., 2009). The relative importance of these mechanisms to explain Southern Hemisphere warming during summer insolation minima is still an issue of intense debate. Atmospheric carbon dioxide, which is rapidly mixed in the atmosphere, appears to play a major role in triggering coeval temperature changes in both hemispheres, although the forcing mechanisms that drive atmospheric *p*CO₂ variability on orbital time scales are unclear.

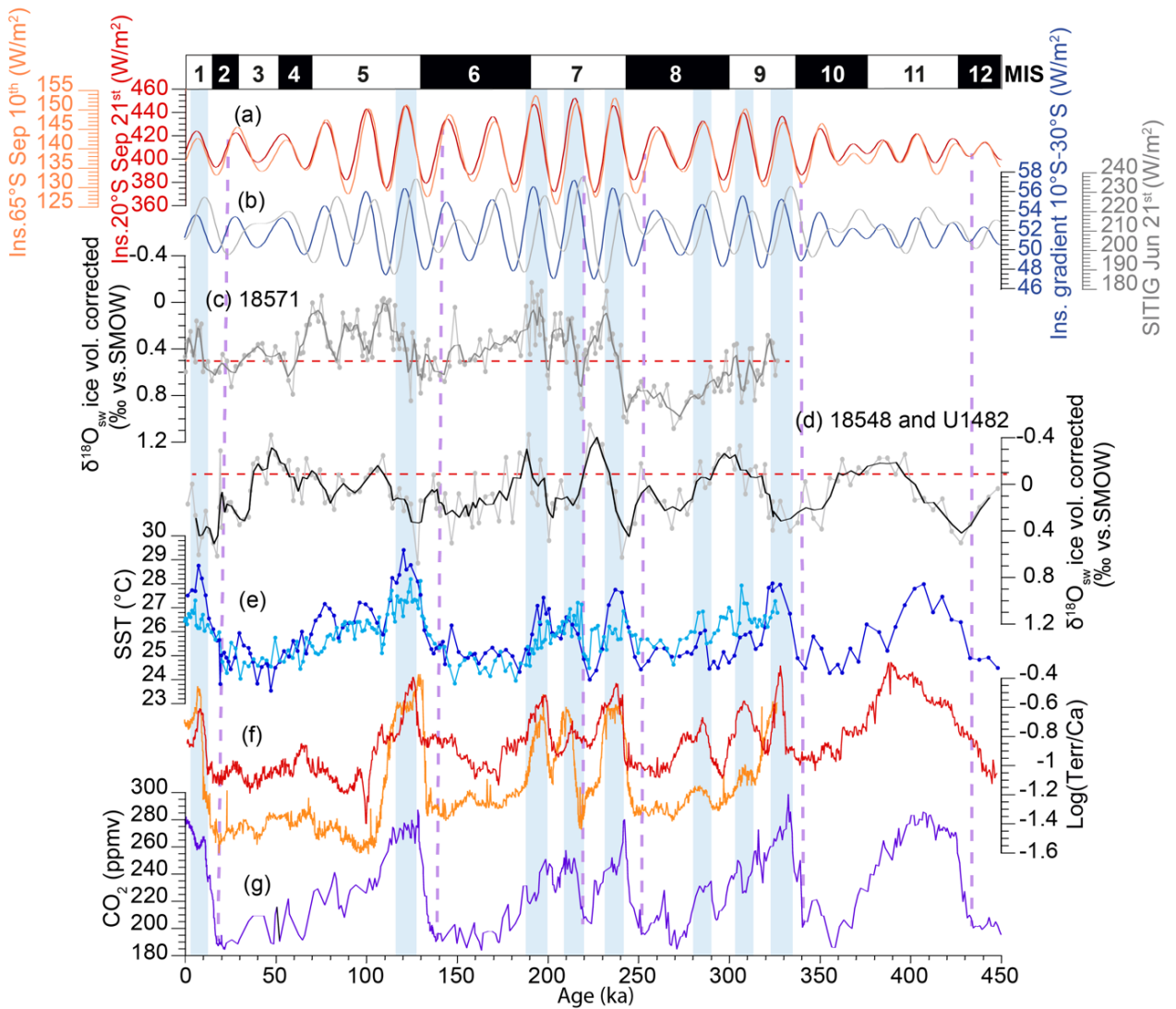


Figure 7. Comparison of temperature and terrigenous discharge in Core SO257-18571, Core SO257-18548 and Site U1482 with insolation and greenhouse gas forcing. Reconstructed SST are based on the calibrations of Anand et al. (2003). (a) 21 September insolation at 20°S and 10 September insolation at 65°S. (b) Insolation gradient between 10 and 30°S; SITIG: boreal summer inter-tropical insolation gradient. (c) Ice volume corrected $\delta^{18}\text{O}_{\text{sw}}$ in Core SO257-18571 (light grey) with 3 pt running average (dark grey). (d) Ice volume corrected $\delta^{18}\text{O}_{\text{sw}}$ in Core SO257-18548 and Site U1482 (light grey) with 3pt running average (black). (e) SST from Core SO257-18571 (light blue), Core SO257-18548 and Site U1482 (blue), (f) XRF-scanner derived $\text{Log}(\text{Terr}/\text{Ca})$ from Core SO257-18571 (orange), Core SO257-18548 and Site U1482 (red) from Pei et al. (2021). (g) EPICA Dome C (EDC) ice core CO_2 record (Lüthi et al., 2008). Blue shading indicates precessional insolation maxima that coincide with elevated SST, increased monsoonal discharge and high atmospheric $p\text{CO}_2$. Horizontal dashed red lines indicate average ice volume corrected $\delta^{18}\text{O}_{\text{sw}}$ from Core SO257-18571 and from Core SO257-18548 and Site U1482. Vertical purple dashed lines indicate onset of deglacial atmospheric $p\text{CO}_2$ and tropical SST rise, which are in phase on millennial-scale time resolution.

5.3. *Hydrological variability during the last four glacial cycles*

Today, the seasonality of SSS along the Northwestern Australian Margin is mainly driven by the advection of low salinity waters originating from the Indonesian archipelago via the ITF and by local precipitation and eddy fluxes along the pathway of the Leeuwin Current that freshen the mixed layer (Pattiaratchi, 2006; Thompson & Richards, 2011; N. Zhang et al., 2016). Salinity fronts migrate seasonally and interannually with the movement of the ITCZ and the El Niño-Southern Oscillation (ENSO)-modulated surface component of the ITF (Hu et al., 2019; Zhang et al., 2016). The strength of the advected freshwater flux is largely dependent on the intensity of the tropical convective rainfall over the Indonesian Maritime Continent, but is also affected by intense vertical mixing in the Banda Sea before reaching the Timor Sea. Differences in the amount and seasonality of precipitation and riverine discharge as well as in the transport and mixing along the ITF pathway, thus, contribute to a complex salinity signal in the eastern Indian Ocean. These intricate interactions ultimately drive variability of $\delta^{18}\text{O}_{\text{sw}}$ and salinity along the Northwestern Australian Margin on seasonal (Condie & Dunn, 2006), interannual (Cahyarini et al., 2014; Hu et al., 2019) and orbital timescales (Spooner et al., 2011).

The ice volume corrected $\delta^{18}\text{O}_{\text{sw}}$ record in the southwestern Core SO257-18571 exhibits clear glacial-interglacial variability with glacial values between 0.4 and 0.8‰ during MIS 2-4 and MIS 6 (Figure 7). Glacial values during MIS 8 were even higher (between 0.8 and 1.2‰), indicating a less expanded IPWP and weaker Leeuwin Current. By contrast, the $\delta^{18}\text{O}_{\text{sw}}$ record in the northeastern location (Core SO257-18548 and Site U1482) exhibits subdued glacial-interglacial variability and is characterized by higher frequency and lower amplitude fluctuations between maxima of $\sim 0.6\text{‰}$ and minima of $\sim -0.4\text{‰}$. This contrast is especially evident during the last glacial cycle, when $\delta^{18}\text{O}_{\text{sw}}$ was lower during the early part of MIS 3 than during the Holocene. These differences in temperature and salinity variations suggest that the northeastern part of the Northwestern Australian Margin remained under the

influence of IPWP water masses throughout the past 450 kyr, even during glacials. By contrast, the southwestern Core SO257-18571 was situated in cooler and more saline water masses, remaining south of the IPWP southwestern front during glacials.

The overall higher SSS during glacials at Site SO257-18571 suggests drier conditions over the entire Maritime Continent and along the pathway of the ITF. Low salinities and unusually warm temperatures in the early phase of interglacials at this location bear similarities to modern conditions during “Ningaloo Niño” events (Feng et al., 2013). During these events, low-salinity anomalies in the Indonesian seas and along the Northwestern Australian Margin, caused by anomalous precipitation in the region and ITF freshwater advection, are carried southward by the Leeuwin Current. These warming and freshening anomalies that are associated with prolonged La Niña periods in the tropical Pacific have been more commonly observed in the ITF and the Leeuwin Current over the past few decades (Feng et al., 2015). Ningaloo-Niño type warming and freshening events seem to become more frequent and intense at elevated $p\text{CO}_2$ levels and may have also contributed to the unusual warm and wet conditions off Australia during intervals of peak $p\text{CO}_2$ levels following glacial terminations.

5.4. Relative influence of ITF and Indonesian-Australian Monsoon on regional hydrology

The contrasting positions of the two sediment successions in relation to the IPWP is reflected by different responses of SST to precessional insolation and atmospheric $p\text{CO}_2$ forcing (Figures S3, S4). Within the IPWP (Core SO257-18548 and Site U1482), SST is highly coherent with both precession (coherence: 0.92) and $p\text{CO}_2$ (coherence: 0.94) and exhibit a phase lag of 5.1 kyr to precession and an in-phase relationship with $p\text{CO}_2$, which suggests a direct response of SST to atmospheric greenhouse gas forcing (Lea et al., 2006; Medina-Elizalde & Lea, 2005). By contrast, SST south of the IPWP (Site SO257-18571) exhibits low

coherence (0.45) with precession, whereas ice-volume corrected $\delta^{18}\text{O}_{\text{sw}}$, a direct proxy for salinity variability, is highly coherent (0.83 in Core SO257-18548 and Site U1482 and 0.72 in Core SO257-18571) and in phase with precession at both sites. This similarity in ice-volume corrected $\delta^{18}\text{O}_{\text{sw}}$ suggests that the transfer of the salinity signal from the Indonesian Seas to the eastern Indian Ocean via the ITF and Leeuwin Current remained consistent over orbital timescales.

However, this temporal variability in circulation-driven salinity is remarkably different from the imprint of local monsoonal precipitation and discharge on the sedimentation along the Northwestern Australian Margin (Figure 7). Monsoonal sediment discharge from the Australian continent, expressed as $\text{Log}(\text{Terr}/\text{Ca})$, is highly coherent (coherence: 0.77) with a consistent phase lag of 5.1 kyr to precession in Core SO257-18548 and Site U1482, which is directly exposed to monsoonal discharge from the Fitzroy River (Figure S3C). Whereas SSS variability at this site represents an integrated signal of monsoonal precipitation and runoff as well as intense advective mixing along the ITF pathway, the terrigenous sediment flux more directly captures the local monsoonal precipitation and runoff signal from the Australian continent (e.g. Milliman & Farnsworth, 2011).

6. Conclusions

Temperature, salinity and oxygen isotope analyses of seawater in combination with stable isotope and Mg/Ca analysis of near-surface dwelling planktonic foraminifers in sediment core tops from a transect along the Northwestern Australian Margin between 15 and 27°S allow monitoring of spatial variations of the southwestern edge of the IPWP. Today, the southwestern edge of the IPWP is characterized by a sharp decrease in SST and concurrent increases in salinity and planktonic $\delta^{18}\text{O}$ between 23 and 24°S off Northwest Cape during the post-

monsoonal austral fall (May). Reconstructed mixed layer temperatures and salinities over the last 450 kyr in two sediment successions at the southwestern edge of the IPWP (Site SO257-18548/U1482 at 15°S) and southwest of the IPWP (Site SO257-18571 at 22°S) suggest that even during glacials the northeastern region remained influenced by IPWP water masses. By contrast, the southwestern Site SO257-18571 was located in colder, more saline and nutrient-rich mixed layer water masses, south of the IPWP front during glacials. Sea surface temperature maxima and salinity minima along the Northwestern Australian Margin in the early parts of MIS 1, 5, 7 and 9 coincided with peak monsoonal discharge during intervals of global $p\text{CO}_2$ peaks at high or increasing Southern Hemisphere spring (September) insolation and maxima in low latitude N-S insolation gradients at precession minima and obliquity maxima. Coherence and phase relationship between insolation forcing, atmospheric $p\text{CO}_2$, SST and monsoonal intensity (SSS and terrigenous discharge) suggest that global greenhouse gas concentrations and Southern Hemisphere spring insolation strongly influenced the spatial extent of the IPWP in the Southern Hemisphere and Australian monsoonal climate.

Acknowledgments, Samples, and Data

This research used data and samples provided by the International Ocean Discovery Program (IODP). We are grateful to the captain, crew and shipboard scientific parties of R/V Sonne 257 and IODP Expedition 363 for all their efforts. This study was funded by the German Federal Ministry of Education and Research (Grant SO-257, WACHEIO, 03G0257A). Renjie Pei gratefully acknowledges the funding from the China Scholarship Council towards her PhD at Kiel University. We thank Dieter Garbe-Schönberg and Karen Bremer for ICP-OES Mg/Ca analyses assistance. Data presented in this study are available from the *Data Publisher for Earth & Environmental Science* (PANGAEA.de, in processing).

References

- Anand, P., Elderfield, H., & Conte, M. H. (2003). Calibration of Mg/Ca thermometry in planktonic foraminifera from a sediment trap time series. *Paleoceanography*, *18*(2). <https://doi.org/10.1029/2002pa000846>
- Ayliffe, L. K., Gagan, M. K., Zhao, J. X., Drysdale, R. N., Hellstrom, J. C., Hantoro, W. S., et al. (2013). Rapid interhemispheric climate links via the Australasian monsoon during the last deglaciation. *Nature Communications*, *4*(May), 1–6. <https://doi.org/10.1038/ncomms3908>
- Barker, S., Greaves, M., & Elderfield, H. (2003). A study of cleaning procedures used for foraminiferal Mg/Ca paleothermometry. *Geochemistry, Geophysics, Geosystems*, *4*(9), 1–20. <https://doi.org/10.1029/2003GC000559>
- Bemis, B. E., Spero, H. J., Bijma, J., & Lea, D. W. (1998). Reevaluation of the oxygen isotopic composition of planktonic foraminifera: Experimental results and revised paleotemperature equations. *Paleoceanography*, *13*(2), 150–160. <https://doi.org/10.1029/98PA00070>
- Bosmans, J. H. C., Drijfhout, S. S., Tuenter, E., Hilgen, F. J., & Lourens, L. J. (2014). Response of the North African summer monsoon to precession and obliquity forcings in the EC-Earth GCM. *Climate Dynamics*, *44*(1–2), 279–297. <https://doi.org/10.1007/s00382-014-2260-z>
- Bosmans, J. H. C., Erb, M. P., Dolan, A. M., Drijfhout, S. S., Tuenter, E., Hilgen, F. J., et al. (2018). Response of the Asian summer monsoons to idealized precession and obliquity forcing in a set of GCMs. *Quaternary Science Reviews*, *188*, 121–135. <https://doi.org/10.1016/j.quascirev.2018.03.025>
- Broccoli, A. J., Dahl, K. A., & Stouffer, R. J. (2006). Response of the ITCZ to Northern Hemisphere cooling. *Geophysical Research Letters*, *33*(1), 1–4. <https://doi.org/10.1029/2005GL024546>
- Cahyarini, S. Y., Pfeiffer, M., Nurhati, I. S., Aldrian, E., Dullo, W. C., & Hetzinger, S. (2014). Twentieth century sea surface temperature and salinity variations at Timor inferred from paired coral $\delta^{18}\text{O}$ and Sr/Ca measurements. *Journal of Geophysical Research: Oceans*, *119*(7), 4593–4604. <https://doi.org/10.1002/2013JC009594>
- Chiang, J. C. H., & Bitz, C. M. (2005). Influence of high latitude ice cover on the marine Intertropical Convergence Zone. *Climate Dynamics*, *25*(5), 477–496. <https://doi.org/10.1007/s00382-005-0040-5>
- Chiang, J. C. H., & Friedman, A. R. (2012). Extratropical cooling, interhemispheric thermal gradients, and tropical climate change. *Annual Review of Earth and Planetary Sciences*, *40*, 383–412. <https://doi.org/10.1146/annurev-earth-042711-105545>
- Chiang, J. C. H., Biasutti, M., & Battisti, D. S. (2003). Sensitivity of the Atlantic Intertropical Convergence Zone to Last Glacial Maximum boundary conditions. *Paleoceanography*, *18*(4), 1–18. <https://doi.org/10.1029/2003PA000916>
- Chiang, J. C. H., Fang, Y., & Chang, P. (2008). Interhemispheric thermal gradient and tropical Pacific climate. *Geophysical Research Letters*, *35*(14), 2–6. <https://doi.org/10.1029/2008GL034166>
- Church, J. A., Cresswell, G. R., & Godfrey, J. S. (1989). The Leeuwin Current. In *Poleward Flows along Eastern Ocean Boundaries*, 230–254. <https://doi.org/10.1029/CE034p0230>

- Claussen, M., Ganopolski, A., Brovkin, V., Gerstengarbe, F. W., & Werner, P. (2003). Simulated global-scale response of the climate system to Dansgaard/Oeschger and Heinrich events. *Climate Dynamics*, *21*(5–6), 361–370. <https://doi.org/10.1007/s00382-003-0336-2>
- Condie, S. A., & Dunn, J. R. (2006). Seasonal characteristics of the surface mixed layer in the Australasian region: Implications for primary production regimes and biogeography. *Marine and Freshwater Research*, *57*(6), 569–590. <https://doi.org/10.1071/MF06009>
- Conroy, J. L., Cobb, K. M., Lynch-Stieglitz, J., & Polissar, P. J. (2014). Constraints on the salinity-oxygen isotope relationship in the central tropical Pacific Ocean. *Marine Chemistry*, *161*, 26–33. <https://doi.org/10.1016/j.marchem.2014.02.001>
- Conroy, J. L., Thompson, D. M., Cobb, K. M., Noone, D., Rea, S., & Legrande, A. N. (2017). Spatiotemporal variability in the $\delta^{18}\text{O}$ -salinity relationship of seawater across the tropical Pacific Ocean. *Paleoceanography*, *32*, 484–497.
- Cresswell, G. R., & Peterson, J. L. (1993). The Leeuwin Current south of Western Australia. *Marine and Freshwater Research*, *44*(2), 285–303. <https://doi.org/10.1071/MF9930285>
- Davis, B. A. S., & Brewer, S. (2009). Orbital forcing and role of the latitudinal insolation/temperature gradient. *Climate Dynamics*, *32*(2–3), 143–165. <https://doi.org/10.1007/s00382-008-0480-9>
- De Deckker, P., Barrows, T. T., & Rogers, J. (2014). Land-sea correlations in the Australian region: Post-glacial onset of the monsoon in northwestern Western Australia. *Quaternary Science Reviews*, *105*, 181–194. <https://doi.org/10.1016/j.quascirev.2014.09.030>
- Deininger, M., McDermott, F., Cruz, F. W., Bernal, J. P., Mudelsee, M., Vonhof, H., et al. (2020). Inter-hemispheric synchronicity of Holocene precipitation anomalies controlled by Earth's latitudinal insolation gradients. *Nature Communications*, *11*(1), 1–9. <https://doi.org/10.1038/s41467-020-19021-3>
- Dekens, P. S., Lea, D. W., Pak, D. K., & Spero, H. J. (2002). Core top calibration of Mg/Ca in tropical foraminifera: Refining paleotemperature estimation. *Geochemistry, Geophysics, Geosystems*, *3*(4), 1–29. <https://doi.org/10.1029/2001gc000200>
- Denniston, R. F., Wyrwoll, K. H., Asmerom, Y., Polyak, V. J., Humphreys, W. F., Cugley, J., et al. (2013). North Atlantic forcing of millennial-scale Indo-Australian monsoon dynamics during the Last Glacial period. *Quaternary Science Reviews*, *72*, 159–168. <https://doi.org/10.1016/j.quascirev.2013.04.012>
- Eroglu, D., McRobie, F. H., Ozken, I., Stemler, T., Wyrwoll, K. H., Breitenbach, S. F. M., et al. (2016). See-saw relationship of the Holocene East Asian-Australian summer monsoon. *Nature Communications*, *7*, 1–7. <https://doi.org/10.1038/ncomms12929>
- Feng, M., Weller, E., & Hill, K. (2009). The Leeuwin Current. *A marine climate change impacts and adaptation report card for Australia 2009*, *92*(2), 67–81.
- Feng, M., McPhaden, M. J., Xie, S. P., & Hafner, J. (2013). La Niña forces unprecedented Leeuwin Current warming in 2011. *Scientific Reports*, *3*(1), 1–9. <https://doi.org/10.1038/srep01277>

- Feng, M., Benthuisen, J., Zhang, N., & Slawinski, D. (2015). Freshening anomalies in the Indonesian throughflow and impacts on the Leeuwin Current during 2010-2011. *Geophysical Research Letters*, 42(20), 8555–8562. <https://doi.org/10.1002/2015GL065848>
- Field, E., McGowan, H. A., Moss, P. T., & Marx, S. K. (2017). A late Quaternary record of monsoon variability in the northwest Kimberley, Australia. *Quaternary International*, 449, 119–135. <https://doi.org/10.1016/j.quaint.2017.02.019>
- Fioux, M., Molcard, R., & Morrow, R. (2005). Water properties and transport of the Leeuwin Current and Eddies off Western Australia. *Deep-Sea Research Part I: Oceanographic Research Papers*, 52(9), 1617–1635. <https://doi.org/10.1016/j.dsr.2005.03.013>
- Gallagher, S. J., Wallace, M. W., Li, C. L., Kinna, B., Bye, J. T., Akimoto, K., & Torii, M. (2009). Neogene history of the West Pacific Warm Pool, Kuroshio and Leeuwin currents. *Paleoceanography*, 24(1). <https://doi.org/10.1029/2008PA001660>
- Gingele, F. X., De Deckker, P., & Hillenbrand, C. D. (2001). Late Quaternary fluctuations of the Leeuwin Current and palaeoclimates on the adjacent land masses: Clay mineral evidence. *Australian Journal of Earth Sciences*, 48(6), 867–874. <https://doi.org/10.1046/j.1440-0952.2001.00905.x>
- Gordon, A. L., Huber, B. A., Metzger, E. J., Susanto, R. D., Hurlburt, H. E., & Adi, T. R. (2012). South China Sea throughflow impact on the Indonesian throughflow. *Geophysical Research Letters*, 39(11), 1–7. <https://doi.org/10.1029/2012GL052021>
- Greaves, M., Caillon, N., Rebaubier, H., Bartoli, G., Bohaty, S., Cacho, I., et al. (2008). Interlaboratory comparison study of calibration standards for foraminiferal Mg/Ca thermometry. *Geochemistry, Geophysics, Geosystems*, 9(8), 1–27. <https://doi.org/10.1029/2008GC001974>
- Holbourn, A., Kuhnt, W., Kawamura, H., Jian, Z., Grootes, P., Erlenkeuser, H., & Xu, J. (2005). Orbitally paced paleoproductivity variations in the Timor Sea and Indonesian throughflow variability during the last 460 kyr. *Paleoceanography*, 20(3), 1–18. <https://doi.org/10.1029/2004PA001094>
- Holbourn, A., Kuhnt, W., & Xu, J. (2011). Indonesian Throughflow variability during the last 140 ka: The Timor Sea outflow. *Geological Society Special Publication*, 355, 283–303. <https://doi.org/10.1144/SP355.14>
- Hu, S., Zhang, Y., Feng, M., Du, Y., Sprintall, J., Wang, F., et al. (2019). Interannual to decadal variability of upper-ocean salinity in the southern Indian Ocean and the role of the Indonesian Throughflow. *Journal of Climate*, 32(19), 6403–6421. <https://doi.org/10.1175/JCLI-D-19-0056.1>
- Huybers, P. (2009). Antarctica's Orbital Beat. *Nature*, 325(5944), 1085–1086. <https://doi.org/10.1126/science.1176186>
- Huybers, P., & Denton, G. (2008). Antarctic temperature at orbital timescales controlled by local summer duration. *Nature Geoscience*, 1(11), 787–792. <https://doi.org/10.1038/ngeo311>

- Ishiwa, T., Yokoyama, Y., Reuning, L., McHugh, C. M., De Vleeschouwer, D., & Gallagher, S. J. (2019). Australian Summer Monsoon variability in the past 14,000 years revealed by IODP Expedition 356 sediments. *Progress in Earth and Planetary Science*, 6(1). <https://doi.org/10.1186/s40645-019-0262-5>
- Kuhnt, W., Holbourn, A., Xu, J., Opdyke, B., De Deckker, P., Röhl, U., & Mudelsee, M. (2015). Southern Hemisphere control on Australian monsoon variability during the late deglaciation and Holocene. *Nature Communications*, 6(1), 1-7. <https://doi.org/10.1038/ncomms6916>
- Kuhnt, W., Holbourn, A., Schönfeld, J., Lindhorst, K., Gallagher, S., Keep, M., et al. (2017). Cruise Report Sonne 257, WACHEIO - Western Australian Climate History from Eastern Indian Ocean Sediment Archives, Darwin - Fremantle, May 12, 2017 - June 04, 2017. *Institut Für Geowissenschaften, Christian-Albrechts-Universität Kiel*, 260. https://doi.org/10.2312/cr_so257
- Laepple, T., Werner, M., & Lohmann, G. (2011). Synchronicity of Antarctic temperatures and local solar insolation on orbital timescales. *Nature*, 471(7336), 91–94. <https://doi.org/10.1038/nature09825>
- Lea, D. W., Pak, D. K., Belanger, C. L., Spero, H. J., Hall, M. A., & Shackleton, N. J. (2006). Paleoclimate history of Galápagos surface waters over the last 135,000 yr. *Quaternary Science Reviews*, 25(11–12), 1152–1167. <https://doi.org/10.1016/j.quascirev.2005.11.010>
- Lisiecki, L. E., & Raymo, M. E. (2005). A Pliocene-Pleistocene stack of 57 globally distributed benthic $\delta^{18}\text{O}$ records. *Paleoceanography*, 20(1), 1–17. <https://doi.org/10.1029/2004PA001071>
- Liu, J., Fu, G., Song, X., Charles, S. P., Zhang, Y., Han, D., & Wang, S. (2010). Stable isotopic compositions in Australian precipitation. *Journal of Geophysical Research Atmospheres*, 115(23), 1–16. <https://doi.org/10.1029/2010JD014403>
- Locarnini, R. A., Mishonov, A. V., Antonov, J. I., Boyer, T. P., Garcia, H. E., Baranova, O. K., et al. (2013). World Ocean Atlas 2013. Vol. 1: Temperature. *World Ocean Atlas 2013, 1(Temperature)*. S. Levitus, Ed.; A. Mishonov, Technical Ed.; NOAA Atlas NESDIS 73, 40.
- Lüthi, D., Le Floch, M., Bereiter, B., Blunier, T., Barnola, J. M., Siegenthaler, U., et al. (2008). High-resolution carbon dioxide concentration record 650,000-800,000 years before present. *Nature*, 453(7193), 379–382. <https://doi.org/10.1038/nature06949>
- Mantsis, D. F., Lintner, B. R., Broccoli, A. J., Erb, M. P., Clement, A. C., & Park, H. S. (2014). The response of large-scale circulation to obliquity-induced changes in meridional heating gradients. *Journal of Climate*, 27(14), 5504–5516. <https://doi.org/10.1175/JCLI-D-13-00526.1>
- Martin, P. A., & Lea, D. W. (2002). A simple evaluation of cleaning procedures on fossil benthic foraminiferal Mg/Ca. *Geochemistry, Geophysics, Geosystems*, 3(10), 1–8. <https://doi.org/10.1029/2001GC000280>
- Medina-Elizalde, M., & Lea, D. W. (2005). The mid-Pleistocene transition in the tropical Pacific. *Science*, 310(5750), 1009–1012. <https://doi.org/10.1126/science.1115933>
- Milliman, J., & Farnsworth, K. (2011). Runoff, erosion, and delivery to the coastal ocean. *River discharge to the coastal ocean: a global synthesis*, Cambridge University Press, Cambridge, 13–39. doi:10.1017/cbo9780511781247.003

- Mohtadi, M., Oppo, D. W., Steinke, S., Stuut, J. B. W., De Pol-Holz, R., Hebbeln, D., & Lückge, A. (2011). Glacial to Holocene swings of the Australian-Indonesian monsoon. *Nature Geoscience*, 4(8), 540–544. <https://doi.org/10.1038/ngeo1209>
- Mohtadi, M., Prange, M., Oppo, D. W., De Pol-Holz, R., Merkel, U., Zhang, X., et al. (2014). North Atlantic forcing of tropical Indian Ocean climate. *Nature*, 508(7498), 76–80. <https://doi.org/10.1038/nature13196>
- Morimoto, M., Abe, O., Kayanne, H., Kurita, N., Matsumoto, E., & Yoshida, N. (2002). Salinity records for the 1997-98 El Niño from Western Pacific corals. *Geophysical Research Letters*, 29(11), 35-1-35–4. <https://doi.org/10.1029/2001GL013521>
- Muller, J., Kylander, M., Wüst, R. A. J., Weiss, D., Martinez-Cortizas, A., LeGrande, A. N., et al. (2008). Possible evidence for wet Heinrich phases in tropical NE Australia: the Lynch’s Crater deposit. *Quaternary Science Reviews*, 27(5–6), 468–475. <https://doi.org/10.1016/j.quascirev.2007.11.006>
- Muller, J., McManus, J. F., Oppo, D. W., & Francois, R. (2012). Strengthening of the Northeast Monsoon over the Flores Sea, Indonesia, at the time of Heinrich event 1. *Geology*, 40(7), 635–638. <https://doi.org/10.1130/G32878.1>
- Pattiaratchi, C. (2006). Surface and sub-surface circulation and water masses off Western Australia. *Bulletin of the Australian Meteorological and Oceanographic Society*, 19(5), 95–104.
- Phillips, H. E., Wijffels, S. E., & Feng, M. (2005). Interannual variability in the freshwater content of the Indonesian-Australian Basin. *Geophysical Research Letters*, 32(3), 1–5. <https://doi.org/10.1029/2004GL021755>
- Ridgway, K. R., & Condie, S. A. (2004). The 5500-km-long boundary flow off western and southern Australia. *Journal of Geophysical Research: Oceans*, 109(C4), 1–18. <https://doi.org/10.1029/2003JC001921>
- Ridgway, K. R., & Godfrey, J. S. (2015). The source of the Leeuwin Current seasonality. *Journal of Geophysical Research: Oceans*, 120(10), 6843-6864. <https://doi.org/10.1002/2015JC011049>
- Rosenthal, Y., Holbourn, A., Kullhanek, D., & Scientists, E. 363. (2017). Expedition 363 Preliminary Report Western Pacific Warm Pool Neogene and Quaternary records of Western Pacific Warm Pool. International Ocean Discovery Program. 11-13. <https://doi.org/10.14379/iodp.pr.363.2017>
- Rosenthal, Y., Holbourn, A., Kullhanek, D., & Scientists, E. 363. (2018). Western Pacific Warm Pool. Proceedings of the International Ocean Discovery Program, 363: College Station, TX(International Ocean Discovery Program). <https://doi.org/10.14379/iodp.proc.363.2018>
- Rosignol-Strick, M. (1983). African monsoons, an immediate climate response to orbital insolation. *Nature*, 304(5921), 46–49. <https://doi.org/10.1038/304046a0>
- Sarnthein, M., Grootes, P. M., Holbourn, A., Kuhnt, W., & Kühn, H. (2011). Tropical warming in the Timor Sea led deglacial Antarctic warming and atmospheric CO₂ rise by more than 500yr. *Earth and Planetary Science Letters*, 302(3–4), 337–348. <https://doi.org/10.1016/j.epsl.2010.12.021>

- Schröder, J. F., Holbourn, A., Kuhnt, W., & Küssner, K. (2016). Variations in sea surface hydrology in the southern Makassar Strait over the past 26 kyr. *Quaternary Science Reviews*, *154*, 143–156. <https://doi.org/10.1016/j.quascirev.2016.10.018>
- Schröder, J. F., Kuhnt, W., Holbourn, A., Beil, S., Zhang, P., Hendrizon, M., & Xu, J. (2018). Deglacial Warming and Hydroclimate Variability in the Central Indonesian Archipelago. *Paleoceanography and Paleoclimatology*, *33*(9), 974–993. <https://doi.org/10.1029/2018PA003323>
- Shakun, J. D., Clark, P. U., He, F., Marcott, S. A., Mix, A. C., Liu, Z., et al. (2012). Global warming preceded by increasing carbon dioxide concentrations during the last deglaciation. *Nature*, *484*(7392), 49–54. <https://doi.org/10.1038/nature10915>
- Smith, R. L., Huyer, A., Godfrey, J. S., & Church, J. A. (1991). The Leeuwin current off western Australia. *Journal of Physical Oceanography*, *21*(2), 323–345. [https://doi.org/10.1175/1520-0485\(1991\)021<0323:TLCOWA>2.0.CO;2](https://doi.org/10.1175/1520-0485(1991)021<0323:TLCOWA>2.0.CO;2)
- Spooner, M. I., De Deckker, P., Barrows, T. T., & Fifield, L. K. (2011). The behaviour of the Leeuwin Current offshore NW Australia during the last five glacial-interglacial cycles. *Global and Planetary Change*, *75*(3–4), 119–132. <https://doi.org/10.1016/j.gloplacha.2010.10.015>
- Stager, J. C., Ryves, D. B., Chase, B. M., & Pausata, F. S. R. (2011). Catastrophic drought in the Afro-Asian monsoon region during Heinrich event 1. *Science*, *331*(6022), 1299–1302. <https://doi.org/10.1126/science.1198322>
- Thompson, A. F., & Richards, K. J. (2011). Low frequency variability of Southern Ocean jets. *Journal of Geophysical Research: Oceans*, *116*(C9), 1–17. <https://doi.org/10.1029/2010JC006749>
- Timmermann, A., Timm, O., Stott, L., & Menviel, L. (2009). The roles of CO₂ and orbital forcing in driving Southern Hemispheric temperature variations during the last 21 000 Yr. *Journal of Climate*, *22*(7), 1626–1640. <https://doi.org/10.1175/2008JCLI2161.1>
- Uemura, R., Motoyama, H., Masson-Delmotte, V., Jouzel, J., Kawamura, K., Goto-Azuma, K., et al. (2018). Asynchrony between Antarctic temperature and CO₂ associated with obliquity over the past 720,000 years. *Nature Communications*, *9*(1), 1–11. <https://doi.org/10.1038/s41467-018-03328-3>
- Waelbroeck, C., Labeyrie, L., Michel, E., Duplessy, J. C., McManus, J. F., Lambeck, K., et al. (2002). Sea-level and deep water temperature changes derived from benthic foraminifera isotopic records. *Quaternary Science Reviews*, *21*(1–3), 295–305. [https://doi.org/10.1016/S0277-3791\(01\)00101-9](https://doi.org/10.1016/S0277-3791(01)00101-9)
- Weller, E., Holliday, D., Feng, M., Beckley, L., & Thompson, P. (2011). A continental shelf scale examination of the Leeuwin Current off Western Australia during the austral autumn–winter. *Continental Shelf Research* *31*(17), 1858–1868. <https://doi.org/10.1016/j.csr.2011.08.008>
- Xu, J., Kuhnt, W., Holbourn, A., Andersen, N., & Bartoli, G. (2006). Changes in the vertical profile of Indonesian Throughflow during Termination II: Evidence from the Timor Sea. *Paleoceanography*, *21*(4), 1–14. <https://doi.org/10.1029/2006PA001278>

- Xu, J., Holbourn, A., Kuhnt, W., Jian, Z., & Kawamura, H. (2008). Changes in the thermocline structure of the Indonesian outflow during Terminations I and II. *Earth and Planetary Science Letters*, 273(1–2), 152–162. <https://doi.org/10.1016/j.epsl.2008.06.029>
- Xu, J., Kuhnt, W., Holbourn, A., Regenberg, M., & Andersen, N. (2010). Indo-Pacific warm pool variability during the Holocene and Last Glacial Maximum. *Paleoceanography*, 25(4). <https://doi.org/10.1029/2010PA001934>
- Zhang, N., Feng, M., Du, Y., Lan, J., & E., W. S. (2016). Seasonal and interannual variations of mixed layer salinity in the southeast tropical Indian Ocean. *Journal of Geophysical Research: Oceans*, 121(7), 4716–4731. <https://doi.org/10.1002/2016JC011854>
- Zhang, P., Xu, J., Holbourn, A., Kuhnt, W., Beil, S., Li, T., et al. (2020). Indo-Pacific Hydroclimate in Response to Changes of the Intertropical Convergence Zone: Discrepancy on Precession and Obliquity Bands Over the Last 410 kyr. *Journal of Geophysical Research: Atmospheres*, 125(14), 1–10. <https://doi.org/10.1029/2019JD032125>
- Zweng, M. M., Reagan, J. R., Antonov, J. I., Mishonov, A. V., Boyer, T. P., Garcia, H. E., et al. (2013). World Ocean Atlas 2013, Volume 2: Salinity. *World Ocean Atlas 2013*, 2(Salinity. S. Levitus, Ed.; A. Mishonov, Technical Ed.; NOAA Atlas NESDIS 74), 39. Retrieved from https://www.ncei.noaa.gov/data/oceans/woa/WOA13/DOC/woa13_vol2.pdf
- Schlitzer, R. (2020). *Ocean Data View*. <https://odv.awi.de>



Paleoceanography and Paleoclimatology

Supporting Information for

**Evolution of sea surface hydrology along the Northwestern Australian
Margin over the past 450 kyr**

Renjie Pei¹, Wolfgang Kuhnt¹, Ann Holbourn¹, Janika Jöhnck¹, Johanna Hingst^{1,2}, Sebastian Beil¹, Julia Lübbers¹, Nils Andersen³

¹*Institute of Geosciences, Christian-Albrechts-University, Kiel D-24118, Germany.*

²*MARUM – Center for Marine Environmental Sciences, University of Bremen, Bremen D-28359, Germany.*

³*Laboratory for Radiometric Dating and Stable Isotope Research, Christian-Albrechts-University, Kiel D-24118, Germany.*

Contents of this file

Figures S1 to S4

Tables S1 to S2

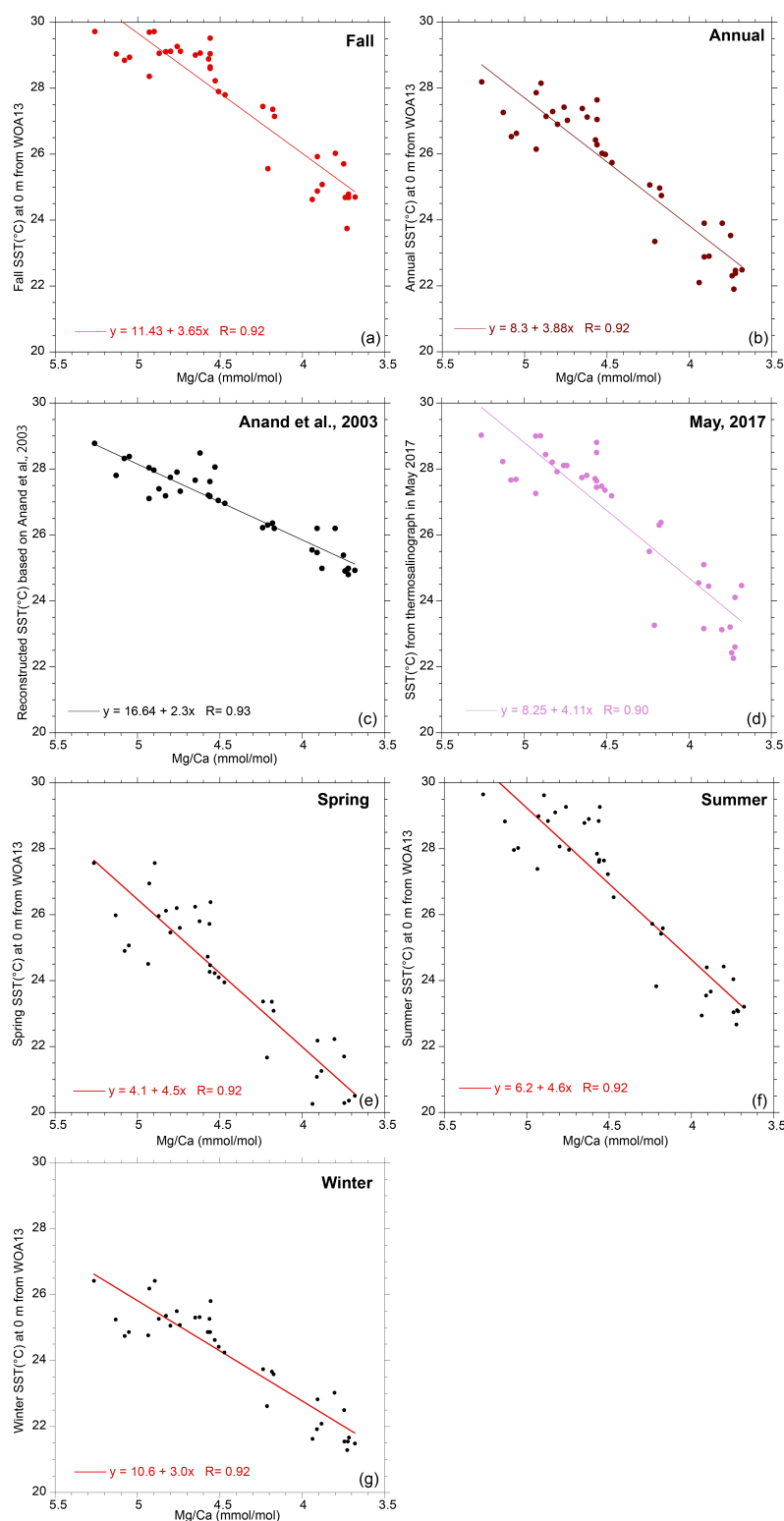


Figure S1A. Mg/Ca of *G. ruber* in core top samples versus (a) fall (March-May) SST (°C) at 0 m from WOA13 (Locarnini et al., 2013), (b) annual average SST (°C) at 0 m from WOA13, (c) Mg/Ca derived SST (°C) in SO257 core top samples using calibration of Anand et al. (2003), (d) SST (°C) from shipboard thermosalinograph measurements in May 2017, (e) spring (September-November) SST (°C) at 0 m from WOA13, (f) summer (December-February) SST (°C) at 0 m from WOA13, and (g) winter (June-August) SST (°C) at 0 m from WOA13.

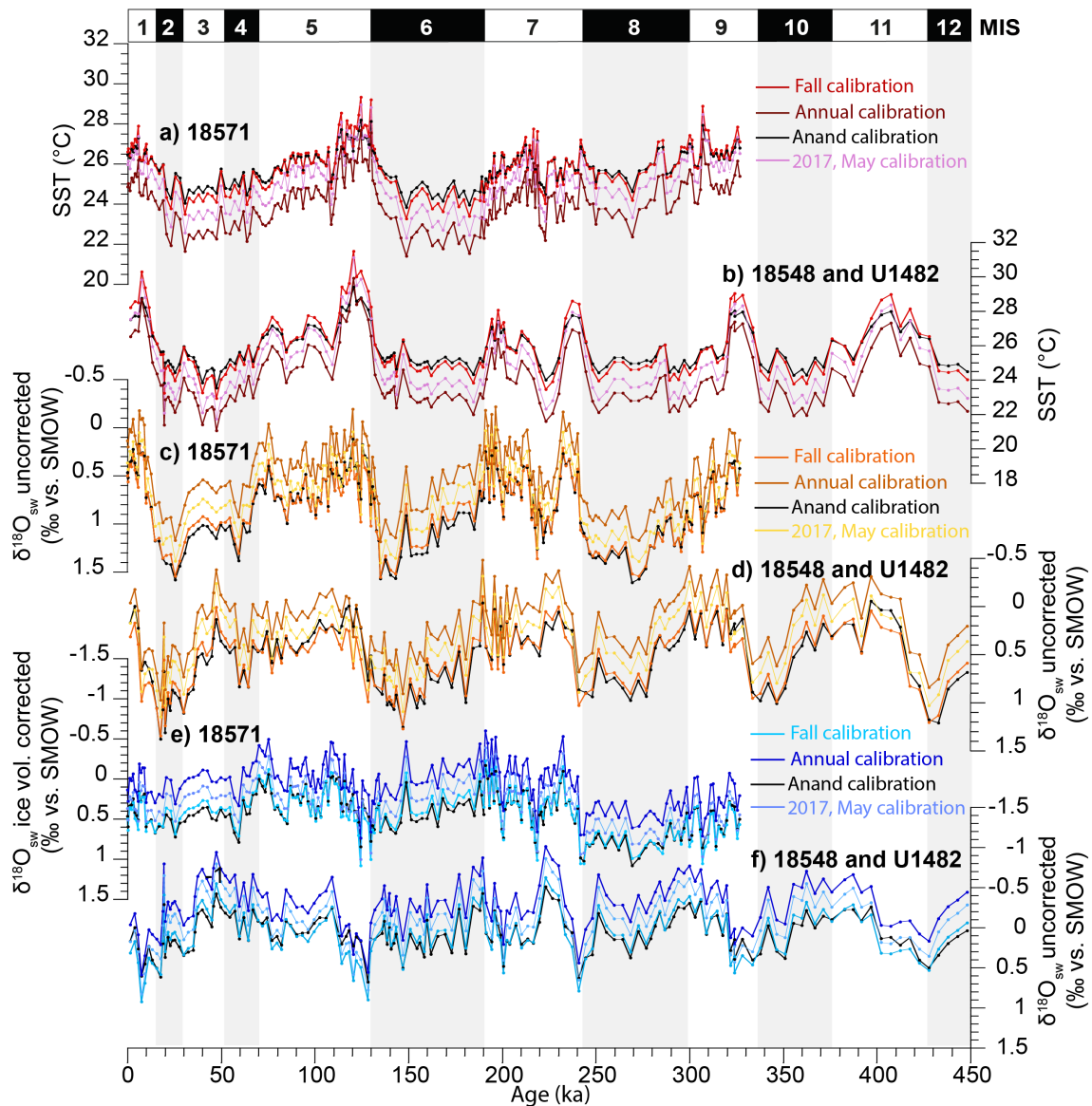


Figure S1B. Comparison of Mg/Ca derived SST (a-b), uncorrected $\delta^{18}\text{O}_{\text{sw}}$ (c-d) and ice volume corrected $\delta^{18}\text{O}_{\text{sw}}$ (e-f) in Sites SO257-18571 and SO257-18548/U1482, based on different calibrations. Fall calibration: based on local calibration derived from linear regression between core top samples Mg/Ca and fall (March-May) SST at 0 m from WOA13 (Supplementary Figure S1A-a); Annual calibration: based on local calibration derived from linear regression between core top samples Mg/Ca and annual SST at 0 m from WOA13 (Supplementary Figure S1A-b); Anand calibration: based on Anand et al. (2003); 2017, May calibration: based on local calibration derived from the linear regression between core top samples Mg/Ca and measured SST during R/V Sonne Cruise SO257 (May 2017) (Supplementary Figure S1A-d). This comparison shows that reconstructed SSTs, based on global Mg/Ca calibrations of Anand et al. (2003), closely match SSTs based on WOA13 fall dataset. Reconstructions based on annual average WOA13 dataset enhance glacial-interglacial SST gradients, whereas glacial-interglacial gradients are lowest in reconstructions based on Anand et al. (2003) and austral fall temperatures. Largest interglacial-glacial gradients of uncorrected $\delta^{18}\text{O}_{\text{sw}}$ and ice volume corrected $\delta^{18}\text{O}_{\text{sw}}$ occur in reconstructions based on annual average WOA13 dataset.

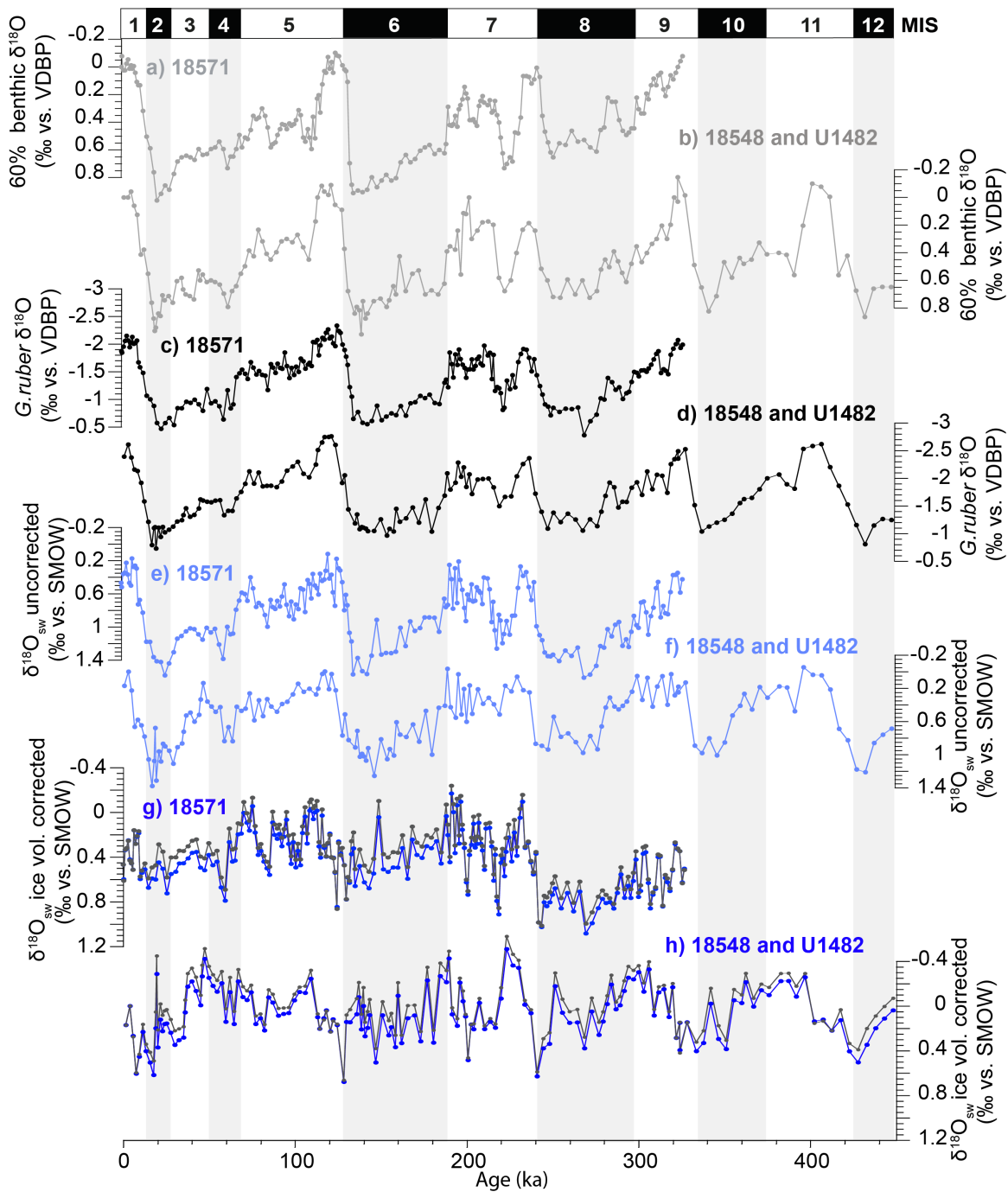


Figure S2. Ice volume correction of $\delta^{18}\text{O}_{\text{sw}}$ in Sites SO257-18548/U1482, and SO257-18571. (a-b) 60% normalized $\delta^{18}\text{O}$ of *C. wuellerstorfi*. Original benthic foraminiferal $\delta^{18}\text{O}$ from Pei et al. (2021). (c-d) planktonic $\delta^{18}\text{O}$. (e-f) Uncorrected $\delta^{18}\text{O}_{\text{sw}}$. (g-h) Comparison of reconstructed $\delta^{18}\text{O}_{\text{sw}}$ after correction for different estimates of benthic foraminiferal $\delta^{18}\text{O}$ ice volume component. $\delta^{18}\text{O}_{\text{sw}}$ calculated after Bemis et al. (1998) with 70 % estimate of $\delta^{18}\text{O}$ ice volume component (dark grey) and 60 % estimate of $\delta^{18}\text{O}$ ice volume component (blue).

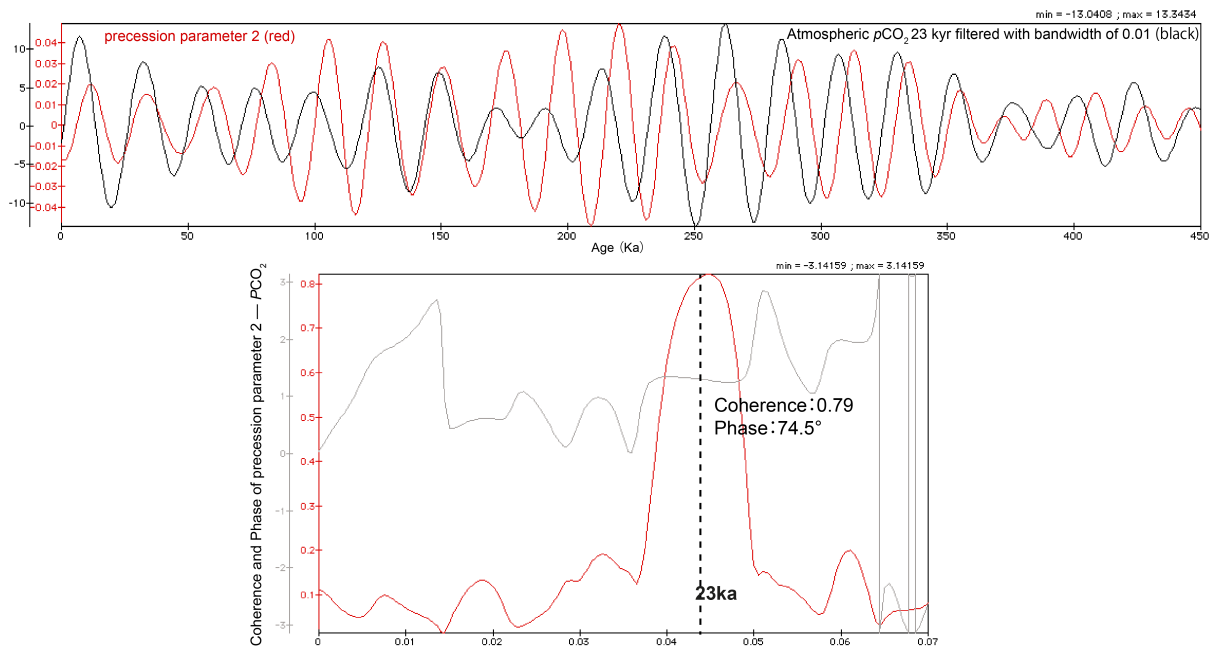


Figure S3A. Comparison of precession parameter 2 (standard precession parameter multiplied by -1, corresponding to Northern Hemisphere insolation, red) to 23 kyr filtered EDC CO_2 record (black) (Lüthi et al., 2008) and coherence (red) and phase (grey) of precession parameter 2 to EDC CO_2 record. Precession parameter 2 (insolation) leads atmospheric $p\text{CO}_2$ by 4.8 kyr. Bandwidth is 0.011194. Non-zero coherence >0.550342 . Error estimation on power spectrum is $0.488632 < \Delta\text{Power} / \text{Power} < 3.0732$.

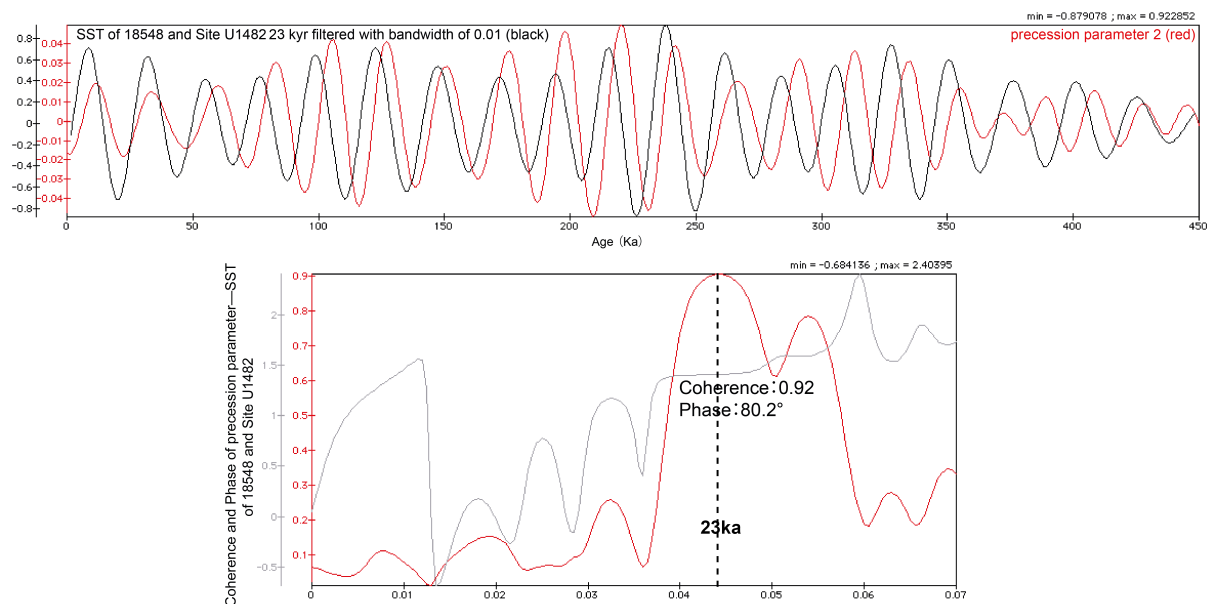


Figure S3B. Comparison of precession parameter 2 (red) to 23 kyr filtered SST in Site SO257-18548/U1482 (black) and coherence (red) and phase (grey) of precession parameter 2 to SST in Site SO257-18548/U1482. Precession parameter 2 (insolation) leads SST by 5.1 kyr. Bandwidth is 0.011194. Non-zero coherence >0.550342 . Error estimation on power spectrum is $0.488632 < \Delta\text{Power} / \text{Power} < 3.0732$.

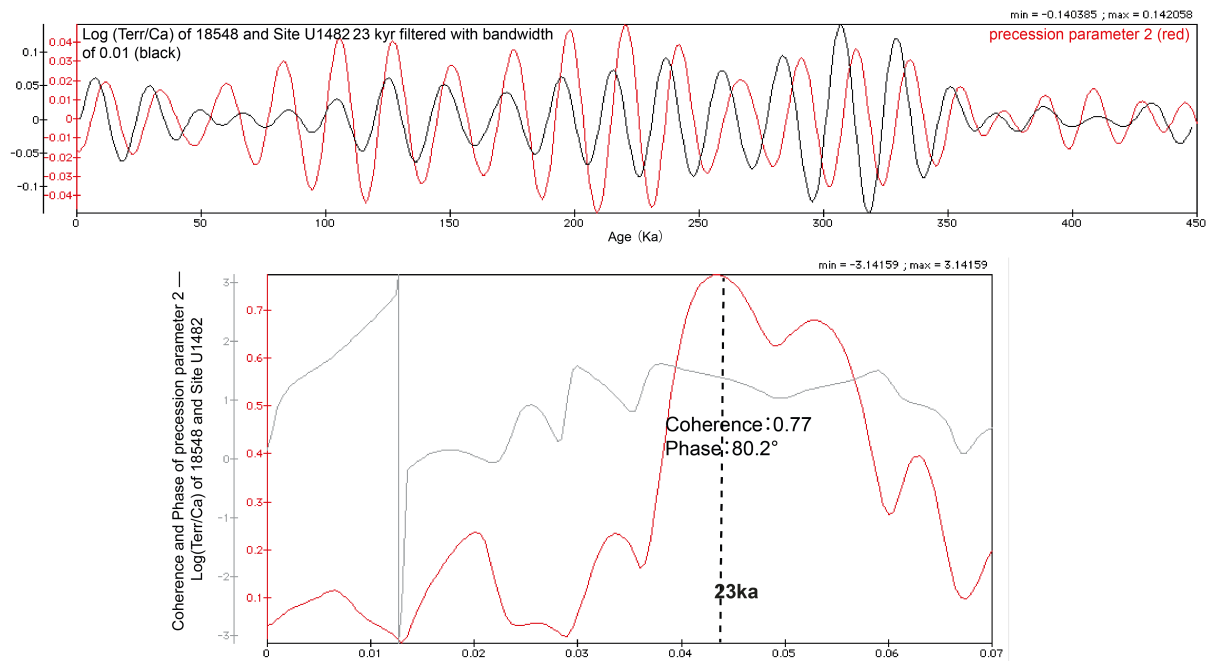


Figure S3C. Comparison of precession parameter 2 (red) to 23 kyr filtered Log(Terr/Ca) in Site SO257-18548/U1482 (black) and coherence (red) and phase (grey) of precession parameter 2 to Log(Terr/Ca) in Site SO257-18548/U1482. Precession parameter 2 (insolation) leads Log(Terr/Ca) by 5.1 kyr. Bandwidth is 0.011194. Non-zero coherence >0.550342 . Error estimation on power spectrum is $0.488632 < \Delta\text{Power} / \text{Power} < 3.0732$.

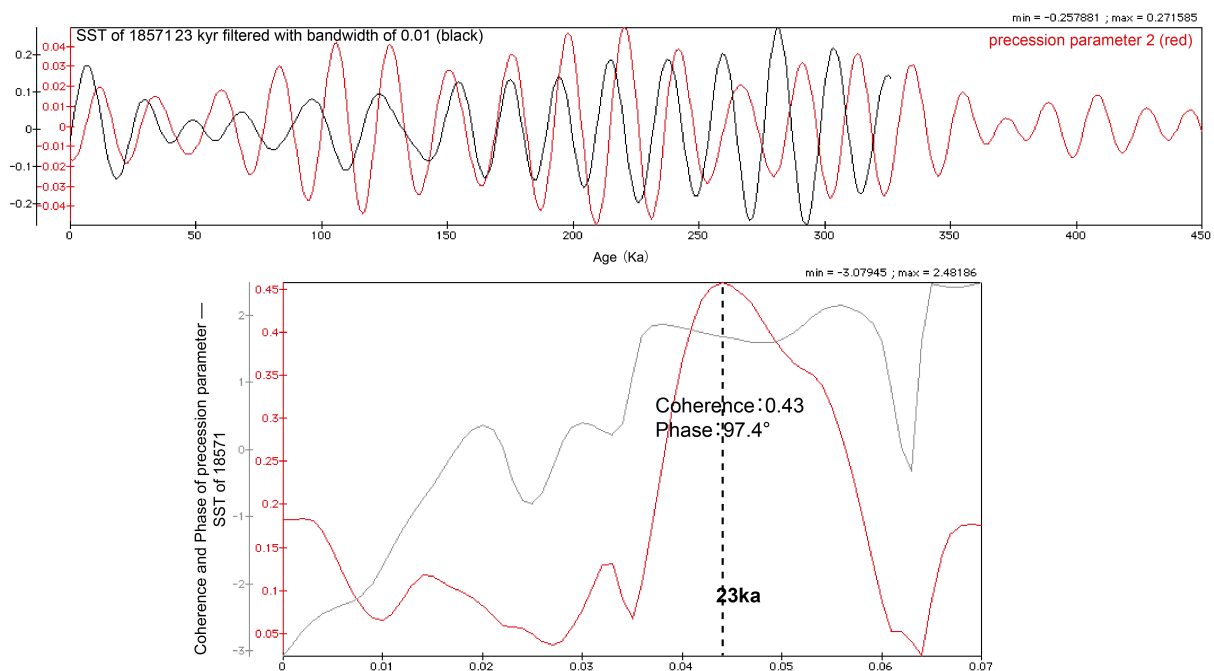


Figure S3D. Comparison of precession parameter 2 (red) to 23 kyr filtered SST in Site SO257-18571 (black) and coherence (red) and phase (grey) of precession parameter 2 to SST in Site SO257-18571. Precession parameter 2 (insolation) leads SST by 6.2 kyr. Bandwidth is 0.011194. Non-zero coherence >0.550342 . Error estimation on power spectrum is $0.488632 < \Delta\text{Power} / \text{Power} < 3.0732$.

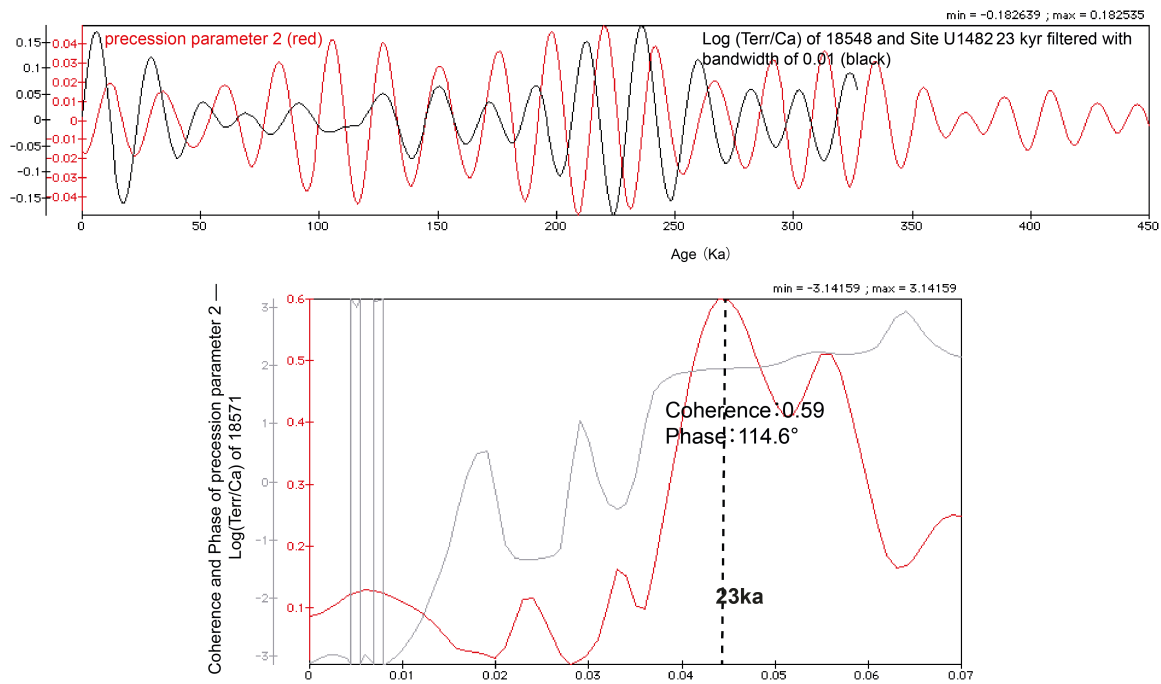


Figure S3E. Comparison of precession parameter 2 (red) to 23 kyr filtered Log(Terr/Ca) in Site SO257-18571 (black) and coherence (red) and phase (grey) of precession parameter 2 to Log (Terr/Ca) in Site SO257-18571. Precession parameter 2 (insolation) leads Log(Terr/Ca) by 7.3 kyr. Bandwidth is 0.011194. Non-zero coherence >0.550342 . Error estimation on power spectrum is $0.488632 < \Delta\text{Power} / \text{Power} < 3.0732$.

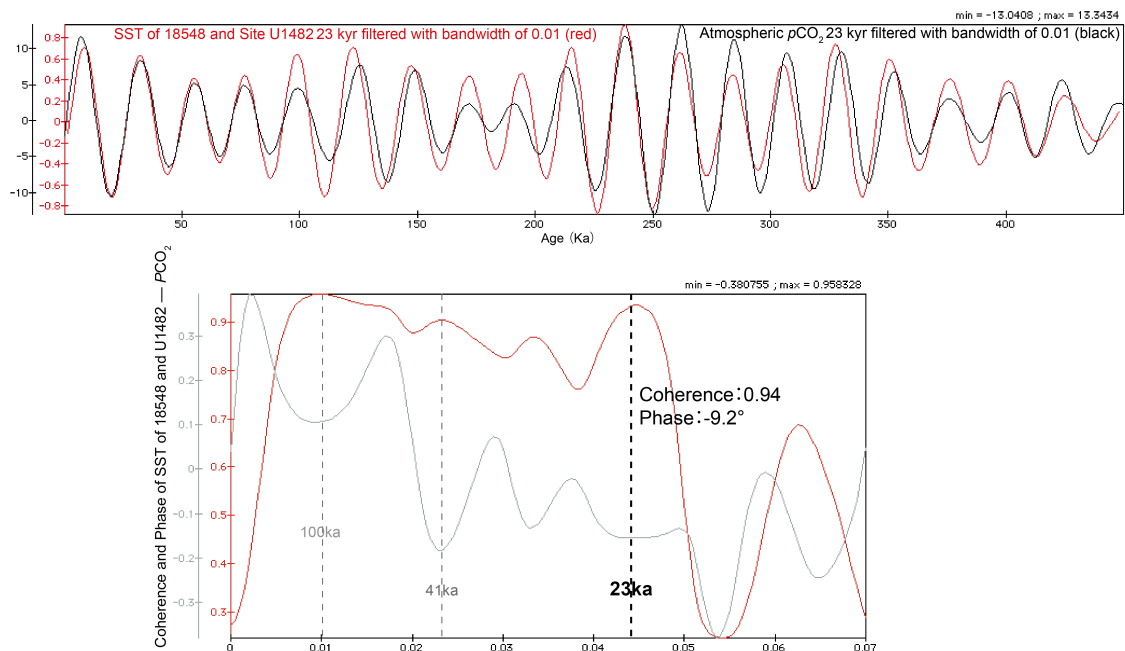


Figure S4A. Comparison of 23 kyr filtered SST (red) to 23 kyr filtered EDC CO₂ record (black) (Lüthi et al., 2008) and coherence (red) and phase (black) of SST to EDC CO₂ record in spliced sediment record from Sites SO257-18548 and U1482. SST lags atmospheric pCO₂ by 0.59 kyr. Bandwidth is 0.011194. Non-zero coherence >0.550342 . Error estimation on power spectrum is $0.488632 < \Delta\text{Power} / \text{Power} < 3.0732$.

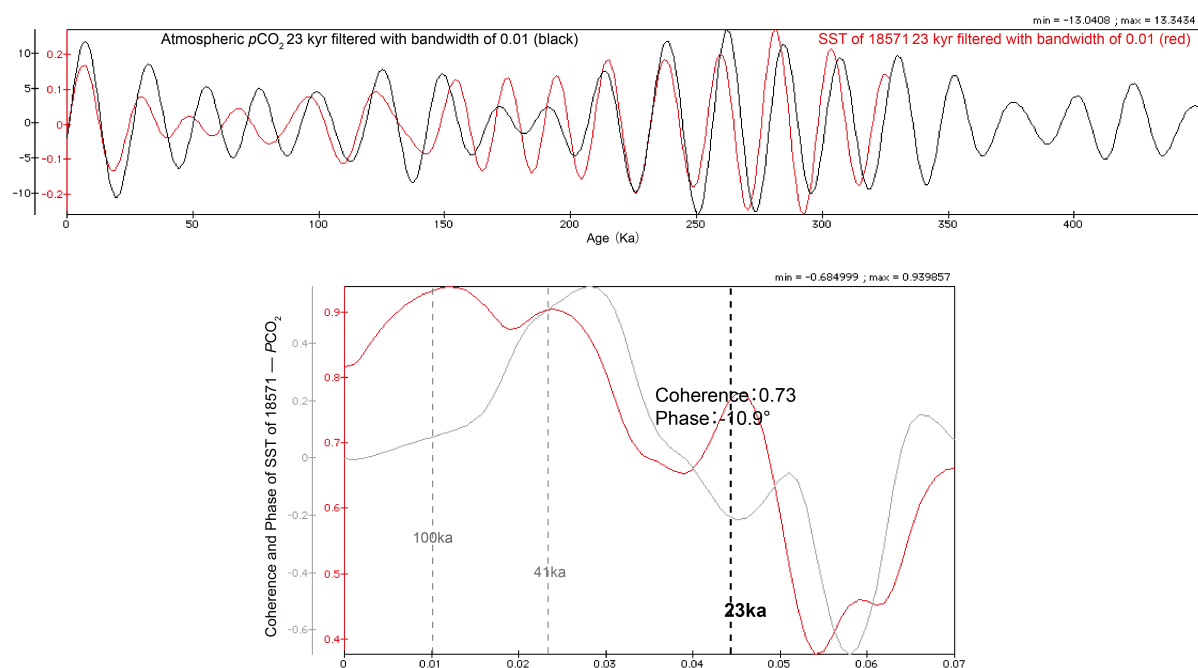


Figure S4B. Comparison of 23 kyr filtered SST (red) to 23 kyr filtered EDC $p\text{CO}_2$ record (black) (Lüthi et al., 2008) and coherence (red) and phase (black) of SST to EDC $p\text{CO}_2$ record in sediment record from Site SO257-18571. SST lags atmospheric $p\text{CO}_2$ by 0.7 kyr. Bandwidth is 0.011194. Non-zero coherence >0.550342 . Error estimation on power spectrum is $0.488632 < \Delta\text{Power} / \text{Power} < 3.0732$.

Supplementary Table 1. R/V Sonne Cruise SO257 stations, Mg/Ca, $\delta^{18}\text{O}$ measured in core top samples. WOA13 annual SST and SSS in comparison to SST and SSS measured by CTD.

GIK station s	Latitude (S)	Longitude (E)	Water depth (m)	Mg/ Ca (mmol/mol) derived from <i>G. ruber</i>	$\delta^{18}\text{O}$ of <i>G. ruber</i> (‰ vs. VPDB)	Annual SST ($^{\circ}\text{C}$) at 0 m from WOA13	Annual SSS (psu) at 0 m from WOA13	SST ($^{\circ}\text{C}$) from Cruise SO257	SSS (psu) from Cruise SO257
18547	15°3.306'	120°26.174'	1460.5	5.26	-2.96	28.19	34.55	29.03	34.66
18548	15°3.595'	120°18.840'	1610.1	4.90	-2.75	28.15	34.55	29.01	34.65
18549	15°57.689'	119°30.580'	1628.5	4.93	-2.67	27.86	34.54	29.00	34.74
18550	16°51.556'	118°45.423'	1388	4.56	-2.65	27.64	34.58	28.81	34.80
18551	17°35.493'	118°26.747'	668.8	4.87	-2.25	27.14	34.68	28.44	34.74
18552	17°40.558'	117°41.640'	1951.3	4.56	-2.70	27.05	34.73	28.50	34.76
18553	18°6.987'	117°6.998'	1619.7	4.65	-2.30	27.38	34.67	27.74	34.87
18554	18°31.997'	117°21986'	497.9	4.74	-2.51	27.02	34.70	28.11	34.83
18555	18°21.050'	117°15.360'	1113.7	5.13	-2.67	27.26	34.69	28.23	34.83
18556	17°6.179'	117°13.816'	1843.6	4.76	-2.30	27.42	34.79	28.11	34.81
18557	17°32.862'	117°8.731'	2405.9	4.83	-2.66	27.29	34.82	28.21	34.48
18558	18°23.972'	115°13.690'	1755.4	4.80	-2.53	26.90	34.71	27.92	34.77
18559	18°5.004'	115°2.862'	1976.5	4.62	-2.51	27.12	34.82	27.81	34.81
18560	19°18.238'	115°25.933'	868.8	5.05	-2.60	26.63	34.83	27.69	34.87
18561	19°14.553'	115°23.948'	1185	5.08	-2.79	26.53	34.87	27.67	34.86
18562	19°25.001'	114°19.143'	1298.8	4.57	-2.69	26.43	34.76	27.71	34.86
18564	20°30.040'	114°47.074'	349.7	4.93	-2.19	26.15	34.75	27.26	34.97
18565	20°0.818'	114°14.357'	1253.9	4.56	-2.51	26.29	34.77	27.64	34.97
18566	19°38.706'	113°48.633'	1133.5	4.56	-2.26	26.28	34.88	27.45	34.90
18567	19°31.236'	113°3.528'	1131	4.53	-2.36	26.02	34.99	27.48	34.89
18568	20°36.580'	113°37.463'	1100	4.51	-2.39	25.99	34.90	27.36	34.98
18570	20°59.468'	113°26.908'	1182.4	4.47	-2.43	25.74	34.91	27.19	35.02
18571	22°6.674'	113°29.677'	1049.3	4.24	-2.23	25.06	35.00	25.50	35.05
18572	22°4.585'	113°13.798'	1327.9	4.18	-2.36	24.97	35.00	26.30	34.95
18573	22°37.245'	112°50.209'	1250.5	4.17	-2.10	24.74	35.02	26.38	34.99
18575	24°13.811'	111°51.181'	1032	3.91	-1.57	23.90	35.18	25.10	35.15
18576	24°8.401'	111°20.499'	1725.9	3.80	-1.53	23.90	35.18	23.13	35.40
18578	25°22.258'	111°5.708'	1678.9	3.75	-1.72	23.53	35.25	23.21	35.44
18579	25°6.114'	111°50.925'	715.1	4.21	-1.35	23.35	35.29	23.26	35.46
18580	24°34.161'	111°14.790'	1369.1	3.88	-1.72	22.90	35.33	24.45	35.24
18582	25°53.896'	111°22.325'	1571.5	3.91	-1.55	22.88	35.36	23.16	35.44
18584	27°46.182'	112°25.228'	1121.1	3.68	-1.41	22.49	35.38	24.47	35.24
18585	27°15.369'	112°2.210'	1182.7	3.72	-1.38	22.47	35.40	24.11	35.26
18586	28°8.509'	112°38.035'	1014.6	3.72	-1.39	22.38	35.43	22.60	35.38
18587	28°7.712'	112°56.258'	797.8	3.74	-1.75	22.31	35.42	22.43	35.44
18588	28°23.085'	113°0.992'	810.2	3.94	-1.70	22.10	35.45	24.55	35.23
18589	28°58.032'	112°52.602'	2485.8	3.73	-1.54	21.90	35.50	22.26	35.48

Supplementary Table 2. CTD stations, water sampling, $\delta^{18}\text{O}_{\text{sw}}$ analysis from R/V Sonne Cruise SO257. Comparison of sea surface temperature (SST) and salinity (SSS) from WOA13 and R/V Sonne Cruise SO257.

Site	Latitude (S)	Longitude (E)	Depth (m) of water samples	measured $\delta^{18}\text{O}_{\text{sw}}$ of water samples	Modern annual average WOA13		Modern autumn average WOA13		CTD (May-June, 2017)	
					SST (°C)	SSS (psu)	SST (°C)	SSS (psu)	SST (°C)	SSS (psu)
18546	15°0.012'	120°23.958'	5	-0.04	28.08	34.53	29.71	34.42	29.01	34.58
			10	-0.02	28.07	34.54	29.66	34.40	29.02	34.58
			20	-0.07	27.92	34.53	29.64	34.48	29.01	34.58
18549	15°58.040'	119°30.978'	5	0.02	27.91	34.51	29.54	34.34	29.01	34.66
			10	0.09	27.87	34.51	29.55	34.40	29.01	34.66
			20	0.16	27.76	34.52	29.50	34.45	29.01	34.66
18553	18°7.024'	117°7.001'	5	0.06	27.08	34.87	29.09	34.87	28.20	34.81
			10	0.12	27.05	34.87	29.09	34.87	28.20	34.81
			20	0.09	26.95	34.87	29.05	34.88	28.21	34.81
18559	18°4.998'	115°2.896'	5	0.19	26.92	34.74	29.09	34.75	27.68	34.85
			10	0.14	26.84	34.76	29.07	34.75	27.66	34.85
			20	0.22	26.72	34.77	28.98	34.77	27.62	34.87
18562	19°24.976'	114°19.131'	5	0.13	26.38	34.74	28.89	34.63	27.33	34.99
			10	0.14	26.36	34.74	28.85	34.63	27.33	34.99
			20	0.21	26.25	34.74	28.74	34.63	27.32	34.99
18567	19°31.234'	113°3.531'	5	0.11	26.22	34.71	28.51	34.41	27.46	34.89
			10	0.17	26.21	34.72	28.48	34.45	27.46	34.89
			20	0.13	26.11	34.73	28.34	34.45	27.46	34.89
18569	21°11.507'	113°21.443'	5	0.16	25.58	34.92	27.76	34.87	26.22	35.06
			10	0.16	25.55	34.92	27.65	34.91	26.23	35.06
			20	0.18	25.45	34.93	27.59	34.88	26.21	35.06
18577	25°25.796'	111°4.991'	5	0.41	23.12	35.32	25.18	35.54	22.87	35.47
			10	0.34	23.12	35.33	25.16	35.55	22.88	35.47
			20	0.39	23.03	35.34	25.07	35.56	22.90	35.47
18583	27°48.773'	112°19.408'	5	0.26	22.49	35.37	24.61	35.21	23.29	35.37
			10	0.29	22.37	35.40	24.61	35.22	23.29	35.37
			20	0.36	22.29	35.41	24.52	35.22	23.04	35.39
18590	29°18.686'	113°6.282'	5	0.28	21.77	35.52	23.73	35.52	21.47	35.64
			10	0.36	21.77	35.52	23.72	35.52	21.45	35.65
			20	0.36	21.74	35.51	23.69	35.52	21.40	35.64

Evolution of paleoproductivity and $\delta^{13}\text{C}$ gradients along the Northwestern Australian Margin over the last 450 kyr

Renjie Pei¹, Wolfgang Kuhnt¹, Ann Holbourn¹, Nils Andersen²

¹*Institute for Geosciences, Kiel University, Ludewig-Meyn Str. 10-14, 24118 Kiel, Germany*

²*Leibniz Laboratory for Radiometric Dating and Stable Isotope Research, Kiel University, Max-Eyth-Str. 11-13, 24118 Kiel, Germany*

Abstract

We present a new multi-proxy reconstruction of paleoproductivity spanning the last 450 kyr from piston Core SO257-18548 and International Ocean Discovery Program Site U1482, situated at the modern southern limit of the seasonal (austral summer) displacement of the Intertropical Convergence Zone (ITCZ) and from Core SO257-18571 retrieved in the southern part of the Exmouth Plateau. Spectral analysis of three different flux-based productivity proxies indicates spectral power concentrated in the 100 kyr (glacial-interglacial) and the 23 kyr and 19 kyr (precessional) periods. Anti-correlation between productivity proxies and terrigenous input records ($\text{Log}(\text{Terr}/\text{Ca})$) on the precessional band and a distinct glacial-interglacial contrast in productivity fluctuations suggest that productivity fluctuations over the last 450 kyr offshore northwestern Australia were strongly influenced by the Australian winter monsoon (23 and 19 kyr) and were also modulated by sea level-related variations in the intensity of the Indonesian Throughflow (100 kyr).

1. Introduction

Numerous studies have attempted to evaluate past bio-productivity changes to decipher the intensity of the biological pump and to tease out the main controls on productivity variations through time. However, high-resolution paleoproductivity records are still geographically too scattered to resolve the role of the tropical ocean in global carbon cycling and to understand

the linkage between productivity variability and orbital forcing. Paleoproductivity reconstructions based on different methodologies and proxies can also yield contradictory results. Low-latitude records from the Atlantic and Pacific Oceans show that productivity rose during glacials (e.g Farrell et al., 2000; Herguera & Berger, 1991; Paytan et al., 1996; Pedersen et al., 1991; Sarnthein et al., 1987), whereas some data argue for higher biogenic fluxes during terminations (Loubere et al., 2004; Pichevin et al., 2009). The $\delta^{13}\text{C}$ of benthic foraminiferal calcite is a well-established carbon cycle and ocean circulation proxy (e.g Mackensen & Schmiedl, 2019), since carbon-13 to carbon-12 ratios (i.e., $\delta^{13}\text{C}$) can chemically fingerprint different carbon reservoirs and many studies assume that $\delta^{13}\text{C}$ of foraminiferal calcite ($\delta^{13}\text{C}_{\text{foram}}$) records the dissolved inorganic carbon $\delta^{13}\text{C}$ value ($\delta^{13}\text{C}_{\text{DIC}}$) of the water mass, in which the foraminifera grow (e.g. Duplessy et al., 1988; Gebbie et al., 2015; Gottschalk et al., 2016; Schmittner et al., 2017; Woodruff & Savin, 1985). The vertical $\delta^{13}\text{C}$ gradient between the surface (high $\delta^{13}\text{C}$) and deep ocean (low $\delta^{13}\text{C}$) primarily results from the remineralization of low $\delta^{13}\text{C}$ particular organic carbon in the deep ocean, which temporarily sequesters carbon from the atmosphere. Conversely, vertical mixing of the ocean will tend to ventilate deep ocean carbon to the surface ocean and atmosphere while simultaneously decreasing the vertical $\delta^{13}\text{C}$ gradient. Therefore, the vertical $\delta^{13}\text{C}$ gradient likely records changes in deep ocean carbon storage, which is an important factor controlling glacial – interglacial changes in atmospheric CO_2 (e.g Eggleston et al., 2016; Schmitt et al., 2012).

Changes in paleoproductivity within and at the southwestern margin of the Indo-Pacific Warm Pool (IPWP) in the eastern equatorial Indian Ocean and their impact on the global carbon cycle over the last glacial cycles remain still largely unexplored and little understood. This is partly due to the complex forcing factors and current systems that influence the oceanographic conditions in this area, which are ultimately related to the transfer of water masses from the Western Pacific to the Eastern Indian Ocean through the “Maritime Continent” of the

Indonesian Archipelago via the Indonesian Throughflow (ITF). The ITF is the only conduit of warm seawater from the Pacific Ocean, through the Indonesian Seas, and into the Indian Ocean at low latitudes. The ITF flow sets up the large-scale pressure gradients that drive the Holloway Current (D'Adamo et al., 2009) and the anomalous poleward-flowing Leeuwin Current in the southeast Indian Ocean (Domingues et al., 2007; Schott & McCreary, 2001). Today, the Leeuwin Current is initiated through a build-up of sea-level by monsoonal winds during December-February in the Gulf of Carpentaria (Ridgway & Godfrey, 2015) and propagates further southwest along the continental shelf of Western Australia as a warm, fresh and oligotrophic current compared to adjacent surface water masses (Weller et al., 2011). During the summer months, the Leeuwin Current mixes with cooler and saltier water from the West Australian Current, which is located further offshore and flowing northward. Compared to other eastern boundary currents, the Leeuwin Current is relatively shallow (< 300 m) and narrow (< 100 km wide) (Schott and McCreary, 2001), while it has the largest eddy kinetic energy among all mid-latitude eastern boundary current systems (Feng et al., 2005). The Leeuwin Current extends eastwards toward the coast, suppressing the large-scale upwelling and manifesting as downward sloping isopycnals along the coast (Feng & Meyers, 2003; Hanson et al., 2005a, 2005b; Smith et al., 1991). As a result, dissolved nutrient levels in the coastal waters are generally low (Johannes et al., 1994) and pelagic primary productivity in southwestern Australia is lower than along the western margins of the other southern hemisphere continents (Pearce & Griffiths, 1991). The Holloway Current, which is the one of the sources of the Leeuwin Current, is an alongshore, southwestward flow off the northwestern coast of Australia (Brink et al., 2007; Cresswell et al., 1993; Holloway and Nye, 1985). The maximum transport of the Holloway Current occurs during late austral autumn (May–June) (Feng & Meyers, 2003). Its interannual variability is also related to ENSO Pacific signals that

propagate poleward along the northwestern and western Australian coast as coastally trapped waves (Clarke & Liu, 1994; Maxime & Ming, 2019; Wijffels & Meyers, 2004).

A further important factor controlling productivity and carbon flux off northwestern Australia is the Australian Monsoon system, which drives changes in wind intensity and direction as well as precipitation and runoff, which have impact on sea surface salinity, stratification and nutrient fluxes. During December–February, NW winds predominate and rainfall increases over Indonesia and northern Australia (Australian summer monsoon), whereas dry SE Trade Winds prevail during austral winter (June–November). In recent years, chlorophyll alpha concentration (1997 – 2010) has shown marked seasonal variations along the Northwestern Australian Margin with concentrations substantially higher in austral winter than in summer (Figure 2A). However, concentrations are also generally higher at the more southerly locations south of the Northwest Cape, the position at and south of the location of our core SO257-18571. Wind speeds (1949 – 2020) also exhibited different trends at the two core locations (Figure 2B). At the southern site, monthly wind speeds decreased significantly during austral winter, whereas at the northern location, located northeast of the Cape and within the main pathway of the Australian monsoons monthly wind speeds increased substantially during the Australian winter (Figures 1 and 2).

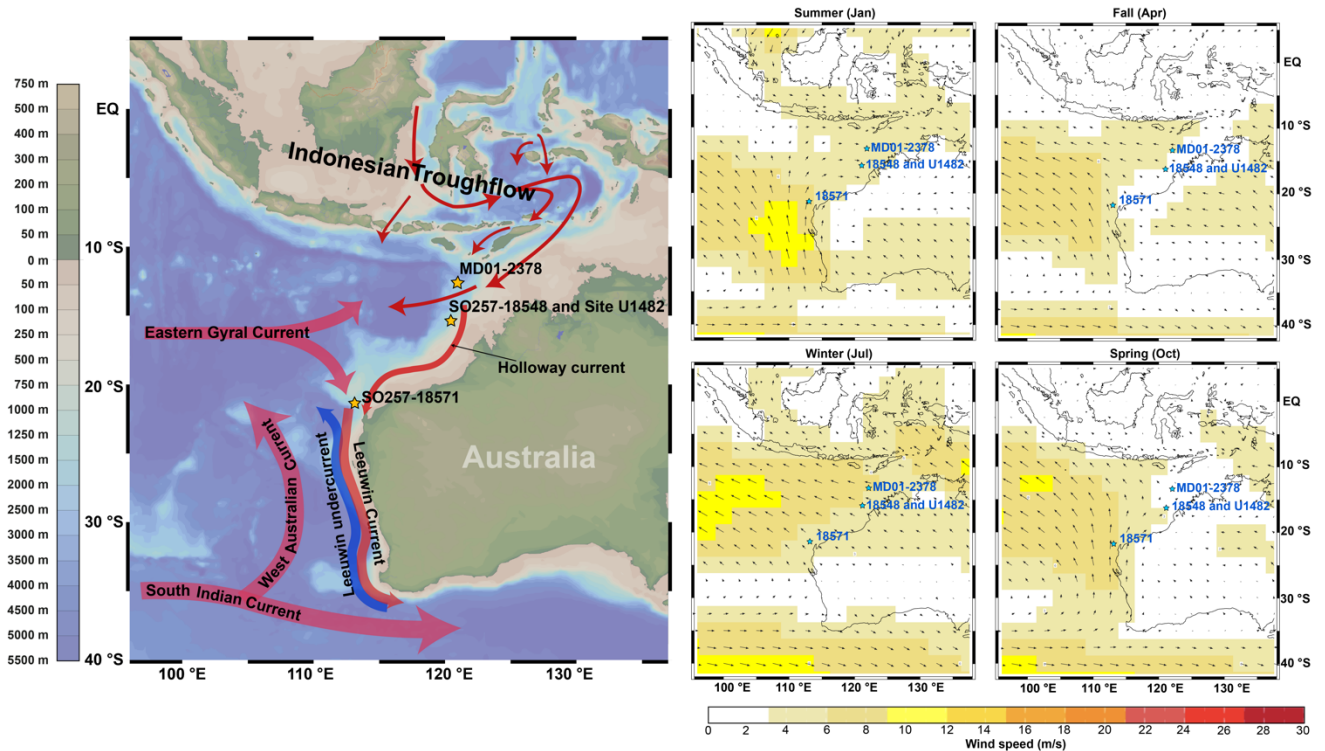


Figure 1. Oceanographic and climatology setting and core locations along the Northwestern Australian Margin. (Left) Major ocean circulation pathways. Red thick arrows: Indonesian Throughflow (Gordon et al., 2012), red and blue thick arrows: Leeuwin Current, Eastern Gyral Current (Domingues et al., 2007). (Right) Seasonal average wind climatology vector from 1981-2010 climatological (<https://iridl.ldeo.columbia.edu>).

In this chapter, we present multiproxy records of productivity from two sediment cores retrieved at the western edge of the IPWP), and within the dust-cyclone belt offshore Northwest Cape to track changes in intermediate water ventilation and paleoproductivity over the last 450 kyr (Figure 1). Both cores are located downstream of the main outflow of the ITF through the Timor Strait and are well suited for investigating variations in tropical productivity that may be related to thermohaline circulation changes and tropical climate dynamics. Our main objectives are (1) to determine the geochemical proxies for reconstruction of paleoproductivity, (2) to investigate changes in the productivity driven particle flux to the deep ocean in relation to orbital forcing, (3) to assess linkages of paleoproductivity and carbon flux variations to Austral Summer monsoon precipitation and winter monsoon (4), to investigate the connections between the benthic $\delta^{13}\text{C}$ and glacial-interglacial global carbon cycle changes.

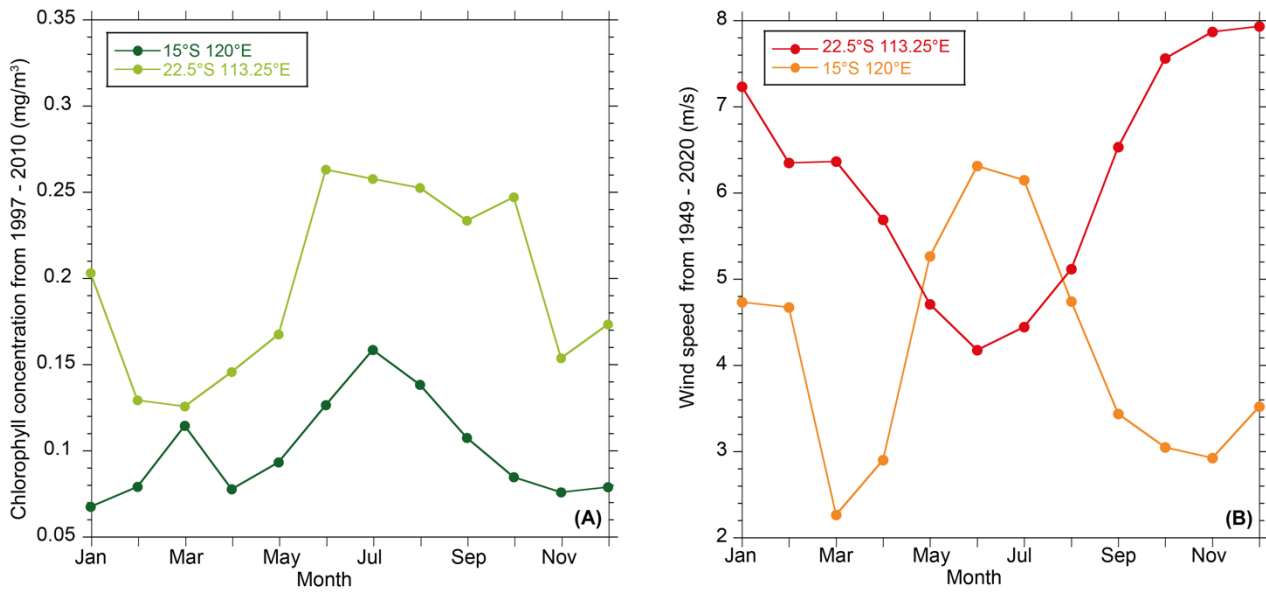


Figure 2. Monthly chlorophyll α concentration and wind speed at 15°S, 120° E (near SO257-18548, Dark green and orange) and at 22.5°S and 113.25°E (near SO257-18571, light green and red). (A) chlorophyll α concentration from MODIS and SeaWifs (<http://oceancolor.gsfc.nasa.gov/>) between 1997 and 2010; (B) wind speed from (<http://iridl.ldeo.columbia.edu/>) between 1949 and 2020.

2. Material and methods

2.1. Core locations

Piston Core SO257-18548 (15°3.591'S / 120°18.846'E, 1608.2 m water depth, 11.2 m core length) and IODP Expedition 363 Site U1482 (15°3.32'S / 120°26.10'E, 1466 m water depth) are located close to the modern southern limit of the seasonal (austral summer) displacement of the Intertropical Convergence Zone (ITCZ) and in proximity to the oceanographic front separating warm, oligotrophic tropical waters from cool, nutrient-rich subtropical waters (Holbourn et al., 2005; Rosenthal et al., 2018). Gravity Core SO257-18571 (22° 6,666'S/ 113° 29,688'N, 1052 m water depth, 20.1 m core length) was retrieved in the southern part of the Exmouth Plateau, offshore the North West Cape Peninsula. This core which is located within the “dust-cyclone” climate belt, is only marginally affected by the austral summer monsoon rain belt (Pei et al., 2021). Surface waters at this location are seasonally influenced by the Leeuwin Current.

New results from these two cores were integrated with published data sets (Pei et al., 2021; Pei et al., in revision) and with records from Core MD01-2378 (Holbourn et al., 2005, 2011; Zhang et al., 2020). Core MD01-2378 (13°04.95'S, 121°47.27'E, 1783 m water depth 1783 m, total core length of ~40 m) was retrieved at the northwestern margin of the Scott Plateau in the Timor Sea during the International Marine Global Change Study by RV Marion-Dufresne in 2001 (Bassinot et al., 2002). Core MD01-2378 is located ~142 nmi northeast of Core SO257-18548 within the hydrographic front between warm, tropical water from the IPWP and subtropical water masses (Holbourn et al., 2011; Rosenthal et al., 2018).

2.2. Sampling and processing

The working halves of Cores SO257-18548 and -18571 and MD01-2378 were initially sampled at 10 cm intervals (1 cm-thick half slices of 11 cm diameter core), additional samples were taken over Termination I (6 samples from Core SO257-18548 between 94.5 and 204.5 cm core depth) and Termination II (10 samples from Core SO257-18548 between 456.5 and 576.5 cm core depth) to refine the age model. Four holes were cored at Site U1482 during IODP Expedition 363 (Rosenthal et al., 2017, 2018). The working halves from the composite sediment succession (shipboard splice) between 24.76 and 30.22 meters composite depth (mcd) were sampled at 20 cm intervals (2 cm-thick half slices of ~7 cm diameter core). The sediment succession from Core SO257-18548 and nearby Site U1482 were combined, based on correlation of the high resolution XRF scanner elemental records (Pei et al., 2021). The tie point between these records, corresponding to an age of ~324 ka, is located at 10.84 m in Core SO257-18548 and at 24.97 mcd in Site U1482.

All samples were oven dried at 40°C and weighed prior to washing over a 63 µm sieve. Residues were oven dried at 40°C on filter paper, then weighed and sieved into the fractions >315, 315-250, 250-150 and 150-63 µm.

2.3. Chronology

The age models of Cores SO257-18548 and -18571 over the last glacial termination and Holocene are based on ^{14}C accelerator mass spectrometry (AMS) dates obtained from *Globigerinoides ruber* (white) $>250\ \mu\text{m}$. The age model prior to 21 ka was generated by correlating the benthic foraminiferal $\delta^{18}\text{O}$ to the benthic isotope stack LR04 (Lisiecki & Raymo, 2005). Details of the ^{14}C and oxygen isotope stratigraphy of Cores SO257-18548, SO257-18571 and Site U1482 between 24.76 and 30.22 mcd are provided in Pei et al. (2021).

The age model of core MD01-2378 for the last 30 kyr is based on 20 AMS ^{14}C and on correlation of the benthic foraminifer $\delta^{18}\text{O}$ record to the benthic isotope stack LR04 (Holbourn et al., 2005a; Lisiecki & Raymo, 2005; Zhang et al., 2020).

2.4. Stable isotopes

We selected ~12 specimens per sample of the planktonic foraminifer *G. ruber* (white) (size fraction 250-315 μm) and 3-6 well preserved specimens per sample of the benthic foraminifer *Cibicidoides wuellerstofi* for stable isotope analysis. *Cibicidoides wuellerstofi* is an epifaunal species, which is considered as a reliable recorder of bottom water DIC and was used in numerous studies to reconstruct past changes in deep and intermediate water circulation (e.g Bickert & Wefer, 1999; Duplessy et al., 1988; Mackensen et al., 1994).

After crushing, samples were cleaned with ethanol ($\geq 99.7\%$) for 2-3 seconds in an ultrasonic bath, decanted and dried at 40 °C prior to analysis with a Thermo Finnigan MAT 253 mass spectrometer at the Leibniz Laboratory for Radiometric Dating and Isotope Research, Kiel University, Kiel. The mass spectrometer is coupled to a *Kiel-Carbo IV* device for automated CO_2 preparation from carbonate samples. Sample reaction was induced by individual acid addition (99 % H_3PO_4 at 75 °C) under vacuum. The evolved carbon dioxide was analysed eight times for each individual sample. As documented by the performance of international [NBS19: +1.95 ‰ VPDB (^{13}C); IAEA-603: +2.46 ‰ VPDB (^{13}C)] and

laboratory-internal carbonate standards [Hela1: +0.91 ‰ VPDB (^{13}C); HB1: -12.10 ‰ VPDB (^{13}C); SHK: +1.74 ‰ VPDB (^{13}C)], analytical precision of stable isotope analysis is better than ± 0.05 ‰ for $\delta^{13}\text{C}$. Values are calibrated relative to Vienna Pee Dee Belemnite (VPDB) scale.

2.4. XRF scanner derived elemental composition

Bulk-chemical composition of the sediment cores was measured on the archive halves at 1 cm intervals using a 2nd generation Avaatech XRF core scanner at the Institute of Geosciences, Kiel University. Measurements were used generator settings of 10, 30 and 50 kV tube volt- ages and for 15 s with 200 μA without filter for the 10 kV runs and for 10 s with 1000 μA using a Pb and Cu-filter for the 30 and 50 kV runs, respectively. The spectra were transferred into elemental area counts using the software bAxil Batch by Brightspec NV and are reported as area counts per second.

We used the elements barium (Ba) which is enriched in Holocene and Plio-Pleistocene sediments beneath the equatorial upwelling, iodine (I) and bromine (Br), which are influenced by the proportion of the organic fraction in marine sediments and by diagenetic reactions involving organic matter degradation as proxies of organic matter accumulation (Calvert & Pedersen, 2007; Harvey, 1980; Seki et al., 2019; Ziegler et al., 2008).

2.5. Spectral Analysis

We used the REDFIT function with a Blackman-Harris window in the Past3 software to perform spectral analysis (Hammer et al., 2001). Significance lines of 95%, 89%, and 85% confidence intervals (CIs) are based on parametric approximation (chi-square test). Cross spectral analysis of our planktonic and benthic $\delta^{13}\text{C}$, $\delta^{13}\text{C}$ difference between planktonic and benthic foraminifers ($\Delta\delta^{13}\text{C}_{\text{PF-BF}}$), and XRF elemental records against precession and obliquity

was performed with AnalySeries 2.0.8 on linear detrended data on a common 1 kyr-spaced scale with the Blackman-Tukey spectral method using a Bartlett window.

3. Results

3.1. Carbon Isotopes of Benthic and Planktonic Foraminifers

In Cores SO257-18571 and SO257-18548 and Site U1482, the benthic (based on *Cibicidoides wuellerstorfi*) and planktonic foraminifer $\delta^{13}\text{C}$ (based on *Globigerinoides ruber*) profiles are characterized by glacial-interglacial variations in $\delta^{13}\text{C}$ values (Figure 3). An overall increasing trend in glacial $\delta^{13}\text{C}$ values is evident, especially during MIS 6 to MIS 5, when the $\delta^{13}\text{C}$ values exhibit a stepwise increase. Glacial intervals from MIS 12 to MIS 6 typically display comparable benthic values between 0 and 0.2‰ in both cores. However, more recent glacials (MIS 2 and 4) exhibit significantly higher benthic $\delta^{13}\text{C}$ values from 0.3 to 0.5 ‰ in Core SO257-18571, whereas benthic $\delta^{13}\text{C}$ values vary from 0.1 to 0.3 ‰ during MIS 2 and 4 in Core SO257-18548. Interglacials are characterized by benthic $\delta^{13}\text{C}$ values between 0.4 and 0.8‰ in both cores. Maximum benthic $\delta^{13}\text{C}$ values occurred during MIS 11, MIS7, MIS 5a and MIS 1. The glacial-interglacial gradient in benthic $\delta^{13}\text{C}$ is 0.4 - 0.6 ‰ in Core SO257-18548 and Site U1482, which is slight lower than the glacial-interglacial gradient in Core SO257-18571 (0.4 – 0.8 ‰).

Planktonic $\delta^{13}\text{C}$ in Core SO257-18571 exhibit lower values than planktonic $\delta^{13}\text{C}$ in Core SO257-18548 and Site U1482 (Figure 3). Glacial intervals in Core SO257-18548 and Site U1482 are characterized by planktonic values between 0.8 and 1.4 ‰, whereas values in Core SO257-18571 during glacial stages are between 0.4 and 0.8 ‰. During Terminations II and I, planktonic $\delta^{13}\text{C}$ increases steadily, reaching 1.6 ‰ in Core SO257-18548 and Site U1482 and 1.2 ‰ in Core SO257-18571. Both records are characterized by high-frequency fluctuations which are stronger than the glacial-interglacial cyclicity. The low values of planktonic $\delta^{13}\text{C}$ in

Core SO257-18571 indicate the presence of nutrient-rich water masses near the sea surface, which originate from upwelling of southern sourced intermediate water masses during intervals of a weakened Leeuwin Current and reduced advection of warm oligotrophic surface water masses from the IPWP. A less pronounced glacial interglacial contrast and generally higher $\delta^{13}\text{C}$ at Site SO257-18548 and U1482 indicate that IPWP water masses remained influential in this area during glacials.

3.2. Vertical $\delta^{13}\text{C}$ gradient

The $\Delta\delta^{13}\text{C}_{\text{PF-BF}}$ ($\delta^{13}\text{C}$ difference between planktonic and benthic foraminifers) is remarkably lower in the southern Core SO257-18571. Higher $\Delta\delta^{13}\text{C}_{\text{PF-BF}}$ values ($>1\%$ in Core SO257-18548 and Site U1482; $>0.3\%$ in Core SO257-18571) occur in glacial intervals, whereas lower $\Delta\delta^{13}\text{C}_{\text{PF-BF}}$ values coincide with warm peaks during the Holocene, MIS 5a and 5e, 7, 9, and 11. The $\Delta\delta^{13}\text{C}_{\text{PF-BF}}$ record from SO257-18571 is also characterized by high-frequency fluctuations that are superimposed over the low-frequency glacial-interglacial periodicity. In contrast, the records from Core SO257-18548 and Site U1482 still show a marked glacial-interglacial periodicity (Figure 3).

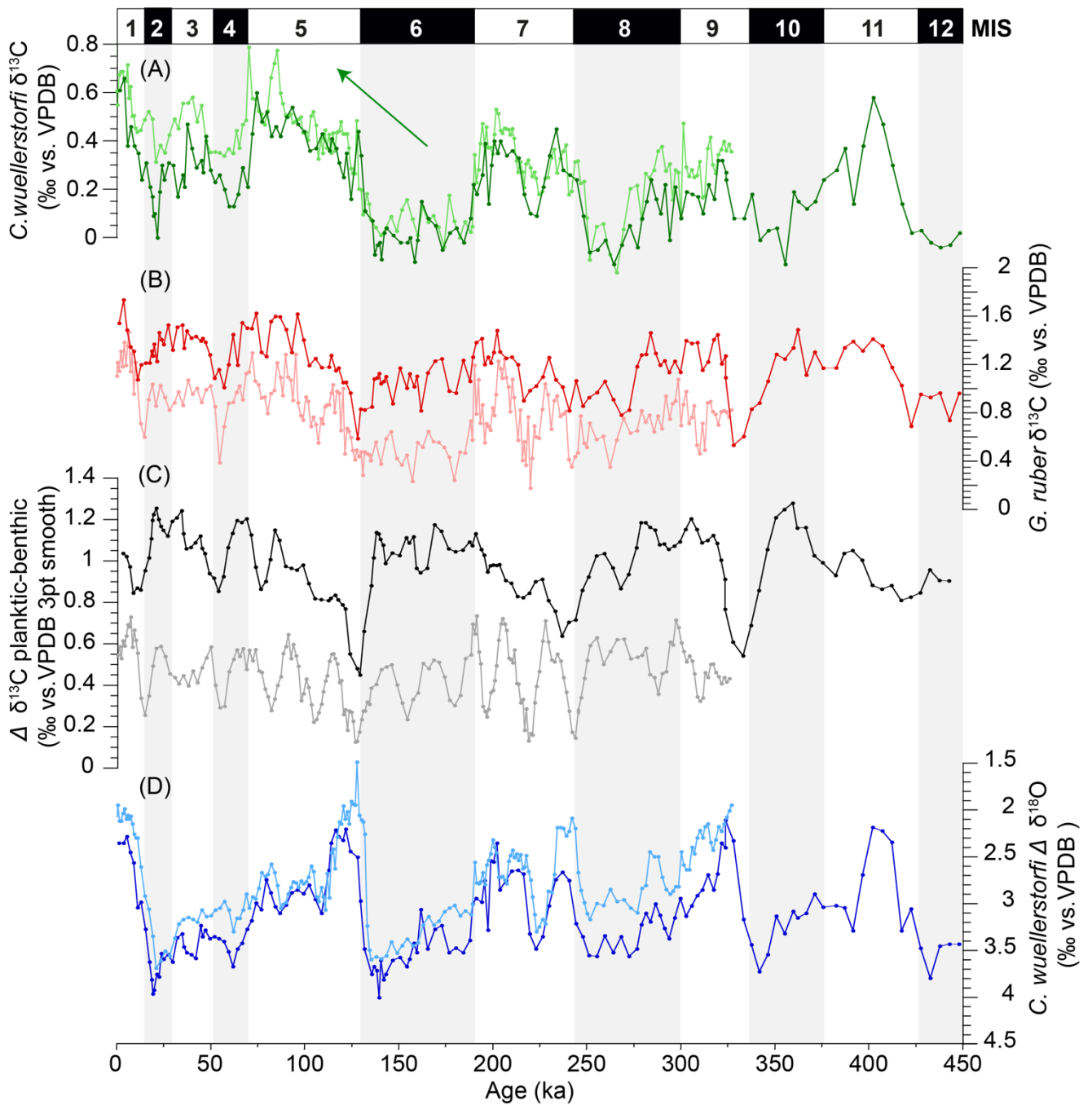


Figure 3. Benthic and planktonic foraminiferal $\delta^{13}\text{C}$ records. (A) Benthic $\delta^{13}\text{C}$ from Core SO257-18548 and Site U1482 (dark green) and from Core SO257-18571 (light green); (B) Planktonic $\delta^{13}\text{C}$ from Core SO257-18548 and Site U1482 (red) and from Core SO257-18571 (pink); (C) $\Delta\delta^{13}\text{C}_{\text{PF-BF}}$ from Core SO257-18548 and Site U1482 (black) and from Core SO257-18571 (grey); (D) Benthic $\delta^{18}\text{O}$ from Core SO257-18548 and Site U1482 (dark blue) and from Core SO257-18571 (light blue).

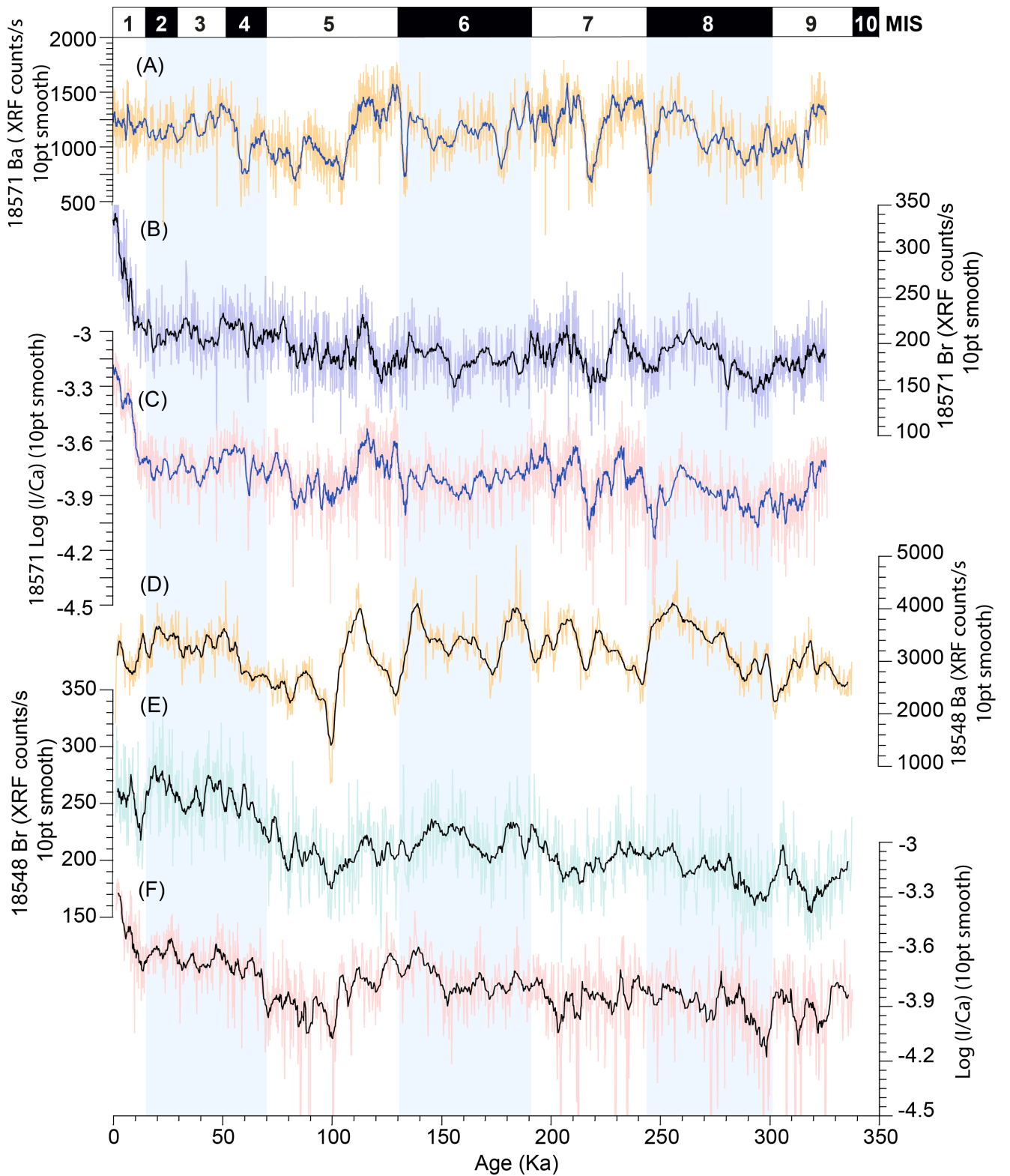


Figure 4. XRF elemental counts and Log ratios in Cores SO257-18571 and SO257-18548. (A-C) Ba (orange); Br (purple) and Log (I/Ca) (pink) from SO257-18571; (D-F) Ba (orange); Br (blue) and Log (I/Ca) (pink) from SO257-18548.

3.3. Barium and halogens (iodine and bromine) as indicators of organic matter flux

We normalized halogens against calcium (Ca), derived from the biogenic carbonate of marine plankton and the results are reported in logarithms of elemental ratios to minimize the risk of measurement artefacts from mutable signal intensities and matrix (Weltje & Tjallingii, 2008).

The Ba, Br and Log (I/Ca) values in Core SO257-18571 is characterized by parallel high-frequency fluctuations. At the end of Termination II (~130 ka), Terminations IIIa and b (~220 and ~ 240 ka), all organic proxies show the abrupt increase. During the last termination Log (I/Ca) and Br exhibits the continuous increase, whereas the Ba values show more consistent trends during recent 50 ka (Figure 4).

In Core SO257-18548, Br and Log (I/Ca) values show similar rhythmic variations with lower frequency fluctuations, while the Ba record exhibits high-frequency oscillations (~20 ka). Br and Log (I/Ca) show a higher level during the glacials and reach the lowest level during end of MIS5. The Log (Br/Ca) and Ba present a consistent high amplitude during 100 – 350 ka and a low variable amplitude during MIS 2 - 4. The Log (I/Ca) and Br present smaller amplitude and higher variability (noise) than the Ba (Figure 4).

3.4. Time series analysis of paleoproductivity proxy records

In Core SO257-18548 and Site U1482, spectral analysis of the variance in the paleoproductivity proxy records reveals spectral power concentrated in the eccentricity period (100ka/125ka) for all proxies except for Ba. In contrast, planktonic $\delta^{13}\text{C}$ and Ba only show power concentrated in the eccentricity period in Core SO257-18571. The 23 kyr precession period is strongly expressed in all proxies in Core SO257-18571 (95% level), but is only significant for Ba in Core SO257-18548 and at Site U1482. At the 41 kyr obliquity period,

spectral peaks are only significant in the Log (I/Ca) and Ba in Core SO257-18571 (95% level) (Figure 5).

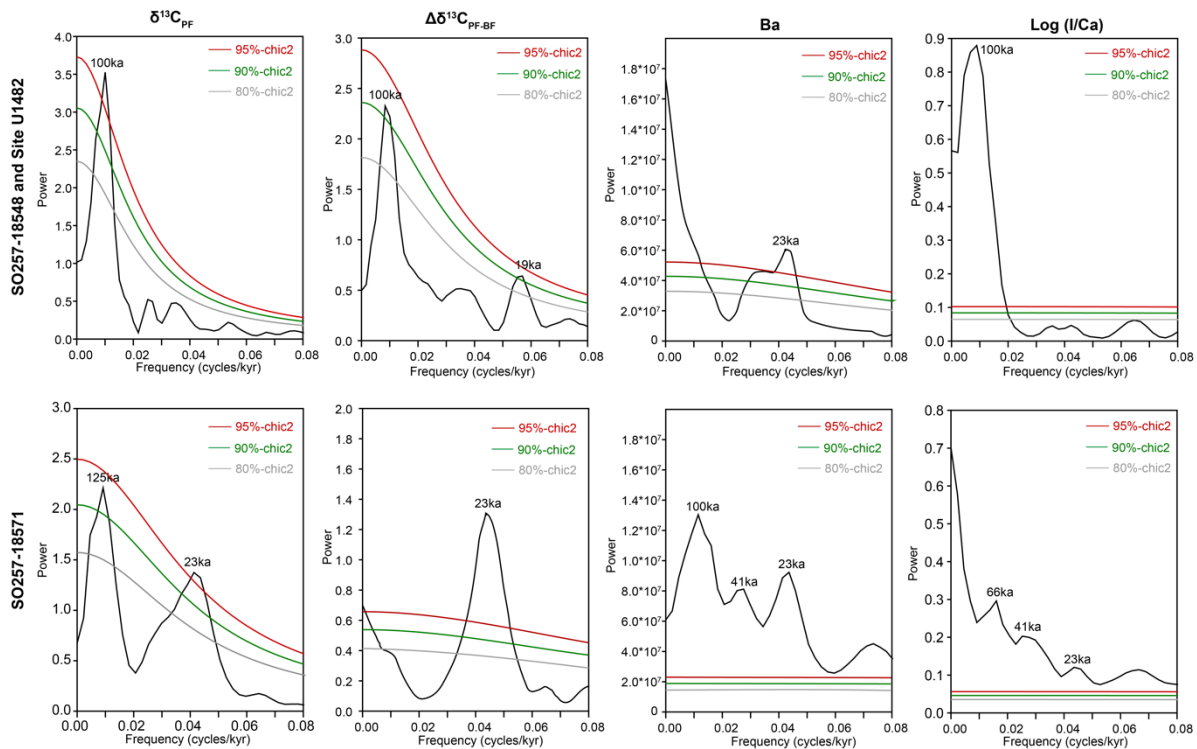


Figure 5. Spectral analysis of paleoproductivity proxies in Core SO257-18548, Site U1482 and Core SO257-18571 computed with a REDFIT function in Past3. Red, green and grey curves indicate confidence intervals (CIs) of 95%, 89%, and 85%, respectively.

4. Discussion

4.1. Evaluation of paleoproductivity proxies

Proxy indicators of paleoproductivity and their relationship to primary productivity, organic flux and bottom water oxygenation are still poorly understood. To overcome the limitations and biases of using a single paleoproductivity proxies, we applied three XRF-scanner derived elemental proxies (Ba area counts, Log(I/Ca) and log (Br/Ca)) and the $\delta^{13}\text{C}$ gradient between the surface dwelling planktonic foraminifer *G. ruber* and the epifaunal foraminifer *C. wuellerstorfi* to evaluate fluctuations in primary production over the last 450 kyr.

The concentration of Ba is related to the accumulation of organic matter and/or the precipitation of barite by marine bacteria, which has a high potential as paleoproductivity indicator deposited in sedimentary oxic and suboxic environments at deep water depositional sites (Von Breymann et al., 1992; Calvert & Pedersen, 2007). Biogenic Ba is enriched in Holocene equatorial sediments and Plio-Pleistocene sediments beneath the equatorial upwelling zone of the Indian Ocean (Calvert & Pedersen, 2007; Schmitz, 1987). Core-top samples from various ocean basins show that Ba accumulation rates are highly correlated to surface ocean primary production (^{14}C and Chlorophyll α), which supports that Ba can be used to reconstruct paleo-carbon export on a global scale (Eagle et al., 2003). In both our records, the Ba counts show a noticeable 23 kyr precessional peak, especially in Core SO257-18548 the Ba records exhibit the most prominent 23 kyr peak of all productivity proxies (clearly above the 95% Chi 2 significance level in Figure 5), which suggests that they provide a sensitive record of productivity fluctuations, largely unbiased by changes in deep water masses that may have operated on a 100 kyr glacial-interglacial scale. However, it is noteworthy that in the southern site, the Ba records exhibit parallel high abundances with the terrigenous input records ($\text{Log}(\text{Terr}/\text{Ca})$) at $\sim 110 - 130$ ka and $\sim 230 - 240$ ka, when the Australian summer monsoon intensified. It might be explained by the fact that Ba may be at this location additionally delivered as riverine discharge from terrestrial sources to ocean (Figure 6).

Iodine and bromine are two of the major elements in seawater and their concentrations in bulk sediments were previously used as indicators of marine productivity, organic matter flux and oxygenation at the seafloor (Elderfield & Truesdale, 1980; Tian et al., 1996; Zhou et al., 2017). The thermodynamically stable state of iodine exists in seawater are iodide (I^-) and iodate (IO_3^-) (Wong & Brewer, 1977). Several studies demonstrated that iodine in carbonates (I/Ca) can be used to monitor seawater oxidation levels in highly dynamic spatial and temporal patterns throughout the Earth's history (e.g., Lu et al., 2010; Zhou et al., 2017). Bromine occurs

in marine water as the bromide (Br^-) ion. Ziegler et al. (2008) established a method using sediments from the Arabian Sea and a Mediterranean brine basin to estimate the TOC content from Br concentration measured by XRF. Seki et al. (2019) provided a high-resolution Quaternary record of marine sediment in the Japan Sea, which shows that the Br counts from XRF are highly correlated with marine organic carbon content. This indicates that XRF-derived Br counts provide a useful tool to reconstruct the organic carbon content. Comparison of discrete sample TOC measurements from Core MD01-2378 (Holbourn et al., 2005) with high-resolution XRF Br counts/s in Core SO257-18548 shows that the two parameters covary in both cores (Figure 7). Maxima in organic carbon are consistently reproduced in the bromine data series. However, in the intervals $\sim 125 - 145$ ka and $\sim 240 - 260$ ka close to Terminations II and III, the amplitude of individual bromine peaks is lower than predicted by the corresponding TOC peaks. This may be explained by a higher contribution of terrestrial organic carbon from river discharge to the TOC during these intervals, while the Br record is linked to the marine organic carbon only.

The $\delta^{13}\text{C}$ gradient between foraminiferal $\delta^{13}\text{C}$ from nutrient depleted surface waters and deeper water foraminiferal $\delta^{13}\text{C}$ has been successfully used to reconstruct glacial/interglacial and precessional changes in export-production related organic carbon flux to the seafloor at a more northerly site within the IPWP (e.g., Holbourn et al., 2005). This proxy is based on the principle that with increased productivity more ^{12}C -enriched organic carbon sinks from the surface to the deep ocean, increasing $\delta^{13}\text{C}$ of near-surface dissolved inorganic carbon (DIC) and decreasing benthic $\delta^{13}\text{C}$ at the seafloor. However, this simple relationship holds only in stratified oceans with nutrient depleted surface water masses, where upwelling and lateral mixing play no significant role. In contrast, in areas of significant mixing, for instance through seasonal upwelling or formation of eddies, low planktonic $\delta^{13}\text{C}$ reflects the lower $\delta^{13}\text{C}$ of DIC in nutrient-rich water masses near the surface. Such conditions prevail along the Northwestern

Australian Margin, which is not influenced by the IPWP, since seasonal upwelling and intense mixing occurs between nutrient rich coastal currents, the Leeuwin Current and the offshore West Australian Current. As a result, planktonic $\delta^{13}\text{C}$ and $\Delta \delta^{13}\text{C}$ can be used to monitor the temporal variability of the southwestern front between the oligotrophic IPWP surface water masses and their transition to nutrient enriched surface water masses along the Northwestern Australian Margin.

4.2. Linkages of paleoproductivity and carbon flux variations to Australian winter monsoon upper ocean mixing

Today, the seasonal maximum in primary production and carbon flux at Site SO257-18548 and IODP Site 1482 offshore northwestern Australia occurs in the later part of the austral winter season (July-August), when intense southeasterly winds result in upper ocean mixing and upwelling of nutrient-rich intermediate waters into the photic zone (Antoine et al., 2020). Spectral analysis reveals that the all paleoproductivity records from Core SO257-18571 and the Ba counts in Core SO257-18548 exhibit strong power at the precessional band. In Core SO257-18548 and Site U1482, the Ba records and $\delta^{13}\text{C}_{\text{PF-BF}}$ exhibit the high coherency (0.92 and 0.66) with the 21st September insolation at 20° with an antiphase relationship. In Core SO257-18571, the productivity index based on the gradient between foraminiferal $\delta^{13}\text{C}$ and is both highly coherent and exhibit an antiphase relationship with 21st September insolation at 20° (coherency: 0.90) (Supplement Figure 3A-C). The Australian summer monsoon occurs during maxima in Southern Hemisphere spring (September) insolation (in phase relationship, coherency >0.9) (Pei et al, 2021). At the precession band, the temporal variability of productivity and carbon flux indicators driven by the precessional insolation is in antiphase to the local monsoonal precipitation and discharge on the sedimentation along the Northwestern Australian Margin.

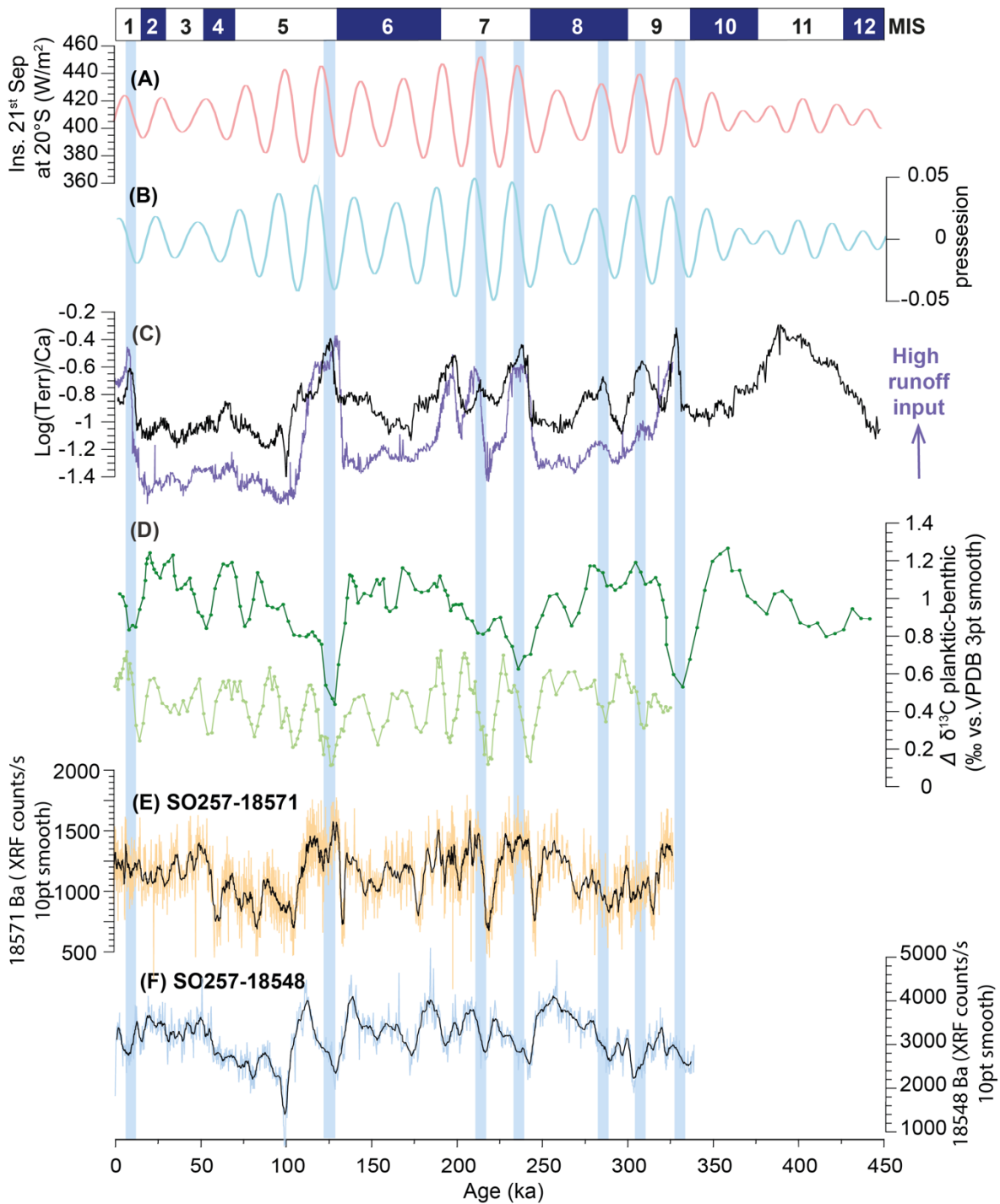


Figure 6. Comparison of productivity proxies from Cores SO257-18571, SO257-18548 and Site U1482 to orbital forcing mechanisms. (A) 21st June insolation at 25°S; (B) Precession parameter; (C) XRF-scanner derived Log(Terr/Ca) from Core SO257-18571 (purple), Core SO257-18548 and Site U1482 (black) from Pei et al. (2021). (D) $\Delta\delta^{13}\text{C}_{\text{PF-BF}}$ from Core SO257-18548 and Site U1482 (dark green) and from Core SO257-18571 (light green). (E) XRF-scanner derived Ba counts (10pt smooth) from SO257-18571; (F) XRF-scanner derived Ba counts (10pt smooth) from SO257-18548. Blue shading indicates the high runoff input.

Several studies showed that ITCZ dynamics played a critical role in tropical continental hydrology, marine productivity and organic carbon burial (Armstrong et al., 2009; Beckmann et al., 2005; Floegel & Wagner, 2006; Loope et al., 2001). In eastern tropical Pacific region, the strengthening of monsoonal precipitation triggered by northward shift of the ITCZ mean position in the eastern tropical Pacific which are also characterized by relatively low bio-productivity during the middle and late Holocene (Pérez-Cruz, 2013). Sea-level induced glacial-interglacial changes in the amplitude of the latitudinal swing of the ITCZ may have contributed to the remarkable differences in productivity between glacial and interglacials along the north Northwestern Australian Margin. During glacial sea-level low stands, large exposures of land (Sundaland) in the center of the Indonesian archipelago may have locked the ITCZ closer to the equator, increased tropical convection and intensified trade winds. These glacial conditions resulted in intensified upwelling during the austral winter season, when the north Northwestern Australian Margin was under the influence of the dry SE monsoon (trades).

4.3. Paleoproductivity Fluctuations and Leeuwin Current Variability

A glacial-interglacial contrast in productivity, with precessional fluctuations, is shown by all productivity proxy records from Core SO257-18571 (Figure 5), which is probably related to oligotrophic Leeuwin Current. The salinity record in the southwestern Core SO257-18571 exhibits clear glacial-interglacial variability with glacial values between 0.4 and 0.8‰ during MIS 2-4 and MIS 6 (Supplement Figure 2). Glacial values during MIS 8 were even higher (between 0.8 and 1.2‰) and the continuously increasing of $\delta^{18}\text{O}_{\text{sw}}$ record during MIS 6 indicating a less expanded IPWP and weaker Leeuwin Current (Pei et al., in review). This glacial salinity variability coincides with the $\Delta\delta^{13}\text{C}_{\text{PF-BF}}$ productivity record, which displays higher values during MIS 8 (0.4 – 0.6 ‰) than during MIS 6 (0.3 – 0.5 ‰). By contrast, the $\Delta\delta^{13}\text{C}_{\text{PF-BF}}$ and Ba record in the northeastern location (Core SO257-18548 and

Site U1482) exhibits subdued glacial-interglacial variability and is characterized by lower frequency and higher amplitude fluctuations between maxima of $\sim 1.4\%$ and minima of $\sim 0.4\%$. The glacial-interglacial contrast is probably related to sea level-controlled changes in the flow of oligotrophic, warm, low-salinity surface water from the ITF (Supplement Figure 1), which moves along the northwestern Australian shelf (Holloway Current). At each termination, there is a strong correlation of the productivity decline with an increase in 25°S September insolation (precessional forcing) which matches the record of $\Delta\delta^{13}\text{C}_{\text{PF-BF}}$ in core MD01-2378 (Figure 7). We speculate that the sharp decline in productivity at terminations was triggered by the intensification of the Australian summer monsoon and a weakening of winter monsoon (trade wind) intensity associated with a decline in upper ocean mixing/upwelling in austral winter.

4.4. Benthic $\delta^{13}\text{C}$ and glacial-interglacial global carbon cycle changes

Global environmental differences between glacial and interglacial climate conditions including the size of the carbon storage in the terrestrial biosphere, the amount of carbon present as CO_2 in the atmosphere and carbon storage in the deep ocean, the largest carbon reservoir, are reflected in changes in the deep water benthic $\delta^{13}\text{C}$ signature. The difference between glacial and interglacial $\delta^{13}\text{C}$ in deep water foraminifers range between 0.3 and 0.7‰ with a mean global decrease during the last deglaciation of $0.38 \pm 0.08\%$ between 0.5 and 5km or $0.34 \pm 0.19\%$, taking into account uncertainties (Peterson et al., 2014). This $\delta^{13}\text{C}$ change can be almost completely explained by the transfer of $\delta^{13}\text{C}$ -depleted carbon ($\delta^{13}\text{C} = -25\%$) from terrestrial vegetation into the deep ocean reservoir (Peterson et al., 2014), which has been previously suggested as the main mechanism for the global glacial-interglacial deep water $\delta^{13}\text{C}$ variability (Shackleton, 1977). These estimates for the last deglaciation provide information about the magnitude of carbon shifts between terrestrial, atmospheric and deep

ocean carbon reservoirs and the timing of the carbon cycle responses to global warming during termination.

Our records of $\delta^{13}\text{C}$ changes during Terminations II, III and IV along a latitudinal and depth transect in the central Indian Ocean water mass, which is mainly sourced from the Southern Ocean (Cresswell & Peterson, 1993; Schott & McCreary, 2001), show that glacial water masses during MIS 6, 8 and 10 that are more depleted than during MIS 2-4. This may indicate the transfer and storage of carbon in the Southern Hemisphere deep-intermediate ocean during these glacials. An important change in deep water benthic $\delta^{13}\text{C}$ occurred at the end of MIS 6 during Termination II when $\delta^{13}\text{C}$ reached a maximum of ~ 0.6 ‰ and continued during MIS5 to a total change of ~ 0.8 ‰, almost doubling the change during Termination I. These local deviations may be explained by an active local biological pump during glacials (Core MD01-2378), but probably relate to different deep water mass properties at the southwesterly site. Given the importance of the Southern Hemisphere ocean as a reservoir for global carbon storage, these differences between the last and the previous glacial cycles are remarkable.

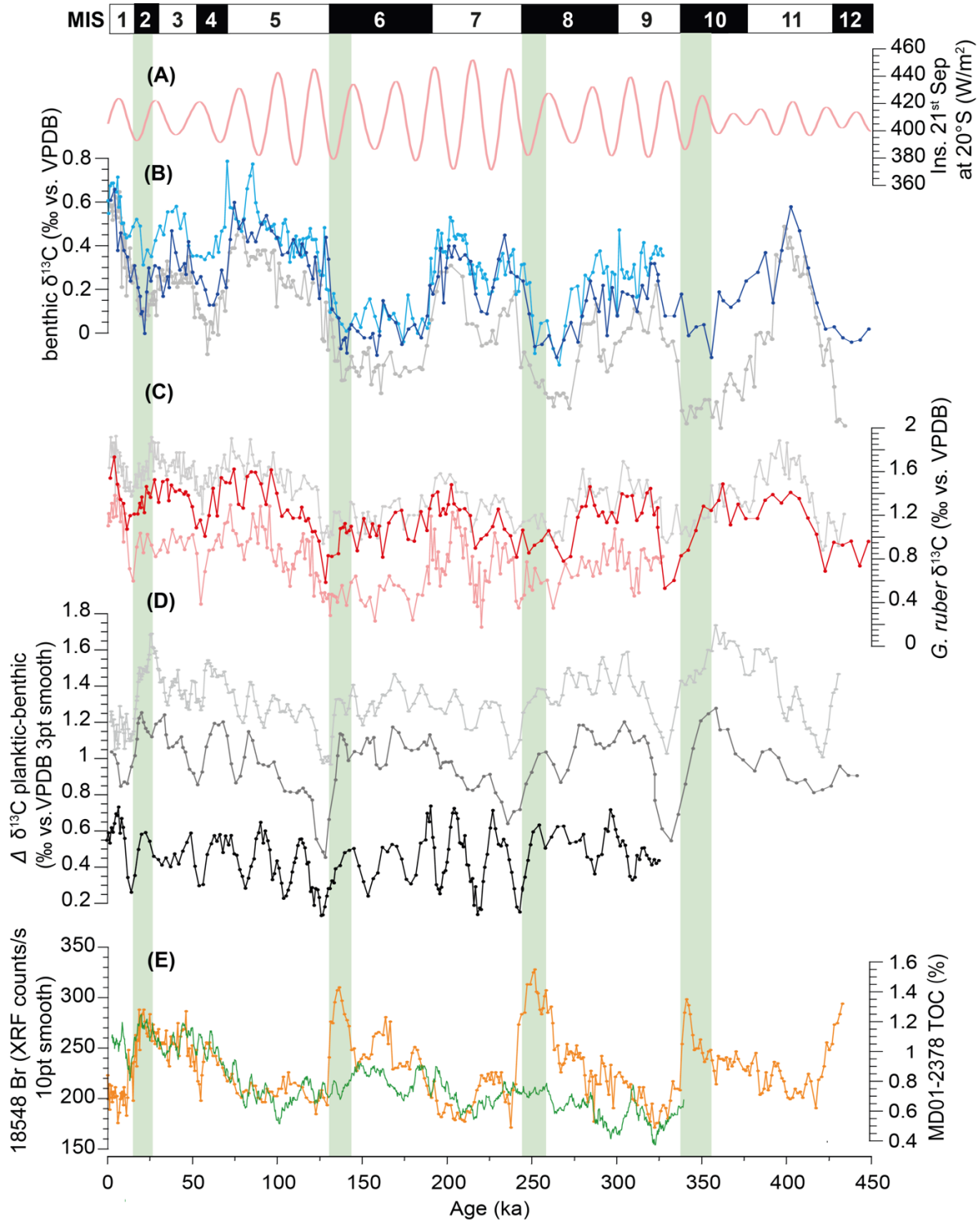


Figure 7. Comparison of productivity proxies and carbon isotopes records from Cores MD01-2378, SO257-18571, SO257-18548 and Site U1482. (A) Insolation 21st of September at 20°S; (B) Benthic foraminiferal $\delta^{13}\text{C}$ from Core SO257-18548 and Site U1482 (dark blue), Core SO257-18571 (light blue) and Core MD01-2378 (light grey); (C) Planktonic foraminiferal $\delta^{13}\text{C}$ from Core SO257-18548 and Site U1482 (red), Core SO257-18571 (pink) and Core MD01-2378 (light grey); (D) $\Delta\delta^{13}\text{C}_{\text{PF-BF}}$ from Core SO257-18548 and Site U1482 (grey), Core SO257-18571 (black) and Core MD01-2378 (light grey); (E) Br counts (10pt smooth) from Core SO257-18548 (green) and TOC from Core MD01-2378 (orange). The green shading indicates Terminations I, II, III and VI that coincide with high TOC from Core MD01-2378.

6. Conclusion

Cores SO257-18548 and Site U1482 from the Scott Plateau and SO257-18571 from the southern part of the Exmouth Plateau provide a continuous, undisturbed sediment archive to reconstruct productivity fluctuations within Holloway Current and Leeuwin Current at the western edge of the present-day IPWP over the past 450 kyr. Ba, I and Br records derived from XRF scanner-records indicate that paleoproductivity records along the northNorthwestern Australian Margin were anticorrelated to Australian summer monsoon intensity. The difference of monsoonal climate between two locations indicate that local wind-induced upper ocean mixing and upwelling are dominant in driving productivity. Our records of $\delta^{13}\text{C}$ changes during Terminations II, III and IV along a latitudinal and depth transect show that glacial water masses during MIS 6, 8 and 10 are more $\delta^{13}\text{C}$ depleted than during MIS 2-4 which may indicate intensified transfer and storage of atmospheric and terrestrial carbon in the Southern Hemisphere deep -intermediate ocean during glacial MIS 6, 8, and 10.

References

- Antoine, D., Mayot, N., & King, E. The seasons of phytoplankton around Australia (2020).
<https://doi.org/10.26198/5e16a91249e7c>
- Armstrong, H. A., Baldini, J., Challands, T. J., Gröcke, D. R., & Owen, A. W. (2009). Response of the Inter-tropical Convergence Zone to Southern Hemisphere cooling during Upper Ordovician glaciation. *Palaeogeography, Palaeoclimatology, Palaeoecology*, 284(3–4), 227–236.
<https://doi.org/10.1016/j.palaeo.2009.10.001>
- Bassinot, F., et al. (2002), Scientific report of the WEPAMA cruise, MD122/IMAGES VII, report, 453 pp., Inst. Fr. pour la Rech. et la Technol. Polaires, France.
- Beckmann, B., Flögel, S., Hofmann, P., Schulz, M., & Wagner, T. (2005). Orbital forcing of Cretaceous river discharge in tropical Africa and ocean response. *Nature*, 437(7056), 241–244.
<https://doi.org/10.1038/nature03976>
- Bickert, T., & Wefer, G. (1999). South Atlantic and benthic foraminifer $\delta^{13}\text{C}$ Deviations: Implications for reconstructing the late quaternary deep-water circulation. *Deep-Sea Research Part II: Topical Studies in Oceanography*, 46(1–2), 437–452. [https://doi.org/10.1016/S0967-0645\(98\)00098-8](https://doi.org/10.1016/S0967-0645(98)00098-8)

- Bock, M., Schmitt, J., Beck, J., Seth, B., Chappellaz, J., & Fischer, H. (2017). Glacial/interglacial wetland, biomass burning, and geologic methane emissions constrained by dual stable isotopic CH₄ ice core records. *Proceedings of the National Academy of Sciences of the United States of America*, 114(29), E5778–E5786. <https://doi.org/10.1073/pnas.1613883114>
- Von Breymann, M. T., Emeis, K. C., & Suess, E. (1992). Water depth and diagenetic constraints on the use of barium as a palaeoproductivity indicator. *Upwelling Systems: Evolution since the Early Miocene*, (64), 273–284.
- Brink, K. H., Bahr, F., & Shearman, R. K. (2007). Alongshore currents and mesoscale variability near the shelf edge off northwestern Australia. *Journal of Geophysical Research: Oceans*, 112(5), 1–19. <https://doi.org/10.1029/2006JC003725>
- Calvert, S. E., & Pedersen, T. F. (2007). Chapter Fourteen Elemental Proxies for Palaeoclimatic and Palaeoceanographic Variability in Marine Sediments: Interpretation and Application. *Developments in Marine Geology*, 1(07), 567–644. [https://doi.org/10.1016/S1572-5480\(07\)01019-6](https://doi.org/10.1016/S1572-5480(07)01019-6)
- Clarke, A. J., & Liu, X. (1994). Interannual Sea Level in the Northern and Eastern Indian Ocean. *Journal of Physical Oceanography*, 24(6), 1224–1235. [https://doi.org/10.1175/1520-0485\(1994\)024<1224:ISLITN>2.0.CO;2](https://doi.org/10.1175/1520-0485(1994)024<1224:ISLITN>2.0.CO;2)
- Cresswell, G. R., & Peterson, J. L. (1993). The Leeuwin Current south of western Australia. *Marine and Freshwater Research*, 44(2), 285–303. <https://doi.org/10.1071/MF9930285>
- D’Adamo, N., Fandry, C., Buchan, S., & Domingues, C. (2009). Northern sources of the Leeuwin Current and the “holloway Current” on the North West Shelf. *Journal of the Royal Society of Western Australia*, 92(2), 53–66.
- Domingues, C. M., Maltrud, M. E., Wijffels, S. E., Church, J. A., & Tomczak, M. (2007). Simulated Lagrangian pathways between the Leeuwin Current System and the upper-ocean circulation of the southeast Indian Ocean. *Deep-Sea Research Part II: Topical Studies in Oceanography*, 54(8–10), 797–817. <https://doi.org/10.1016/j.dsr2.2006.10.003>
- Duplessy, J. C., Shackleton, N. J., Fairbanks, R. G., Labeyrie, L., Oppo, D., & Kallel, N. (1988). Deepwater source variations during the last climatic cycle and their impact on the global deepwater circulation. *Paleoceanography*, 3(3), 343–360. doi:10.1029/pa003i003p00343
- Eagle, M., Paytan, A., Arrigo, K. R., van Dijken, G., & Murray, R. W. (2003). A comparison between excess barium and barite as indicators of carbon export. *Paleoceanography*, 18(1), 1–13. <https://doi.org/10.1029/2002pa000793>
- Eggleston, S., Schmitt, J., Bereiter, B., Schneider, R., & Fischer, H. (2016). Evolution of the stable carbon isotope composition of atmospheric CO₂ over the last glacial cycle. *Paleoceanography*, 31(3), 434–452. <https://doi.org/10.1002/2015PA002874>.
- Elderfield H, Truesdale VW (1980) On the biophilic nature of iodine in seawater. *Earth and Planetary Science Letters* 50:105-114

- Farrell, J. ., Pedersen, T. ., Calvert, S. ., & Nielsen, B. (2000). Glacial-interglacial changes in nutrient utilization and paleoproductivity in the Indonesian Throughflow sensitive Timor Trough. *Paleoceanography*, 15(1), 85–94. <https://doi.org/10.1029/1999PA900046>
- Feng, M., & Meyers, G. (2003). Interannual variability in the tropical Indian Ocean: A two-year time-scale of Indian Ocean Dipole. *Deep-Sea Research Part II: Topical Studies in Oceanography*, 50(12–13), 2263–2284. [https://doi.org/10.1016/S0967-0645\(03\)00056-0](https://doi.org/10.1016/S0967-0645(03)00056-0)
- Floegel, S., & Wagner, T. (2006). Insolation-control on the Late Cretaceous hydrological cycle and tropical African climate-global climate modelling linked to marine climate records. *Palaeogeography, Palaeoclimatology, Palaeoecology*, 235(1–3), 288–304. <https://doi.org/10.1016/j.palaeo.2005.09.034>
- Gebbie, G., Peterson, C. D., Lisiecki, L. E., & Spero, H. J. (2015). Global-mean marine $\delta^{13}\text{C}$ and its uncertainty in a glacial state estimate. *Quaternary Science Reviews*, 125, 144–159. <https://doi.org/10.1016/j.quascirev.2015.08.010>
- Gordon, A. L., Huber, B. A., Metzger, E. J., Susanto, R. D., Hurlburt, H. E., & Adi, T. R. (2012). South China Sea throughflow impact on the Indonesian throughflow. *Geophysical Research Letters*, 39(11), 1–7. <https://doi.org/10.1029/2012GL052021>
- Gottschalk, J., Vázquez Riveiros, N., Waelbroeck, C., Skinner, L. C., Michel, E., Duplessy, J. C., et al. (2016). Carbon isotope offsets between benthic foraminifer species of the genus *Cibicides* (*Cibicidoides*) in the glacial sub-Antarctic Atlantic. *Paleoceanography*, 31(12), 1583–1602. <https://doi.org/10.1002/2016PA003029>
- Hammer, Ø., Harper, D. A., & Ryan, P. D. (2001). Paleontological statistics software package for education and data analysis. *Current Science*, 4(1), 9.
- Hanson, C. E., Pattiaratchi, C. B., & Waite, A. M. (2005a). Seasonal production regimes off south-western Australia: Influence of the Capes and Leeuwin Currents on phytoplankton dynamics. *Marine and Freshwater Research*, 56(7), 1011–1026. <https://doi.org/10.1071/MF04288>
- Hanson, C. E., Pattiaratchi, C. B., & Waite, A. M. (2005b). Sporadic upwelling on a downwelling coast: Phytoplankton responses to spatially variable nutrient dynamics off the Gascoyne region of Western Australia. *Continental Shelf Research*, 25(12–13), 1561–1582. <https://doi.org/10.1016/j.csr.2005.04.003>
- Harvey, G. . (1980). A study of the chemistry of iodine and bromine in marine sediments, 8(4), 327–332. [https://doi.org/10.1016/0304-4203\(80\)90021-3](https://doi.org/10.1016/0304-4203(80)90021-3)
- Herguera, J. C., & Berger, W. H. (1991). Paleoproductivity from benthic foraminifera abundance: glacial to postglacial change in the west-equatorial Pacific. *Geology*, 19(12), 1173–1176. [https://doi.org/10.1130/0091-7613\(1991\)019<1173:PFBFAG>2.3.CO;2](https://doi.org/10.1130/0091-7613(1991)019<1173:PFBFAG>2.3.CO;2)
- Holloway, P. E., & Nye, H. C. (1985). Leeuwin Current and wind distributions on the southern part of the Australian North West Shelf between January 1982 and July 1983. *Marine and Freshwater Research*, 36(2), 123–137. <https://doi.org/10.1071/MF9850123>

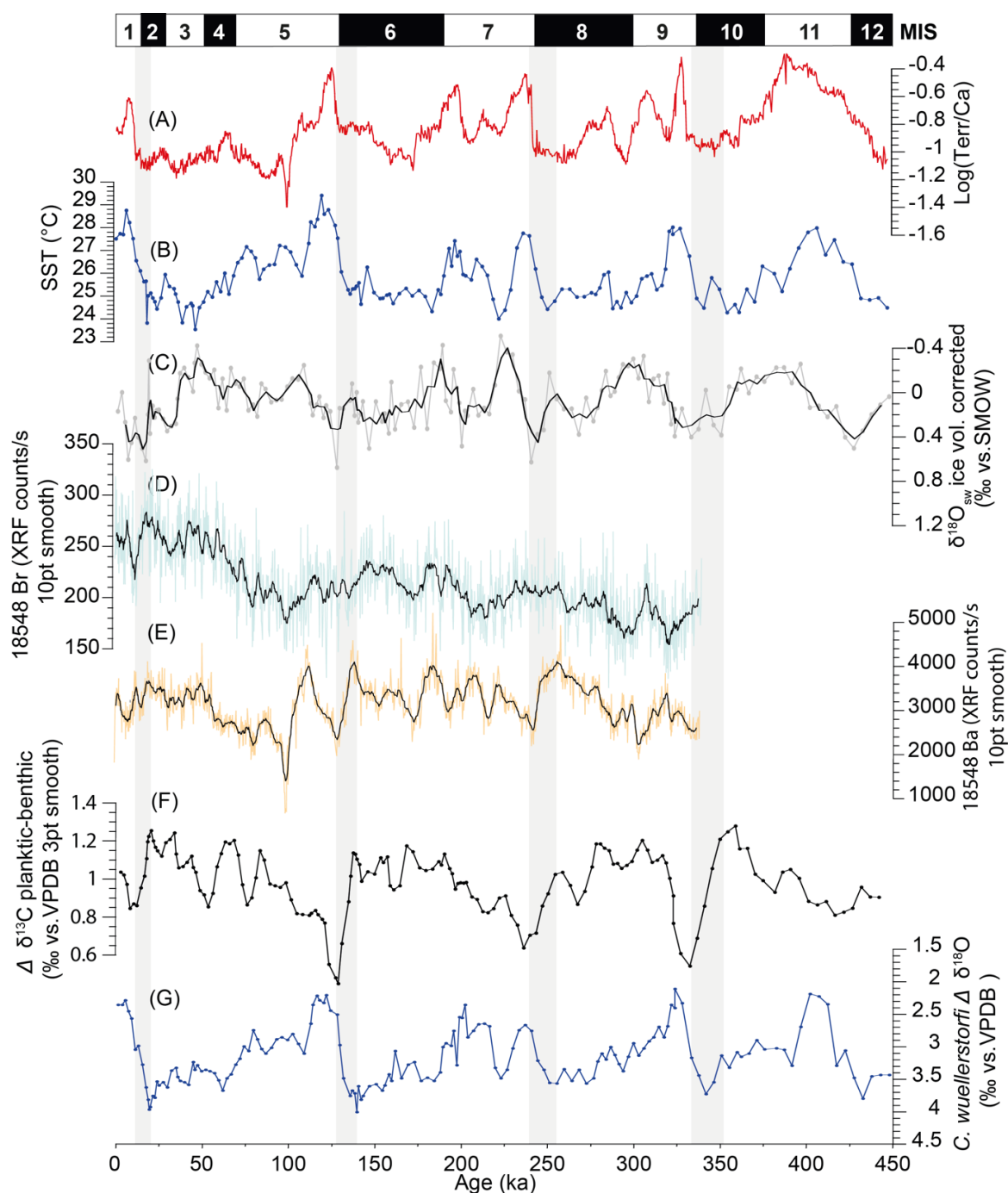
- Holbourn, A., Kuhnt, W., Kawamura, H., Jian, Z., Grootes, P., Erlenkeuser, H., & Xu, J. (2005). Orbitally paced paleoproductivity variations in the Timor Sea and Indonesian throughflow variability during the last 460 kyr. *Paleoceanography*, 20(3), 1–18. <https://doi.org/10.1029/2004PA001094>
- Holbourn, A., Kuhnt, W., & Xu, J. (2011). Indonesian Throughflow variability during the last two glacial cycles: The Timor Sea outflow. Geological Society, London, Special Publications, The SE Asian gateway: history and tectonics of Australia-Asia collision, 355, 283–303, <http://doi.org/10.1144/SP355.14>
- Johannes, R. E., Pearce, A. F., Wiebe, W. J., Crossland, C. J., Rimmer, D. W., Smith, D. F., & Manning, C. (1994). Nutrient Characteristics of Well-mixed Coastal Waters off Perth, Western Australia. *Estuarine, Coastal and Shelf Science*. <https://doi.org/10.1006/ecss.1994.1064>
- Lisiecki, L. E., & Raymo, M. E. (2005). A Pliocene-Pleistocene stack of 57 globally distributed benthic $\delta^{18}\text{O}$ records. *Paleoceanography*, 20(1), 1–17. <https://doi.org/10.1029/2004PA001071>
- Loope, D. B., Rowe, C. M., & Joeckel, R. M. (2001). Annual monsoon rains recorded by Jurassic dunes. *Nature*, 412(6842), 64–66. <https://doi.org/10.1038/35083554>
- Loubere, P., Mekik, F., Francois, R., & Pichat, S. (2004). Export fluxes of calcite in the eastern equatorial Pacific from the Last Glacial Maximum to present. *Paleoceanography*, 19(2). <https://doi.org/10.1029/2003PA000986>
- Lu, Z., Jenkyns, H. C., & Rickaby, R. E. M. (2010). Iodine to calcium ratios in marine carbonate as a paleo-redox proxy during oceanic anoxic events. *Geology*, 38(12), 1107–1110. <https://doi.org/10.1130/G31145.1>
- Mackensen, A., & Schmiedl, G. (2019). Stable carbon isotopes in paleoceanography: atmosphere, oceans, and sediments. *Earth-Science Reviews*, 197(December 2018), 102893. <https://doi.org/10.1016/j.earscirev.2019.102893>
- Mackensen, A., Grobe, H., Hubberten, H. W., & Kuhn, G. (1994). Benthic foraminiferal assemblages and the $\delta^{13}\text{C}$ -signal in the Atlantic sector of the southern ocean: Glacial-to-interglacial contrasts. In *Carbon cycling in the glacial ocean: constraints on the ocean's role in global change* (pp. 105-144). Springer, Berlin, Heidelberg.
- Maxime, M., & Ming, F. (2019). Intra-annual variability of the North West Shelf of Australia and its impact on the Holloway Current: Excitement and propagation of coastally trapped waves. *Continental Shelf Research*, 186(February 2018), 88–103. <https://doi.org/10.1016/j.csr.2019.08.001>
- Paytan, A., Kastner, M., & Chavez, F. P. (1996). Glacial to interglacial fluctuations in productivity in the equatorial Pacific as indicated by marine barite. *Science*, 274(5291), 1355–1357. <https://doi.org/10.1126/science.274.5291.1355>
- Pearce, A. F., & Griffiths, R. W. (1991). The mesoscale structure of the Leeuwin Current: a comparison of laboratory models and satellite imagery. *Journal of Geophysical Research*, 96(C9). <https://doi.org/10.1029/91jc01712>

- Pedersen, T. ., Nielsen, B., & Pickering, M. (1991). Timing of late Quaternary productivity pulses in the Panama Basin and implications for atmospheric CO₂, 6(6), 657–677.
<https://doi.org/10.1029/91PA02532>
- Pei, R., Kuhnt, W., Holbourn, A., Hingst, J., Koppe, M., Schultz, J., et al. (2021). Monitoring Australian Monsoon variability over the past four glacial cycles. *Palaeogeography, Palaeoclimatology, Palaeoecology*, 568(February), 110280. <https://doi.org/10.1016/j.palaeo.2021.110280>
- Pérez-Cruz, L. (2013). Hydrological changes and paleoproductivity in the Gulf of California during middle and late Holocene and their relationship with ITCZ and North American Monsoon variability. *Quaternary Research*, 79(02), 138–151. doi:10.1016/j.yqres.2012.11.007
- Peterson, C. D., Lisiecki, L. E., & Stern, J. V. (2014). Deglacial whole-ocean $\delta^{13}\text{C}$ change estimated from 480 benthic foraminiferal records. *Paleoceanography*, 29(6), 549–563.
<https://doi.org/10.1002/2013PA002552>
- Pichevin, L. E., Reynolds, B. C., Ganeshram, R. S., Cacho, L., Pena, L., Keefe, K., & Ellam, R. M. (2009). Enhanced carbon pump inferred from relaxation of nutrient limitation in the glacial ocean. *Nature*, 459(7250), 1114–1117. <https://doi.org/10.1038/nature08101>
- Ridgway, K. R., & Godfrey, J. S. (2015). *Journal of Geophysical Research : Oceans*. *Journal of Geophysical Research: Oceans*, 120(10), 6843–6864. <https://doi.org/10.1002/2015JC011049>
- Rosenthal, Y., Holbourn, A., Kullhanek, D., & Scientists, E. 363. (2017). Expedition 363 Preliminary Report Western Pacific Warm Pool Neogene and Quaternary records of Western Pacific Warm Pool paleoceanography. <https://doi.org/10.14379/iodp.pr.363.2017>
- Rosenthal, Y., Holbourn, A., Kullhanek, D., & Scientists, E. 363. (2018). Western Pacific Warm Pool. *Proceedings of the International Ocean Discovery Program, 363*: College Station, TX.
<https://doi.org/10.14379/iodp.proc.363.2018>
- Sarnthein, M., Winn, K., & Zahn, R. (1987). Paleoproductivity of oceanic upwelling and the effect on atmospheric CO₂ and climatic change during deglaciation times. *Abrupt Climatic Change. Proc.* 1985, 311–337. https://doi.org/10.1007/978-94-009-3993-6_27
- Shackleton, N. J. (1977). Carbon 13 in *Uvigerina*: Tropical rainforest history and the equatorial Pacific carbonate dissolution cycles. *Marine science*.
- Schmitt, J., Schneider, R., Elsig, J., Leuenberger, D., Lourantou, A., Chappellaz, J., et al. (2012). Carbon isotope constraints on the deglacial CO₂ rise from ice cores. *Science*, 336(6082), 711–714.
<https://doi.org/10.1126/science.1217161>
- Schmittner, A., Bostock, H. C., Cartapanis, O., Curry, W. B., Filipsson, H. L., Galbraith, E. D., et al. (2017). Calibration of the carbon isotope composition ($\delta^{13}\text{C}$) of benthic foraminifera. *Paleoceanography*, 32(6), 512–530. <https://doi.org/10.1002/2016PA003072>
- Schmitz, B. (1987). Barium, equatorial high productivity, and the northward wandering of the Indian continent, 2(1), 63–77. <https://doi.org/10.1029/PA002i001p00063>

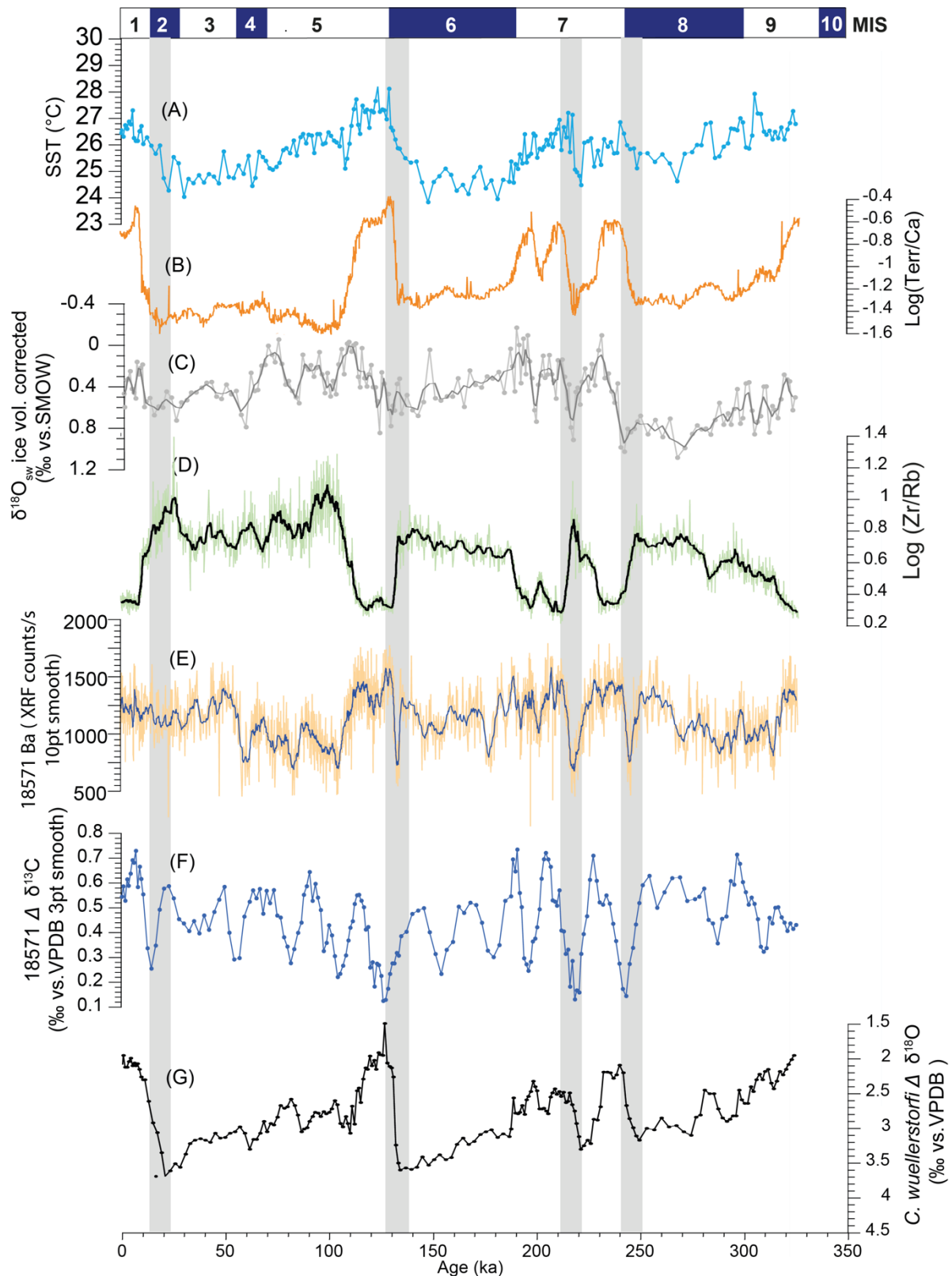
- Schott, F. A., & McCreary, J. P. (2001). The monsoon circulation of the Indian Ocean. *Progress in Oceanography*, 51(1), 1–123. [https://doi.org/10.1016/S0079-6611\(01\)00083-0](https://doi.org/10.1016/S0079-6611(01)00083-0)
- Seki, A., Tada, R., Kurokawa, S., Mitake, K., & Murayama, M. (2019). Reconstruction of marine organic carbon content in the Japan Sea sediments from Br variability measured by XRF core scanner. *Progress in Earth and Planetary Science*, 6(1), 1–12. Retrieved from <https://confit.atlas.jp/guide/event/jpguagu2017/subject/MIS06-P07/detail>
- Smith, R. L., Huyer, A., Godfrey, J. S., & Church, J. A. (1991). The Leeuwin current off western Australia. *Journal of Physical Oceanography*, 21(2), 323–345. [https://doi.org/10.1175/1520-0485\(1991\)021<0323:TLCOWA>2.0.CO;2](https://doi.org/10.1175/1520-0485(1991)021<0323:TLCOWA>2.0.CO;2)
- Tian, R. C., Marty, J. C., Nicolas, E., Chiaverini, J., Ruiz-Pino, D., & Pizay, M. D. (1996). Iodine speciation: A potential indicator to evaluate new production versus regenerated production. *Deep-Sea Research Part I*, 43(5), 723–738. [https://doi.org/10.1016/0967-0637\(96\)00023-4](https://doi.org/10.1016/0967-0637(96)00023-4)
- Weller, E., Holliday, D., Feng, M., Beckley, L., & Thompson, P. (2011). A continental shelf scale examination of the Leeuwin Current off Western Australia during the austral autumn-winter. *Continental Shelf Research*, 31(17), 1858–1868. <https://doi.org/10.1016/j.csr.2011.08.008>
- Weltje, G. J., & Tjallingii, R. (2008). Calibration of XRF core scanners for quantitative geochemical logging of sediment cores: Theory and application. *Earth and Planetary Science Letters*, 274(3–4), 423–438. <https://doi.org/10.1016/j.epsl.2008.07.054>
- Wijffels, S., & Meyers, G. (2004). An intersection of oceanic waveguides: Variability in the Indonesian throughflow region. *Journal of Physical Oceanography*, 34(5), 1232–1253. [https://doi.org/10.1175/1520-0485\(2004\)034<1232:AIOOWV>2.0.CO;2](https://doi.org/10.1175/1520-0485(2004)034<1232:AIOOWV>2.0.CO;2)
- Wong, G. T. F., & Brewer, P. G. (1977). The marine chemistry of iodine in anoxic basins. *Geochimica et Cosmochimica Acta*, 41(1), 151–159. [https://doi.org/10.1016/0016-7037\(77\)90195-8](https://doi.org/10.1016/0016-7037(77)90195-8)
- Woodruff, F., & Savin, S. M. (1985). $\delta^{13}\text{C}$ values of Miocene Pacific benthic foraminifera: correlations with sea level and biological productivity. *Geology*, 13(2), 119–122. [https://doi.org/10.1130/0091-7613\(1985\)13<119:CVOMP>2.0.CO;2](https://doi.org/10.1130/0091-7613(1985)13<119:CVOMP>2.0.CO;2)
- Zhang, P., Xu, J., Holbourn, A., Kuhnt, W., Beil, S., Li, T., et al. (2020). Indo-Pacific Hydroclimate in Response to Changes of the Intertropical Convergence Zone: Discrepancy on Precession and Obliquity Bands Over the Last 410 kyr. *Journal of Geophysical Research: Atmospheres*, 125(14), 1–10. <https://doi.org/10.1029/2019JD032125>
- Zhou, X., Jenkyns, H. C., Lu, W., Hardisty, D. S., Owens, J. D., Lyons, T. W., & Lu, Z. (2017). Organically bound iodine as a bottom-water redox proxy: Preliminary validation and application. *Chemical Geology*, 457, 95–106. <https://doi.org/10.1016/j.chemgeo.2017.03.016>
- Ziegler, M., Jilbert, T., de Lange, G. J., Lourens, L. J., & Reichert, G.-J. (2008). Bromine counts from XRF scanning as an estimate of the marine organic carbon content of sediment cores. *Geochemistry, Geophysics, Geosystems*, 9(5). <https://doi.org/10.1029/2007GC001932>. 1.

Supporting information for

Evolution of paleoproductivity and $\delta^{13}\text{C}$ gradients along the Northwestern Australian Margin over the last 450 kyr



Supplementary Figure 1. Climate related proxies in SO257-18548 and Site U1482. (A – G) XRF scanner derived Log (Terr/Ca), Mg/Ca based SST, ice volume corrected $\delta^{18}\text{O}_{\text{sw}}$, XRF scanner derived Br counts, XRF scanner derived Ba counts, $\Delta \delta^{13}\text{C}_{\text{PF-BF}}$ and benthic oxygen isotopes.



Supplementary Figure 2. Climate related proxies in SO257-18571. (A – G) XRF scanner derived Log (Terr/Ca), Mg/Ca based SST, ice volume corrected $\delta^{18}\text{O}_{\text{sw}}$, XRF scanner derived Br counts, XRF scanner derived Ba counts, $\Delta\delta^{13}\text{C}_{\text{PF-BF}}$ and benthic oxygen isotopes.

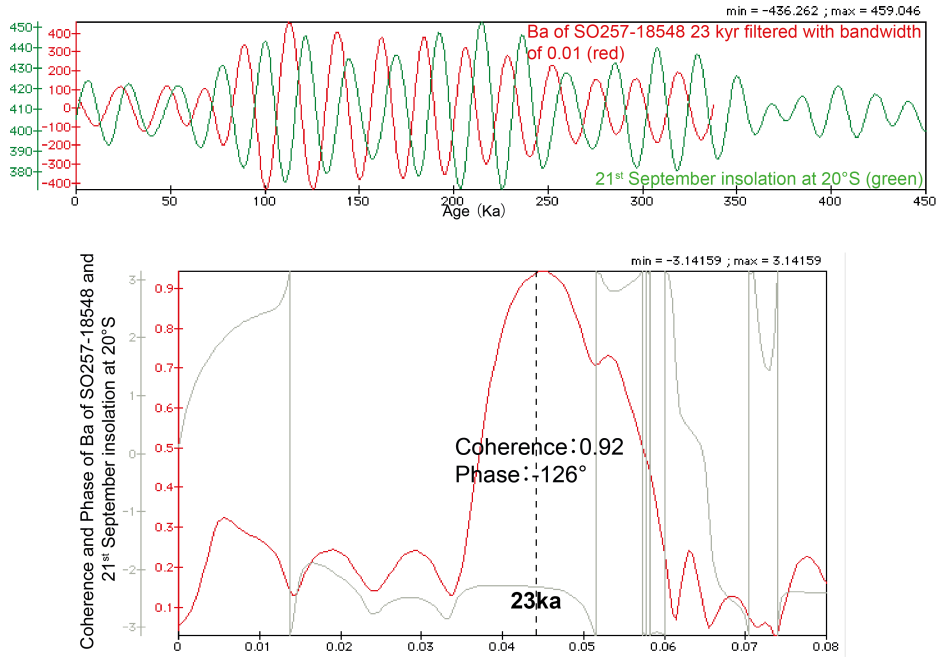


Figure 8A. Comparison of 21st September insolation at 20°S (green) to 23 kyr filtered XRF-scanner derived Ba record (red) from Core SO257-18548 and coherence (red) and phase (grey) of 21st September insolation at 20°S to XRF-scanner derived Ba record from Core SO257-18548. Bandwidth is 0.011194. Non-zero coherence >0.550342. Error estimation on power spectrum is $0.488632 < \Delta\text{Power} / \text{Power} < 3.0732$.

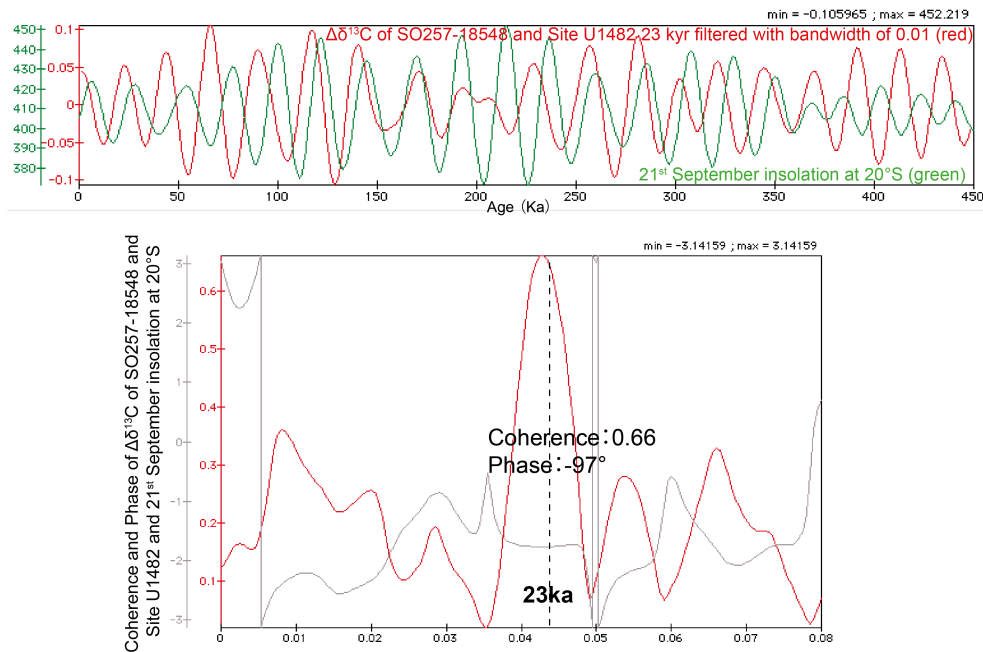


Figure 8B. Comparison of 21st September insolation at 20°S (green) to 23 kyr filtered $\Delta\delta^{13}\text{C}_{\text{PF-BF}}$ from Core SO257-18548 and Site U1482 (red) and coherence (red) and phase (grey) of 21st September insolation at 20°S to $\Delta\delta^{13}\text{C}_{\text{PF-BF}}$ record from Core SO257-18548 and Site U1482. Bandwidth is 0.011194. Non-zero coherence >0.550342. Error estimation on power spectrum is $0.488632 < \Delta\text{Power} / \text{Power} < 3.0732$.

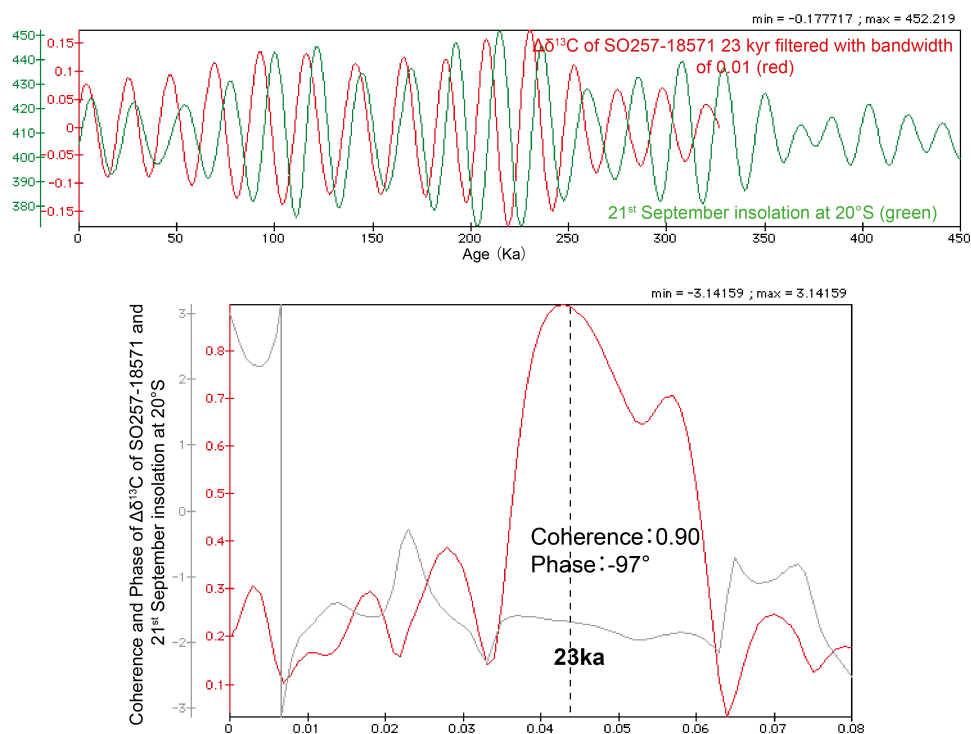


Figure 8C. Comparison of 21st September insolation at 20°S (green) to 23 kyr filtered $\Delta\delta^{13}\text{C}_{\text{PF-BF}}$ from Core SO257-18571 (red) and coherence (red) and phase (grey) of 21st September insolation at 20°S to $\Delta\delta^{13}\text{C}_{\text{PF-BF}}$ record from Core SO257-18571. Bandwidth is 0.011194. Non-zero coherence >0.550342 . Error estimation on power spectrum is $0.488632 < \Delta\text{Power} / \text{Power} < 3.0732$.

Indo-Pacific Hydroclimate in Response to Changes of the Intertropical Convergence Zone: Discrepancy on Precession and Obliquity Bands Over the Last 410 kyr

Peng Zhang¹, Jian Xu¹, Ann Holbourn², Wolfgang Kuhnt², Sebastian Beil², Tiegang Li³, Zhifang Xiong³, Haowen Dang⁴, Hong Yan⁵, **Renjie Pei**², Yazhou Ran¹, and Hanning Wu¹

¹*State Key Laboratory of Continental Dynamics, Department of Geology, Northwest University, Xi'an, China.*

²*Institute of Geosciences, Christian-Albrechts-University, Kiel, Germany.*

³*Key Laboratory of Marine Sedimentology and Environmental Geology, First Institute of Oceanography, Ministry of Natural Resources, Qingdao, China.*

⁴*State Key Laboratory of Marine Geology, Tongji University, Shanghai, China.*

⁵*State Key Laboratory of Loess and Quaternary Geology, Institute of Earth Environment, Chinese Academy of Sciences, Beijing, China.*

Abstract

The Intertropical Convergence Zone (ITCZ), which is the heaviest rain belt on Earth, significantly influences global hydroclimate change and livelihood of nearly 40% of the global population. However, long-term precipitation records are sparse from the Indo-Pacific region, especially from the southern margin of the Indo-Pacific ITCZ, restricting our understanding of the overall natural variability of the ITCZ in the past. In this study, we present a new summer monsoonal precipitation record that spans the last 410 kyr from the southern margin of the Indo-Pacific ITCZ, based on the logarithmic ratio between terrigenous fraction K and pelagic fraction Ca ($\ln(K/Ca)$). Contents of both elements were derived from X-ray fluorescence scanning on sediment cores from Site U1483 (13°05.24'S, 121°48.25'E, water depth 1,733 m) that was drilled offshore northwestern Australia during International Ocean Discovery Program Expedition 363. Comparison of the new precipitation record with published precipitation records from the northern margin and meteorological center of the Indo-Pacific

ITCZ shows that precipitation changed nearly in-phase between the hemispheres on the precession band, possibly linked to expansion and contraction in the latitudinal extent of the Indo-Pacific ITCZ. In contrast, interhemispheric precipitation was nearly in anti-phase on the obliquity band, likely due to latitudinal migration of the Indo-Pacific ITCZ. Our findings imply that tropical hydroclimate cycles were regulated by the orbital forcing but with significantly different response to changes of the ITCZ on precession and obliquity bands.

1. Introduction

The Intertropical Convergence Zone (ITCZ) defines a low-pressure belt near the equator where southeasterly and northeasterly winds come together. As the ascending branch of the Hadley circulation (Waliser & Gautier, 1993), the ITCZ is characterized by deep convective and heavy precipitation (Schneider et al., 2014) and thus exerts a significant influence on global hydroclimate change. Today, the ITCZ moves seasonally toward the Southern or Northern Hemisphere, but the mean position of the ITCZ is mostly north of the equator, likely linked to the northward energy transport of the Atlantic meridional overturning circulation (Marshall et al., 2014).

With the seasonal latitudinal migration of the ITCZ, an interhemispheric anti-phasing precipitation pattern occurs: The precipitation decreases in the Northern Hemisphere but increases in the Southern Hemisphere along with the southward migration of the ITCZ and vice versa. On millennial to orbital timescales, paleoclimatic and modeling studies suggest that the interhemispheric anti-phasing precipitation can be attributed to latitudinal migration of the ITCZ (Ayliffe et al., 2013; Dang et al., 2015; Haug et al., 2001; Huang et al., 2019; Liu et al., 2015; Wang et al., 2006).

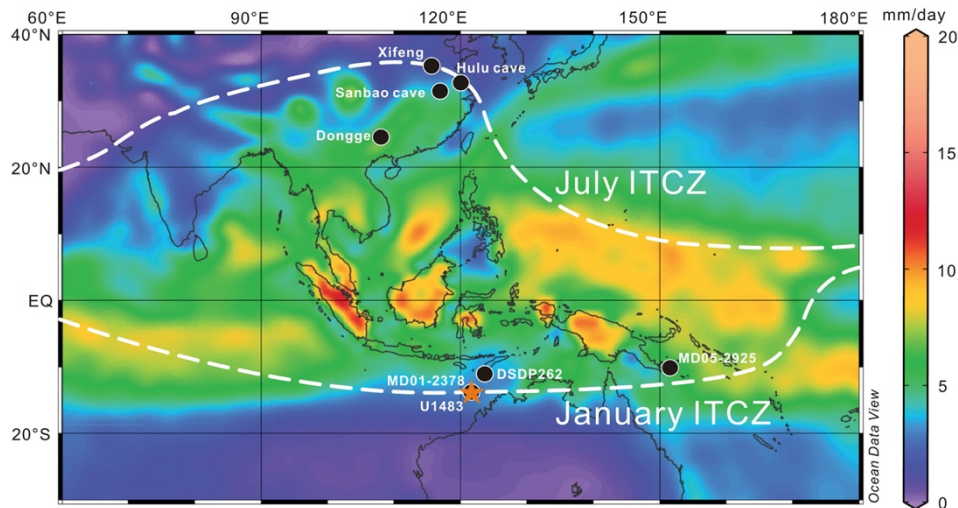


Figure 1. Map of annual average precipitation and study sites (modified from Schröder et al., 2016). White dashed lines denote the mean positions of the ITCZ in July and January (Liu et al., 2015). Orange star marks Site U1483 (this study). Black dots mark Chinese cave stalagmites (Hulu, Sanbao and Dongge caves) (Cheng et al., 2016), the Xifeng Loess Section (Li et al., 2017), DSDP Site 262 (Vroon et al., 1995), Core MD01-2378 (this study), and Core MD05-2925 (Liu et al., 2015), respectively.

While the interhemispheric anti-phasing precipitation pattern has almost become a consensus on different timescales, increasing numbers of studies have found that the interhemispheric precipitation is in-phase at (sub-) millennial timescales (Collins et al., 2010; Denniston et al., 2016; Konecky et al., 2013; Scroxtion et al., 2017; Yan et al., 2015). This in-phase precipitation behavior between the hemispheres violates the classic migration theory of the ITCZ but can be well explained by expansion and contraction in the latitudinal extent of the ITCZ, which is likely caused by lower global mean temperatures (Collins et al., 2010), symmetrical solar irradiance changes (Scroxtion et al., 2017; Yan et al., 2015), strengthening Walker circulation (Konecky et al., 2013), and changes in the meridional atmospheric circulation (Denniston et al., 2016).

To date, understanding of the overall dynamics of the ITCZ is still poor, especially on orbital timescales, due to sparse long-term precipitation records from the Indo-Pacific region. Meanwhile, the majority of studies focus on the northern margin and meteorological center of the Indo-Pacific ITCZ (e.g., Cheng et al., 2016; Li et al., 2017; Liu et al., 2015), while the

southern margin of the Indo-Pacific ITCZ remains less studied, thus limiting a full understanding of the ITCZ dynamics on orbital timescales. In this study, we present a new well-dated and high-resolution long-term summer monsoonal precipitation record spanning the past 410 kyr from International Ocean Discovery Program (IODP) Site U1483 situated at the southern margin of the Indo-Pacific ITCZ (Figure 1). In addition, published long-term rainfall records from the Indo-Pacific region were collected, including the Chinese cave stalagmite $\delta^{18}\text{O}$ record (Cheng et al., 2016) and the Sr/Ca record of the Xifeng Loess section (Li et al., 2017) from the northern margin of the Indo-Pacific ITCZ, as well as the *Globigerinoides ruber* Nd/Ca record of Core MD05-2925 (Liu et al., 2015) from the meteorological center of the Indo-Pacific ITCZ (Figure 1). These precipitation records form a meridional transect across the full extent of the Indo-Pacific ITCZ, providing an unprecedented opportunity for us to gain insight into the overall dynamics of the ITCZ on orbital timescales.

2. Materials and Methods

2.1. Site U1483

Site U1483 (13°05.24'S, 121°48.25'E, water depth 1,733 m, penetration of ~290 m) was drilled offshore northwestern Australia during IODP Expedition 363 by JOIDES Resolution in 2016 (Figure 1) (Rosenthal et al., 2017). Sediments used in this study were sampled along the revised SPLICE (see details in Text S1 of supporting information) from 0 to 41 m composite depth scale.

Semi-quantitative elemental analyses were performed on the sediment surface of the archive half at 2 cm intervals using the Avaatech XRF core scanner at the Institute of Geosciences, University of Kiel. Measurements were conducted at settings of 10 kV and 0.75 mA with 10 s of counting time, and the results were given in counts per second (cps). The quantitative chemical composition of bulk sediments was determined on discrete samples at 20

cm intervals by conventional XRF (Rikagu RIX 2100), and 11 of the samples selected from Marine Isotope Stage (MIS) 1–11 were measured using inductively coupled plasma mass spectrometry (Agilent 7500a) at the State Key Laboratory of Continental Dynamics, Northwest University. Analyses of USGS and Chinese national rock standards (BCR-2, GSR-1, and GSR-3) showed that the analytical precision and accuracy for the major elements are generally better than 5%. For the trace element analyses, the analytical error is less than 2%, and the precision is greater than 10% (Liu et al., 2007). Stable isotope analysis was carried out on benthic foraminifer *Planulina wuellerstorfi* at 20 cm intervals on a DeltaV Advantage instrument at the Institute of Earth Environment, Chinese Academy of Sciences. Analyses of the Chinese national standard GBW04405 (certified $\delta^{18}\text{O} = -8.49 \pm 0.15\text{‰}$) at the Institute of Earth Environment showed a mean $\delta^{18}\text{O}$ of $-8.65 \pm 0.15\text{‰}$. This result is nearly consistent with the result ($-8.62 \pm 0.15\text{‰}$) yielded at Institute of Global Environmental Change, Xi'an Jiaotong University. Hence, the precision is better than $\pm 0.15\text{‰}$ on the basis of the performance of inter-lab and lab-internal standard carbonates.

The initial age model of Site U1483 was based on benthic $\delta^{18}\text{O}$ stratigraphy (Figure S1), and on this basis, the final age model was then established by correlating XRF-derived high-resolution records of $\ln(\text{K}/\text{Ca})$ from Site U1483 and Core MD01-2378 using QAnalySeries (Kotov & Pälike, 2018) (Figure 2a) (see details in Text S2).

2.2 Core MD01-2378

Core MD01-2378 (13°04.95'S, 121°47.27'E, water depth 1,783 m, a total core length of ~40 m), from the location situated ~0.8 nmi northwest of Site U1483 (Figure 1), was retrieved during the International Marine Global Change Study by RV Marion-Dufresne in 2001 (Bassinot et al., 2002). Semi-quantitative elemental analyses were performed on the sediment surface of the archive half at 2 cm intervals using the XRF Core Scanner I with a generator setting of 20 kV, 0.08 mA, and a sampling time of 20 s at MARUM, University of Bremen.

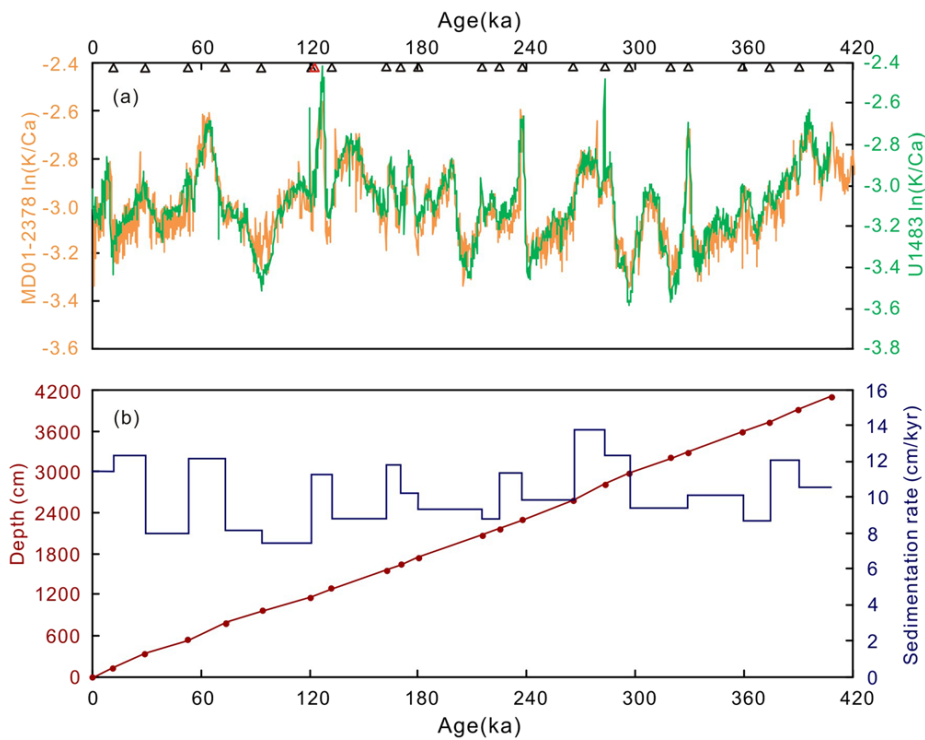


Figure 2. Age model and sedimentation rate of Site U1483. (a) XRF-derived $\ln(K/Ca)$ values for Site U1483 and Core MD01-2378; and (b) depth-age model and sedimentation rate of Site U1483. Black triangles represent $\ln(K/Ca)$ tie points and red triangle denotes the last occurrence of planktonic foraminiferal species *G. ruber* (pink). Note that K and Ca contents in this plot were not corrected for attenuation effect.

3. Results and Discussion

3.1. Precipitation Proxy From Site U1483

Combinations of trace element and Nd-Pb isotope ratios demonstrate that the terrigenous fractions at Deep Sea Drilling Project (DSDP) Site 262 (Figure 1), northeast of Site U1483, are originated from northwestern Australia (Vroon et al., 1995). Distribution pattern of upper continental crust (UCC) (Taylor & McLennan, 1985, 1995) normalized rare earth elements has ever been considered to characterize provenances of lithogenic fractions (Wu et al., 2013). To identify provenance of the terrigenous fractions at Site U1483, we compared the distribution patterns of UCC-normalized rare earth elements between Site U1483 and DSDP Site 262. The comparison shows that distribution patterns of UCC-normalized rare earth elements are quite alike at Site U1483 and DSDP Site 262 (Figure S2c), indicating the northwestern Australia origin of the terrigenous fractions at Site U1483. However, UCC-normalized rare earth elements at DSDP Site 262 are much richer than at Site U1483 (Figure S2c), probably related to different grain sizes of terrigenous fractions at these two sites since the different transport distances to the source area of the terrigenous fractions (Figure 1). Eolian dust from northwestern Australia may contribute little to the terrigenous fraction at Site U1483, as is supported by the estimated terrigenous dust accumulation offshore northwestern Australia (Kuhnt et al., 2015). Therefore, the terrigenous fractions at Site U1483 mainly stemmed from riverine transport from the northwestern Australia. This result supports a previous study of Kuhnt et al. (2015), which suggested that the terrigenous fractions at the coring site of MD01-2378 (Site U1483) originated mainly from the Fitzroy and Ord Rivers in northwestern Australia. In addition, similar distribution patterns of UCC-normalized major, trace, and rare earth elements through MIS 11 to MIS 1 (Figure S2) may indicate that the provenance of the terrigenous fractions at Site U1483 was relatively stable during the past 410 kyr. Natural logarithmic ratio of K and Ca ($\ln(K/Ca)$) in sediments of Core MD01-2378 which has the same

coordinate with Site U1483 (Figure 1) has been used as a proxy for summer monsoonal precipitation associated river-runoff from northwestern Australia (Kuhnt et al., 2015). As for Site U1483, we thus also used the $\ln(K/Ca)$ to indicate summer monsoonal precipitation associated river-runoff from northwestern Australia as in the study of Kuhnt et al. (2015). Both K and Ca contents were derived from XRF scanning on sediments from Site U1483. The element K predominantly represents clay mineral-bound fine-grained fraction of riverine terrigenous runoff (Calvert & Pedersen, 2007), and thus, K in sediments is terrigenous, likely dominated by river runoff from northwestern Australia. The content of K in sediments will increase with enhanced river runoff and vice versa. In contrast, the element Ca in sediments is derived from the biogenic carbonate of marine planktons, because sediments from Site U1483 consist of undisturbed, homogenous, nannoplankton ooze with ~50% carbonate (see details in Text S4). Discharge of the main northwestern Australian rivers exhibits an extremely seasonal pattern with more than 90% of fluvial discharge related to summer monsoonal rainfall (Doupé & Pettit, 2002; Lindsay & Commander, 2006). Therefore, the content of K in sediments depends ultimately on the amount of summer monsoonal rainfall. It is worthy to mention that the fluctuations in the Ca-normalized terrigenous elemental curves are caused by fluctuations in terrigenous input rather than by changing marine carbonate production/dissolution at the coring site of MD01-2378 (Site U1483) due to the consistent behaviors of Ca- or Ba-normalized terrigenous elements and vague relationship between carbonate percentages and sedimentation rates (Figures 2b and S3b) (Kuhnt et al., 2015).

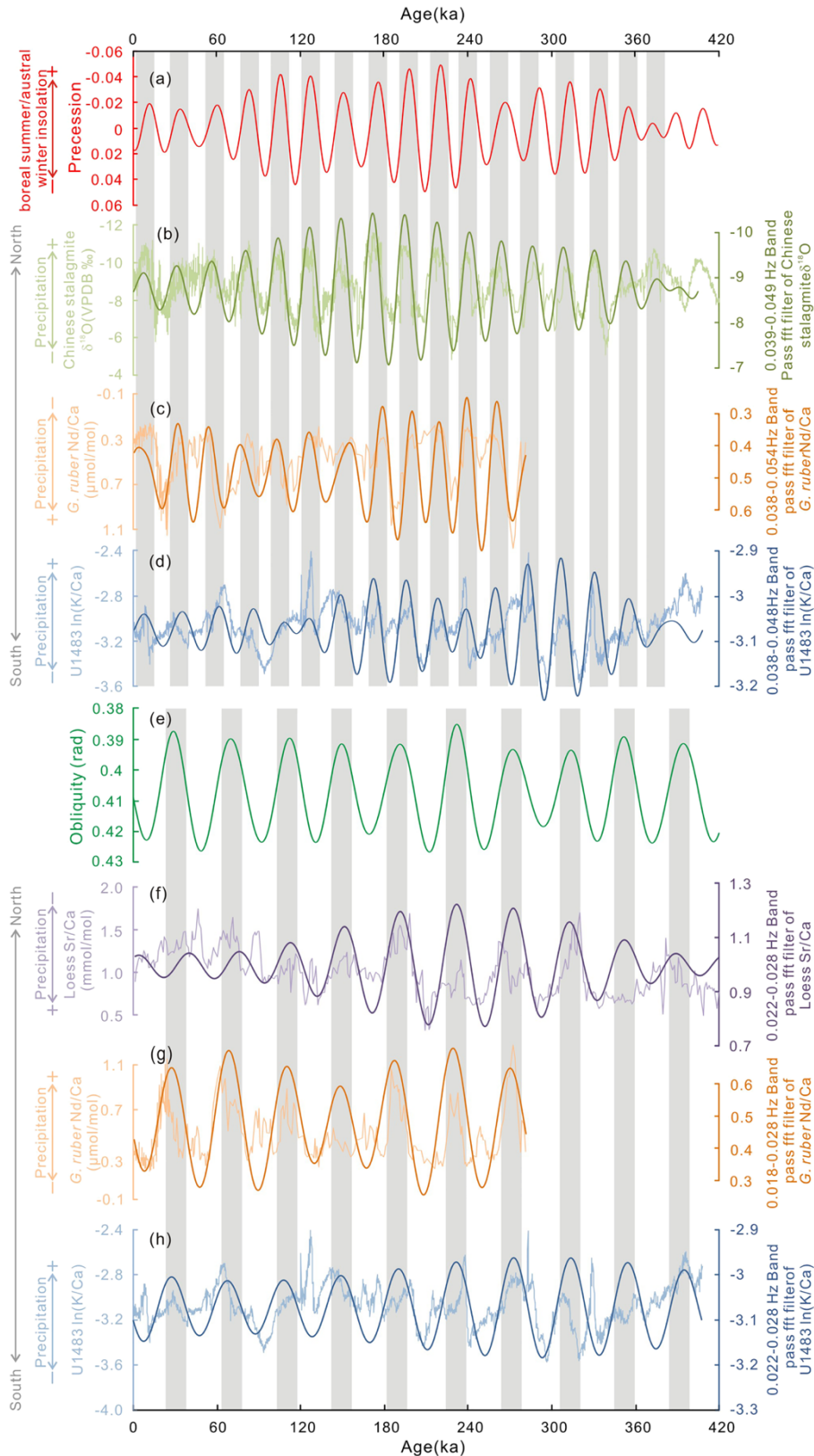


Figure 3. Proxy records of precipitation oscillate on precession and obliquity bands. (a) Precession and (e) obliquity parameters (Berger & Loutre, 1991); (b) Chinese cave stalagmite $\delta^{18}\text{O}$ (Cheng et al., 2016); (c) and (g) *G. ruber* Nd/Ca from Core MD05-2925 (Liu et al., 2015); (d) and (h) $\ln(\text{K}/\text{Ca})$ from Site U1483 (this study); (f) Sr/Ca from the Xifeng section (Li et al., 2017). Superimposed on the raw data curves are precession and obliquity bandpass filtering curves.

3.2. Interhemispheric In-Phase Precipitation on Precession Band in Response to Expansion/Contraction in the Latitudinal Extent of the Indo-Pacific ITCZ

Ln(K/Ca) from Site U1483 is used as the precipitation proxy with more positive value indicating higher precipitation and vice versa. Detailed profiles of element counting and logarithm ratio of element/Ca are shown respectively in Figures S3 and S4. Spectral analysis and bandpass filtering on Ln(K/Ca) record show that precipitation at the southern margin of the ITCZ over the past 410 kyr was dominated by precession band variance (Figures 3d, 4a, and S5h), which has been regarded as the most important orbital activity for tropical hydrologic change (Cheng et al., 2009, 2016; Dang et al., 2015; Liu et al., 2015; Tachikawa et al., 2011; Wang et al., 2008; Wu et al., 2013). Cross-spectral analysis on Ln(K/Ca) and precession time series reveals that the Ln(K/Ca) maximum lagged the precession minimum by $\sim 42^\circ$ (Figure 4d), indicating that precipitation at the southern margin of the ITCZ oscillated almost in anti-phase with precession from 0 to 410 ka. This result is supported not only by the precession bandpass filtering result (Figures 3a and 3d) but also by the simulated precipitation record for northwestern Australia (Singarayer et al., 2017), which shows that variations in precipitation at the southern margin of the ITCZ were in anti-phase with precession over the past 120 kyr.

Both Chinese cave stalagmite $\delta^{18}\text{O}$ and *G. ruber* Nd/Ca of Core MD05-2925 have been regarded as proxies for summer monsoonal precipitation with depleted stalagmite $\delta^{18}\text{O}$ and enriched *G. ruber* Nd/Ca denoting increased precipitation and vice versa (Bayon et al., 2017; Cheng et al., 2009, 2012; Liu et al., 2015; Wang et al., 2001, 2008). Chinese cave stalagmite $\delta^{18}\text{O}$ as a proxy of summer monsoonal precipitation is discussed in detail in Text S5. A strong precession signal occurs in both of the time series (Figures 3b, 3c, 4b, and 4c), indicating that precipitation at the northern margin and center of the ITCZ has also been dominated by precession band variance during the past 410 kyr (Cheng et al., 2016; Liu et al., 2015). Based on the cross-spectral analysis of these time series against precession parameter, we observed

an anti-phase angle between stalagmite $-\delta^{18}\text{O}$ ($\sim -146^\circ$) and *G. ruber* Nd/Ca of Core MD05-2925 ($\sim 30^\circ$) (Figure 4d). Precession bandpass filtering results also show that Chinese cave stalagmite $-\delta^{18}\text{O}$ changed in anti-phase while *G. ruber* Nd/Ca of Core MD05-2925 in-phase with precession (Figures 3a–3c).

In summary, on the precession band, precipitation oscillated in-phase between the southern and northern margins but in anti-phase to the center of the ITCZ. In other words, precipitation synchronously increases at the southern and northern margins but decreases at the center of the ITCZ and vice versa. (Figures 3a–3d and 4d). In previous studies, this anti-phase precipitation behavior was attributed to the latitudinal displacement of the ITCZ, driven by precession-dominated (Haug et al., 2001; Liu et al., 2015). However, it is difficult using the traditional migration theory of the ITCZ to interpret the interhemispheric precipitation in-phasing.

It is worth noting that interhemispheric in-phase precipitation change occurs not only on orbital timescales but also on (sub-) millennial timescales. For instance, an integrated series of precipitation records from the Indo-Pacific suggested that droughts occurred at the southern and northern margins of the ITCZ, while moist conditions prevailed at the center of the ITCZ during the Little Ice Age (Yan et al., 2015). A comparison of stalagmite $\delta^{18}\text{O}$ records from between Chinese cave and Australia KNI-51 cave showed that precipitation varied nearly in-phase at the southern and northern margins of the ITCZ during the last 3 kyr (Denniston et al., 2016). This in-phase precipitation pattern between the hemispheres on (sub-) millennial timescales has been attributed to expansion and contraction of the ITCZ (Denniston et al., 2016; Scroxton et al., 2017; Yan et al., 2015). We thus speculate that interhemispheric in-phase precipitation on precession band may also be caused by expansion and contraction of the ITCZ. Changes in both orbital parameters and solar irradiance directly influence solar insolation on the Earth (Bard et al., 2000; Laskar et al., 2011). Yan et al. (2015) suggested that the north–

south migration of the ITCZ mainly happens on orbital timescales due to asymmetrical insolation variations between the hemispheres, which are caused by variations in precessional insolation rather than in solar irradiance. In contrast, expansion and contraction of the ITCZ mainly occurs on sub-millennial timescales and is linked to symmetrical insolation variations between the hemispheres, which are ascribed to variations dominantly in solar irradiance over precessional insolation. Nevertheless, a recent model study by Singarayer et al. (2017) suggested that precession directly regulates the expansion and contraction of the ITCZ on orbital timescales with expansion of the ITCZ related to weak precession, and vice versa, which is in agreement with our results. Specifically, the ITCZ expanded (contracted) in accordance with weak (strong) precession, as indicated by enriched (depleted) precipitation at the southern and northern margins and depleted (enriched) precipitation at the centre of the ITCZ. Precessional expansion and contraction of the ITCZ is possibly due to the different responses of the northern and southern extremes of the ITCZ to changes in the interhemispheric temperature gradient (Singarayer et al., 2017).

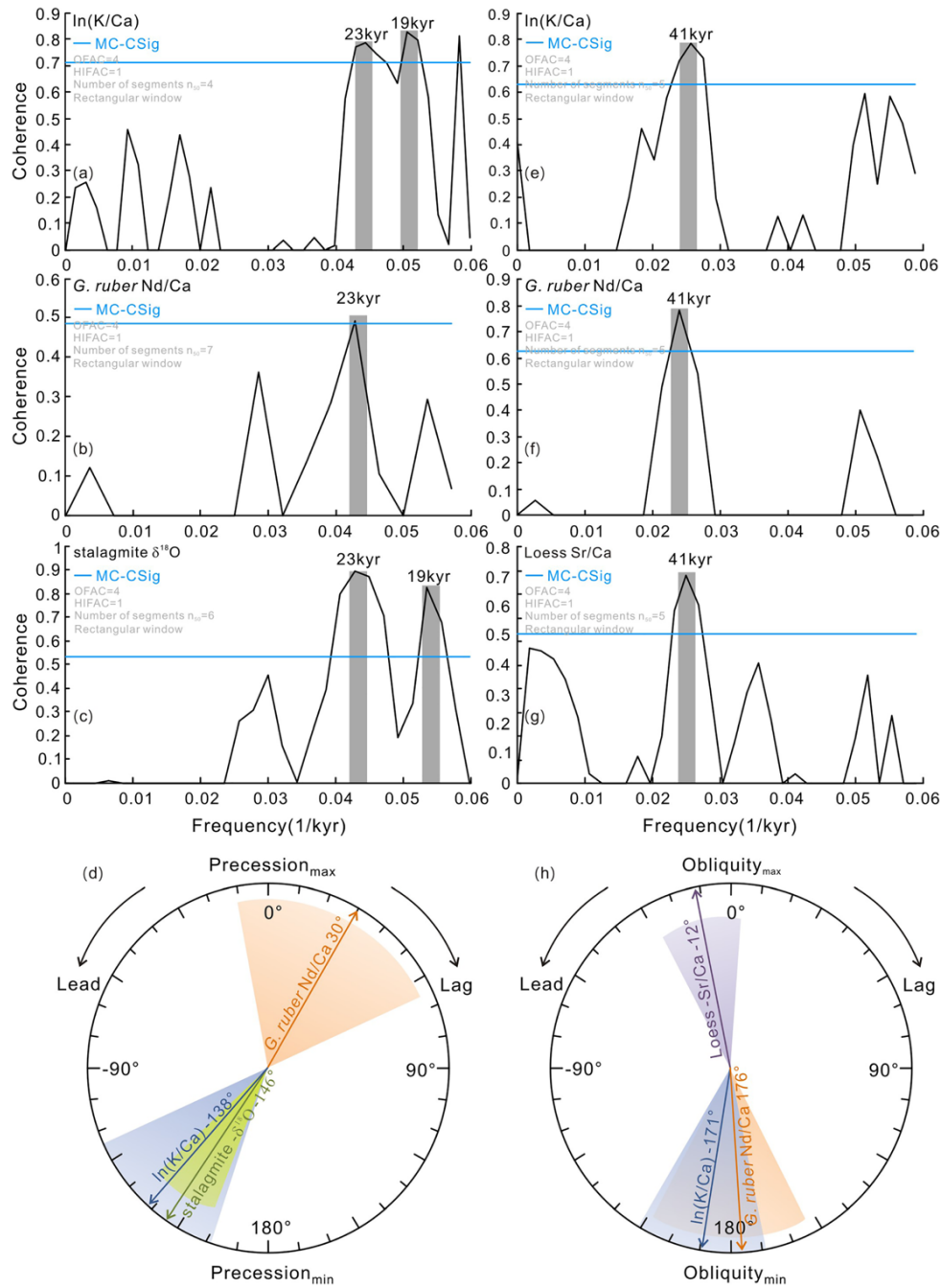


Figure 4. Coherence and phase relationship of paleoclimatic proxies with orbital parameters precession (a–d) and obliquity (e–h) (Berger & Loutre, 1991), respectively. Coherence with precession: (a) $\ln(K/Ca)$ from Site U1483 (this study); (b) *G. ruber* Nd/Ca from Core MD05-2925 (Liu et al., 2015); (c) Chinese cave stalagmite $\delta^{18}O$ (Cheng et al., 2016). Coherence with obliquity: (e) $\ln(K/Ca)$ from Site U1483; (f) *G. ruber* Nd/Ca from Core MD05-2925; (g) Sr/Ca from the Xifeng Loess Section (Li et al., 2017). Phase: (d) $\ln(K/Ca)$ from Site U1483, *G. ruber* Nd/Ca from Core MD05-2925 and Chinese cave stalagmite $\delta^{18}O$ against precession; (h) $\ln(K/Ca)$ from Site U1483, *G. ruber* Nd/Ca from Core MD05-2925 and Sr/Ca from the Xifeng Loess Section against obliquity. In panels of coherence, horizontal cyan lines denote the mean Monte Carlo false-alarm level. In panels of phase wheel, the zero phase is set at the maximum precession in (d) and at the maximum obliquity in (h). Light blue, green, orange, and purple shadings denote the uncertainties. Cross-spectral analyses were performed using the software program Redfit-X (Ólafsdóttir et al., 2016).

3.3. Interhemispheric Anti-Phase Precipitation on Obliquity Band in Response to Latitudinal Migration of the Indo-Pacific ITCZ

In addition to the precession signal, a strong obliquity signal occurs in the $\ln(\text{K}/\text{Ca})$ record from Site U1483 (Figures 3h, 4e, and S5h). Strong precession and obliquity signals also occur in a $\ln(\text{Ti}/\text{Ca})$ record from the north of Papua New Guinea (Hollstein et al., 2018; Tachikawa et al., 2011). However, as discussed in detail in Tachikawa et al. (2011), obliquity-related variations in the $\ln(\text{Ti}/\text{Ca})$ record were mainly caused by carbonate content changes on obliquity band. For Site U1483, spectral analysis of Ca abundance shows no obliquity signal (Figure S5a). Moreover, as mentioned above, at the coring site of Core MD01-2378 (Site U1483), terrigenous elements normalized against Ca or Ba show consistent behavior, and carbonate percentages change inconsistent with sedimentation rates (Kuhnt et al., 2015). Therefore, the occurrence of obliquity signal in the $\ln(\text{K}/\text{Ca})$ record from Site U1483 was very likely caused by variations in terrigenous input rather than carbonate dilution. This result implies that precipitation at the southern margin of the ITCZ was dominated by obliquity band variance during the past 410 kyr. Besides, *G. ruber* Nd/Ca of Core MD05-2925 and Sr/Ca of the Xifeng Loess Section (a proxy of East Asian summer monsoonal precipitation with depleted values denoting increased precipitation and vice versa) display clear variations on obliquity band (Figures 3f, 3g, 4f, and 4g), indicating that precipitation at the northern margin and center of the ITCZ was also dominated by obliquity band variance from 410 to 0 ka (Li et al., 2017; Liu et al., 2015).

Cross-spectral analysis shows that the maximum of $\ln(\text{K}/\text{Ca})$ from Site U1483 lagged the minimum of obliquity by $\sim 9^\circ$ (Figure 4h), indicating that precipitation at the southern margin of the ITCZ varied nearly in anti-phase with obliquity, agreeing with Singarayer et al. (2017) on their simulated precipitation records for northwestern Australia. Similarly, the maximum of *G. ruber* Nd/Ca in Core MD05-2925 led the minimum of obliquity by $\sim 4^\circ$ (Figure

4h), indicating that precipitation at the center of the ITCZ changed also in anti-phase with obliquity. On the contrary, the minimum of Sr/Ca at the Xifeng Loess Section led the maximum of obliquity by $\sim 12^\circ$ (Figure 4h), suggesting in-phase change of precipitation at the northern margin of the ITCZ in relation to obliquity. This scenario is also supported by obliquity bandpass filtering results, which reveal anti-phase change of $\ln(K/Ca)$ and *G. ruber* Nd/Ca but in-phase change of $-Sr/Ca$ with respect to obliquity (Figures 3e–3h). These results suggest that precipitation increases (decreases) in the northern hemisphere while decreases (increases) in the southern hemisphere on obliquity band.

In general, the influence of obliquity is very weak on low-latitude insolation but significant on Northern Hemisphere high-latitude insolation. Thus, the strong obliquity signal in low-latitude paleoclimate records is always ascribed to high-latitude forcing. For instance, rainfall records from the East China Sea agree with obliquity-paced global climate cycles, suggesting a close link between changes in low-latitude precipitation and glacial variability (Clemens et al., 2018). However, it is unclear how high-latitude forcing can cause interhemispheric anti-phasing precipitation on obliquity band. In contrast, modeling studies imply that obliquity directly influences tropical circulation by reorganizing the Hadley circulation (Bosmans et al., 2015; Mantsis et al., 2011, 2014) and regulating the north-south shift of the ITCZ (Liu et al., 2015). Some other modeling studies suggested that high obliquity can cause an extremely strong Siberian high pressure and Australian low pressure (Kutzbach et al., 2008; Shi et al., 2011), thus leading to a strong pressure gradient between hemispheres that enhances the cross-equatorial flow of northerly winds (Liu et al., 2015). The enhanced northerly winds subsequently reinforce the southward shift of the ITCZ (Liu et al., 2015). The opposite situation occurs at low obliquity. Thus, the south-north shifts of the ITCZ dominated by obliquity produced the anti-phase precipitation between hemispheres.

4. Conclusions

In this study, we investigated the history of northwestern Australia summer monsoonal precipitation over the past 410 kyr based on $\ln(K/Ca)$ of sediments from IODP Site U1483. By integrating the new precipitation record with published precipitation records from the northern margin and meteorological center of the Indo-Pacific ITCZ, we found that expansion and contraction in the latitudinal extent of the Indo-Pacific ITCZ could be responsible for interhemispheric precipitation in-phasing on precession band. In contrast, interhemispheric precipitation anti-phasing on obliquity band could be attributed to latitudinal migration of the Indo-Pacific ITCZ.

Acknowledgments

We are grateful to Haobai Fei (Institute of Earth Environment, Chinese Academy of Sciences) for stable isotopes analyses. We appreciate Xingxing Wang and Yue Wang (Tongji University) for software analysis. We are also grateful to Rui Cui and Heng Liu (Northwest University) for their contribution to the geochemical analysis. This research used samples and data provided by the International Ocean Discovery Program (IODP). We greatly thank members of the shipboard science party and crews of IODP Expedition 363 for their efforts. This work was supported by the National Natural Science Foundation of China (grant numbers 41806066, 41776060, 41830539, 41576045, and 91855211) and Undergraduate Training Program for Innovation and Entrepreneurship of Northwest University (grant number 2020258). XRF scanning was enabled through institutional funds from the Institute of Geosciences, Kiel University, Germany. We thank three anonymous reviewers for constructive comments that helped us to clarify our thoughts and improve the manuscript.

References

- Ayliffe, L. K., Gagan, M. K., Zhao, J., Drysdale, R. N., Hellstrom, J. C., Hantoro, W. S., et al. (2013). Rapid interhemispheric climate links via the Australasian monsoon during the last deglaciation. *Nature Communications*, 4(1), 2908. <https://doi.org/10.1038/ncomms3908>
- Bard, E., Raisbeck, G., Yiou, F., & Jouzel, J. (2000). Solar irradiance during the last 1200 years based on cosmogenic nuclides. *Tellus B*, 52(3), 985–992. <https://doi.org/10.3402/tellusb.v52i3.17080>
- Bassinot, F. C., Baltzer, A., Chen, M. T., DeDeckker, P., Khuhnt, W., Levitan, M., et al. (2002). Scientific Report of the WEPAMA Cruise, MD122/IMAGES VII, 453 pp. Polaires, France: Inst. Fr. pour la Rech. et la Technol.
- Bayon, G., Deckker, P. D., Magee, J. W., Germain, Y., Bermell, S., Tachikawa, K., & Norman, M. D. (2017). Extensive wet episodes in Late Glacial Australia resulting from high-latitude forcings. *Scientific Reports*, 7(1), 44054. <https://doi.org/10.1038/srep44054>
- Berger, A. L., & Loutre, M. F. (1991). Insolation values for the climate of the last 10 million years. *Quaternary Science Reviews*, 10(4), 297–317. [https://doi.org/10.1016/0277-3791\(91\)90033-Q](https://doi.org/10.1016/0277-3791(91)90033-Q)
- Bosmans, J. H. C., Hilgen, F. J., Tuenter, E., & Lourens, L. J. (2015). Obliquity forcing of low-latitude climate. *Climate of the Past*, 11(10), 1335–1346. <https://doi.org/10.5194/cp-11-1335-2015>
- Calvert, S. E., & Pedersen, T. F. (2007). In proxies in Late Cenozoic paleoceanography. In C. Hillaire, & A. de Vernal (Eds.), *Developments in quaternary research 1*, (pp. 567–644). Amsterdam: Elsevier.
- Cheng, H., Edwards, R. L., Broecker, W. S., Denton, G. H., Kong, X., Wang, Y., et al. (2009). Ice age terminations. *Science*, 326(5950), 248–252. <https://doi.org/10.1126/science.1177840>
- Cheng, H., Edwards, R. L., Sinha, A., Spöt, C., Yi, L., Chen, S., et al. (2016). The Asian monsoon over the past 640,000 years and ice age terminations. *Nature*, 534(7609), 640–646. <https://doi.org/10.1038/nature18591>
- Clemens, S. C., Holbourn, A., Kubota, Y., Lee, K. E., Liu, Z., Chen, G., et al. (2018). Precession-band variance missing from East Asian monsoon runoff. *Nature Communications*, 9(1), 3364. <https://doi.org/10.1038/s41467-018-05814-0>
- Collins, J. A., Schefuß, E., Heslop, D., Mulitza, S., Prange, M., Zabel, M., et al. (2010). Interhemispheric symmetry of the tropical African rainbelt over the past 23,000 years. *Nature Geoscience*, 4(1), 42–45. <https://doi.org/10.1038/NGEO1039>
- Dang, H., Jian, Z., Kissel, C., & Bassinot, F. (2015). Precessional changes in the western equatorial Pacific hydroclimate: A 240 kyr marine record from the Halmahera Sea, East Indonesia. *Geochemistry, Geophysics, Geosystems*, 16, 148–164. <https://doi.org/10.1002/2014GC005550>

- Denniston, R. F., Ummenhofer, C. C., Wanamaker, J. A. D., Lachniet, M. S., Villarini, G., Asmerom, Y., et al. (2016). Expansion and contraction of the Indo-Pacific tropical rain belt over the last three millennia. *Scientific Reports*, 6(1), 34485. <https://doi.org/10.1038/srep34485>
- Doupé, R. G., & Pettit, N. E. (2002). Ecological perspectives on regulation and water allocation for the Ord River, Western Australia. *River Research and Applications*, 18(3), 307–320. <https://doi.org/10.1002/rra.676>
- Haug, G. H., Hughen, K. A., Sigman, D. M., Peterson, L. C., & Rohl, U. (2001). Southward migration of the intertropical convergence zone through the Holocene. *Science*, 293(5533), 1304–1308. <https://doi.org/10.1126/science.1059725>
- Hollstein, M., Mohtadi, M., Rosenthal, Y., Prange, M., Oppo, D. W., Mendez, G. M., et al. (2018). Variations in Western Pacific Warm Pool surface and thermocline conditions over the past 110,000 years: Forcing mechanisms and implications for the glacial Walker circulation. *Quaternary Science Reviews*, 201, 429–445. <https://doi.org/10.1016/j.quascirev.2018.10.030>
- Huang, J., Wan, S., Li, A., & Li, T. (2019). Two-phase structure of tropical hydroclimate during Heinrich Stadial 1 and its global implications. *Quaternary Science Reviews*, 222, 105900. <https://doi.org/10.1016/j.quascirev.2019.105900>
- Konecky, B. L., Russell, J. M., Rodysill, J. R., Vuille, M., Bijaksana, S., & Huang, Y. (2013). Intensification of southwestern Indonesian rainfall over the past millennium. *Geophysical Research Letters*, 40, 386–391. <https://doi.org/10.1029/2012GL054331>
- Kotov, S., and Pälke, H. (2018). QAnalySeries—a cross-platform time series tuning and analysis tool. AGU Fall Meeting. <https://doi.org/10.1002/essoar.10500226.1>
- Kuhnt, W., Holbourn, A., Xu, J., Opdyke, B., Deckker, P. D., Röhl, U., & Mudelsee, M. (2015). Southern Hemisphere control on Australian monsoon variability during the late deglaciation and Holocene. *Nature Communications*, 6(1), 5916. <https://doi.org/10.1038/ncomms6916>
- Kutzbach, J. E., Liu, X., Liu, Z., & Chen, G. (2008). Simulation of the evolutionary response of global summer monsoons to orbital forcing over the past 280,000 years. *Climate Dynamics*, 30(6), 567–579. <https://doi.org/10.1007/s00382-007-0308-z>
- Laskar, J., Fienga, A., Gastineau, M., & Manche, H. (2011). La2010: A new orbital solution for the long-term motion of the earth. *Astronomy & Astrophysics*, 532, A89. <https://doi.org/10.1051/0004-6361/201116836>
- Li, T., Liu, F., Abels, H. A., You, C., Zhang, Z., Chen, J., et al. (2017). Continued obliquity pacing of East Asian summer precipitation after the mid-Pleistocene transition. *Earth and Planetary Science Letters*, 457, 181–190. <https://doi.org/10.1016/j.epsl.2016.09.045>
- Lindsay, R. P., and Commander, D. P. (2006). Hydrological assessment of the Fitzroy alluvium. Government of Western Australia, Department of Water Report N°, HG16, 41 pp.

- Liu, Y., Liu, X., Hu, Z., Diwu, C., Yuan, H., & Gao, S. (2007). Evaluation of accuracy and long-term stability of determination of 37 trace elements in geological samples by ICP-MS. *Acta Petrologica Sinica*, 23(5), 1203–1210.
- Liu, Y., Lo, L., Shi, Z., Wei, K., & Shen, C. (2015). Obliquity pacing of the western pacific intertropical convergence zone over the past 282,000 years. *Nature Communications*, 6(1), 10018. <https://doi.org/10.1038/ncomms10018>
- Mantsis, D. F., Clement, A. C., Broccoli, A. J., & Erb, M. P. (2011). Climate feedbacks in response to changes in obliquity. *Journal of Climate*, 24(11), 2830–2845. <https://doi.org/10.1175/2010jcli3986.1>
- Mantsis, D. F., Lintner, B. R., Broccoli, A. J., Erb, M. P., Clement, A. C., & Park, H. S. (2014). The response of large-scale circulation to obliquity-induced changes in meridional heating gradients. *Journal of Climate*, 27(14), 5504–5516. <https://doi.org/10.1175/jcli-d-13-00526.1>
- Marshall, J., Donohoe, A., Ferreira, D., & McGee, D. (2014). The ocean's role in setting the mean position of the inter-tropical convergence zone. *Climate Dynamics*, 42(7-8), 1967–1979. <https://doi.org/10.1007/s00382-013-1767-z>
- Ólafsdóttir, B. K., Schulz, M., & Mudelsee, M. (2016). REDFIT-X: Cross-spectral analysis of unevenly spaced paleoclimate time series. *Computational Geosciences*, 91, 11–18. <https://doi.org/10.1016/j.cageo.2016.03.001>
- Rosenthal, Y., Holbourn, A., Kulhanek, D.K., & the Expedition 363 Scientists, (2017). International Ocean Discovery Program Expedition 363 Preliminary Report Western Pacific Warm Pool Neogene and Quaternary records of Western Pacific Warm Pool paleoceanography. <https://doi.org/10.14379/iodp.pr.363.2017>.
- Schneider, T., Bischoff, T., & Haug, G. H. (2014). Migrations and dynamics of the intertropical convergence zone. *Nature*, 513(7516), 45–53. <https://doi.org/10.1038/nature13636>
- Schröder, J. F., Holbourn, A., Kuhnt, W., & Küssner, K. (2016). Variations in sea surface hydrology in the southern Makassar Strait over the past 26 kyr. *Quaternary Science Reviews*, 154, 143–156. <http://doi.org/10.1016/j.quascirev.2016.10.018>
- Scroxton, N., Burns, S. J., McGee, D., Hardt, B., Godfrey, L. R., Ranivoharimanana, L., & Faina, P. (2017). Hemispherically in-phase precipitation variability over the last 1700 years in a Madagascar speleothem record. *Quaternary Science Reviews*, 164, 25–36. <https://doi.org/10.1016/j.quascirev.2017.03.017>
- Shi, Z., Liu, X., Sun, Y., An, Z., Liu, Z., & Kutzbach, J. (2011). Distinct responses of East Asian summer and winter monsoons to astronomical forcing. *Climate of the Past*, 7(4), 1363–1370. <https://doi.org/10.5194/cp-7-1363-2011>
- Singarayer, J. S., Valdes, P. J., & Roberts, W. H. G. (2017). Ocean dominated expansion and contraction of the late Quaternary tropical rainbelt. *Scientific Reports*, 7(1), 9382. <https://doi.org/10.1038/s41598-017-09816-8>

- Tachikawa, K., Cartapanis, O., Vidal, L., Beaufort, L., Barlyaeva, T., & Bard, E. (2011). The precession phase of hydrological variability in the Western Pacific Warm Pool during the past 400 ka. *Quaternary Science Reviews*, 30(25-26), 3716–3727. <https://doi.org/10.1016/j.quascirev.2011.09.016>
- Taylor, S. R., & McLennan, S. M. (1985). *The continental crust: Its composition and evolution*, (p. 312). Malden: Blackwell.
- Taylor, S. R., & McLennan, S. M. (1995). The geochemical evolution of the continental-crust. *Reviews of Geophysics*, 33(2), 241–265. <https://doi.org/10.1029/95RG00262>
- Vroon, P. Z., Bergen, M. J. V., Klaver, G. J., & White, W. M. (1995). Strontium, neodymium, and lead isotopic and trace-element signatures of the East Indonesian sediments: Provenance and implications for Banda Arc magma genesis. *Geochimica et Cosmochimica Acta*, 59(12), 2573–2598. [https://doi.org/10.1016/0016-7037\(95\)00151-4](https://doi.org/10.1016/0016-7037(95)00151-4)
- Waliser, D. E., & Gautier, C. (1993). A satellite-derived climatology of the ITCZ. *Journal of Climate*, 6(11), 2162–2174. [https://doi.org/10.1175/1520-0442\(1993\)006<2162:ASDCOT>2.0.CO;2](https://doi.org/10.1175/1520-0442(1993)006<2162:ASDCOT>2.0.CO;2)
- Wang, X., Auler, A. S., Edwards, R. L., Cheng, H., Ito, E., & Solheid, M. (2006). Interhemispheric anti-phasing of rainfall during the last glacial period. *Quaternary Science Reviews*, 25(23-24), 3391–3403. <https://doi.org/10.1016/j.quascirev.2006.02.009>
- Wang, Y., Cheng, H., Edwards, R. L., An, Z., Wu, J., Shen, C., & Dorale, J. A. (2001). A high-resolution absolute-dated Late Pleistocene monsoon record from Hulu Cave, China. *Science*, 294(5550), 2345–2348. <https://doi.org/10.1126/science.1064618>
- Wang, Y., Cheng, H., Edwards, R. L., Kong, X., Shao, X., Chen, S., et al. (2008). Millennial- and orbital-scale changes in the East Asian monsoon over the past 224,000 years. *Nature*, 451(7182), 1090–1093. <https://doi.org/10.1038/nature06692>
- Wu, J., Liu, Z., & Zhou, C. (2013). Provenance and supply of Fe-enriched terrigenous sediments in the western equatorial Pacific and their relation to precipitation variations during the late Quaternary. *Global and Planetary Change*, 108, 56–71. <https://doi.org/10.1016/j.gloplacha.2013.06.002>
- Yan, H., Wei, W., Soon, W., An, Z., Zhou, W., Liu, Z., et al. (2015). Dynamics of the intertropical convergence zone over the western Pacific during the Little Ice Age. *Nature Geoscience*, 8(4), 315–320. <https://doi.org/10.1038/ngeo2375>

Supporting Information for

Indo-Pacific hydroclimate in response to changes of the Intertropical Convergence Zone: Discrepancy on precession and obliquity bands over the last 410 kyr

Introduction

There are five texts and six figures in this file. Text S1 introduces the revision of shipboard core SPLICE. Text S2 addresses the age model of Site U1483. Text S3 brings up the element compositions of bulk sediments for discrete samples. Text S4 introduces the XRF scanning derived elements. Text S5 discusses Chinese cave stalagmite $\delta^{18}\text{O}$ as a proxy of East Asian summer monsoon precipitation. Figure S1 shows the age models for Site U1483 and Core MD01-2378. Figure S2 displays the distribution patterns of UCC-normalized major, trace and rare earth elements in bulk sediment samples of MIS 1-11 from Site U1483. Figure S3 exhibits the profiles of major elements in sediments from Site U1483. Figure S4 plots the records of Ca-normalized major elements. Figure S5 shows spectral analysis on time series of major elements and Ca-normalized major elements. Figure S6 shows the relationship of XRF element ratios and CIX.

Text S1. Revision of shipboard core SPLICE

Based on new high-resolution X-ray fluorescence (XRF) scanner elemental data and benthic stable isotope records, we adjusted the original tie points of the shipboard SPLICE (14.57 m below sea floor (mbsf) in U1483C-2H-6 and 13.19 mbsf in U1483B-3H-2) to new positions (14.58 mbsf in U1483C-2H-6 and 12.26 mbsf in U1483B-3H-2). This adjustment resulted in the overall addition of 0.94 m to the meters composite depth (mcd) scale.

Text S2. Age model of Site U1483

The preliminary age model for Site U1483 over the past 410 kyr (Fig. S1a) was established by tuning the benthic $\delta^{18}\text{O}$ to the global benthic stack (Lisiecki and Raymo, 2005) with the QAnalySeries software (Kotov and Pälike, 2018). The original age model of Core MD01-2378 was published in Holbourn et al. (2005) based on AMS ^{14}C dates (0-30 ka) and correlation to the benthic $\delta^{18}\text{O}$ to the Byrd ice core (Blunier and Brook, 2001) (30-60 ka), the benthic stack of Martinson et al. (1987) (60-290 ka) and the stack record of Bassinot et al. (1994) (290-460 ka). We retuned the age model of Core MD01-2378 by correlating its benthic $\delta^{18}\text{O}$ with the global benthic stack (Lisiecki and Raymo, 2005) (Fig. S1b) using QAnalySeries (Kotov and Pälike, 2018).

The benthic $\delta^{18}\text{O}$ records from Site U1483 and Core MD01-2378 matched almost perfectly and showed the same glacial-interglacial amplitudes for the past 410 kyr (Fig. S1c), since they have the same coordinates (Fig. 1). A very small phase shift in the benthic $\delta^{18}\text{O}$ records, however, was linked to the higher resolution of the benthic $\delta^{18}\text{O}$ record of Core MD01-2378 (Fig. S1c). To further improve the age model for Site U1483, XRF- derived high-resolution records of $\ln(\text{K}/\text{Ca})$ from Site U1483 and Core MD01-2378 were correlated using QAnalySeries (Kotov and Pälike, 2018) (Fig. 2a). According to the new age model for Site U1483, the last occurrence of *Globigerinoides ruber* (pink) at ~11.81 mcd (Fig. 2a) is equivalent to an age of ~122.91 ka, consistent with the biostratigraphic datum given by Thompson et al. (1979). The estimated sedimentation rate ranges from 7.46 to 13.8 cm/kyr with a mean value of 10.31 cm/kyr and displays no obvious glacial-interglacial changes (Fig. 2b). The sampling temporal resolution for benthic foraminiferal $\delta^{18}\text{O}$ is ~2 kyr and for $\ln(\text{K}/\text{Ca})$ is ~0.2 kyr.

Text S3. Element compositions of bulk sediments for discrete samples

The major element compositions of bulk sediments from MIS 1-11 at Site U1483 normalized to the upper continental crust (UCC) (Taylor and McLennan, 1985, 1995) are very similar, with enriched MnO and highly enriched CaCO₃ (Fig. S2a). The average CaCO₃ content of ~50% reflects that the pelagic fractions compose the main components of sediments at Site U1483. The trace and rare earth element compositions of bulk sediments from MIS 1-11 at Site U1483 normalized to the UCC are also very similar (Figs. S2b and S2c). For trace elements, Ni and Y are enriched relative to other elements (Fig. S2b). With respect to rare earth elements, the middle and heavy rare earth elements (Sm to Lu) are enriched relative to the light rare earth elements (La to Nd) with positive Eu anomalies (Fig. S2c).

Text S4. XRF scanning derived elements

Abundances of Al, K, Ti and Fe derived by XRF scanning oscillated very similarly and in an opposite way to abundance of Ca in the past 410 kyr (Figs. S3b-S3f). The XRF scanning results are highly supported by measurements of bulk sediment major elements on discrete samples (Figs. S3b-S3f). Nevertheless, there are still difference in the case of lighter elements, i.e. Ca, Al and K. The difference can be reflected in the scanning abundances of the lighter elements decreasing during the past 120 kyr and increasing from 120 to 410 kyr (Figs. S3b-S3d), which indicates an anti-phase linkage to the variation in the scanned Cl abundance as a monitor of water content in cores (Fig. S3a).

Previous studies have shown that the water content in cores has a strong attenuation effect on the scanning abundances of lighter elements (e.g., Tjallingii et al., 2007; Hennekam and de Lange, 2012). Thus, the deviations of the scanning abundances of lighter elements should be related to the attenuation effect of water content in cores. Here, we correct the

influence of the attenuation effect on the scanning abundance of lighter elements following the method of Dang et al. (2015). We can see that the corrected results match better with the measuring results (Figs. S3b-S3d). Subsequently, we reconstructed the variation of Ca-normalized major elements based on the corrected results, and found that Ca-normalized major elements co-varied with each other throughout the whole study interval (Fig. S4).

Spectral analysis of the XRF scanning results shows that, on orbital timescale, precession and obliquity bands dominate variations in abundances of Al, K, Ti and Fe but the eccentricity and precession bands occur in Ca for the past 410 kyr (Figs. S5a-S5e). Meanwhile, precession and obliquity bands also dominate variations of Ca-normalized terrigenous elements, i.e. $\ln(\text{Al}/\text{Ca})$, $\ln(\text{K}/\text{Ca})$, $\ln(\text{Ti}/\text{Ca})$ and $\ln(\text{Fe}/\text{Ca})$ (Figs. S5f-S5i). It is worth noting that strong eccentricity signals occur in $\ln(\text{Al}/\text{Ca})$ and $\ln(\text{Fe}/\text{Ca})$ (Figs. S5f and S5g), but this signal should be ascribed to variation in Ca abundance as it is non-existent in variation of Al and Fe abundances (Figs. S5b and S5e).

Overall, all of the records above from Site U1483 don't show glacial-interglacial cycles besides Ca (Figs. S3-S5). This phenomenon contrasts with the palynological record from the Timor Sea (Kawamura et al., 2006), organic geochemical record from the northern perimeter of Australia (Kershaw et al., 2003) and XRF scanning records from the

Halmahera Sea (Dang et al., 2015) and offshore northwestern Australia (Stuut et al., 2019), all of which have obvious glacial-interglacial contrasts. In general, terrigenous input increases during sea level low-stands of glacial periods because of increased shelf exposure and decreased distance of river mouths to the sedimentary basin, and vice versa. Moreover, chemical weathering associated terrigenous input may be also different between glacial and interglacial. However, we did not see conspicuous glacial and interglacial contrasts in the terrigenous elements records and estimated sedimentation rate of Site U1483 (Figs. 2b and S3).

Thus, glacial-interglacial changes in sea level and chemical weathering may not influence the depositional environment at Site U1483.

In addition, Al and Ti are known to be chemically resistant to erosion and weathering (Nesbitt et al., 1980; Nesbitt and Markovics, 1997). Using the CIX index (i.e. Chemical Index of Alteration that does not consider CaO; Garzanti et al., 2014) as an indicator of chemical weathering, the long-term trend of K/Al largely differs from that of CIX (Fig. S6a), indicating a minor influence of chemical weathering on the leaching of K. This is supported by the close correspondence between Al/Ti and K/Ti profiles (Fig. S6b). Furthermore, the CIX ranges from 56.7 to 68.7 in value, reflecting a relative weak of weathering intensity (Fig. S6a). The scattered data distributions of K/Al and K/Ti against CIX (Fig. S6c and 6d) further supports that chemical weathering exerted a very minor, if any, influence on the leaching of K in sediments of Site U1483.

As for Ca, the occurrence of glacial-interglacial cycles (Figs. S3b and S5a) is possibly indirectly linked to the variation in sea level. Holbourn et al. (2005) found that productivity fluctuations in the Timor Sea over the last 460 kyr were strongly influenced by monsoonal wind patterns offshore northwestern Australia (23 and 19 kyr) and were also modulated by sea level-related variations in the intensity of the Indonesian Throughflow (100 kyr). Hence, the variations in Ca content on precession and eccentricity bands may be linked to the variations in the productivity of Timor Sea, indicating that Ca was derived from the biogenic carbonate of marine planktons.

Text S5. Chinese cave stalagmite $\delta^{18}\text{O}$ as a proxy of East Asian summer monsoon precipitation

Among paleo-precipitation indices, Chinese cave stalagmite $\delta^{18}\text{O}$ has been considered to reflect rainfall associated with East Asian summer monsoon (Wang et al., 2001 and 2008; Cheng et al., 2009 and 2012). Later, some studies however revealed that Chinese cave stalagmite $\delta^{18}\text{O}$ could be influenced by a variety of factors, such as upstream water vapour $\delta^{18}\text{O}$ (Pausata et al., 2011), moisture sources (Maher and Thompson, 2012; Liu et al., 2014), sea level changes (Xue et al., 2019) and the position of the westerlies (Zhang et al., 2018). Moreover, Liu et al. (2017) debated that ‘Chinese cave $\delta^{18}\text{O}$ records do not represent northern East Asian summer monsoon rainfall’. In contrast, some other studies still considered Chinese cave stalagmite $\delta^{18}\text{O}$ as a proxy of East Asian summer monsoonal precipitation, with depleted value denoting enhanced precipitation and vice versa (e.g. Liu et al., 2015; Yan et al., 2015; Denniston et al., 2016 and 2017; Huang et al., 2019). Recently, Goldsmith et al. (2017a) discovered a good correlation between Chinese cave stalagmite $\delta^{18}\text{O}$ and lake-level of Lake Dali in Inner Mongolia (a proxy of East Asian summer monsoonal precipitation) during the past 125 kyr, and suggested that Chinese cave stalagmite $\delta^{18}\text{O}$ well denotes change of the East Asian summer monsoonal precipitation on both orbital and millennial timescales. In reply to rebuttal of Liu et al. (2017) against the viewpoint of Goldsmith et al. (2017a), Goldsmith et al. (2017b) supplied more lines of evidence, and again claimed that the scaling between the Lake Dali record and Chinese cave speleothem $\delta^{18}\text{O}$ is robust.

The assertion of ‘Chinese cave $\delta^{18}\text{O}$ records do not represent northern East Asian summer monsoon rainfall’ by Liu et al. (2017) is partially based on the occurrence time of precipitation maximum in the Holocene. The record of Lake Dali lake-level indicates a mid-Holocene maximum and in contrast Chinese cave stalagmite $\delta^{18}\text{O}$ shows an early- Holocene

maximum (Liu et al., 2017). With a compilation of pollen profiles across China, Zhou et al. (2016) proposed that the onset of precipitation maximum was progressively later from the south to the north in the East Asian monsoon region in the early- to mid- Holocene. Hence, it seems that the occurrence time of precipitation maximum in the mid-Holocene for lake-level of Lake Dali record doesn't conflict with an early Holocene precipitation maximum inferred from Chinese cave stalagmite $\delta^{18}\text{O}$ record.

It is noteworthy that a more recent study of Yang et al. (2019) suggested that Chinese cave stalagmite $\delta^{18}\text{O}$ should be regarded as a proxy of East Asian summer monsoonal intensity rather than of local precipitation. These authors also pointed out that the stacked Chinese cave stalagmite $\delta^{18}\text{O}$ record shows a high similarity with other East Asian summer monsoon/precipitation records in China on the orbital timescale, although differences exist among individual cave stalagmite $\delta^{18}\text{O}$ records on the centennial- millennial timescale. Two points stand out that the Chinese cave stalagmite $\delta^{18}\text{O}$ record used in our study may represent the mean state of summer monsoon/precipitation on the orbital timescale, on the one hand, and an individual cave stalagmite $\delta^{18}\text{O}$ does not represent local precipitation at the site but monsoon intensity on the centennial- millennial timescale, on the other hand. Moreover, long-term monsoon intensity proxied by the stacked cave stalagmite $\delta^{18}\text{O}$ record covaried well with the precipitation record from the Gonghai Lake (Yang et al., 2019), suggesting high precipitation happened in coincidence with strong monsoon intensity on the orbital timescale. As in this study we discussed variations in a large spatial coverage of the mean state of precipitation on orbital timescale, we are thus pro to stalagmite $\delta^{18}\text{O}$ as an indirect proxy of precipitation before the complexity of the factors affecting the stalagmite $\delta^{18}\text{O}$ are fully understood.

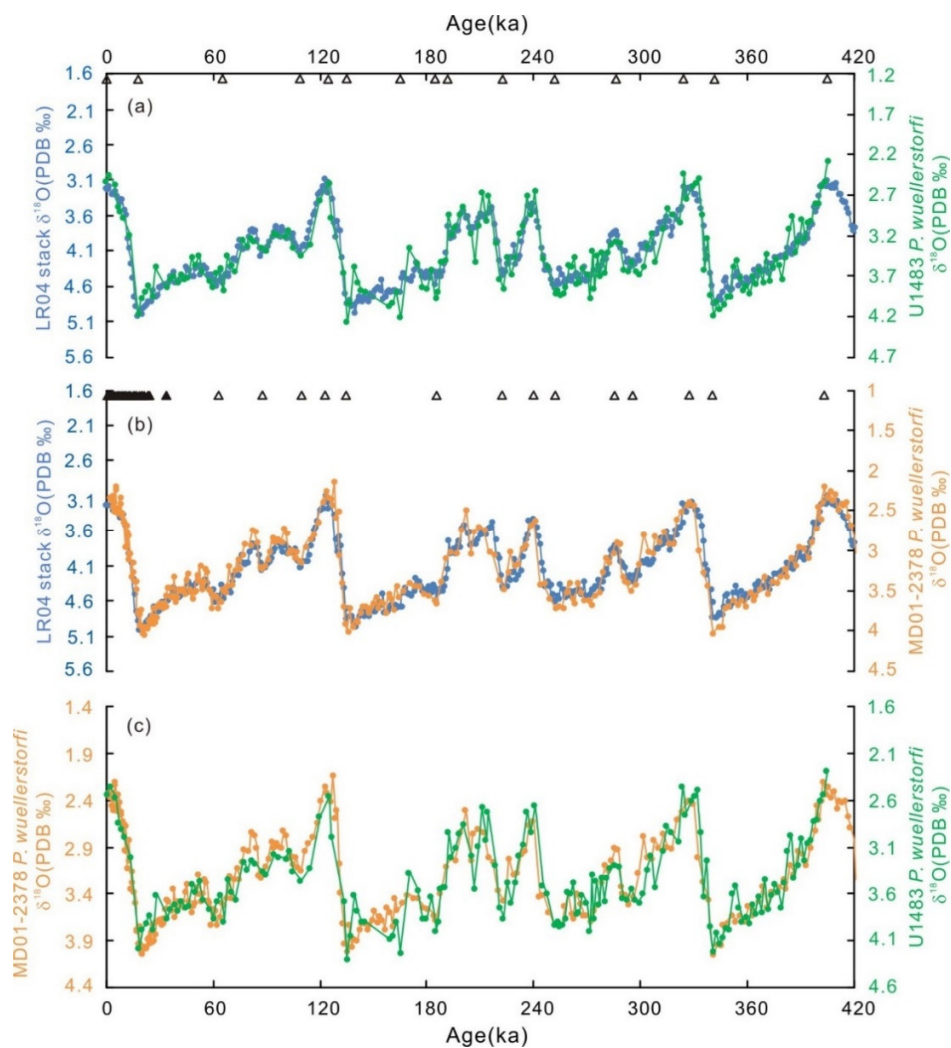


Figure. S1. Age models for Site U1483 and Core MD01-2378. Comparison of benthic $\delta^{18}\text{O}$ records from Site U1483 (a) and Core MD01-2378 (b) respectively with the global benthic stack (Lisiecki and Raymo, 2005). (c) Comparison of benthic $\delta^{18}\text{O}$ records from Site U1483 and Core MD01-2378. Filled and open triangles represent AMS ^{14}C dates and benthic $\delta^{18}\text{O}$ tie points, respectively. Benthic $\delta^{18}\text{O}$ and AMS ^{14}C data for Core MD01-2378 were published in Holbourn et al. (2005).

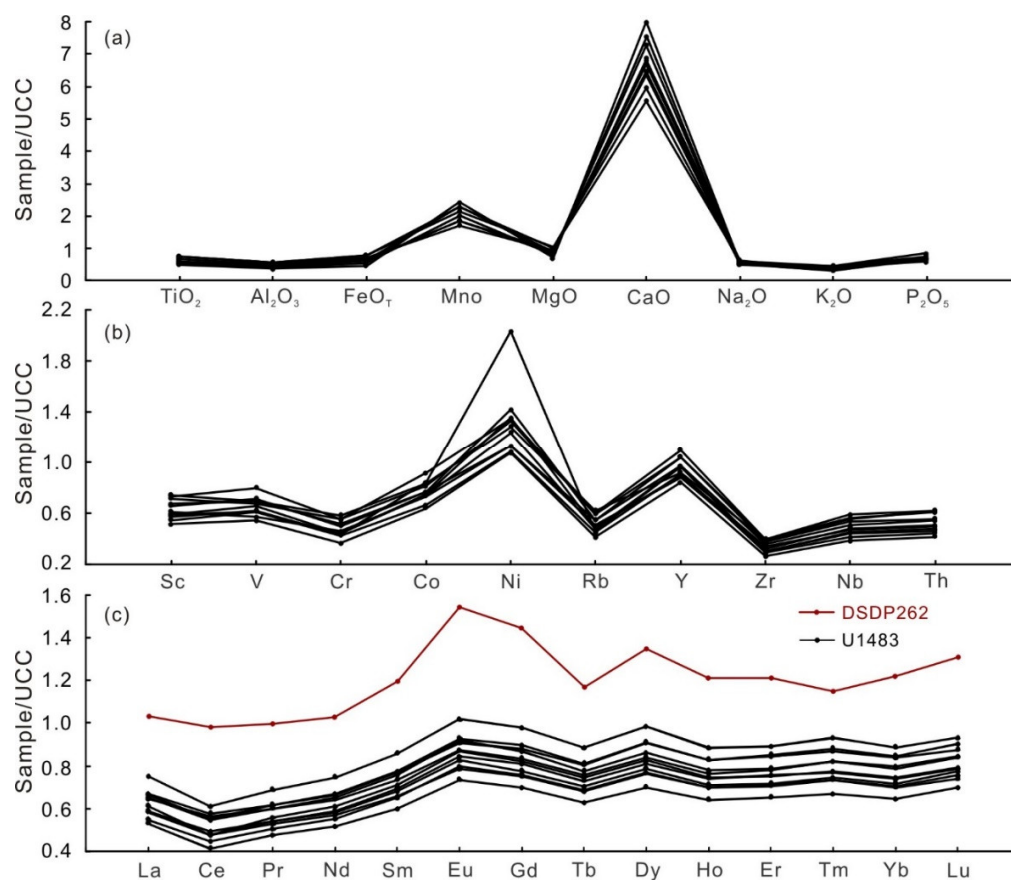


Figure. S2 Distribution patterns of UCC-normalized major (a), trace (b) and rare earth (c) elements in bulk sediment samples of MIS 1-11 from Site U1483.

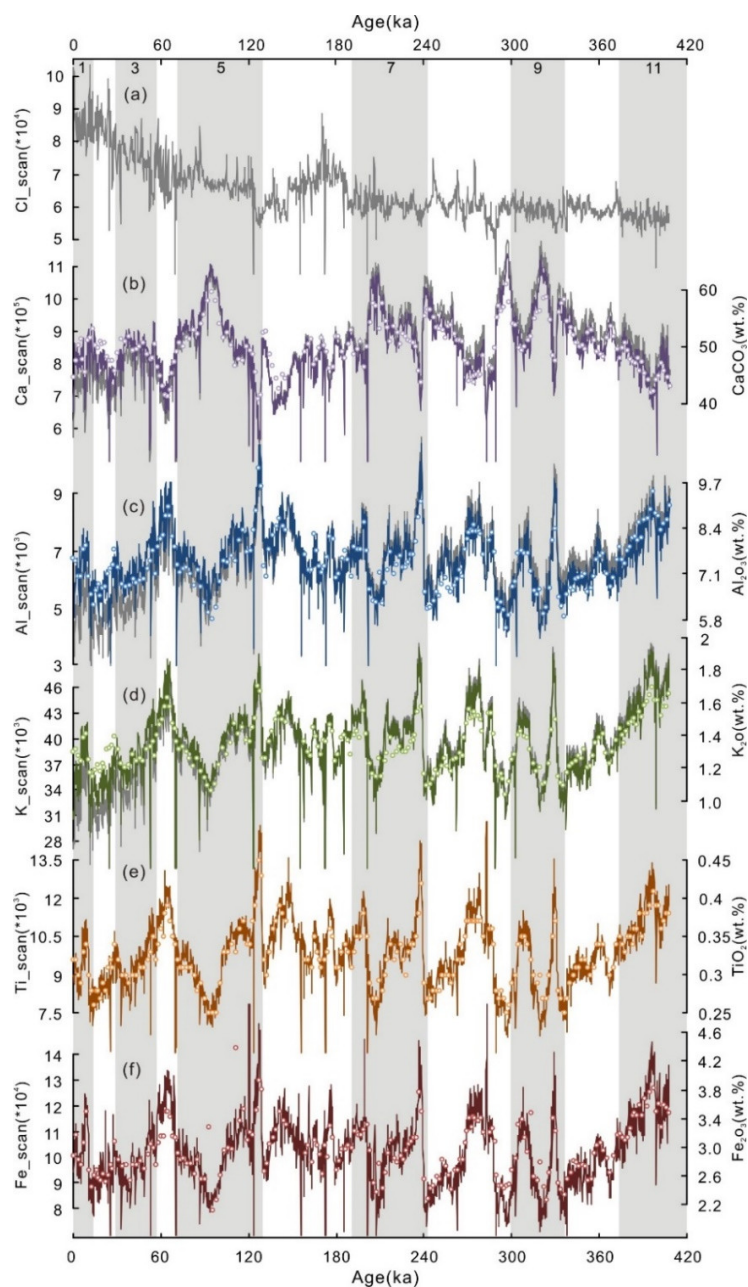


Figure. S3 Profiles of major elements in sediments from Site U1483. (a) Cl scanning; (b, c and d) raw scanning (thin grey lines) and CI-corrected (thin coloured lines) results for Ca, Al and K; (e, f) Ti and Fe scanning. Open dots on each panel denote XRF measurements on discrete sediment samples and thin lines XRF scanning results. Grey shadings mark interglacials and numbers above the grey shadings indicate marine isotope stages.

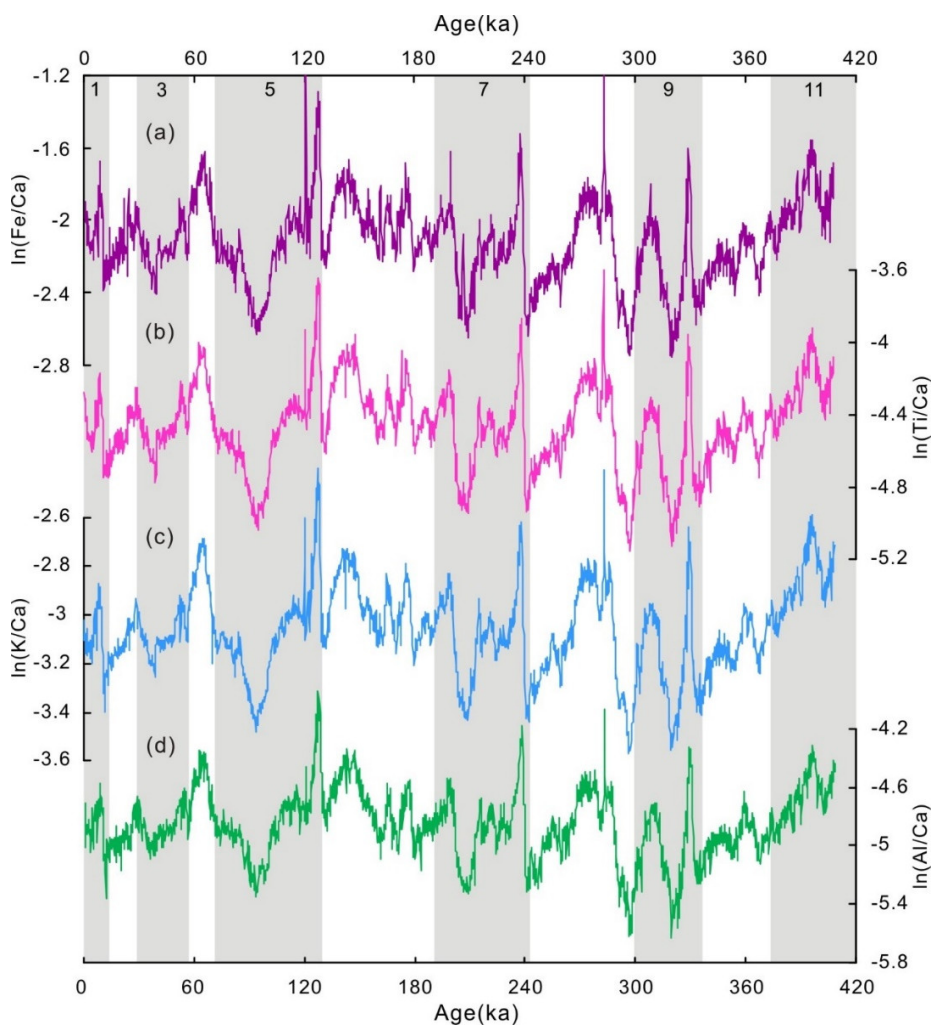


Figure. S4 Records of Ca-normalized major elements. (a) $\ln(\text{Fe}/\text{Ca})$; (b) $\ln(\text{Ti}/\text{Ca})$; (c) $\ln(\text{K}/\text{Ca})$; and (d) $\ln(\text{Al}/\text{Ca})$. Grey shadings mark interglacials and numbers over the shadings indicate marine isotope stages.

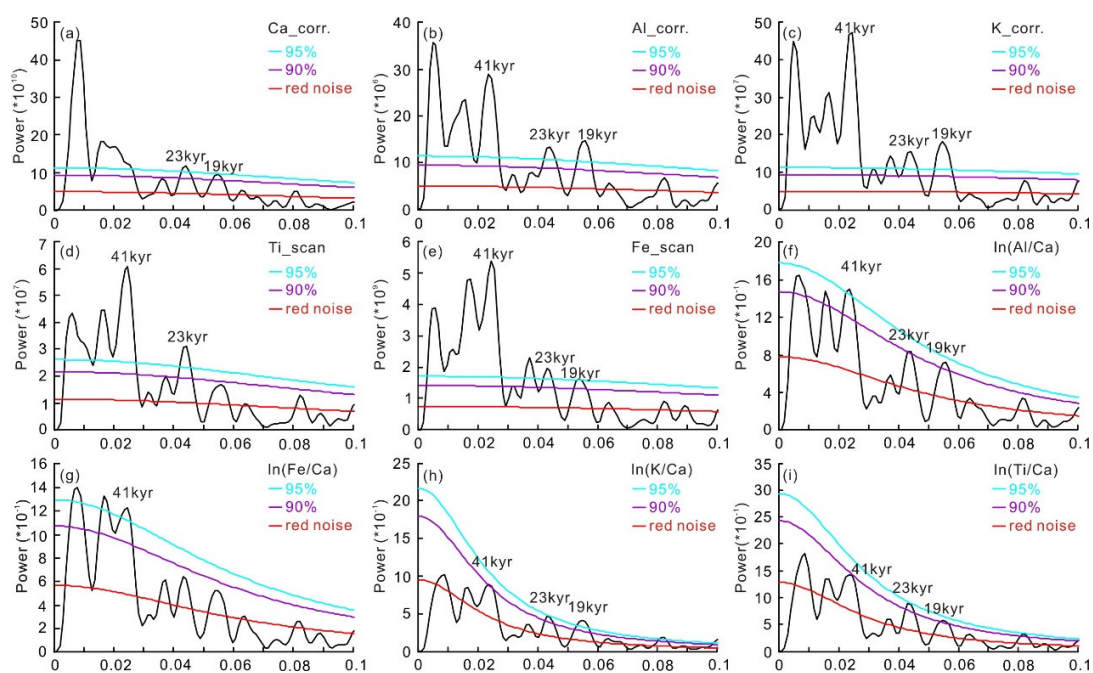


Figure. S5 Spectral analysis on time series of major elements and Ca-normalized major elements. (a) Ca; (b) Al; (c) K; (d) Ti; (e) Fe; (f) $\ln(\text{Al}/\text{Ca})$; (g) $\ln(\text{Fe}/\text{Ca})$; (h) $\ln(\text{K}/\text{Ca})$; and (i) $\ln(\text{Ti}/\text{Ca})$. Spectral analysis was performed using REDFIT (Schulz and Mudelsee, 2002) with Rectangle window (Oversample=5; Segments=3) from software program Past3 (Hammer et al., 2001).

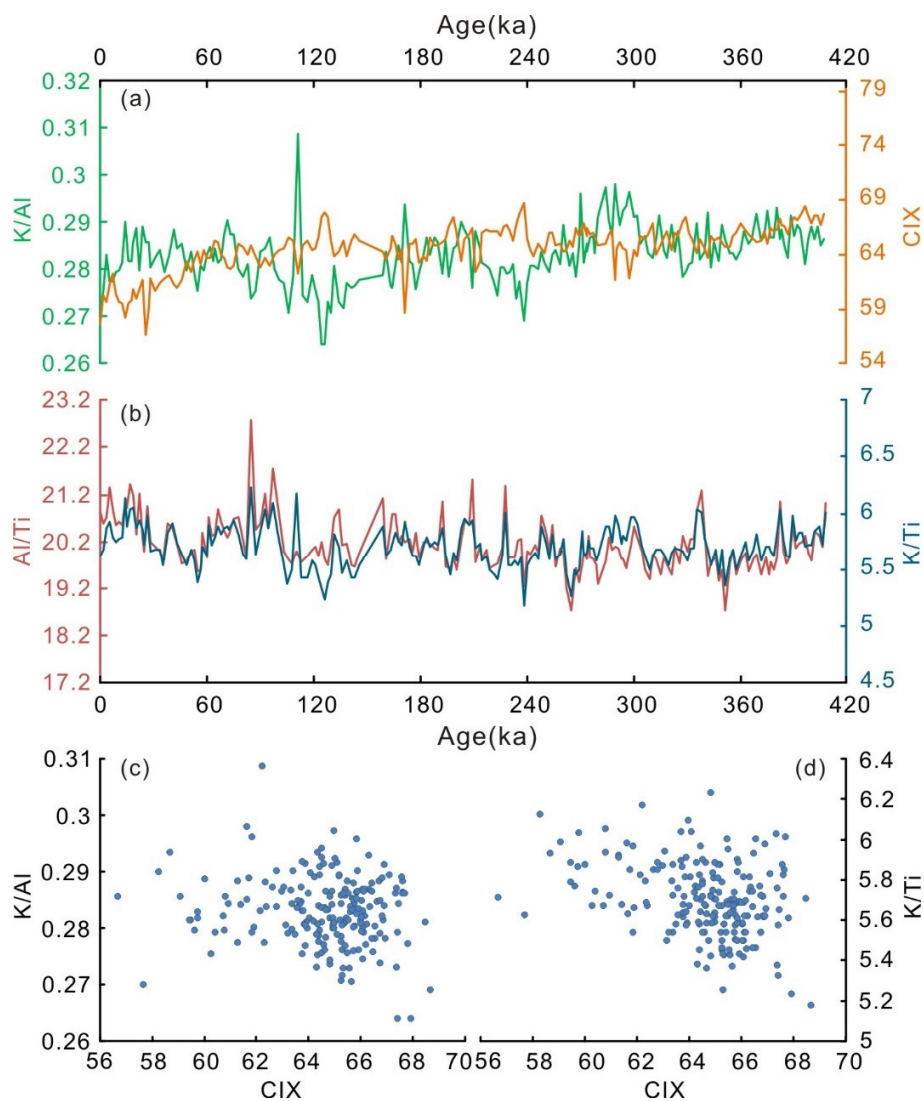


Figure. S6 Relationship of XRF element ratios and CIX. (a) K/Al and CIX; (b) Al/Ti and K/Ti; (c) K/Al and CIX; (d) K/Ti and CIX. All the elemental contents were derived from XRF measurements on discrete sediment samples. The value of CIX is calculated following the way of Garzanti et al. (2014). Note that salinity correction has been carried out for the content of Na when calculating CIX values.

References From the Supporting Information

- Bassinot, F., Labeyrie, L., Vincent, E., Quidelleur, X., Shackleton, N. J., & Lancelot, Y. (1994). The astronomical theory of climate and the age of the Brunhes-Matuyama magnetic reversal. *Earth and Planetary Science Letters*, 126(1-3), 91–108. [https://doi.org/10.1016/0012-821X\(94\)90244-5](https://doi.org/10.1016/0012-821X(94)90244-5)
- Blunier, T., & Brook, E. J. (2001). Timing of millennial-scale climate change in Antarctica and Greenland during the last glacial period. *Science*, 291(5501), 109–112. <https://doi.org/10.1126/science.291.5501.109>
- Cheng, H., Sinha, A., Wang, X., Cruz, F. W., & Edwards, R. L. (2012). The Global Paleomonsoon as seen through speleothem records from Asia and the Americas. *Climate Dynamics*, 39(5), 1045–1062. <https://doi.org/10.1007/s00382-012-1363-7>
- Denniston, R. F., Asmerom, Y., Polyak, V. J., Wanamaker, A. D. Jr., Ummenhofer, C. C., Humphreys, W. F., et al. (2017). Decoupling of monsoon activity across the northern and southern Indo-Pacific during the Late Glacial. *Quaternary Science Reviews*, 176, 101–105. <https://doi.org/10.1016/j.quascirev.2017.09.014>
- Garzanti, E., Padoan, M., Setti, M., López-Galindo, A., & Villa, I. M. (2014). Provenance versus weathering control on the composition of tropical river mud (Southern Africa). *Chemical Geology*, 366, 61–74. <https://doi.org/10.1016/j.chemgeo.2013.12.016>
- Goldsmith, Y., Broecker, W. S., Xu, H., Polissar, P. J., deMenocal, P. B., Porat, N., et al. (2017a). Northward extent of East Asian monsoon covaries with intensity on orbital and millennial timescales. *Proceedings of the National Academy of Sciences of the United States of America*, 114(8), 1817–1821. <https://doi.org/10.1073/pnas.1616708114>
- Goldsmith, Y., Broecker, W. S., Xu, H., Polissar, P. J., deMenocal, P. B., Porat, N., et al. (2017b). East Asian summer monsoon rainfall dominates Lake Dali lake area changes. *Proceedings of the National Academy of Sciences of the United States of America*, 114(15), E2989–E2990. <https://doi.org/10.1073/pnas.1703511114>
- Hammer, Ø., Harper, D. A. T., & Ryan, P. D. (2001). PAST: Paleontological statistics software package for education and data analysis. *Palaeontologia Electronica*, 4(1), 9.
- Hennekam, R., & Lange, G. D. (2012). X-ray fluorescence core scanning of wet marine sediments: Methods to improve quality and reproducibility of high resolution paleoenvironmental records. *Limnology and Oceanography: Methods*, 10(12), 991–1003. <https://doi.org/10.4319/lom.2012.10.991>
- Holbourn, A., Kuhnt, W., Kawamura, H., Jian, Z., Grootes, P., Erlenkeuser, H., & Xu, J. (2005). Orbitally paced paleoproductivity variations in the Timor Sea and Indonesian Throughflow variability during the last 460 kyr. *Paleoceanography*, 20, PA3002. <https://doi.org/10.1029/2004PA001094>
- Kawamura, H., Holbourn, A., & Kuhnt, W. (2006). Climate variability and land-ocean interactions in the Indo Pacific Warm Pool: A 460-ka palynological and organic geochemical record from the Timor Sea. *Marine Micropaleontology*, 59(1), 1–14. <https://doi.org/10.1016/j.marmicro.2005.09.001>

- Kershaw, A. P., van der Kaars, S., & Moss, P. T. (2003). Late Quaternary Milankovitch-scale climatic change and variability and its impact on monsoonal Australasia. *Marine Geology*, 201(1-3), 81–95. [https://doi.org/10.1016/S0025-3227\(03\)00210-X](https://doi.org/10.1016/S0025-3227(03)00210-X)
- Lisiecki, L. E., & Raymo, M. E. (2005). A Pliocene-Pleistocene stack of 57 globally distributed benthic $\delta^{18}\text{O}$ records. *Paleoceanography*, 20, PA1003. <https://doi.org/10.1029/2004PA001071>
- Liu, J., Chen, S., Chen, J., Zhang, Z., & Chen, F. (2017). Chinese cave $\delta^{18}\text{O}$ records do not represent northern East Asian summer monsoon rainfall. *Proceedings of the National Academy of Sciences of the United States of America*, 114, (15), E2987–E2988. <https://doi.org/10.1073/pnas.1703471114>
- Liu, Z., Wen, X., Brady, E., Otto-Bliesner, B., Yu, G., Lu, H., et al. (2014). Chinese cave records and the East Asia summer monsoon. *Quaternary Science Reviews*, 83, 115–128. <https://doi.org/10.1016/j.quascirev.2013.10.021>
- Maher, B. A., & Thompson, R. (2012). Oxygen isotopes from Chinese caves: Records not of monsoon rainfall but of circulation regime. *Journal of Quaternary Science*, 27(6), 615–624. <https://doi.org/10.1002/jqs.2553>
- Martinson, D. G., Pisias, N. G., Hays, J. D., Imbrie, J., Moore, T. C. J., & Shackleton, N. J. (1987). Age dating and the orbital theory of the Ice Ages: Development of a high-resolution 0 to 300,000 year chronostratigraphy. *Quaternary Research*, 27(1), 1–29. [https://doi.org/10.1016/0033-5894\(87\)90046-9](https://doi.org/10.1016/0033-5894(87)90046-9)
- Nesbitt, H. W., & Markovics, G. (1997). Weathering of grandioritic crust, long-term storage of elements in weathering profiles, and petrogenesis of siliciclastic sediments. *Geochimica et Cosmochimica Acta*, 61, 1653–1670.
- Nesbitt, H. W., Markovics, G., & Price, R. C. (1980). Chemical processes affecting alkalis and alkaline earths during continental weathering. *Geochimica et Cosmochimica Acta*, 44(11), 1659–1666. [https://doi.org/10.1016/0016-7037\(80\)90218-5](https://doi.org/10.1016/0016-7037(80)90218-5)
- Pausata, F. S., Battisti, D. S., Nisancioglu, K. H., & Bitz, C. M. (2011). Chinese stalagmite $\delta^{18}\text{O}$ controlled by changes in the Indian monsoon during a simulated Heinrich event. *Nature Geoscience*, 4(7), 474–480. <https://doi.org/10.1038/ngeo1169>
- Schulz, M., & Mudelsee, M. (2002). REDFIT: Estimating red-noise spectra directly from unevenly spaced paleoclimatic time series. *Computers & Geosciences*, 28(3), 421–426. [https://doi.org/10.1016/S0098-3004\(01\)00044-9](https://doi.org/10.1016/S0098-3004(01)00044-9)
- Stuut, J. W., Deckker, P. D., Saavedra-Pellitero, M., Bassinot, F., Drury, A., Walczak, M. H., et al. (2019). A 5.3-million-year history of monsoonal precipitation in northwestern Australia. *Geophysical Research Letters*, 46, 6946–6954. <https://doi.org/10.1029/2019GL083035>
- Thompson, P. R., Bé, A. W. H., Duplessy, J. C., & Shackleton, N. J. (1979). Disappearance of pink-pigmented *Globigerinoides ruber* at 120,000 yr BP in the Indian and Pacific oceans. *Nature*, 280(5723), 554–558. <https://doi.org/10.1038/280554a0>

- Tjallingii, R., Röhl, U., Kölling, M., & Bickert, T. (2007). Influence of the water content on X-ray fluorescence core scanning measurements in soft marine sediments. *Geochemistry, Geophysics, Geosystems*, 8, Q02004. <https://doi.org/10.1029/2006GC001393>
- Xue, G., Cai, Y., Ma, L., Cheng, X., Cheng, H., Edwards, R. L., et al. (2019). A new speleothem record of the penultimate deglacial: Insights into spatial variability and centennial-scale instabilities of East Asian monsoon. *Quaternary Science Reviews*, 210, 113–124. <https://doi.org/10.1016/j.quascirev.2019.02.023>
- Yang, X., Yang, H., Wang, B., Huang, L., Shen, C., Edwards, R. L., & Cheng, H. (2019). Early-Holocene monsoon instability and climatic optimum recorded by Chinese stalagmites. *Holocene*, 29(6), 1059–1067. <https://doi.org/10.1177/0959683619831433>
- Zhang, H., Griffiths, M. L., Chiang, J. C., Kong, W., Wu, S., Atwood, A., et al. (2018). East Asian hydroclimate modulated by the position of the westerlies during Termination I. *Science*, 362(6414), 580–583. <https://doi.org/10.1126/science.aat9393>
- Zhou, X., Sun, L., Zhan, T., Huang, W., Zhou, X., Hao, Q., et al. (2016). Time-transgressive onset of the Holocene Optimum in the East Asian monsoon region. *Earth and Planetary Science Letters*, 456, 39–46. <https://doi.org/10.1016/j.epsl.2016.09.052>

3. Conclusions and highlights for future research

3.1. Conclusions

Results and interpretations given in the individual chapters of the thesis enable to advance our understanding to the evolution of Eastern Indian Ocean climate history off Western Australia over the past 450 kyr.

In *Chapter 1*, the new XRF scanner derived terrigenous discharge records from Core SO257-18548 and IODP Site U1482 and Core SO257-18571 enable the rapid intensification of the Australian Monsoon at the end of glacial terminations with short-lived peaks in the early Holocene (~10 ka), MIS 5e (~130 ka), MIS 7 (~200, ~220 and ~240 ka), and MIS 9 (~280, ~305 and ~330 ka). Riverine transported fine-grained terrigenous discharge and aeolian dust input in southern location exhibit a clear antiphase relationship, suggesting coeval and abrupt changes towards wetter climate and increased fluvial discharge during glacial terminations and rapid re-aridification at the end of the unusually warm isotope stages MIS 9, 7 and 5e. The monsoonal precipitation highly correlate to high latitude temperature and atmospheric greenhouse gas concentrations during the past 450 kyr which indicates that increasing CO₂ and CH₄ concentrations in conjunction with a low insolation gradient between Southern Hemisphere tropics and subtropics and rising and/or high Southern Hemisphere spring-early summer insolation drove the intensification of heat low pressure cells over northwestern Australia at the end of glacial terminations. The formation of intense heat low pressure cells in the Pilbara region of northwestern Australia in late September may have played a crucial role in driving the ITCZ southwards and triggering intensified monsoonal rainfall on orbital timescales, when Southern Hemisphere insolation was at a maximum. Southward swings of the ITCZ amplified and deglacial monsoonal onsets intensified with aridification of northwestern Australia ~350 kyr ago.

In *Chapter 2*, the planktonic $\delta^{18}\text{O}$ and Mg/Ca derived SST of near surface dwelling planktonic foraminifers in sediment core tops along the Northwestern Australian Margin 15°S

and 27°S combined with temperature, salinity and oxygen isotopes of seawater along the SO257 transect, which suggested that seasonal position of the oceanic front at the edge of the IPWP was between 23° and 24° S off Northwest Cape during the post-monsoonal austral fall (May). The variances in reconstructed mix layer temperatures and salinities at the locations of Core SO257-18548 and U1482 and Core SO257-18571 indicates that the northeastern area along the Northwestern Australian Margin influence by IPWP water masses even during glacials. By contrast, the more southerly Core SO257-18571 was situated in colder, more saline and nutrient-rich mixed layer water masses, south of the southwestern IPWP margin and only influence by the IPWP during warm stages. SST maxima and salinity minima along the Northwestern Australian Margin at the end of glacial terminations I, II, III and IV (onset of MIS 1, 5e, 7e and 9) coincided with peak monsoonal precipitation proxies along the northwest Australian margin together with global $p\text{CO}_2$ peaks at high Southern Hemisphere spring (September) insolation and maxima in low latitude N-S insolation gradients (precession minima and obliquity maxima). Coherence and phase relationship between insolation forcing, atmospheric $p\text{CO}_2$, SST and monsoonal intensity (SSS and terrigenous discharge) suggest that global greenhouse gas concentrations together with low latitude insolation gradients and Southern Hemisphere spring insolation influenced the spatial extent of the IPWP in the South Hemisphere and Australian monsoonal climate.

In *Chapter 3*, carbon isotopes based on planktonic and benthic foraminifers integrated high-resolution XRF scanner derived geochemical elements counts from NorthNorthwestern Australian Margin sediment archive provide opportunity to reconstruct productivity fluctuations main out of the ITF at the western edge of the present-day IPWP over the past 450 kyr. The variability of reconstructed paleoproductivity from different locations indicate that local wind and circulation are dominant in driving productivity rather than tropical influences. Our records of $\delta^{13}\text{C}$ changes during Terminations II, III and IV along a latitudinal and depth

transect show that glacial water masses during MIS 6, 8 and 10 that are more depleted than during MIS 2-4 which may indicate the transfer and storage of carbon in the Southern Hemisphere deep -intermediate ocean during glacials.

In *Chapter 4*, the new high-resolution XRF scanner derived Australia summer monsoonal precipitation records (Log(K/Ca) integrated with published precipitation records from the northern margin and meteorological centre of the Indo-Pacific ITCZ allow us to investigate the history of northwestern Australia summer monsoonal precipitation over the past 410 kyr. We found that the in-phase behavior of interhemispheric precipitation on the precession band could be influenced by expansion and contraction in the latitudinal extent of the Indo-Pacific ITCZ. In contrast, latitudinal migration of the Indo-Pacific ITCZ could be attribute to the anti-phase behaviour of interhemispheric precipitation on the obliquity band.

3.2. Highlights for future research

Results and interpretations presented herein also shed light on possibilities for future research that would have the potential to increase our understanding on the evolution of climate from past and future. For instance: Explore the effects of tropical/Southern Hemisphere warming on the Indian Ocean Dipole (IOD) and Southern Annual Mode (SAM) along the coast of Western Australia. The challenging concept in understanding the climate variability in the eastern Indian Ocean is the IOD events and the Southern Annular Mode describes the north-south movement of the westerly wind belt. With a time resolution of 50-100 years in our sediment archives, we will not capture the variability of IOD and SAM on seasonal or decadal timescales. However, longterm changes in IOD mode and SAM may be an important component in the variability of SST, productivity (vertical mixing), wind and precipitation patterns, derived from reconstructions of climate variability along the coast of Western Australia.

Acknowledgement

I would like to dedicate my paper to all those who have offered me tremendous assistance during the three years in Kiel University.

First of all, my heartiest thanks flow to my supervisors, Prof. Dr. Wolfgang Kuhnt and Dr. Ann Holbourn, for their helpful guidance, valuable suggestions and constant encouragement both in my study and in my life. Their profound insight and accurateness about my thesis taught me so much that they are engraved on my heart. I would also like to thank the China Scholarship Council (CSC) for awarding me a PhD scholarship, which enabled me to develop the studies presented herein.

Also, I would like to express my sincere gratitude to all the researchers who have helped me with my research, I would specially like to thank Nils Andersen, Karen Bremer and Dieter Garbe-Schönberg. Particular thanks go to all the colleagues at MiPa, Institut für Geowissenschaften, for providing me a great deal of help and encouragement during these three years: Li, Janika, Sebastian, Dörte, Peng, Kenji, Johanna, Tina, Julia, and please forgive me if I forgot someone else. Particularly, I want to thank my dear roommate: Li, and the neighbour of my office and home: Janika, for their invariable encouragement and happy time sharing. I also extend my thanks to all my Chinese friends in Kiel, who spent a lot of precious time with me and helped me go through the loneliness.

I am mostly indebted to my boyfriend Pengfei Zhang (张鹏飞), who suffered from our long-distance relationship. Without his unlimited understanding and constant support, nothing would be easy.

最后我将郑重地用中文表达我对父母的感激之情，感谢你们不求回报的爱以及无穷无尽的支持。我想特别感谢我的母亲程茵老师，我知道一直以来您并不希望我离家太远，不希望我太累，但为了我的梦想，您总是隐忍，将担心化为默默的关注。您是我的铠甲，也是我的软肋，是我一直奋斗不停的动力，谢谢您！

Appendix

- * Published data for Chapter 1 is available at <https://doi.org/10.1016/j.palaeo.2021.110280>
- * Published data for Chapter 2 is available at PANGAEA.de (in processing).
- * Published data for Chapter 4 is available at <https://doi.org/10.1594/PANGAEA.918054>